

**Laser Additive Manufacturing of Embedded 3D Circuit
System and Microstructure Manipulation Using
Gaussian and Holographic Optical Elements
Reconstructed Beams**

By

Shuai Hou

Doctoral thesis submitted in partial fulfilment of the requirements of the award of Doctor
of Philosophy of Loughborough University

March 2015

© by Shuai Hou 2015

TABLE OF CONTENTS

| | |
|---|-------------|
| TABLE OF CONTENTS..... | i |
| ABSTRACT..... | iv |
| ACKNOWLEDGEMENTS | v |
| LIST OF FIGURES | vi |
| LIST OF TABLES..... | xii |
| ABBREVIATIONS | xiii |
| NOMENCLATURE | xv |
| CHAPTER 1: INTRODUCTION..... | 1 |
| 1.1 Thesis Context | 1 |
| 1.2 Research Questions | 2 |
| 1.3 Aims and objectives | 3 |
| 1.4 Chapter synopsis | 3 |
| CHAPTER 2: LITERATURE REVIEW..... | 5 |
| 2.1 Printed circuit board (PCB) manufacturing | 5 |
| 2.1.1 Additive printing technology for PCB | 5 |
| 2.1.2 Material used in conductive track formation | 7 |
| 2.1.2.1 Isotropic conductive adhesives (ICA)..... | 7 |
| 2.1.2.2 Nano-sized conductive ink..... | 11 |
| 2.1.2.3 Intrinsically conductive polymers (ICPs) | 13 |
| 2.1.3 Embedded 3D circuit system | 14 |
| 2.2 Laser additive manufacturing | 15 |
| 2.2.1 Laser principles and selective laser scanning | 16 |
| 2.2.2 Beam reconstruction with Holographic Optical Elements (HOE)..... | 20 |
| 2.2.3 Material used in laser additive manufacturing..... | 23 |
| 2.3 Numerical simulation of laser welding/cladding | 26 |
| 2.3.1 Laser energy absorption | 26 |
| 2.3.2 Molten pool formation and solidification | 30 |
| 2.3.2.1 Heat transfer and fluid flow | 31 |
| 2.3.2.2 Multiphase flow and interface tracking | 32 |
| 2.4 Summary | 35 |
| CHAPTER 3: MODELLING OF LASER WELDING/CLADDING | 37 |
| 3.1 Model description | 37 |
| 3.2 Governing equations | 40 |
| 3.2.1 Heat transfer and fluid flow | 40 |
| 3.2.2 Evolution of the L/V free surface | 42 |
| 3.2.3 Evolution of the S/L interface | 46 |
| 3.3 Model calculation methodology | 48 |
| 3.3.1 Model assumptions | 48 |
| 3.3.2 Laser welding/cladding dynamics and the treatment of source terms ... | 49 |
| 3.4 Model verification cases and simulation conditions | 56 |
| 3.5 Laser cladding of 316L stainless steel | 62 |

| | | |
|---|---|------------|
| 3.5.1 | Development of the molten pool under Gaussian beam | 62 |
| 3.5.2 | Comparison between the Gaussian and Pedestal cladding | 66 |
| 3.6 | Laser keyhole welding of mild steel | 75 |
| 3.6.1 | Keyhole formation and development | 75 |
| 3.6.2 | Keyhole collapse and solidification | 79 |
| 3.7 | Laser melting of HDPE powder | 80 |
| 3.8 | Summary | 83 |
| CHAPTER 4: LASER MELTING OF HIGH DENSITY POLYETHYLENE POWDER | | 86 |
| 4.1 | Experimental procedure | 86 |
| 4.1.1 | Powder deposition and laser melting method | 86 |
| 4.1.2 | Sample preparation and characterisation | 88 |
| 4.2 | Tensile test and sample microstructure analysis | 90 |
| 4.2.1 | The influence of input laser power | 90 |
| 4.2.2 | The influence of scanning speed | 99 |
| 4.2.3 | The influence of scan spacing | 103 |
| 4.3 | Thermal analysis | 105 |
| 4.3.1 | Temperature measurement using IR camera | 105 |
| 4.3.2 | Thermal tests using DSC | 106 |
| 4.4 | Summary | 113 |
| CHAPTER 5: LASER CURING OF SILVER PASTE | | 115 |
| 5.1 | Experimental procedures | 115 |
| 5.1.1 | Silver paste investigation | 115 |
| 5.1.2 | Paste deposition and curing | 116 |
| 5.1.3 | Characterisation | 119 |
| 5.2 | Paste characterisation results | 120 |
| 5.3 | Electrical resistivity measurement | 124 |
| 5.4 | Morphology and microstructure | 126 |
| 5.4.1 | A comparison between laser and oven cured samples | 126 |
| 5.4.2 | The influence of laser input power and scanning speed | 129 |
| 5.4.3 | A comparison between Gaussian and HOE beam cured samples | 132 |
| 5.5 | Building a 2D flexible circuit system | 134 |
| 5.6 | Summary | 136 |
| CHAPTER 6: LASER MELTING OF COPPER/HDPE POWDER MIXTURE | | 138 |
| 6.1 | Experimental procedure | 138 |
| 6.1.1 | Set up HOE based galvo scanning system | 138 |
| 6.1.2 | Laser beam profile characterisation | 140 |
| 6.1.3 | Copper/HDPE mixture preparation and laser melting process | 144 |
| 6.1.4 | Sample characterisation | 146 |
| 6.2 | Raw copper/HDPE mixture characterisation | 147 |
| 6.3 | Electrical resistivity analysis | 148 |
| 6.4 | Laser processing mechanism investigation | 154 |
| 6.4.1 | The investigation of G-s-3/7 series | 154 |
| 6.4.1.1 | Microstructure analysis | 155 |

| | | |
|--------------------------------------|---|------------|
| 6.4.1.2 | The movement of copper particles in HDPE matrix..... | 159 |
| 6.4.2 | The investigation of G-s-6/4 series | 162 |
| 6.4.2.1 | Microstructure analysis | 163 |
| 6.4.2.2 | Temperature measurement during laser melting process | 167 |
| 6.4.3 | The investigation of G-s series with different copper/HDPE ratios | 169 |
| 6.4.4 | The investigation of G-r-6/4 series | 172 |
| 6.4.5 | The investigation of P-s-6/4 series..... | 174 |
| 6.5 | Additive manufacturing of multi-layer embedded circuit system | 177 |
| 6.5.1 | Circuit system design | 177 |
| 6.5.2 | Additive manufacturing of 3D embedded timer circuits and its performance test..... | 178 |
| 6.6 | Summary | 181 |
| CHAPTER 7: CONCLUSIONS | | 184 |
| 7.1 | Development of FEM model | 184 |
| 7.2 | Circuit substrate manufacturing using HDPE powder..... | 186 |
| 7.3 | Circuit manufacturing using silver paste / copper mixture and 3D embedded system fabrication | 188 |
| CHAPTER 8: FURTHER WORK | | 193 |
| REFERENCES..... | | 195 |
| APPENDIX..... | | 213 |

ABSTRACT

In Printed Circuit Board (PCB) manufacturing, making the conductive tracks 3D and embedding the electronic components in substrate can effectively reduce the circuit board volume, and improve the power delivery performance. Laser based additive manufacturing has been developed for many years but currently it is still used to create non-functional product. This PhD work will combine the two technologies together to generate a complete 3D embedded circuit system. In addition, the laser beam will be reconstructed using Holographic Optical Elements (HOE) to control the microstructure of the product.

A finite element method (FEM) model was established to describe the material thermo-fluid and phase transition behaviour at different beam irradiance distributions. Steel wire cladding, steel keyhole welding and polymer powder melting were used for model verification. An experiment of laser melting of high density polyethylene (HDPE) as a circuit substrate was then carried out. Fully dense HDPE components can be generated using laser and their tensile strength (7.97 ± 0.03 MPa) and elongation at break (E_{ab} , $92.7 \pm 6.8\%$) were comparable with the compression moulding samples; according to thermal analysis using Differential Scanning Calorimetry (DSC), the growth of imperfect spherulites was revealed.

In conductive circuit manufacturing, two different materials were selected: silver paste and copper/HDPE powder mixture. The laser cured silver paste exhibits a lower electrical resistivity ($0.65 \pm 0.03 \times 10^{-4} \Omega\text{cm}$) than oven cured sample ($1.32 \pm 0.04 \times 10^{-4} \Omega\text{cm}$) since its porous structure reduce the distance between different silver flakes. A pedestal beam can reduce the laser induced thermal ejection due to its low Marangoni force on the sample surface. A flexible 2D circuit board is manufactured using silver paste on a HDPE substrate. The copper/HDPE mixture was processed using a galvo scanning system, which included a commercial Gaussian laser and a self-designed novel HOE laser. The copper was found melted above a copper/HDPE ratio of 6/4 and its electrical resistivity ($0.35 \pm 0.04 \times 10^{-4} \Omega\text{cm}$) can be reduced to 20 times of pure copper. By using the pedestal beam, the outward flow of copper particles could be reduced. A new process is developed to manufacture 3D embedded circuit system using copper/HDPE mixture as conductive tracks and HDPE as substrate. It successfully demonstrated functional electronic devices can be achieved by additive layer manufacturing of dissimilar materials.

ACKNOWLEDGEMENTS

I would like to register my sincere thanks to my supervisor, Professor John Tyrer. He provided me such a wonderful opportunity to do research on this subject. Without his brilliant advice and great encouragement, the completion of this project would be impossible. Special thanks to Dr David Hutt for his help in circuit system design and manufacturing; and Mr Henk Versteeg for the assistance in thermo-fluid modelling work.

I would also like to thank the technical staff for their support in the experiments. I greatly appreciate the kindly help provided by David Britton and Mark Capers in the laser lab; and Andy Sandaver who is retired now but gave me a lot of help in the material characterisation lab.

I must thank my colleagues and friends in both Wolfson School and Department of Materials, for their encouragement throughout my PhD career. Special thanks should go to Dr Daniel Lloyd for his help in manufacturing the HOE, Siyuan Qi for his help in synthesising copper powder, Nick Goffin and Lewis Jones for their help in laser work.

Finally I would like to thank my parents Dianlin Hou and Guangfeng Li for their support and inspiration through my life and my girlfriend Liping Zhang for her encouragement during the final stage of my PhD.

LIST OF FIGURES

| | |
|--|----|
| Figure 2.1: Schematic representations of (a) Screen printing process; (b) Inkjet printing process | 6 |
| Figure 2.2: Electrical conductivity against conductor content curve, known as ‘percolation threshold’ | 8 |
| Figure 2.3: (a) Difference between ‘surface induced melting point’ and ‘end melting point’ with varied particle sizes for Pb [36]; (b) Schematic representation of the QLL thickness for different particles at a given temperature [35] | 12 |
| Figure 2.4: Examples of (a) surface mounting system; (b) embedded system | 14 |
| Figure 2.5: Schematic representation of a galvo scanner based additive manufacturing machine | 17 |
| Figure 2.6: Schematic representation of fused deposition based additive manufacturing with (a) powder feeder and (b) wire feeder | 19 |
| Figure 2.7: Non-uniform energy distribution during (a) Gaussian beam and (b) ‘Top Hat’ beam scan | 20 |
| Figure 2.8: (a) Surface pattern of HOE; (b) 2D arrays of pixels; (c) working mechanism of the HOE pixel; (d) An example of beam reconstruction [133] | 22 |
| Figure 2.9: Chemical structure of polyethylene | 23 |
| Figure 2.10: Structure of the crystalline phase and amorphous phase | 24 |
| Figure 2.11: The DSC examples of Nylon-12 and HDPE showing the difference in super-heating region | 25 |
| Figure 2.12: Photon interaction with different polymers: (a) thermoplastic; (b) thermoset | 28 |
| Figure 2.13: Different polarised beams of laser | 29 |
| Figure 2.14: Illustrations of (a) explicit and (b) implicit method [96] | 32 |
| Figure 3.1: Schematic representation of the laser material interaction process | 38 |
| Figure 3.2: Laser welding/cladding model structure | 39 |
| Figure 3.3: A schematic representation of differential control volume, where E , $\mathbf{q}\mathbf{x}(\mathbf{y})$ and $p_u(\mathbf{v})$ represent the stored energy, heat flow term and fluid flow term respectively .. | 40 |
| Figure 3.4: Illustration of level set function | 43 |
| Figure 3.5: The comparison between (a) original Heaviside function; (b) smoothed Heaviside function; (c) original Delta function; (d) smoothed Delta function | 44 |
| Figure 3.6: Illustration of velocities on the L/V interface, where the interface velocity is a sum of fluid velocity normal to the interface and evaporation velocity | 45 |
| Figure 3.7: S/L interface and velocity/temperature conditions of the liquid and solid phases | 47 |
| Figure 3.8: Schematic representation of the 2D cross section model | 49 |
| Figure 3.9: Laser profile of (a) Gaussian distribution; (b) uniform Pedestal distribution .. | 54 |
| Figure 3.10: The comparison between a (a) stationary; (b) line source and (c) time-dependant Gaussian energy distributions on a 2D substrate | 55 |
| Figure 3.11: An example of close-packing of equal spheres model (face-centred cubic) .. | 59 |
| Figure 3.12: Model mesh for (a) cladding: Case A and B; (b) keyhole welding: Case C; (c) | |

| | |
|--|----|
| conduction welding: D and E..... | 61 |
| Figure 3.13: Image registration between simulation and experiment molten pool shape . | 62 |
| Figure 3.14: Temperature field and fluid flow pattern of the molten pool for case A (260W-1.6mm/s)..... | 63 |
| Figure 3.15: Velocity vectors (a) u and (b) v on the L/V interface of case A (260W-1.6mm/s) | 65 |
| Figure 3.16: Temperature field and fluid flow pattern of the molten pool for case B (260W-1.6mm/s)..... | 67 |
| Figure 3.17: Temperature distribution on the L/V interface for case A and B (260W-1.6mm/s)..... | 68 |
| Figure 3.18: Velocity vectors (a) u and (b) v on the L/V interface of case B (260W-1.6mm/s) | 70 |
| Figure 3.19: L/V interface central point temperature variation with time for case A (260W-1.6mm/s) and B (260W-1.6mm/s)..... | 71 |
| Figure 3.20: Comparison between simulation and practical molten pool geometries for laser cladding at different conditions | 73 |
| Figure 3.21: Temperature field and fluid flow pattern of the molten pool during the keyhole development in case C (500W-10mm/s)..... | 75 |
| Figure 3.22: (a) L/V interface central point temperature variation with time for case C (500W-10mm/s) and (b) surrounding vapour temperature field at t=15ms..... | 76 |
| Figure 3.23: L/V interface central point velocity in Y axis variation with time for case C (500W-10mm/s)..... | 77 |
| Figure 3.24: Keyhole depth variation with time for case C (500W-10mm/s) | 78 |
| Figure 3.25: Directions of three forces on the keyhole surface | 79 |
| Figure 3.26: Temperature field and fluid flow pattern of the molten pool during the keyhole collapse in case C (500W-10mm/s) | 80 |
| Figure 3.27: Temperature field and fluid flow pattern of the molten pool for (a) case D (2W-10mm/s) and (b) case E (2W-10mm/s)..... | 81 |
| Figure 3.28: Comparison between simulation and practical molten pool geometries for laser melting of HDPE at 2W-10mm/s | 82 |
| Figure 3.29: Molten pool geometries, temperature field and fluid flow pattern for laser melting of HDPE at 4W-10mm/s..... | 83 |
| Figure 4.1: Structure of (a) the powder bed and (b) steel backup plate..... | 86 |
| Figure 4.2: Setting up an IR thermal camera with a filter | 88 |
| Figure 4.3: (a) Tensile bar raster scanning programme and (b) product shape during manufacturing | 89 |
| Figure 4.4: Preparation of the specimen for microstructure characterisation: (a) scalpel cutting; (b) liquid nitrogen cutting..... | 89 |
| Figure 4.5: 60° view (left) and top view (right) of the tensile bar samples at different input power for series G-X-240-0.2 | 91 |
| Figure 4.6: Sample series G-X-240-0.2 variation with input power (a) tensile strength and (b) Eab..... | 93 |
| Figure 4.7: Stress-strain plots for sample G-11-240-0.2..... | 94 |
| Figure 4.8: Powder particle melting/cooling situation ('c' in the last figure represent | |

| | |
|--|-----|
| ‘cooling’) | 95 |
| Figure 4.9: Schematic representation of the particle phase transition during a heating/cooling process..... | 96 |
| Figure 4.10: The SEM cross-section images of (a) scalpel cut and (b) liquid N2 cut for G-10-260-0.2..... | 97 |
| Figure 4.11: The SEM cross-section images of sample series G-X-240-0.2..... | 98 |
| Figure 4.12: 60° view (left) and top view (right) of the tensile bar samples at different scanning speed for series G-10-X-0.2..... | 100 |
| Figure 4.13: Sample series G-10-X-0.2 variation with scanning speed (a) tensile strength and (b) Eab | 101 |
| Figure 4.14: The SEM cross-section images of sample series G-10-X-0.2..... | 102 |
| Figure 4.15: 60° view (left) and top view in the central region (right) of the tensile bar samples for series G-10-X-X | 103 |
| Figure 4.16: Schematic representations of surface lines formation during raster scan (a) low scan spacing; (b) high scan spacing | 104 |
| Figure 4.17: Sample G-10-480-0.1, G-10-240-0.2 and G-10-160-0.3 (a) tensile strength and (b) Eab | 104 |
| Figure 4.18: Temperature patterns of sample G-10-240-0.2 at (a) t=0.68s, (b) t=3.18s; (c) t=5.64s; (d) t=6.88s..... | 105 |
| Figure 4.19: Temperature variation with time for (a) points A, B and C of sample G-10-240-0.2; (b) points A of sample G-10-240-0.2 and G-12-240-0.2 | 106 |
| Figure 4.20: Plots of DSC tests at different conditions: (a) G-X-240-0.2 series and (b) G-10-X-0.2 series..... | 107 |
| Figure 4.21: Structure of a spherulite | 108 |
| Figure 4.22: 1 st order derivative of the heat flow against temperature at different conditions: (a) G-X-240-0.2 series and (b) G-10-X-0.2 series | 109 |
| Figure 4.23: Melting curves of LDPE after varies annealing heat treatment plotted by Menczel et al [126] | 110 |
| Figure 4.24: 2 nd heating of HDPE sample cooling at different rates | 111 |
| Figure 4.25: (a) Illustration of spherulites growth at fast/slow cooling rate and the formation of imperfect spherulites; (b) Pakula's [128] spherulites distribution measurement at different cooling rate, where from 1-6, the water bath temperature was setting as 0, 25, 50, 70, 80, 90°C | 112 |
| Figure 5.1: (a) Stencil printing method and (b) laser curing of deposited silver paste.... | 116 |
| Figure 5.2: Beam construction for: (a) Gaussian irradiance distribution; (b) HOE modified distribution | 117 |
| Figure 5.3: Laser curing system with both Gaussian and HOE head | 119 |
| Figure 5.4: Schematic representation of 4 point probe | 120 |
| Figure 5.5: FT-IR patterns of (a) paste matrix on glass film and (b) glass film | 121 |
| Figure 5.6: TGA curve of the silver paste (from room temperature to 800°C, at a heating rate of 10°C/min) | 122 |
| Figure 5.7: DSC results of the silver paste before and after HOE laser curing (P-2.3-1)..... | 123 |
| Figure 5.8: the cross-section profile of oven cured sample at 150°C for 0.5h..... | 124 |
| Figure 5.9: Resistivity comparison between Gaussian beam, Pedestal HOE beam and cured | |

| | |
|---|-----|
| sample at: (a) varied input power at constant scanning speed 1mm/s; (b) varied scanning speed at constant input power 2.3W | 125 |
| Figure 5.10: The surface morphology of sample (a) P-2.3-0.1 by Pedestal HOE laser; (b) 150°C-0.5h by oven | 126 |
| Figure 5.11: The cross-sectional SEM images of: (a) P-2.3-0.1; (b) P-2.3-1 and (c) oven (150°C-0.5h) cured samples..... | 127 |
| Figure 5.12: The reduction of distance between silver flakes during polymer degradation in laser curing, the SEM image was achieved at P-2.3-0.3..... | 128 |
| Figure 5.13: Surface morphology measured by Alicona for samples: (a) P-2.3-0.1, (b) P-2.3-0.3, (c) P-2.3-0.6, (d) P-2.3-1, (e) P-1.5-1, (f) P-1.9-1, (g) P-2.7-1, (h) P-3.1-1 | 130 |
| Figure 5.14: Images achieved from high speed video for samples: (a) P-2.3-0.1; (b) P-2.3-1 and (c) the mechanism of bubble growth at different scanning speeds | 131 |
| Figure 5.15: Direct comparison between an undamaged track (a) P-2.3-1 and damaged track (b) P-3.1-1 | 132 |
| Figure 5.16: Photography of laser cured samples at 2.3W and different scanning speeds using Gaussian and Pedestal beam | 133 |
| Figure 5.17: Schematic of timer circuit and list of different electronic components | 134 |
| Figure 5.18: The screen printing system used in the timer circuit pattern deposition | 134 |
| Figure 5.19: (a) Printed timer circuit pattern; (b) original cured circuit with electronic components; (c) bent circuit with electronic components, where LED is flashing .. | 135 |
| Figure 6.1: (a) Schematic representation and (b) setting up of the HOE galvo scanning laser | 139 |
| Figure 6.2: Internal structures of (a) 3X beam expander; (b) HOE box; (c) galvo scanner | 140 |
| Figure 6.3: (a) Burn print for Gaussian beam; (b) burn print for Pedestal beam achieved from galvo scanning system; (c) burn print 3D profile for Gaussian beam; (d) burn print 3D profile for Pedestal beam..... | 141 |
| Figure 6.4: 3D burn print profiles of HOE Pedestal beam achieved from (a) stand-off alteration test; (b) spot location alternation test..... | 142 |
| Figure 6.5: Comparison between samples generated by Gaussian and Pedestal beams using the same raster scan programme: 8W-240mm/s-0.3mm | 143 |
| Figure 6.6: The edge effect of beam shape during a single track scan | 144 |
| Figure 6.7: Laser melting of copper/HDPE conductive track on a HDPE substrate and the structure of micron-copper particles with SAM coating..... | 145 |
| Figure 6.8: High resolution XPS scans for ODT coated and uncoated copper powders at: (a) Cu2p region; (b) O1s region; (c) C1s region and (d) S2p region | 147 |
| Figure 6.9: (a) copper/HDPE powder mixture (6/4) and (b) pure copper particle | 148 |
| Figure 6.10: Cross-section area calculation using ImageJ for sample G-s-3/7-15-120 (a) raw image; (b) processed image | 149 |
| Figure 6.11: Resistivity variation for sample series: (a) G-s-3/7; (b) G-s-6/4 at different scanning speeds; (c) G-s-6/4 at different input powers. The letter 'X' means the sample resistivity value is quite high and can be thought as dielectric..... | 150 |
| Figure 6.12: Resistivity variation for sample series G-s-X-20-120 at different copper | |

| | |
|--|-----|
| volume content..... | 151 |
| Figure 6.13: Resistivity variation for sample series: G-r-6/4 for raster scanning programme | 152 |
| Figure 6.14: Resistivity variation for sample series: G-s-6/4 and P-s-6/4 at constant input power of 8W and different scanning speeds | 153 |
| Figure 6.15: Surface morphology of sample series G-s-3/7 achieved by SEM..... | 154 |
| Figure 6.16: Microstructures of sample G-s-3/7-15-120 from: (a) top view; (b) cross-section view | 156 |
| Figure 6.17: Comparison between a 5 layer copper/HDPE mixture (3/7) and pure HDPE sample at the same laser raster processing condition of Gaussian beam, 10W power, 240mm/s scanning speed, 0.2mm scan spacing..... | 157 |
| Figure 6.18: Microstructures of sample G-s-3/7-20-120 from: (a) top view; (b) cross-section view | 158 |
| Figure 6.19: Copper/HDPE (3/7) mixture melting/cooling situation ('c' in the last figure represent 'cooling')..... | 160 |
| Figure 6.20: High magnification microstructures of sample G-s-3/7-20-120 from cross-section view | 161 |
| Figure 6.21: Surface morphology of sample series G-s-6/4 achieved by SEM..... | 163 |
| Figure 6.22: Microstructures of sample G-s-6/4-20-120 from: (a) top view; (b) cross-section view | 164 |
| Figure 6.23: High magnification microstructures of sample G-s-6/4-20-120: (a) laser direct melting zone (top view); (b) laser direct melting zone (cross-section view); (c) heat conduction affected zone (top view); (d) heat conduction affected zone (cross-section view) | 165 |
| Figure 6.24: Schematic representation of the melting mechanism for the copper particles with cracks | 166 |
| Figure 6.25: Temperature patterns of sample G-s-6/4-20-120 at (a) $t=0.02s$, (b) $t=0.14s$; (c) $t=0.22s$; (d) $t=0.32s$ | 167 |
| Figure 6.26: Temperature variation with time for track middle points of sample G-s-6/4-20-120..... | 168 |
| Figure 6.27: Surface morphology of sample series G-s-X/Y-20-120 achieved by SEM..... | 169 |
| Figure 6.28: Temperature variation with time for track middle points of sample G-s-pure copper-20-120 | 170 |
| Figure 6.29: Microstructures of sample G-s-pure copper-20-120 from: (a) top view; (b) cross-section view | 171 |
| Figure 6.30: Surface morphology of sample series G-r-6/4 achieved by SEM | 173 |
| Figure 6.31: Comparison between sample (a) G-r-6/4-20-120 and (b) G-s-6/4-20-120, where the spot and red arrow represent the Gaussian beam and its scanning directly, respectively | 174 |
| Figure 6.32: Surface morphology of sample series G-s-6/4 and P-s-6/4 at constant input power of 8W and different scanning speeds achieved by SEM..... | 175 |
| Figure 6.33: Microstructures of laser direct melting zone of sample (a) G-s-6/4-8-20 and (b) P-s-6/4-8-20 | 176 |
| Figure 6.34: schematic representation of 3D embedded circuit system, where the black and | |

| | |
|--|-----|
| red lines are the 1 st and 2 nd circuit layer; yellow blocks are electronic components | 177 |
| Figure 6.35: The additive manufacturing process of a 3D timer circuits system (transverse view) | 179 |
| Figure 6.36: Finished sample at each step of the additive manufacturing process..... | 180 |
| Figure 6.37: Flashing conditions of the LED acquired from a video | 181 |
| Figure 7.1: The novel production cycle for a FEM assisted HOE design system | 185 |
| Figure A.1: (a) Setting up of the IR camera calibration system; (b) location of the measured point | 213 |
| Figure A.2: Calibration plot of temperature with filter against direct measured temperature | 214 |
| Figure B.1: Original stress-strain plots for HDPE tensile test ('G-X-X-X' represents 'Gaussian beam-power-scanning speed-scan spacing')..... | 222 |

LIST OF TABLES

| | |
|--|-----|
| Table 3.1: Governing equations and source terms used in the model..... | 57 |
| Table 3.2: Five different cases in the simulation | 58 |
| Table 3.3: Material properties and processing parameters used in the simulation | 59 |
| Table 4.1: Selected laser processing conditions for tensile test | 89 |
| Table 5.1: Laser and oven curing conditions | 118 |
| Table 6.1: Selected laser melting conditions for a single layer conductive track | 146 |
| Table 6.2: Measured widths of sample series G-s-3/7 (unit: mm)..... | 155 |
| Table 6.3: Measured widths of sample series G-r-6/4 and G-s-6/4 (unit: mm) | 173 |
| Table 6.4: Measured widths of sample series G-s-6/4 and P-s-6/4 (unit: mm)..... | 175 |
| Table C.1: The resistivity comparisons of silver paste tracks cured at different conditions | 223 |
| Table D.1: The resistivity comparisons of sintered copper/HDPE mixture at different conditions (the measured length is fixed as 1cm)..... | 225 |

ABBREVIATIONS

| | |
|--------|--|
| ALE | Arbitrary lagrangian eulerian |
| ATR | Attenuated total reflection |
| CAD | Computer aided design |
| CNC | Computer numerical control |
| CW | Continuous wave |
| DOD | Drop-on-demand |
| DPM | Degree of particle melt |
| DSC | Differential scanning calorimetry |
| Eab | Elongation at break |
| EM | Electromagnetic |
| FEM | Finite element method |
| HDPE | High density polyethylene |
| HOE | Holographic optical elements |
| ICA | Isotropic conductive adhesive |
| ICPs | Intrinsically conductive polymers |
| IFTA | Iterative Fourier transform algorithm |
| IR | Infrared |
| LDPE | Low density polyethylene |
| LLDPE | Linear low density polyethylene |
| MCB | Moulded circuit board |
| MFI | Melt flow index |
| Nd:YAG | Neodymium-doped yttrium aluminium garnet |
| ODT | Octadecanethiol |
| OPD | Optical penetration depth |
| PCB | Printed circuit boards |
| PE | Polyethylene |
| PEDOT | Poly(3,4-ethylenedioxythiophene) |

| | |
|------|----------------------------------|
| PEEK | Polyether ether ketone |
| PMMA | Poly(methyl methacrylate) |
| PP | polypropylene |
| PSS | Poly(styrenesulfonate) |
| PWM | Pulse width modulation |
| QLL | Quasi-liquid layer |
| SAM | Self-assembled monolayer |
| SEM | Scanning electron microscope |
| TGA | Thermo-gravimetric analysis |
| UV | Ultraviolet |
| VoF | Volume of fluid |
| XPS | X-ray photoelectron spectroscopy |

NOMENCLATURE

| | | |
|---|---------------------------------------|---|
| A | mm^2 | Cross-section area |
| a | mm | Laser beam size |
| b | | Small constant |
| C | | Large-valued constant |
| C_p | $\text{J}/(\text{kg}\cdot\text{K})$ | Heat capacity |
| d | m | Distance from the zero level set |
| E_d | $\text{W}/(\text{mm}/\text{s})$ | Beam energy density |
| $\dot{E}_{in}/\dot{E}_{out}/\dot{E}_g/\dot{E}_{st}$ | J | Energy inflow/outflow/generation/storage |
| e_f | m | Half of the level set interface ‘band’ thickness |
| f_L | | Liquid fraction |
| H | | Heaviside function |
| H_{EN} | J | Enthalpy |
| h_c | $\text{W}/(\text{m}^2\cdot\text{K})$ | Thermal convection coefficient |
| \mathbf{I} | | Unit diagonal matrix |
| I | A | Current |
| J | $1/(\text{m}^2\cdot\text{s})$ | Net evaporation rate |
| k | $\text{W}/(\text{m}\cdot\text{K})$ | Thermal conductivity |
| k_d | | Damping constant |
| L_f | J/kg | Latent heat of fusion |
| L_v | J/kg | Latent heat of evaporation |
| l | mm | Distance between two inner probes for 4 point probe |
| l_s | mm | Scanning length |
| M | Kg/mol | Molecular weight |
| m | kg | Mass of single molecule |
| \dot{m} | $\text{kg}/(\text{m}^2\cdot\text{s})$ | Mass evaporation rate |
| N | | Properties of power mixture |
| n | | Refractive index |

| | | |
|----------------------------|------------------|---|
| \vec{n} | | Normal direction |
| P | W | Laser power |
| p | Pa | Pressure |
| p_0 | Pa | Atmospheric pressure |
| $p_{sat}(T)$ | Pa | Saturated vapour pressure |
| Q | J | Total energy during laser processing |
| \dot{q} | W/m ² | Heat flux rate |
| R | J/(K·mol) | Universal gas constant |
| R_e | Ωcm | Resistivity |
| R_f | | Reflectivity |
| r_0 | | Reinitialisation parameter |
| S | | Source terms |
| \mathbf{T} | | Deviatoric stress tensor |
| T | K | Temperature |
| T_l | K | Liquidus melting temperature |
| T_{lv} | K | Liquid-vapour equilibrium temperature |
| T_s | K | Solidus melting temperature |
| T_{vapour} | K | Average temperature of the vapour phase |
| t | S | Time |
| \vec{t} | | Tangential direction |
| U | m/s | Velocity vector |
| u | m/s | Velocity in x direction |
| u_s | mm/s | Beam scanning velocity |
| $\overrightarrow{u^{evp}}$ | m/s | Evaporation velocity |
| $\overrightarrow{u_{int}}$ | m/s | Interface velocity |
| V | V | Voltage |
| v | m/s | Velocity in y direction |
| $V\%$ | | Volume fractions |
| W | J | Work for adhesive |

| | | |
|---------------|-------------------|---------------------------------|
| $\%S$ | | Sulphur content |
| α_b | | Back-scattered flux coefficient |
| α_e | | Evaporation flux coefficient |
| β | 1/K | Thermal expansion coefficient |
| Γ | | Curvature |
| γ | N/m | Surface tension coefficient |
| δ | | Dirac Delta function |
| ε | | Thermal emissivity |
| η | | Energy absorptivity |
| $\eta(x)$ | | Level set function perturbation |
| θ | ° | Angle of incidence |
| θ_A | ° | Contact angle |
| μ | Pa·s | Viscosity |
| ρ | kg/m ³ | Density |
| Σ | J/K | Boltzmann constant |
| σ | | Stress tensor |
| σ_{LV} | J | Interface tension |
| $\Phi(x, t)$ | | Signed distance function |
| ∇ | | Divergence term |

CHAPTER 1: INTRODUCTION

This chapter presents a brief background introduction to this research work and states the research questions and aims of the project. A synopsis of each chapter is also listed.

1.1 Thesis Context

Printed circuit board (PCB) is an extremely important part in today's industrial activities. Modern electronics need low manufacturing loss, environmentally friendly processes and the integration of electronics as a part of other structures. The traditional PCB is a device that interconnects electronic components using conductive tracks laminated onto a dielectric substrate. Since the electronic components need to be placed in a planar array, the design freedom is reduced and space requirement is increased. Making the conductive tracks 3D and embedding the electronic components in substrate cannot only reduce the circuit volume, but also significantly reduce the footprint between different electronic components and improve power delivery performance. However, this 3D structure is difficult to manufacture due to its high complexity. This thesis focuses on an innovative technique to generate 3D PCB – laser additive manufacturing.

Laser additive manufacturing is mainly used to build non-functional part such as prototypes. Research is mainly carried out on the product mechanical performance and it also lacks a complete understanding of the material characteristics during laser processing. This thesis addresses the issue of functional dissimilar materials additive manufacturing. The work presented here includes the generation of 3D PCB using dissimilar materials, laser beam reconstruction, and simulation of material behaviour during laser processing. This provides an opportunity to expand the application of additive manufacturing in industry; while optimising the laser based manufacturing by using holographic optical elements (HOE) to gain control of the illuminating beam.

1.2 Research Questions

Traditional laser sintering and cladding manipulate round laser beams using control of the laser power/energy parameters to build up components using a wide range of polymers and metals. The majority of these components suffer some level of porosity. Central to the approach taken in this research is that if 3D control of the focussed beam in terms of profile/shape and energy distribution were possible – then a level of control not currently widely investigated could provide a breakthrough in the manufacturing of fully dense 3D components. According to the research context, if such control is available the following questions are raised in this project:

- Can we establish a mathematical model to predict the heat distributions and flow pattern during laser processing with different beam irradiance distributions?
- Can we generate fully dense polymeric components as the circuit substrate?
- Can we make use of different polymers such as high density polyethylene (HDPE) which presently thought of as unsuitable for laser additive manufacturing?
- Does the redistribution of input energy provide a means of controlling/improving the properties of the resultant polymeric part?
- Can we use laser to generate conductive circuits which have similar or improved performance compared with conventional method?
- Can we make circuits using low cost copper during laser processing without oxidation?
- Does the redistribution of input energy provide a method of controlling/improving the properties of the resultant conductive circuits?

- Can we generate a 2D circuit on flexible substrate using laser curing?
- Can we extend the present 2D circuit system to 3D using laser additive manufacturing technology?

1.3 Aims and objectives

The ultimate goal of this project is to generate a complete 3D PCB system using additive manufacturing. This includes laser manufacturing of both dielectric substrate and conductive track. The original Gaussian beam and HOE reconstructed beam are both used in the manufacturing process to gain control of the processed materials. The second major goal of this project is to investigate the material behaviour when processed by laser. To achieve these goals, a number of steps have to be investigated and experimented with. Firstly, a mathematic model is established using finite element method (FEM) so that the laser processing mechanism and influence of beam profile can be theorised. Then investigation of laser processing for both substrate (using high density polyethylene (HDPE)) and conductive track (using silver paste and copper/HDPE powder mixture) are carried out. The final step is combining individual manufacturing steps together to generate embedded 3D PCB.

1.4 Chapter synopsis

Chapter 2 is a literature review of the areas of interest in this project, which includes PCB manufacturing, laser processing and additive manufacturing, beam reconstruction, and laser welding/cladding simulation.

Chapter 3 is the simulation work for laser welding/cladding. Heat transfer, fluid flow and phase transition are included in this model and the influences of different beam irradiance distributions in the molten pool formation are also investigated. The model is verified by

relative experiments.

Chapter 4 is the main body of the results concerning laser melting of HDPE, which will be used as the substrate material in PCB manufacturing. Investigation includes the mechanical properties, microstructures and thermal properties. In addition, the mechanism of imperfect crystalline growth during laser processing of HDPE is presented.

Chapter 5 is the main body of the results concerning laser curing of silver paste, which will be used as the conductive track material in PCB manufacturing. Different beam irradiance distributions are used and investigation includes electrical resistivity, surface morphology, microstructures and thermal properties. In addition, a flexible PCB is designed and manufactured using silver paste and HDPE substrate.

Chapter 6 is the main body of the results concerning laser melting of copper/HDPE powder mixture, which will be used as the conductive track material in PCB manufacturing. Different beam irradiance distributions are used and investigation includes electrical resistivity, microstructures and thermal properties. In addition, a 3D embedded PCB is designed and manufactured using copper/HDPE mixture and HDPE substrate.

Chapter 7 gives the conclusions that are drawn from the works in this project.

Chapter 8 gives the ideas for further work.

CHAPTER 2: LITERATURE REVIEW

This chapter presents a review of the current work relating to this project, which involves PCB manufacturing, laser processing and additive manufacturing, beam reconstruction, and laser welding/cladding simulation.

2.1 Printed circuit board (PCB) manufacturing

The PCB is a structure which can provide both the physical mounting of electronic components as well as the electrical interconnections between them. The history of PCB development begins in the early of 20th century but it has not been in commercial use until 1950s [1]. The basic model of a PCB consists of a dielectric substrate and a single-layer, single-sided conductive pattern on it. A structure with higher complexity can be achieved by producing multi-layer and double-sided structures [2]; where the interconnections between different layers are generated by plated through-holes [3]. The traditional manufacture technique of PCB is usually a subtractive process, where the term used ‘printing’ is somewhat of a misnomer when describing it. This process includes depositing a metallic foil (e.g. copper) on the substrate, then covering etch resist on the designed track pattern and finally using etchant to remove the excess material and leaving the copper tracks [2]. This process has a long production cycle and will lead a waste of materials; meanwhile, since the solvent used in the etching step is corrosive, toxic waste is usually generated [4, 5]. To solve these problems, the concept of additive process has been generated, i.e. directly deposit the conductive track on the substrate surface.

2.1.1 Additive printing technology for PCB

Screen printing

For the traditional printing world, the screen printing technique is widely used. This is a process based on the application of mesh and squeegee. A typical screen printing process

is shown in Figure 2.1.a, from which, the screens are generally woven-like cloth fabrics and the paste/ink must flow through the screen mesh under pressure created by the squeegee movement, and at those parts of fabrics no paste/ink should be pressured through [3]. Moreover, the parameters like mesh density and thickness are the determining factors of the emulsion thickness of the paste/ink.

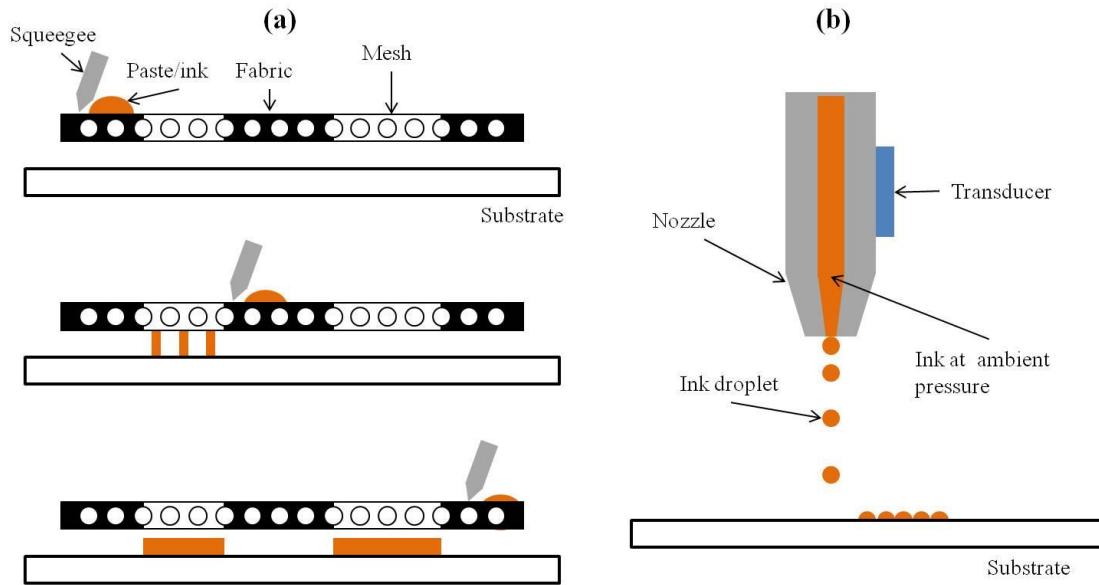


Figure 2.1: Schematic representations of (a) Screen printing process; (b) Inkjet printing process

Inkjet printing

However, the screen printing method can only create 2D output in the X-Y plane. A more flexible deposition method is Drop-on-demand (DOD) inkjet printing, which is represented in Figure 2.1.b. In this computer assisted process, the ink is jetted from the nozzle and deposited on the substrate, where a piezo or thermal transducer is applied to provide a suitable pressure for the jetting process. This technique has been widely used in electronics manufacturing [4, 5, 6], especially for micro-patterns due to its high resolution. It is suitable for inviscid fluids like polymer solutions [7] or nano-metal suspensions [8] and the output resolutions are determined by the diameter of the nozzles. Until now, inkjet printing is mainly used as a 2D circuit printing technique because the viscosities of the printing materials are usually quite low and it is hard to restrict the flow of the inks during 3D structure construction. However, to build a 3D part, it is usually combined with a

thermal post-curing step. Sanchez-Romaguera et al [9] generated a simple 3D all inkjet printed metal/insulator/metal crossover. In their research, after the deposition of the first nano-silver track on the substrate, they used the hotplate to sinter the nano-silver and then followed by printing the UV curable insulator; after that another conductive track was deposited and sintered. Ko et al [5] made the similar structure, but they selected laser as the heating source, i.e., an inkjet – laser – inkjet process.

Selective laser printing

Due to its monochromatic and coherent properties, the laser can be used to provide highly directional localised heat to create desirable conductive pattern during PCB manufacturing. Different ways of laser PCB processing have been reported in previous researches: laser ablation [7, 10, 11], which is actually a subtractive process similar to conventional PCB manufacturing but replace the etchant by laser; laser direct curing of isotropic conductive adhesives (ICA) [12, 13] and laser direct sintering/melting of nano-sized metal particles [5, 14, 15].

2.1.2 Material used in conductive track formation

In physics, the conductivity of material is a result of the motion of electric charges, e.g. free electrons in metals, ions in electrolyte and holes in semiconductors. Metals are the most widely used conductive materials because of their high conductivities; other materials like carbon or conductive polymers are also used although their conductivities are lower than metal. In PCB manufacturing, the traditional etching method uses pure metal such as copper as the conductive material but for the direct additive writing techniques, the printed material should have high fluidity and therefore conductive paste/ink are usually selected.

2.1.2.1 Isotropic conductive adhesives (ICA)

Polymers are typically dielectrics and can be made conductive by adding natural

conductors like metals. The polymer binder, usually dissolved in solvent, is used to establish a matrix phase as the carrier vehicle for the conductive fillers – this product is often named as ‘isotropic conductive adhesive’ (ICA) in industrial applications. In order to achieve high conductivity, a continuous pathway of fillers is required so that the electrons can move freely throughout the ICA. As a result, the conductivity for ICA is influenced by three main factors [16]:

- Volume fraction of the filler. Figure 2.2 represents a typical electrical conductivity against filler content curve for most ICA, where at a specific value, the conductivity has a dramatic increase and convert the system from dielectric/semi-conductive to conductive. This phenomenon is known as ‘percolation threshold’;
- Intrinsic resistance of the conductor and matrix;
- Particle-particle contact resistance, i.e. the tunnelling resistance.

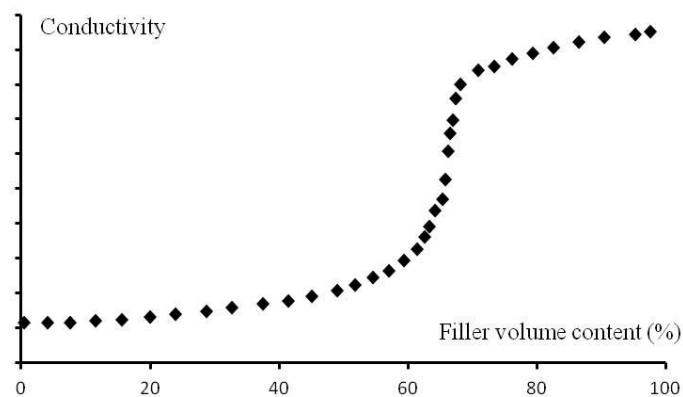


Figure 2.2: Electrical conductivity against conductor content curve, known as ‘percolation threshold’

Conductive filler

Metals are the primary conductor material used in ICA. Micron-sized conductors have gain significant success in industrial applications. Among these materials, silver might be the most widely used filler because its balance on price and stability when compared with other materials, like gold (expensive) and copper (which suffers a loss in conductivity after oxidation). A typical silver paste contains about 60% silver and they can be either

flakes or particles. Sometimes, submicron particles are added in ICA to increase the number of filler contact and therefore improve the conductivity [3]. ICA usually has a much higher resistivity than bulk material, for instance, the sheet resistance of DuPont's 5000 silver phase is $15\text{m}\Omega/\text{m}^2$, which is about 20 times of bulk silver [17].

Moreover, to reduce the high cost of using gold and silver, cheap metals like copper are always selected during manufacturing. Compared with noble metals another advantage of copper is its electromigration effect (the ions flow in a conductor due to the applied current and may lead to circuit failure [18]) is weaker [3]. The main limitation for copper lies in its low resistance against oxide, especially under high temperature or humidity conditions. To prevent oxidation, a stable copper complex should be formed [3] and usually, this complex can be achieved by various methods, e.g. vapour deposition, electrochemical reduction, radiolytic reduction, thermal decomposition and chemical reduction [19]. Chemical reduction is thought as the most effective way among these methods, especially for nano-sized particles; the particle size and shape can be controlled by different reaction parameters. A wet method is usually used in chemical reduction, i.e. dissolving metal copper salts in an aqueous phase with the creation of micelle-like structures using organic surfactants, which is known as a 'self-assembly-monolayer' (SAM). Then a reducing agent is introduced into the mixture to reduce the copper ions to zero-valent copper.

Yang et al [20] reported a two-step reduction using oleic acid as the surfactant and explained the reduction process. Khanna [19] focused on the effect of different reducers and found a weaker reducer was more suitable to avoid agglomeration compared with strong reducer hydrazine hydrate. Engels et al [21] found that a high concentration of surfactant will lead a high anti oxidation property of copper nano-particles but it will also increase the particle size.

Another way to reduce the cost is replacing the metal filler by carbon (e.g. carbon black, carbon nanotubes and carbon fibres); although the resulting conductivity is lower than

that for metals. Carbon fillers provide satisfactory performance in biomedical devices or mobile phones. Kelkar et al [12] carried out an experiment using the carbon-based paste. They proved laser curing was applicable for carbon-filled paste with a resistance of $34.04\Omega/\text{m}^2$, which is similar to the sheet resistance of this paste ($34.00\Omega/\text{m}^2$, DuPont's 7105 [17]). Athreya et al [22] tried to generate a carbon black-filled nylon-12 conductive polymer by laser sintering, which is not a paste-based composite but in powder mixture form. They reported the agglomeration of filler particles due to the lack of dispersant, which led to a high porosity of the product and will contributed to a high electrical resistance. The product in the experiment is increased in electrical resistivity by $10^5\sim 10^6$ times compared with bulk carbon black.

Supporting matrix

The matrix materials are normally thermosets. Their viscosity must be low enough to enable the printing before curing, therefore the monomeric or oligomeric precursors are usually used. During a thermal curing, those precursors will polymerise and provide excellent adhesive property. Epoxies, phenolics and other formaldehyde condensation resins [3] are widely used in ICA and some modified epoxies e.g. butadiene modification [23] or vinyl modification [24] are applied to vary the properties of the products. For a thermoset based ICA, the curing temperature is usually too low compared with the melting point of pure metal (e.g. for DuPont's 5000, the processing temperature is just 120°C [17]; while the melting point of bulk silver is 962°C). Therefore no phase transition occurs on the metal fillers. From Lu and Wong's work [25], the intimate contact between conductive fillers caused by matrix shrinkage during curing was the main mechanism for conductivity formation. Sometimes, to achieve a real 'sintered' conductive track, a high processing temperature is required (e.g. DuPont's QS300, which should be processed at 850°C but can achieve a high conductivity of 36% of that for bulk silver [15]). The high temperature restricts the selection of substrate.

Meanwhile, thermoplastics can also be used as the matrix material. In paste or ink, they are usually dissolved in a specific solvent; after printing the solvent will be evaporated at

a high temperature and the thermoplastic binder will be ‘functionalised’ [12], which not only includes the melting and re-solidification of the thermoplastic, but also the contact of conductive fillers. The typical thermoplastic matrixes are acrylic, acrylonitrile butadiene styrene, cellulose derivatives, nylons, polycarbonates, polyesters, thermoplastic polyurethanes and polar vinyls [3]. Moreover, the crystallinity [26] of certain polymers is also found having influence in the properties of the products, since the fillers are extruded from the crystal region and only exist in the amorphous region, this kind of ‘aggregation’ will reduce the value of percolation threshold.

2.1.2.2 Nano-sized conductive ink

The basic principle of using nano-sized materials comes from their low melting point which attributes to the thermodynamic finite size effect [27]. For small particles, they have a larger proportion of surface atoms when compared with large particles; and the total attractive force between those surface atoms is lower than core atoms, which lead a lower energy requirement for thermal motion [28]. This so called ‘melting point depression’ phenomenon can be expressed clearly according to Buffat’s [27] investigation on nano-gold, where the gold has a dramatic decreasing in melting temperature (from 1300K to 500K) when its size is reduced to 5nm and above this size, the melting temperature is similar to that of bulk gold.

However, it has been reported many times [29, 30, 31, 32, 33, 34] that to achieve a sintered phase at low temperature, the particle size could be larger than a small value like 5nm, which indicates the sintering temperature is lower than the melting temperature. According to Garrigos et al [35], the transition of entire particles from solid to liquid state does not occur at a single temperature. In addition, a quasi-liquid layer (QLL) is generated at a temperature below the bulk melting point. Moreover, the minimum temperature at which QLL appears is defined as ‘surface induced melting point’ while the fully melting temperature is called ‘end melting point’. Based on Sakai’s investigation in Figure 2.3.a [36], the bigger the particle is, the larger the difference between the two

temperatures. Meanwhile, at a given temperature higher than the ‘surface induced melting point’, the thickness of QLL is determined by the size of particles (as indicated in Figure 2.3.b). Thus for a sintering process, the possible working temperature is lower than the bulk melting point.

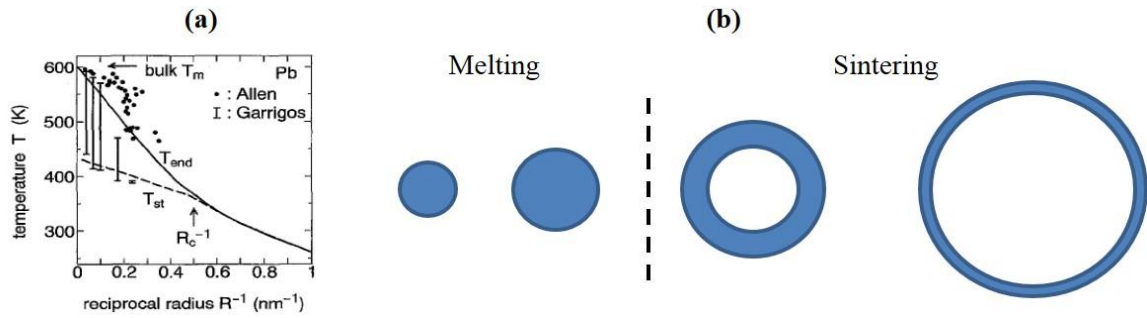


Figure 2.3: (a) Difference between ‘surface induced melting point’ and ‘end melting point’ with varied particle sizes for Pb [36]; (b) Schematic representation of the QLL thickness for different particles at a given temperature [35]

It is not necessary to use matrix material as the binder since the nano-fillers can be fully sintered and normally a vaporisable solvent is used as the suspension agent. When use the conductive ink in circuits manufacturing, Ko et al [5, 37] reported a series experiments carried out using nano-gold. They demonstrated a multilayer electric components fabrication using laser on plastic substrate. Chung et al [14] indicated that because of the thermo-capillary flow of the organic solvent, the increase in temperature will not be restricted in the laser exposure region only. They improved the deposition method by preheating the substrate to make the solvent evaporating. Kim et al [29] showed a comparison between laser sintering and oven sintering on silver nano-particles and investigate the influence of processing conditions in the damage of substrate. Zhang et al [38] further indicated that it is the coated SAM on the surface of nano-particles, which could not be decomposed at low temperature, preventing the formation of a conductive pathway. Thus they adopted a combustion method to remove the organic phase from the particles’ surfaces. Moreover, they also applied a flake and nano-particles mixture to replace the pure nano-particles filler system, which reduced the cost effectively.

2.1.2.3 Intrinsically conductive polymers (ICPs)

Another kind of conductor used in electrics manufacturing is ICPs, which is pure polymer without any metallic fillers. ICPs have extensive conjugated structures on their polymer chains and after doping, the conductivity of these polymers can reach to 70% of bulk copper [3]. Moreover, due to their polymer nature, ICPs are potentially more suitable to fabricate on the plastic substrate than metals and their fluidity makes them suitable for direct printing. However, ICPs have not been widely used like ICA or nano-sized conductive ink because of their instability in air. Meanwhile, after doping they become inflexible and brittle, which makes them more like inorganic materials than polymers and therefore significantly reduce the processability.

Nowadays, the most common ICPs in electronic industries are based on polyacetylene, polythiophene or polypyrrole. Among them, poly(3,4-ethylenedioxythiophene) (PEDOT) is the most common case in researches [39]. However, PEDOT cannot be dissolved in water and therefore the soluble poly(styrenesulfonate) (PSS) is usually used as a charge balancing dopant [40]. The generated PEDOT-PSS colloidal solution has a relatively high processability and it is mainly used in the thin film circuits industry. Sirringhaus et al [41, 42] used PEDOT-PSS to produce transistors; they applied a surface treatment to increase the resolution of the inkjet printing and then selected the conventional oven curing to form the track. Laser assisted techniques are also used on PEDOT-PSS conductive pathway formation. However, almost all these investigations [43, 44] using laser as an ablation method rather than a curing method. In Lasagni's experiment [43], the efficiency of laser ablation was further improved by a double-laser interference method.

Moreover, ICPs can also be used in ICA system to enhance their conductivities. Genetti et al [16] generated a coating of polypyrrole on the surface of nickel flakes and added the complex into a low density polyethylene (LDPE) matrix. The conductivity of this composite was 10^3 times of pure nickel-LDPE system. They stated that the increasing of conductivity was a result of polypyrrole chain entanglements between nickel flakes.

2.1.3 Embedded 3D circuit system

The traditional PCB is actually a 2D system with a non-conductive substrate and conductive pattern on it; however at some point in a design, it will not be possible to route all conductors in a single-layer format [45] and therefore multi-layer packaging system is designed to solve this problem. The circuits at different layers are interconnected by drilling holes through the stack and producing plated through-holes. Another approach to generate a 3D circuit system is embedding the electronic circuits in geometrically-complex substrate at various depths [46]. This embedded system can significantly reduce the footprint between different electronic components and improve power delivery performance [47], as indicated in Figure 2.4; meanwhile the overall device size is also reduced.

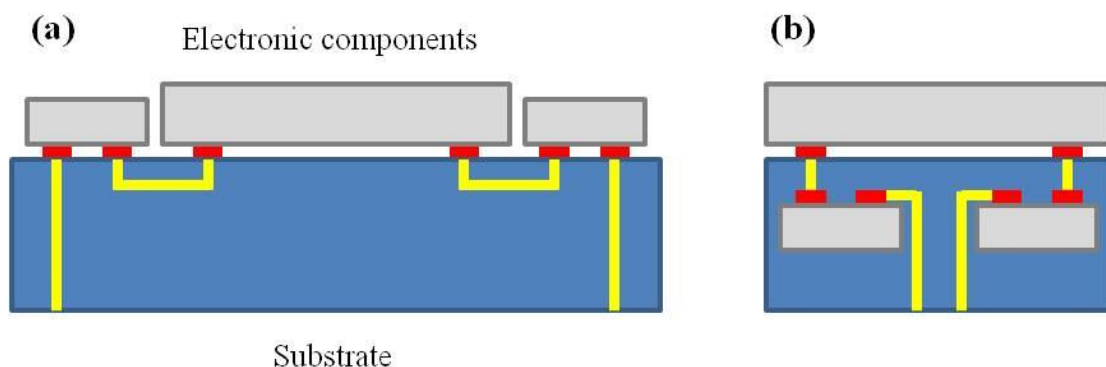


Figure 2.4: Examples of (a) surface mounting system; (b) embedded system

The earlier concept of 3D circuit is moulded circuit board (MCB), which combines plastic components and circuits in one part through a selective metallisation process. Some researches on this subject were carried out in the 1980s, resulting in a number of processes being developed, but success has been limited for both technical and business reasons [3]. Nowadays, a two moulding process is the most successful commercial case, which involves using one mould with catalysed plastic, while placing the resulting part in another mould and covering all except the area that will have circuit tracks. Then the finished part is placed in an electroless plating bath and metallisation will occur where

catalyst is exposed. This method has been used in an antenna system by Nokia and Hitachi Cable Ltd [48]. Moreover, in some cases a more straightforward method is developed [49], the substrate is firstly covered with metallic additives and a laser selective treatment is applied to create circuit pattern, which is followed by an electroplating process to enable metallisation in the treated region.

However, MCB can only generate a PCB with circuit pattern on surface; to produce the embedded system, Min et al [47] reported an injection moulding technique. During this process, the core of the circuit board is firstly manufactured using the traditional multi-layer packing method, then a cavity was made and the circuit was placed into it, finally the moulding material was filled into the cavity. Meanwhile, the additive manufacturing has also been used in embedded circuit system formation. This work has been carried out by Palmer et al [50], Medina et al [51], Navarrete et al [52] and Lopes et al [53] during the past 10 years. They used layer-by-layer stereolithography to build the substrate structure with designed slot for the electric components; then use micro dispensing deposition to fabricate the conductive paste on it. They combine the two processes in a repeating cycle so that a complete 3D embedded PCB can be eventually manufactured. Meanwhile, Pique et al [54] did the similar work; however, they use laser ablation to create slots for components instead of the additive process.

2.2 Laser additive manufacturing

The additive manufacturing is one of the numerous advanced manufacturing technologies in recent days. It can construct 3D components based on a computer aided design (CAD) model. The term ‘additive’ refers to a layer-by-layer adding process and contrasts with traditional manufacturing such as subtractive (machining) or formative (injection moulding) [55]. The earliest available additive manufacturing is known as stereolithography in 1986, other technologies including Laminated object modelling, Fused deposition modelling, Laser power bed melting and 3D inkjet printing are then also developed [56]. The laser additive manufacturing normally a powder based system, where

the 3D structure is built up by powder melting and solidification.

2.2.1 Laser principles and selective laser scanning

The laser is actually an acronym for ‘light amplification by stimulated emission of radiation’ [57]. In practice, the laser could either be continuous wave (CW) or pulsed mode, the CW laser is generated by a continuous excitation of the reactive medium and its energy output is almost constant and therefore it is thought to heat the workpiece homogeneously. The pulsed output is usually achieved through modulation of the excitation power (known as a pulse width modulation (PWM)) or by external attenuation of CW beam [58]. The pulse laser is characterised by parameters such as pulse energy, pulse duration and repetition rate. Moreover, the pulse shaping technique has been used in process optimisation in a laser-metal melting experiment [59], where the pulse shape was used to control the heat flow in processed material: a ramp-up pulse was found can reduce the distortion and residual stresses; and a ramp-down pulse increased the time for which the material was kept in the molten state and help improve the surface finish.

Another important parameter for laser beam is its wavelength, which is classified by different kinds of active medium (gas, liquid or solid). Among those types, carbon dioxide (CO₂) laser and neodymium-doped yttrium aluminium garnet (Nd:YAG) laser are the most extensively used sources for laser-material processing. A CO₂ laser is produced using a gas mix of CO₂, N₂ and He. The gas is continually excited by electrodes, to produce a collimated photon beam, which has an wavelength of 10.6μm; while for Nd:YAG, the active media is a synthetic crystal with a garnet-like structure, whose chemical formula is Y₃Al₅O₁₂, and the output wavelength is 1.06μm [58]. The different laser wavelengths are selected based upon material surface absorption. Metals have high absorptivity at short wavelength therefore the Nd:YAG laser is normally used to process metal. However, for polymers processing, CO₂ laser is the most widely used heat source.

Beam manipulation by galvo scanning

Basically, there are two different types of scanning methods when laser is used in additive manufacturing process: galvo scanning and computer numerical control (CNC) controlled 2 axis mechanical movements. The galvo scanning is a commercialised additive method currently used in additive manufacturing, which is combined with a powder bed system and the first machine was developed by DTM in 1992 [60]. Figure 2.5 represents a typical internal machine set up and the building process includes several steps.

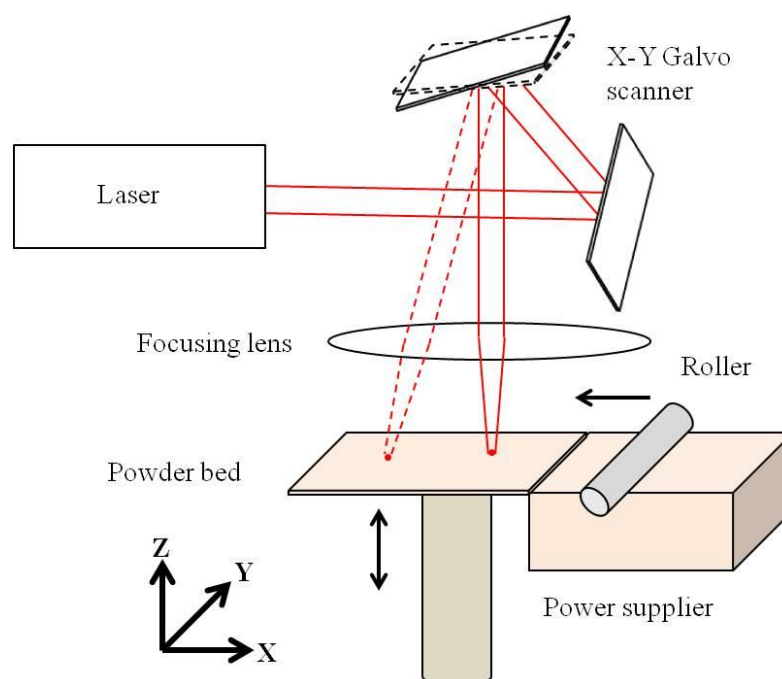


Figure 2.5: Schematic representation of a galvo scanner based additive manufacturing machine

1. Prior to build, a 3D CAD file is created to provide the data of objective geometry; the 3D object must be sliced to a series of 2D files, representing the cross-section geometry for different layers.
2. In a normal building sequence, the system is pre-heated to a suitable temperature and according to Gibson et al [61]; this value should be kept just below the melting temperature but above the crystallisation temperature. This can minimise the input laser power and reduce the thermal warpage of the part. However, during some experiments,

this pre-heating was replaced by a supporting structure [62], which will also eliminate the warpage. Actually, this supporting structure has been widely used in metallic parts additive manufacturing [63], since it is difficult to pre-heat them to suitable temperature.

3. A single layer of powder is deposited on the powder bed by a roller from the powder supplying container, and the laser selectively scans across the powder and fuse them. The coordinate of laser beam on the work plane is controlled by the galvo scanner, which consist of two reflection mirrors. After receiving data from sliced CAD file, the mirrors will rotate to create scanning behaviour in both X and Y axis. The reflected laser beam will then pass through a focusing lens and the surface of the power bed is kept at the focal point. During this step, the scanning parameters such as input power, scanning speed, scan spacing and scan orientation are adjustable and many related researches [64, 65, 66] are carried out to improve product mechanical property. Those studies suggested a higher energy will generate more consolidation of powder and the mechanical properties are actually determinted by internal structure of the product. Goodridge et al [67] found out the part orientation plays a vital role in the sample mechanical property, where the tensile strength and elongation at break (Eab) in X and Y axis are higher than those in Z axis. Zarringhalam [68] provided further quantitative analysis concerning the degree of particle melt (DPM) of nylon-12 using DSC. He stated a high DPM will lead to high mechanical properties.

4. The platform in power bed cylinder moves downward a specific distant and another layer of powder is deposited by the roller again. The 3D structure is built up by repeating step 2 to 4. For most polymer powders, the typical layer thickness is usually controlled between 100 to 200 μ m and this value is mainly reliant on the scan parameters and powder properties [55].

5. After building up the whole structure at the setting temperature, a low cooling rate is applied to avoid the formation of thermal residual stress. Meanwhile, to separate the product from unsintered powders, a hand brush or a bead blaster with compressed air is

used. However, due to the limitation of the powder bed system, for some specific structures such as long tube, the unsintered powders will be trapped in the structure and difficult to remove. This is believed as a significant disadvantage of the galvo scanner based additive manufacturing.

CNC controlled deposition

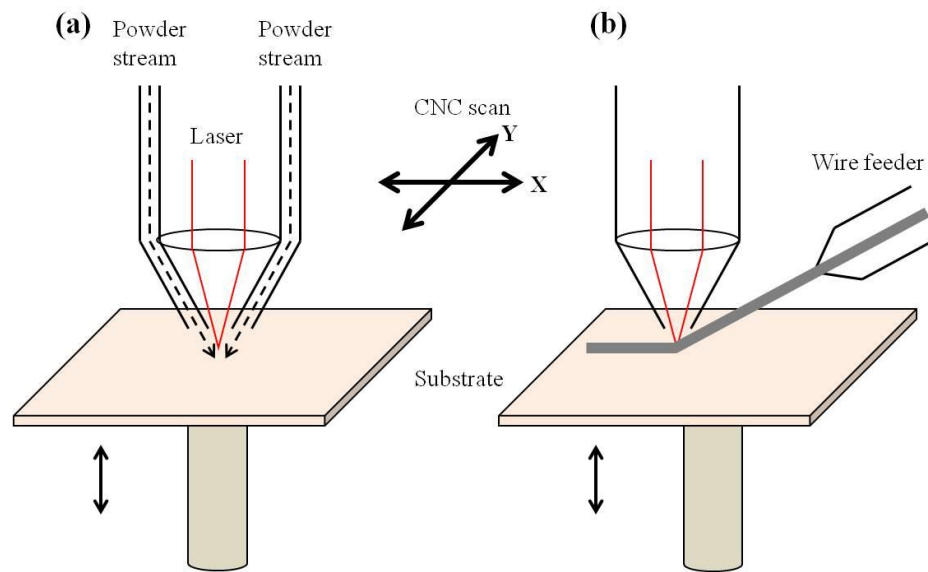


Figure 2.6: Schematic representation of fused deposition based additive manufacturing with (a) powder feeder and (b) wire feeder

Although the galvo scanning method is widely adopted in commercial cases, the product porosity is always a critical issue cited by many researches [64, 65, 67]. This is thought as a result of high scanning speed of the galvo system, which can minimise the heat transfer among powers and produce precise product, but meanwhile is unable to fully melt the powders. This is the reason why this method is also called ‘selective laser sintering’ in many literatures [65, 66, 67, 68]. An alternative way for laser additive manufacturing is the fused deposition method, as illustrated in Figure 2.6. It is actually a traditional laser cladding system, which includes a CNC laser scanning system and an extra material feeding system (powder or wire). For galvo scanning system, due to the nature of powder bed energy will transfer from the direct exposed material to surrounding material and this

will reduce the resolution. However, during fused deposition the deposition and melting occurs simultaneously therefore heat transfer is not an issue even at a low scanning speed. As a result, a complete molten pool [71, 72] can be formed at a desirable point on the substrate and multi-layers structure is further build up by substrate height adjusting.

2.2.2 Beam reconstruction with Holographic Optical Elements (HOE)

Majority of laser users focus the beam onto the work piece without any beam reconstructions, i.e. a round beam with the energy cross-section governed by the original laser manipulation. Typically, the energy cross-section is either a Gaussian profile or a high mode number thought of as a ‘Top Hat’. The two kinds of beams are illustrated in Figure 2.7. For the Gaussian beam, it has majority of the energy at the centre, with a rapidly decreasing towards the beam edges, which is believed to generate a non-uniform heat distribution on the work piece according to Higginson et al [73]. Moreover, since the Gaussian beam has a round shape when projected on the working plane, during a normal scan the exposure time for the central region is longer than that for the edge. This will further enhance the non-uniform distribution of the overall energy. For the ‘Top Hat’ beam, although its intensity distribution is nearly uniform, the round shape will also generate a non-uniform temperature distribution on the working plane.

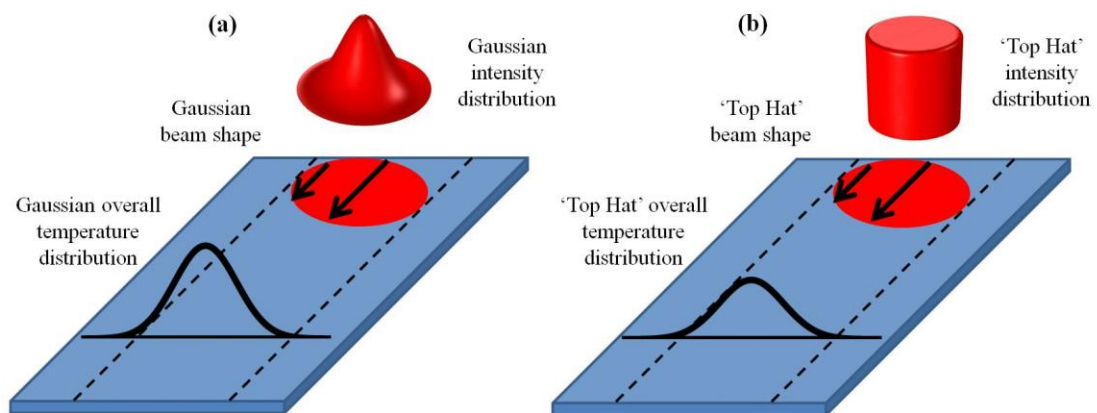


Figure 2.7: Non-uniform energy distribution during (a) Gaussian beam and (b) ‘Top Hat’ beam scan

However, many experiments and industrial applications require a laser beam irradiance that is nominally constant over a specified area, especially for laser-material processing. Thus the laser beam needs reconstruction, which is a process of redistributing the irradiance and phase of the original beam [74]. The techniques using beam reflection, refraction and diffraction are developed. The earliest research on this topic was carried out by Frieden in 1965. He successfully reshaped a single-mode Gaussian beam into a beam with a uniform profile, and the method he used was called the ‘geometric method’, which is an optical system based on beam reflection and refraction [74]. This complex system consists of a series of lens arrays, beam stops or masks and many investigations can be found using this method. Steen [75] used simple beam stops to change a laser beam shape and use it on surface coating. Farooq et al [76] used a resonator to produce a uniform beam profile, although the actual distribution contained spikes at the corners. This distribution was applied to steel during laser welding and compared with a Gaussian beam; the generated molten pool had a slightly flatter floor from the transverse direction. Bianco et al [77] and Konig et al [78] had reported laser cladding by using rectangular beams, and the beam was shaped by kaleidoscope optics or faceted mirrors. Various investigations in laser deposition and laser re-melting had been carried out in University of Manchester [79, 80] using different beam shapes including uniform circle, rectangle and diamond. The beam reconstruction was achieved by a ‘Gaussian beam array’ and therefore beam intensity distribution is always uniform and only the beam shape can be reconstructed.

Using the coherent and monochromatic properties of the laser a diffractive method of beam intensity redistribution is possible. This technique is known as Holographic Optical Elements (HOE) and it works by diffraction rather than refraction/reflection. The HOE is a kinoform with a computer generated pattern on it. It is a phase only element, which will impose phase change (from 0 to 2π) on the illuminating beam. Figure 2.8.a and b shows the surface profile of a HOE, which consists of a 2D array of pixels and each assigned a different phase level. Each pixel can be thought as a point source of a spherical wave-front, emitting with controlled phase retardation. Those diffracted wave-fronts

interfere in the reconstruction plane to produce the required energy profile [81], as illustrated in Figure 2.8.c and d.

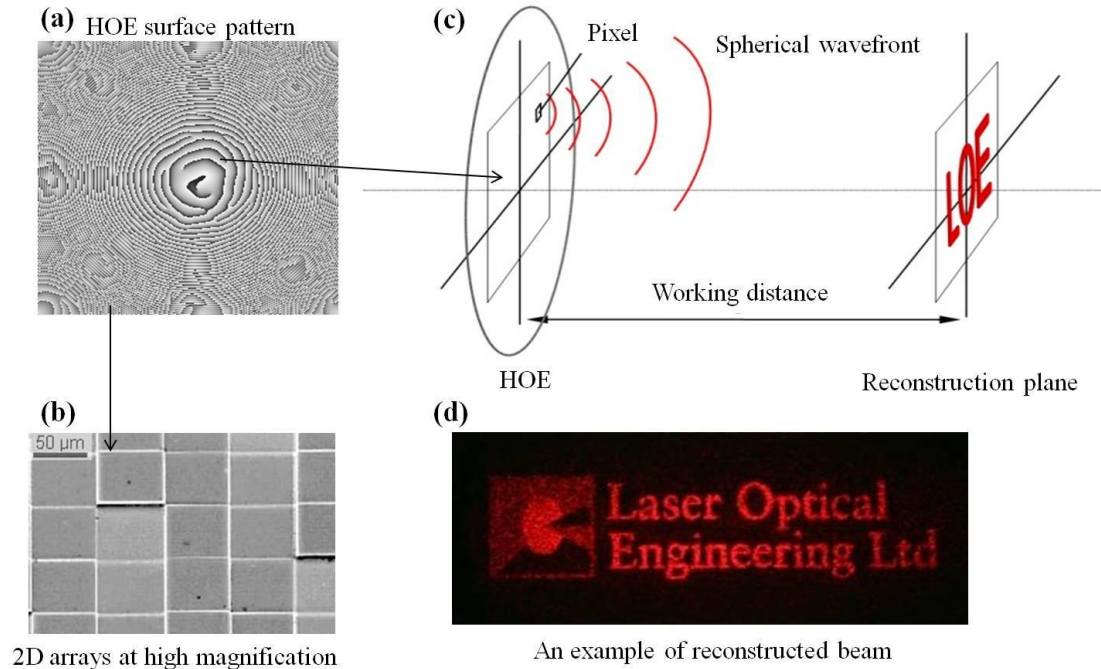


Figure 2.8: (a) Surface pattern of HOE; (b) 2D arrays of pixels; (c) working mechanism of the HOE pixel; (d) An example of beam reconstruction [133]

Noden [70] described a general process for generating a HOE. Its surface array is firstly calculated using error reduction Iterative Fourier Transform Algorithm (IFTA) based on both the original and reconstructing beam. Then a photolithographic technique is applied in the manufacturing step. The mask is prepared by printing the generated pattern onto a photographic film. Then a silicon substrate is spun with photo-resist to a controlled depth (half of the wavelength of the illuminating beam). This system is exposed to UV light through the attenuating mask and the depth of the cured resist is determined by the amount of received UV light. Finally, a metallic coating with 3 layers (aluminum, copper and gold) is developed on the resist to provide a highly reflective surface.

HOE has been used by Babin et al [82] and they create a twin spot and an open circle beam in the experiment. However, the beam reconstruction was incomplete since an

undesired spot with high intensity was found in the output beam. Ekberg et al [83] applied the HOE on the Nd:YAG laser and successfully drilled an array of holes on a stainless steel sheet. Kell et al [81, 84] carried out a series laser steel welding test using Gaussian and several HOE reconstructed beams. They investigated the influence of the beam shape in the weld pool shape and microstructures. They found the grain orientation can be controlled by providing different beam profiles, since the growth of grains is mainly determined by temperature gradient and by using HOE a user defined temperature profile on the work-piece can be generated. Gibson et al [69] and Higginson et al [73] compared the thermal profile of Gaussian beam and HOE reconstructed beams (including square uniform beam and ‘Rugby Post’ beam with high energy intensity at the edges) during laser metal deposition and they stated the different temperature profile generated a driven force in the molten pool to control the material flow. However, all those HOE tests were reported in metal processing and no application was found in other laser processing field such as polymer additive manufacturing or conductive track printing.

2.2.3 Material used in laser additive manufacturing

All three types of materials (metal, polymer, ceramic) have been reported in additive manufacturing and the topic is therefore extremely broad. Since high density polyethylene (HDPE) is the material used in the substrate manufacturing in this project, this chapter will provide knowledge relevant to it.

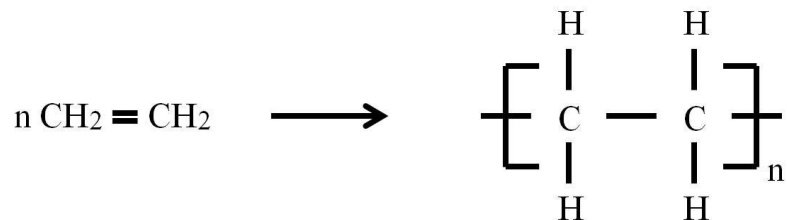


Figure 2.9: Chemical structure of polyethylene

Polymers are material with a ‘long-chain molecule’ structure and they are formed by cross-linking of different monomers. For instance, the basic chemical structure of polyethylene (PE) is indicated in Figure 2.9 and its monomer is ethylene. PE is a typical

thermoplastic polymer and it will melt when heated and become solid again after cooling.

One of the important properties for thermoplastic is its crystallinity, which is a concept used to describe the crystalline percentage in the material. For polymer, if the molecular chains arrange themselves in an ‘orderly’ manner this will form the crystalline phase; however in some regions, the chains exist without any order, which is so called amorphous phase. The structures of the two phases are illustrated in Figure 2.10. The mechanical properties of a polymer, including its strength and modules, are mainly determined by its crystallinity [85] and an increasing crystallinity normally led to increased strength and modules. Generally speaking, solidification and stretching are two mechanisms for crystalline phase formation. The former one is a temperature dependent process; when the polymer is in melted state, it is always amorphous and during cooling, the chains will rearrange and form crystalline phase. During stretching, the polymer chains will be forced to align and the crystallinity will also increase.

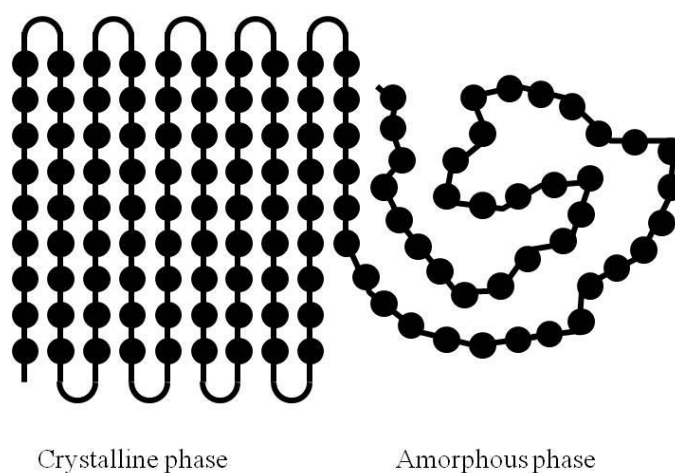


Figure 2.10: Structure of the crystalline phase and amorphous phase

PE is a typical semi-crystalline polymer which consists of both crystalline and amorphous phase. As one of the most common plastic material, it can be classified as three main catalogues according to the density and branching structure: high density polyethylene (HDPE), low density polyethylene (LDPE), linear low density polyethylene (LLDPE). Among them, HDPE has fewer branching and therefore the polymer chains are

well-packed and therefore generate a high density and crystallinity. In laser additive manufacturing, although more materials such as PE, polypropylene (PP), polyether ether ketone (PEEK) are developing in current years, polyamide 12 (Nylon-12) remains by far the most widely used material and making up 95% of the market [65, 66, 67]. Compared with other materials, one advantage of Nylon-12 is its broader ‘super-heating region’, which is the temperature region between crystallisation peak and melting peak from a DSC curve (Figure 2.11). It is often described as the process window for laser additive manufacturing since the material need to be pre-heated to this region [55]. The crystallisation peak is selected as the lower limit because if the polymer is cooled below this point it will have a significant shrinkage and this will lead product warpage; the melting peak is selected as the upper limit because above this point the powder will be fully melted and it is impossible to construct a desirable product by selective laser processing.

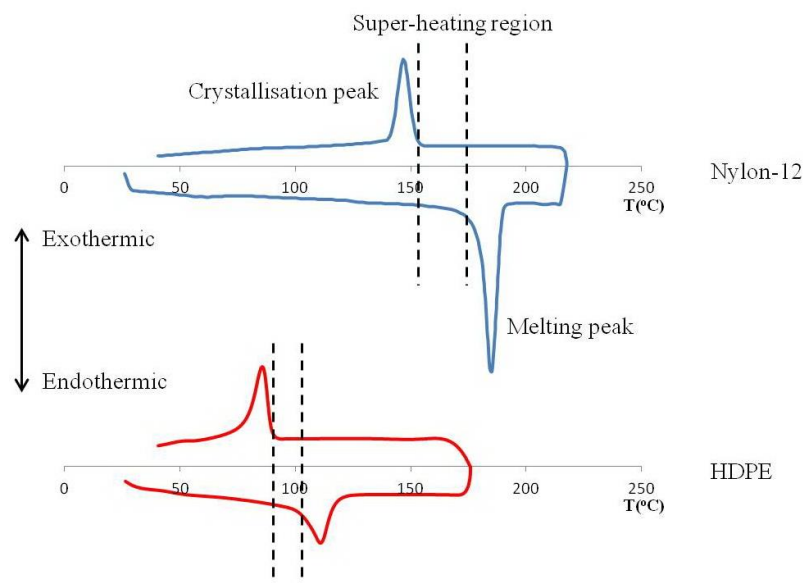


Figure 2.11: The DSC examples of Nylon-12 and HDPE showing the difference in super-heating region

Although Nylon-12 is a suitable material for laser additive manufacturing, the product usually has a high porosity of 5~10% [67]; this will lead to a poor (about 20% [55]) Elongation at break (Eab) and limits its application in industry. In addition, if laser

manufactured Nylon-12 is selected as PCB substrate, the fabrication of conductive tracks will become an issue due to the porous structure. It will be valuable if a more functional material such as HDPE can be developed; however, as shown in Figure 2.11, the process window of HDPE is smaller than Nylon-12, thus it need a carefully controlled heating process.

Since the material used in galvo scanner based additive manufacturing is in powder form, the powder properties such as particle size, flowability and melt flow index (MFI) are important factors. Goodridge et al [67] indicates the common material used for laser additive manufacturing has a diameter between 45-90 μm and small particles will improve the density and surface finish of the product. Schmid et al [86] investigated the flowability of Nylon-12 powder and indicated the flowability plays an important role in powder compacting and consolidation during laser processing.

2.3 Numerical simulation of laser welding/cladding

It is difficult to gain a complete understanding of the physical mechanism of laser interaction with materials, since the physical processes of laser-materials interaction are very complex, both from modelling and experimental aspects. The additive manufacturing in this project is actually a laser welding/cladding process, a review of fundamentals related to this subject and simulation methods will be presented in this section.

2.3.1 Laser energy absorption

Generally speaking, laser welding/cladding can be divided into 3 steps: energy absorption, molten pool formation and solidification. As described before, laser consists of a large amount of photons which have the same phase; therefore, a laser energy absorption is actually a 'photons interaction with materials' process. This interaction can either occur on the chemical bonds or through collision with electrons, lattice phonons, ionised

impurities and et al [87], where in the latter case the photon energy is converted to thermal energy. Meanwhile, due to the wave-particle duality of light, one can also treat the laser beam as an electromagnetic (EM) radiation. When the EM radiation strikes the surface of a work piece, it undergoes absorption, reflection and transmission and they has a sum equal to 1. Normally, the Beer-Lambert's law is used to describe the absorption of EM energy inside a material:

$$I = I_0 e^{-\eta z} \quad (2.1)$$

where z is the depth, I and I_0 are the intensities of transmitted and original radiation and η is the material absorptivity. This law can be used to calculate the 'optical penetration depth' (OPD), at which the intensity of the incident radiation falls to $1/e$, i.e. $OPD = 1/\eta$.

In general, most materials used for laser welding/cladding are opaque to the selected laser; therefore transmission part is thought as 0 and the absorption is determined by several factors listed as follow:

Material absorptivity

In metals, most of the energies are absorbed by free electrons, and those electrons in the surface are free to oscillate and reradiate without disturbing the solid atomic structure. If the absorbed energy increase, the electron vibration becomes intense but penetration depth doesn't change significantly, the molecular bonds will then be stretched and the molecules starts moving, which is described as melting. If more energy is applied, the molecular bonds are broken and the materials are evaporated. In addition, keep increasing the energy will further lead the ionisation of the vapour and finally generate plasma. The absorptivity for metals is determined by both the material type and laser wavelength. Generally speaking, the lower the wavelength, the higher the photon energy. Near-IR lasers (0.8-2.5 μ m) such as Nd:YAG laser (1.06 μ m) and fibre laser (1.07 μ m) interact with the material by stimulating electron oscillations, therefore metals which have free electrons have a high absorptivity at these wavelength. In the spectral range of middle-IR (2.5-25 μ m), interaction between radiation and materials occurs by excitation of oscillation of macromolecule chains [89]; as a result, CO₂ laser (10.6 μ m) is more suitable

to process materials with long chain such as plastics.

In polymers, the photons usually interact with the chemical bonds directly. However, based on the different type of polymers, the interaction mechanisms are totally different. As shown in Figure 2.12, for thermoplastic, the chemical bonds are broken after absorbing the photon energy and two kinds of results might be generated: for polymers formed by successive addition of free radical building blocks, i.e. radical polymerisation, depolymerisation will occur; while for polymers formed by stepwise reaction between functional groups of monomers and losing small molecules, i.e. polycondensation, they will decompose into fragments upon irradiation [88]. However, if the processed materials are precursors of the thermoset (e.g. oligomers or monomers), the photon-initiator are excited by the photons and then lead the crosslinking of the system. Shorter wavelength laser, e.g. UV laser [141] is usually used to induce polymerisation.

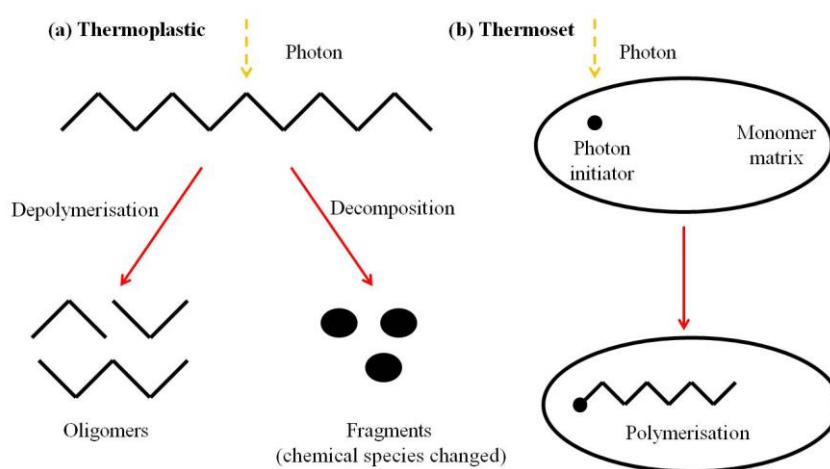


Figure 2.12: Photon interaction with different polymers: (a) thermoplastic; (b) thermoset

Surface roughness

Since powders are usually used in laser additive manufacturing, the surface roughness is a critical issue that one should consider. The surface roughness is a geometrical factor for laser absorption. For a surface with high roughness, the multiple-reflection of the incident beam in the undulation is easy to form and more energy will be absorbed by the material. However, to determine whether a surface is ‘rough’ or ‘flat’, one should not only consider

the geometrical factor, but also the beam wavelength. If the roughness is less than the wavelength, the beam will be easily reflected and the surface can be treated as flat; if the roughness is much larger than the wavelength, beam will be scattered and multiple-reflection occurs [90].

Beam polarisation and angle of incidence

Normally, the laser beam is polarised, which means the electric field oscillates in a certain direction perpendicular to the propagation direction of the laser beam. As shown in Figure 2.13, if the polarisation plane is perpendicular to the plane of incidence, the light is known as ‘perpendicular-polarised’ and if the polarisation plane is parallel to the plane of incidence, it is known as ‘parallel-polarised’.

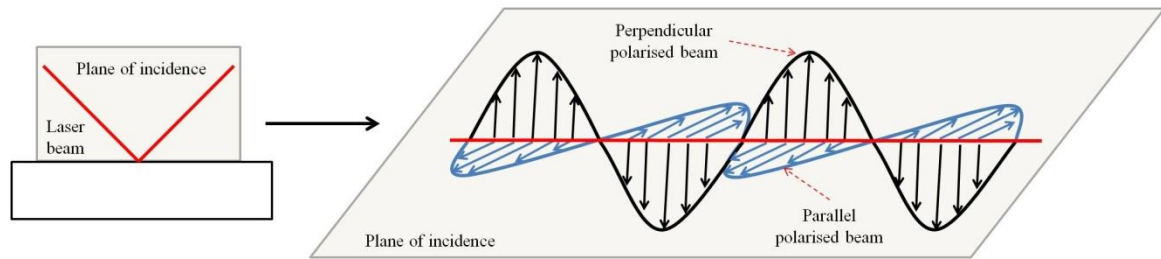


Figure 2.13: Different polarised beams of laser

For the parallel polarised beam, since the electric vector is in the plane of incidence, the surface electrons will be more likely to vibrate and interact with the surface matrix, therefore the energy absorption is high. However, if the electric vector is perpendicular to the plane of incidence, the electron vibration can proceed without interfere with the surface and reflection is preferred [90]. The influence of angle of incidence and beam polarisation in the reflectivity can be expressed using the following equations [112]:

For parallel polarisation:

$$R_f = \frac{(ncos\theta - 1)^2 + (k_dcos\theta)^2}{(ncos\theta + 1)^2 + (k_dcos\theta)^2} \quad (2.1)$$

For perpendicular polarisation:

$$R_f = \frac{(n - \cos\theta)^2 + k_d^2}{(n + \cos\theta)^2 + k_d^2} \quad (2.2)$$

where θ is the angle of incidence, n is the refractive index and k_d is a damping constant.

Temperature

The energy transfer in the material after photon-electron interaction can be explained by a phonon theory [90]. According to it, the energy transfer in the material is a result of the vibration the atoms, however, in a rigid crystal lattice those atoms are tied together and cannot vibrate independently. Therefore, the vibration occurs as a ‘collective mode’ and propagates through the material with a speed of sound, which are called ‘phonons’. As the temperature of the material increases, more phonons will be generated and it will lead more phonon-electron energy exchanges. As a result, electrons are more likely to interact with the phonons rather than the incident photons, therefore the reflectivity will decrease with a rise in temperature.

Other factors

Except those factors mentioned above, the angle of incidence, the surface oxide film and the formation of plasma [90] also have effects on the absorption. However, in most numerical simulation cases, the value of absorptivity is usually set as constant and only the geometric effect such as keyhole wall multiple reflections in a keyhole welding case [91] are considered.

2.3.2 Molten pool formation and solidification

After absorption, the energy will transfer inside the material and relative physical phenomena such as melting, fluid flow are the key factors for determining the final product conditions. Numerical techniques like FEM are usually used to simulate this process. The details of establishing a laser welding/cladding FEM model using level set method will be described in Chapter 3 and in this section a brief introduction and relative

early works will be presented.

2.3.2.1 Heat transfer and fluid flow

The basic heat transfer model in a solid is conduction, which refers to the transport of energy in a medium due to a temperature gradient. Moreover, in a fluid there is another energy transfer mode known as convection, which is based on the motion of the fluid. On the other hand, the fluid flow itself is an important phenomenon for molten pool formation. To describe them numerically, a differential control volume method has been introduced [92]. At an equilibrium condition; the system must follow three rules:

- First, the conservation of mass is considered; it requires that liquid flows through the control volume without mass loss, i.e. inflow minus outflow equals to 0;
- The second rule is Newton's second law of motion; it states that the sum of all forces acting on the control volume must equal to the net rate at which momentum leaves the control volume;
- The third requirement is energy conservation; it requires the overall energy in the control volume including inflow, outflow, generated and stored energies equal to 0.

The above statements are the basic mechanisms for a thermo-fluid case. In welding simulation, the earliest numerical model was established by Rosenthal [93], which only predicts the heat conduction situation under a moving heat source. In 1980s, the numerical simulation of molten pool flow was carried out for both arc and laser welding [94]. However, the early work was focusing on conduction welding and only a single phase flow is considered during the molten pool formation. Although Brent et al [95] developed an 'Enthalpy-Porosity' method to describe solid-liquid phase transition in single phase system; the removal of material, for example evaporation which always occurs in laser processing, is not simulated. Therefore conditions like keyhole welding, drilling and cutting are difficult to predict by these models and it is necessary to develop the multiphase flow techniques.

2.3.2.2 Multiphase flow and interface tracking

If only the melting behavior of material is considered, a single phase flow model is enough; however, since a polymer is investigated in this project and it usually has very low degradation temperature (compared with metal), it is sensitive to high intensity energy source such as laser. During heating, thermal degradation and decomposition will easily occur and it is a mass loss process similar to evaporation. The previous researches in this field are mainly focusing on metal evaporation during laser processing, which is known as keyhole welding and in this section those works will be introduced.

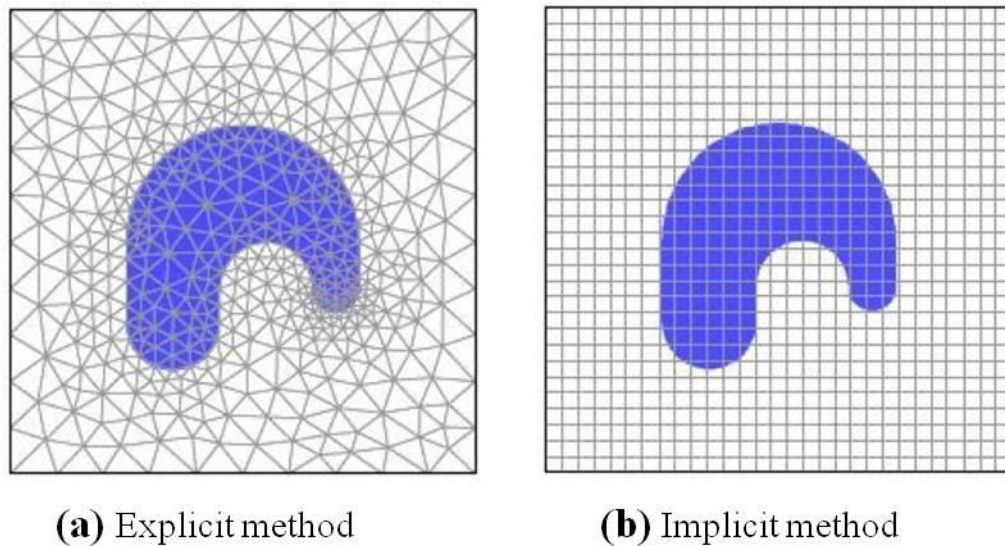


Figure 2.14: Illustrations of (a) explicit and (b) implicit method [96]

If the evaporation is considered in the welding/cladding case, the flow conditions of both the vapour and liquid phases must be included in the model. Each phase is described using thermo-fluid equations separately with different physical properties. However, the steep change of those properties across the interface is difficult to simulate since the geometry of the interface is actually a function of time and space. The current interface computational method for two phase system can be either explicit or implicit [96]. The explicit (Lagrangian) method will generate computational cells whose edges are aligned with the interface (Figure 2.14.a), and therefore the interface location is explicitly tracked

with the help of a moving mesh. However, the implicit (Eulerian) method using fixed grids and the interface is represented implicitly by a function defined on a higher dimension (Figure 2.14.b) [97]. The following part will introduce the advantages and disadvantages of those methods and their applications on laser processing model.

Explicit interface tracking

Since the interface is tracked explicitly, it enables a sharp interface representation but meanwhile it is difficult to handle complex deformation such as break up and merging of the interface. Periodic remeshing is necessary and it will introduce additional errors [96]. The most common explicit technique is called Arbitrary Lagrangian Eulerian (ALE), which is a combination of explicit and implicit methods. Due to the limitation of this method in dealing with complex interface geometries, rare report based on it can be found in laser processing model. Morville et al [98] using the ALE in a laser cladding simulation and evaporation is ignored in their work.

Implicit interface tracking

The implicit method will introduce an extra function to represent the interface geometry and this function can be simply treated as any other physical variables of the two phase fluid system. It offers highly robust and accurate advantages in complex interface tracking. Meanwhile, the drawback of this method is just the advantage of explicit method, since it deals with the extra functions rather than the mesh directly, the functions must be smoothed across the interface; or it will be very hard to solve those functions using standard numerical approximation. However, the smoothing process will expand the width of the interface and it may include more than one mesh width. As a result, the calculated interface may not be as sharp as the explicit method.

One implicit technique is known as the volume of fluid (VoF), which select the volume fraction as the interface variable. The VoF has been widely used in the laser keyhole welding cases. Lee et al [99] started investigating the molten pool surface for a spot laser welding in 2002 using Vof. Han et al [100] used their model for different laser modes

such as original TEM_{00} , cylindrical TEM_{01} and TEM_{10} . Cho et al [91, 94] generated the simulation of a laser-arc hybrid keyhole welding, where input beam was treated based on Fresnel's reflection mode. They reported the real beam profile after multiple reflections is a 'disk-like' shape but the simulation result is similar to that of the original Gaussian beam; they also found that the Marangoni effect in the keyhole welding is largely insignificant and recoil pressure is the primary force for molten pool shaping. Zhao et al [101] also used VoF in keyhole welding but they focused on the keyhole oscillation during the molten pool development. Tomashchuk et al [102] described a dissimilar welding therefore in their case the interface is not for liquid/vapour phase but for two melts. Koch et al [103] generated a 3D keyhole welding model for zinc coated steel system and they further verified this model by using a high speed imaging camera. Otto et al [139] created a laser metal drilling model in their work and they found the backflow of the melted metal is reason for the defects formation on the cutting edge.

Another typical implicit method is level set approach, which is similar to Vof but the interface is represented by level set function. Compared with Vof it need extra reinitialisation step to maintain interface stability; however, it can compute the interface normal and curvature easily, which is very important for laser evaporation modeling, since some forces such as recoil pressure are related to those variables [104]. By using the level set method, Ki et al [105, 106] created a keyhole welding model and physical variables such as multiple reflections, recoil pressure, capillary force and et al are all incorporated. The liquid/vapour interface was represented using a Kundsén layer and based on it the thermodynamic equilibrium between the two phases was established. Han et al [107] and Wen et al [108] established laser powder cladding models, although the phase transition between liquid and vapour is insignificant for the cladding case. Pang et al [109] investigated the keyhole oscillations using the level set method and Zhou et al [110] focused on the keyhole collapse and porosity formation during pulsed laser welding. Tan et al [111] are the first to introduce the plume attenuation of laser as a result of particle absorption/scattering in keyhole welding case, where the attenuation can be as high as 22% of the input energy in their study. Courtois et al [112] applied a new

technique to compute the multiple reflections of input beam by solving Maxwell's equation. They reported that compared with the traditional ray-tracing method [91, 94], the new approach is more suitable in solving interface with high complexity.

2.4 Summary

The PCB manufacturing is not a new process and laser has been reported used in this field in recent years. However, the laser is simply treated as a heating source and the production process is still a '2D circuit deposition – 3D packing' process. The laser based additive manufacturing has also been developed for many years but it can only generate non-functional product such as plastic prototypes. The combination of PCB and laser additive manufacturing to generate complete 3D embedded circuit system is a subject that both the academia and industry would interest in and rare related reports can be found (only Lopes et al reported a stereolithography process [53]). Considering the material used for laser manufacturing of PCB, ICA has acceptable conductivity and high stability, but it can only be deposited by 2D technique such as screen printing. Nano-sized conductive ink can be deposited by ink-jetting printing but due to its high cost, it is mainly used in microelectronics; and the main problem is to build a 3D structure, it needs high viscosity but to inkjet, it is necessary to keep it at low viscosity. The powder mixture has also been reported in circuit manufacturing, however the current work only uses carbon filler and due to both the material nature and lack of laser energy control, the product conductivity is very low.

The theoretical part for this manufacturing process is actually laser material interaction, which has been studied for many years, since the laser was developed. The problem of the current round beams (Gaussian and Top Hat) is their non-uniform temperature distribution on the processed material, which is a result of both the beam intensity distribution and shape. This will lead unexpected thermal degradation and melt flow. However, limited works around the world are reported using beam reconstruction method to control the properties of the processed material, as a result of the difficult in generating a completely bespoke beam irradiance distribution. Laser Optical Engineering offered a

HOE manufacturing process with high resolution, which is a major advantage in this project. Gibson [69] and Kell [81] carried out a series of works on laser metal processing using HOE technique and they stated the microstructure and fluid flow is controllable by providing suitable beam profile. Therefore the investigation of material conductive property control during HOE laser processing is valuable.

Moreover, the simulation works of the laser material interaction are well documented. The thermo-fluid theory can be used to describe the heat transfer and fluid flow behaviour in melted material. For phase transition, the ‘Enthalpy-Porosity’ method can be used to track the S/L interface during melting; the L/V interface tracking include many techniques, a implicit method known as level set exhibits advantages in both robust and accuracy and it will used in this project. Currently, rare works have been reported in simulating different beam irradiance distributions and investigating their influence in the molten pool formation; and the laser processing of polymeric materials also need more simulation works.

CHAPTER 3: MODELLING OF LASER WELDING/CLADDING

In this chapter, a 2D model is established using commercial Finite Element Method (FEM) software Comsol Multiphysics, with the purpose to describe the material behaviour in laser welding/cladding cases. Comsol is designed to solve coupled or multiphysics phenomena and it is idea to analysis the thermo-fluid problem in laser processing. More specifically, this model will be focused on the temperature field development and melt flow conditions of different materials during laser welding/cladding. Different beam irradiance distributions are applied as the energy source and phase transition (melting, evaporation, solidification) is also included. During melting, the evolution of solid/liquid interface is tracked using ‘enthalpy-porosity’ method and during evaporation, the evolution of liquid/vapour interface is tracked using ‘level set’ method. Extra force and energy source terms are considered in this work, which includes gravity, Marangoni force, capillary force, recoil pressure, buoyancy force, thermal convection and radiation. Three basic cases are studied: laser cladding of 316L stainless steel using Gaussian and Pedestal beams, which is focusing on the development of molten pool without evaporation; laser keyhole welding of mild steel using Gaussian beam, which is focusing on the removal of material at a high laser power intensity; laser melting of HDPE powder using Gaussian and Pedestal beams, which is focusing on the behaviour of materials with low melting and evaporation temperature. Meanwhile, relative experiments are carried out to verify those models, which include the characterisation of sample shapes and structures.

3.1 Model description

A lot of simulation studies based on laser cladding/welding have been carried out by different researchers [100, 105, 106]. The core design for most of the models is developing a method to solve the multiphase flow problem, which not only includes the flow phenomenon itself, but also the phase transition such as melting, solidification and evaporation in the process. A typical schematic diagram of laser-material interaction is

illustrated in Figure 3.1. The details of the model are described as follow:

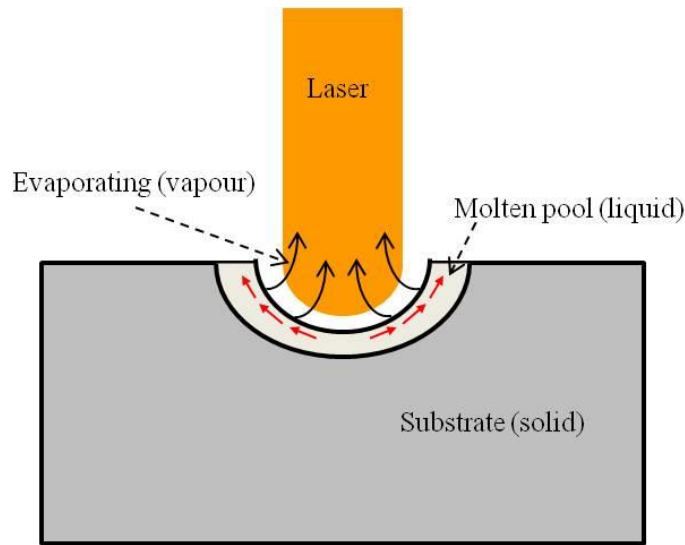


Figure 3.1: Schematic representation of the laser material interaction process

- The substrate with specified material properties is assumed as a solid state at the beginning and it is placed below the focal point of the laser beam.
- After the laser beams (including a Gaussian and a uniform Pedestal beam) applied on the interface between vapour phase (V) and substrate, the substrate will be heated and a molten pool is formed beneath the laser beam. The thermo-fluid mechanism can be used to describe the temperature distribution and melt flow condition in the substrate. The interface between solid (S) and liquid (L) phases is tracked using ‘enthalpy-porosity’ method, which is achieved by introducing a damping factor into the original thermo-fluid equation set. The fluid velocity is kept as 0 (i.e. solid state) when the temperature is below the melting point; while above the melting point, this damping factor itself equal to 0 (i.e. liquid state). Moreover, gravity and buoyancy force are applied on the body of the molten material; Marangoni force and capillary force are applied on the L/V interface; in addition, the heat loss due to convection and radiation on the substrate boundary is also included.
- Then as the temperature of the melt keeps increasing, evaporation of the material occurs. The L/V interface is tracked using level set method, which convert the interface

location to a partial differential equation. The evaporation is actually a phenomenon that material loss from liquid phase to vapour phase, as a result the velocity difference appears between the two phases and this account for the location of the interface. The recoil pressure is applied on the L/V interface during evaporation and the energy loss due to mass flux from liquid to vapour is also considered.

According to above descriptions, a general model structure can be set up in Figure 3.2, where the basic physical phenomena are generally described using the governing equations. Extra source terms are added to those equations as the boundary conditions. It should be noticed that although the S/L interface (melting) is a basic phenomenon, the ‘enthalpy-porosity’ method only considers it as an extra source term in the momentum equation. The modeling is achieved by solving the final governing equation sets and the details will be given in following sections.

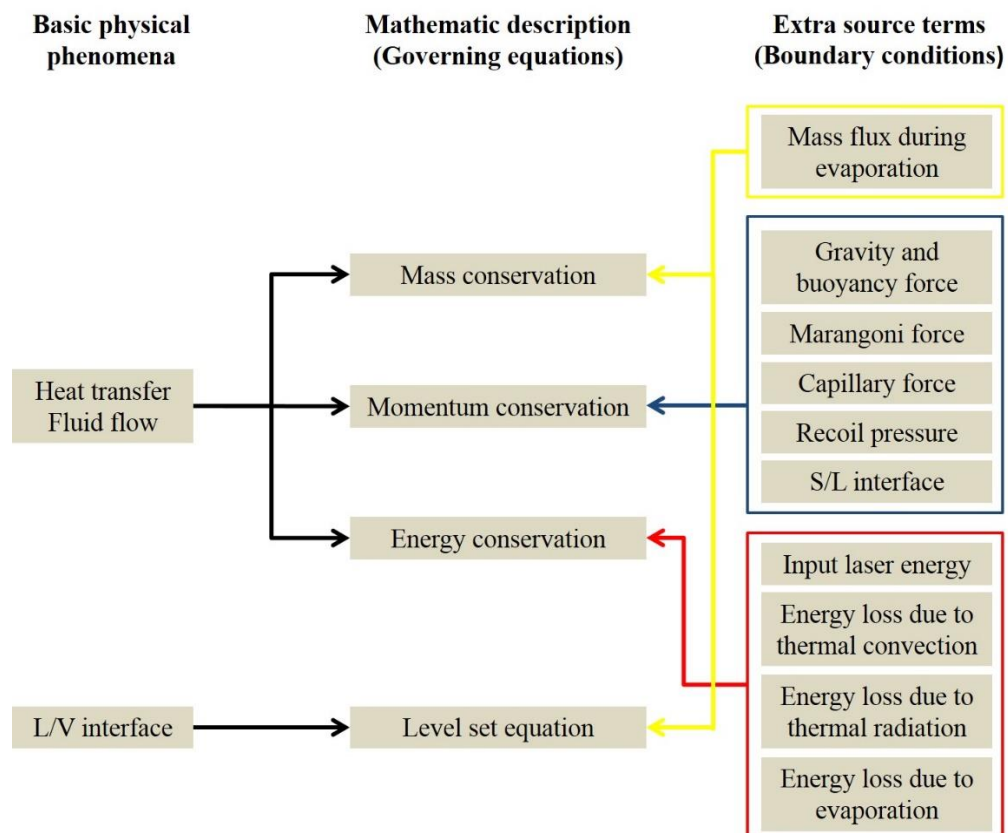


Figure 3.2: Laser welding/cladding model structure

3.2 Governing equations

3.2.1 Heat transfer and fluid flow

The heat transfer and fluid flow occur simultaneously in the molten pool; therefore, a coupled thermo-fluid model should be used to analysis this problem. A differential control volume method is used to set up the model. According to Incropera et al [92], the differential control volume can be assumed as a square in 2D, as illustrated in Figure 3.3. In this system, heat transfer and viscous, incompressible fluid flow will occur across each of the control surface. As a result, three conservations can be established to describe the system mathematically [113].

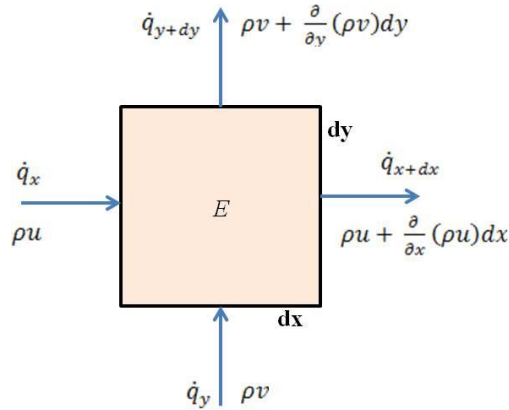


Figure 3.3: A schematic representation of differential control volume, where E , $\dot{q}_{x(y)}$ and $\rho u(v)$ represent the stored energy, heat flow term and fluid flow term respectively

- Firstly, the difference between inward flow into the control volume and outward flow must equal to the mass variation in the volume, which is known as the mass conservation. From Figure 3.3, the inward flow and outward flow in x axis can be expressed as $(\rho u)dy$ and $(\rho u + \frac{\partial(\rho u)}{\partial x} dx)dy$, respectively; where ρ is density, u is the velocity in x direction. Same expressions can be set up for flow in y axis and the mass variation with time is $-\frac{\partial \rho}{\partial t} dxdy$, therefore:

$$\begin{aligned}
& (\rho u)dy + (\rho v)dx - \left\{ \rho u + \frac{\partial(\rho u)}{\partial x} dx \right\} dy - \left\{ \rho v + \frac{\partial(\rho v)}{\partial y} dy \right\} dx \\
& = -\frac{\partial \rho}{\partial t} dxdy
\end{aligned} \tag{3.1}$$

This can be simplified and rewritten using the divergence term ∇ as:

$$\frac{\partial \rho}{\partial t} + \nabla \cdot (\rho U) = 0 \tag{3.2}$$

where U is the velocity vector in two directions. One must notice that Equation 3.2 is only applied to single phase flow without any mass transfer. To describe the mass loss behaviour during evaporation, an extra source term must be introduced into this equation and it will be described specifically later in Section 3.3.2.

● Secondly, the sum of all forces acting on the control volume must equal the net rate at which momentum leaves the control volume. This known as the momentum conservation, or the Navier-Stokes equation. In x axis, the basic linear conservation can be expressed as:

$$\rho \frac{\partial u}{\partial t} + \rho \left(u \frac{\partial u}{\partial x} + v \frac{\partial u}{\partial y} \right) = -\frac{\partial p}{\partial x} + \mu \left(\frac{\partial^2 u}{\partial x^2} + \frac{\partial^2 u}{\partial y^2} \right) \tag{3.3}$$

where t is time, p is pressure and μ is viscosity. The terms on the left side represent the net rate of momentum flow from the control volume, while the first term in the right side represents the net pressure force; the second term represents the net effect of viscous normal and shear stress. Same equation can be achieved in y axis and the complete momentum conservation can be expressed as:

$$\rho \left(\frac{\partial U}{\partial t} + U \cdot \nabla U \right) = \nabla \cdot \sigma + S_m \tag{3.4.1}$$

$$\sigma = -p\mathbf{I} + \mathbf{T} \tag{3.4.2}$$

Where σ is a stress tensor; \mathbf{I} is the unit diagonal matrix; \mathbf{T} is defined as the deviatoric stress tensor which describes the viscous force. In the current work, the fluid was assumed as an isotropic incompressible system, therefore \mathbf{T} is expressed as:

$$\mathbf{T} = \mu(\nabla U + (\nabla U)^T) \tag{3.5}$$

where T is the temperature.

Moreover, S_m in Equation 3.4.1 is a source term, which represents extra forces applied on the fluid such as gravity, surface tension and et al. The details of S_m will be given in Section 3.3.2.

● Finally, the energy balance must be established, which requires the sum of all energy sources in the control volume equal to 0:

$$\dot{E}_{in} + \dot{E}_g - \dot{E}_{out} - \dot{E}_{st} = 0 \quad (3.6)$$

where \dot{E}_{in} and \dot{E}_{out} are the energy inflow and outflow. \dot{E}_g is the energy generation/consumption and \dot{E}_{st} is the energy storage. The energy inflow and outflow in x axis are defined as $(q_x)dy$ and $(q_x + \frac{\partial q_x}{\partial x} dx)dy$, where q_x can be calculated based on temperature gradient and thermal conductivity k :

$$q_x = k \frac{\partial T}{\partial x} \quad (3.7)$$

The energy storage \dot{E}_{st} is dependent on the time rate of storage of the thermal energy in the medium per unit volume, i.e.

$$\dot{E}_{st} = \rho c_p \frac{\partial T}{\partial t} dxdy \quad (3.8)$$

where C_p is the heat capacity. Moreover, if the convection energy transfer during fluid flow is expressed as $\rho c_p U \cdot \nabla T$, the finial energy conservation can be written as:

$$\rho c_p \frac{\partial T}{\partial t} + \rho c_p U \cdot \nabla T = \nabla \cdot (k \nabla T) + S_e \quad (3.9)$$

where the source term S_e represents the energy generation/consumption \dot{E}_g and the details will given in Section 3.3.2.

3.2.2 Evolution of the L/V free surface

The above three governing equations are used to describe the thermo-fluid situation in a single phase flow system. However, to describe the phase transition such as evaporation, the system must be multiphase and a method of tracking the free surface is necessary. In this project, the level set method, which has been developed by Osher and Sethian [114]

is selected. This method shows many advantages in complex surface movement (e.g. merging and splitting of multiple surfaces) tracking according to previous researches [96, 100, 105, 106, 115], since it can transform the interface tracking problem into a partial differential equation. Meanwhile, the surface properties such as normal and curvature are well represented in level set method, which is very important during the evaporation modeling.

In level set method, a signed distance function Φ is introduced to represent the interface between the liquid and vapour phase at time t , which is defined as:

$$\Phi(x, t) = \pm d \quad (3.10)$$

where d is the distance from the zero level set Φ_0 . A positive value means one side of the interface and negative value means the other. An example of the definition of level set function is plotted in Figure 3.4.

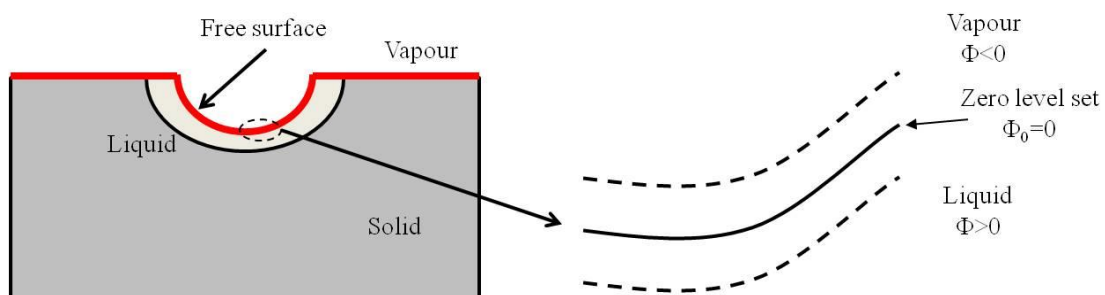


Figure 3.4: Illustration of level set function

As a result, a Heaviside function is used to represent the different phases:

$$\Phi = H = \begin{cases} -1 & d < 0 \\ 0 & d = 0 \\ 1 & d > 0 \end{cases} \quad (3.11)$$

The first order derivative of the Heaviside function is the Dirac Delta function, which equal to 0 except at $\delta(\Phi=0)$ but at a overall integral of 1 from $-\infty$ to $+\infty$. The two functions are plotted in Figure 3.5.a and c. Clearly, the Heaviside function can be used to represent the different fluid properties of the two phases and the Dirac Delta function can be used to represent the interface location.

However, due to the sharp jump of the Heaviside function at the interface and the existence of infinity in the Delta function, it is unlikely to solve the level set function using standard numerical approximation. Therefore the original Heaviside function is smoothed and takes the following form [116].

$$\Phi = H = \begin{cases} 0 & d < -e_f \\ \frac{1}{2} \left(1 + \frac{d}{e_f} + \frac{1}{\pi} \sin \left(\frac{d\pi}{e_f} \right) \right) & -e_f < d < e_f \\ 1 & d > e_f \end{cases} \quad (3.12)$$

And the $\delta(\Phi)$ is therefore smoothed as:

$$\delta(\Phi) = \begin{cases} \frac{1}{2} \left(\frac{1}{e_f} + \frac{1}{e_f} \cos \left(\frac{d\pi}{e_f} \right) \right) & -e_f < d < e_f \\ 0 & d < -e_f \text{ and } d > e_f \end{cases} \quad (3.13)$$

where e_f is defined as the half of the interface ‘band’ thickness. The new functions are plotted in Figure 3.5.b and d.

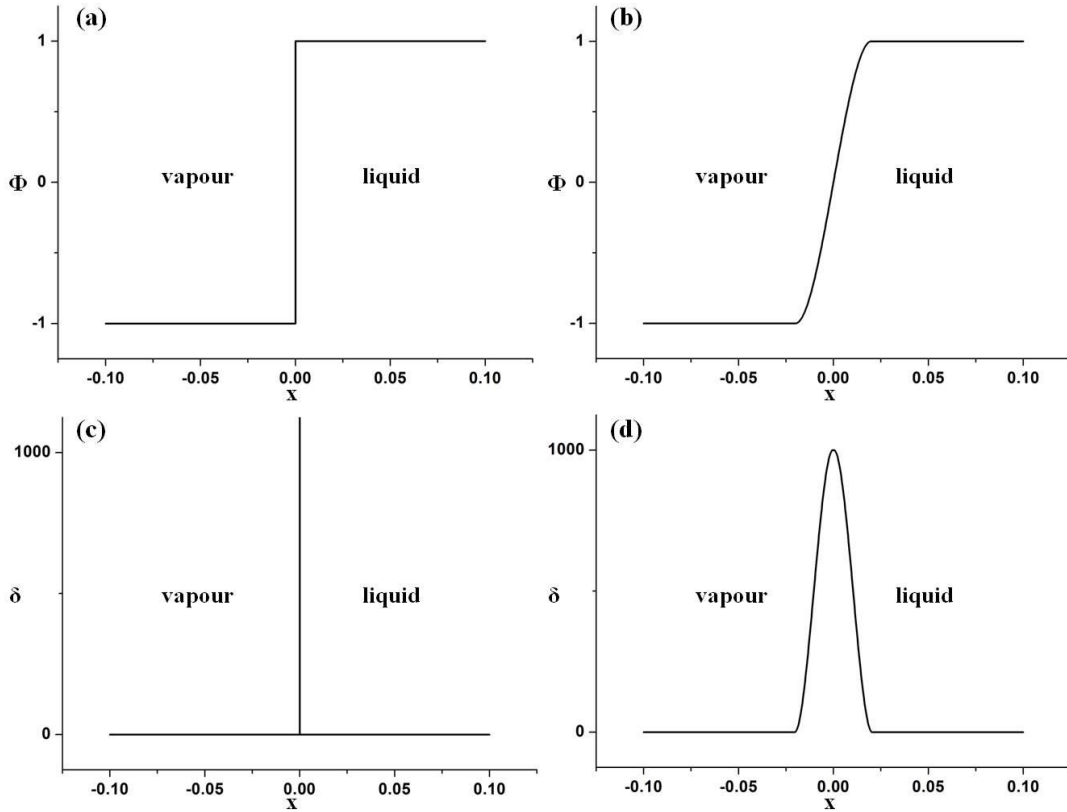


Figure 3.5: The comparison between (a) original Heaviside function; (b) smoothed Heaviside function; (c) original Delta function; (d) smoothed Delta function

Based on the smoothed functions, the interface normal vector \vec{n} and curvature Γ has been derived from the level set function gradient and the divergence of the gradient [114].

$$\vec{n} = \frac{\nabla\Phi}{|\nabla\Phi|} \quad (3.14.1)$$

$$\Gamma = -\nabla \cdot \left(\frac{\nabla\Phi}{|\nabla\Phi|} \right) \quad (3.14.2)$$

Now the problem is how to track the interface during its motion. To achieve this, it is necessary to combine the velocity expression and the level set function together. Since during the flow of liquid and vapour phases, the shape of the interface is only determined by the interface velocity which normal to the interface direction as shown in Figure 3.6; the tangential velocity component is ignored and the normal component is assumed as \vec{u}_{int} . For each point x on the interface there is [116]:

$$\frac{d\vec{x}}{dt} = \vec{u}_{int}(\vec{x}) \quad (3.15)$$

When linked to the level set function Φ there is:

$$\frac{\partial\Phi}{\partial t} + \vec{u}_{int} \cdot \nabla\Phi = 0 \quad (3.16)$$

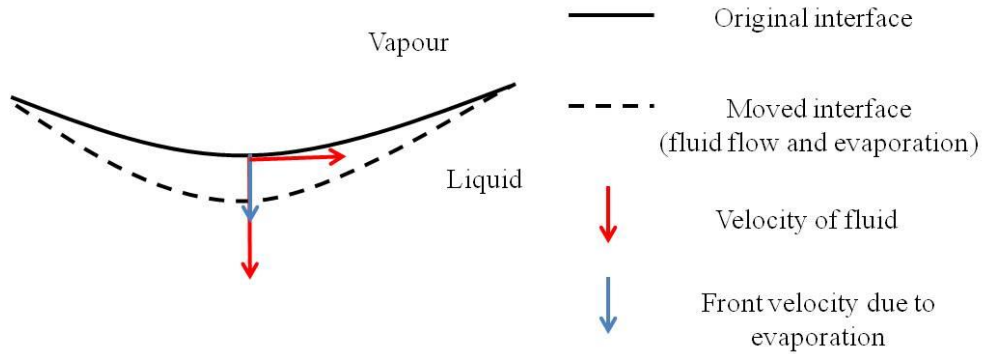


Figure 3.6: Illustration of velocities on the L/V interface, where the interface velocity is a sum of fluid velocity normal to the interface and evaporation velocity

Equation 3.16 is the basic level set governing equation which is used to represent the L/V interface in this work. From the fluid flow view, the interface velocity \vec{u}_{int} is normally thought as the velocity of the liquid phase; however, if evaporation occurs, the velocity is no longer continuous across the interface and the contribution of mass loss must be

considered, as indicated in Figure 3.6. As a result, $\overrightarrow{u_{int}}$ can be expressed as:

$$\overrightarrow{u_{int}} = U + \overrightarrow{u^{evp}} \quad (3.17)$$

where $\overrightarrow{u^{evp}}$ indicates the velocity due to evaporation (named as ‘evaporation velocity’).

The calculation of $\overrightarrow{u^{evp}}$ will be given in Section 3.3.2.

However, when using Equation 3.16 to describe the interface motion, the profile of Φ does not remain constant if a non-uniform flow occurs. As the development of the interface, assuming the initial level set function undergoes a perturbation $\eta(x)$, then at time t there is: [96]

$$\Phi(x, t) = \Phi_0(x - \vec{u}t) + \eta(x - \vec{u}t) \quad (3.18)$$

It indicates the as time evolves, the perturbation $\eta(x - \vec{u}t)$ will not be dampened but Φ will become more and more distorted. Therefore it is necessary to reinitialise the level set function at the beginning of each step during the computation. As reported by Harten [117] an artificial compression flux could be introduced into Equation 3.16 to maintain stability of the interface.

$$\frac{\partial \Phi}{\partial t} + \overrightarrow{u_{int}} \cdot \nabla \Phi + r_0 \nabla \cdot (\Phi(1 - \Phi)\vec{n} - e_f \nabla \Phi) = 0 \quad (3.19)$$

where r_0 is named as a reinitialisation parameter.

3.2.3 Evolution of the S/L interface

To simulate the melting and solidification of the material, it is necessary to track the interface between the solid and liquid phases. However, in the current model, the level set method is already applied at the L/V interface; therefore a new ‘enthalpy-porosity’ method developed by Brent et al [95] will be introduced in this part.

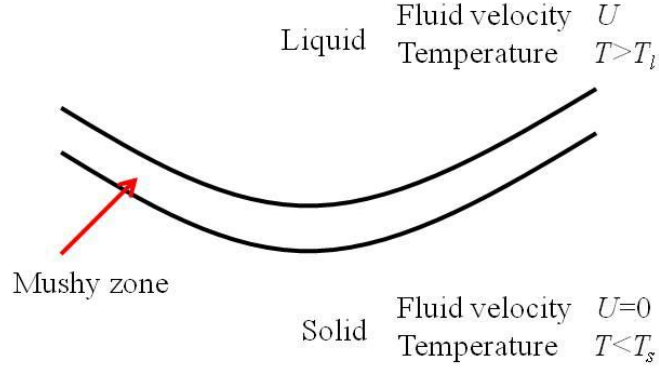


Figure 3.7: S/L interface and velocity/temperature conditions of the liquid and solid phases

Considering the melting process, two distinct regions are present: the solid and liquid, as shown in Figure 3.7. A mushy zone which contains both the two phases at the interface is also formed. The phase transition can be treated using the classical mixture theory. The velocity is the best parameter to distinguish the solid and liquid phase. To keep the velocity as its theoretical value in the liquid phase but always 0 in the solid phase, a damping factor should be introduced into the momentum conservation as the source term S_m in Equation 3.4.1. A Carman-Kozeny equation for permeability can be used as this damping factor:

$$S_{md} = -C \frac{(1 - f_L)^2}{(f_L^3 + b)} U \quad (3.20)$$

where f_L is the liquid fraction which can be thought as the porosity of the ‘liquid element’ in a mushy cells. C is a large-valued constant (10^{12}) accounting for the mushy region morphology and b is added as a small constant (0.001) to avoid division by zero. f_L is assumed to vary linearly with the temperature from the fully solid cell to fully liquid cell. Here the solidus (the lowest temperature for melting) and liquidus (the temperature that whole system has melted) temperature of the material is set as T_s and T_l .

$$f_L = \begin{cases} 0 & T_s \leq T \\ \frac{T - T_s}{T_l - T_s} & T_s < T \leq T_l \\ 1 & T_l < T \end{cases} \quad (3.21)$$

Clearly, if $T < T_s$, the $-C \frac{(1-f_L)^2}{(f_L^3+b)}$ term in Equation 3.20 is a huge value that the solved velocity in momentum conservation will be extremely small and nearly 0; if $T > T_l$,

$-C \frac{(1-f_L)^2}{(f_L^3+b)}$ term is 0 and only the original momentum conservation is considered.

Now considering the energy conservation in Equation 3.8, the ‘enthalpy-porosity’ theory indicates that during phase transition, the latent heat of fusion L_f (J/kg) is adjusted to account for latent heat absorption or evolution, which means its value also depends on the liquid fraction f_L . The enthalpy H_{EN} is therefore expressed as:

$$H_{EN} = \begin{cases} \int_0^T C_{ps} dT & T_s \leq T \\ \int_0^{T_s} C_{ps} dT + L_f f_L & T_s < T \leq T_l \\ \int_0^{T_s} C_{ps} dT + L_f + \int_{T_l}^T C_{pl} dT & T_l < T \end{cases} \quad (3.22)$$

And in this work, the heat capacity C_p for each of the liquid and solid part is assumed as constant, if the heat capacity in the mushy zone is consider, a general of C_p can be obtained from Equation 3.22:

$$C_p = L_f \frac{df_L}{dT} + C_{ps} \quad (3.23)$$

3.3 Model calculation methodology

In this part, the assumptions, laser welding/cladding dynamics and boundary conditions are introduced into the model and the source term in the governing equations are listed.

3.3.1 Model assumptions

The current model includes heat transfer, fluid flow and three phase transition, which is quite complex therefore some simplifications are necessary:

- The system is under steady state, i.e. the liquid density is not varied with time. Equation 3.2 can be simplified as:

$$\nabla \cdot U = 0 \quad (3.24)$$

- The fluid is assumed as Newtonian laminar flow. Moreover, an incompressible flow mechanism is applied.
- Most of the material properties are considered as non-temperature dependent in individual phase; including the density, viscosity, heat capacity, thermal conductivity, laser absorptivity, thermal expansion coefficient, heat transfer coefficient and thermal emissivity. Data for material properties have been selected referencing from several journal articles and listed in Section 3.4.
- The model is set as 2D in an x-y plane and different phases are solved in a single computational domain.
- The input laser beam is always perpendicular to the working plane and its energy is absorbed by the interface of the S/V or L/V directly, which means the Fresnel absorption, beam polarisation and multiple reflection [91] in a keyhole (for a keyhole welding case) are all neglected.
- During the evaporation the effect of Knudsen layer [105] on the vapour parameter is neglected and the existence of laser-induced plasma is simplified.

3.3.2 Laser welding/cladding dynamics and the treatment of source terms

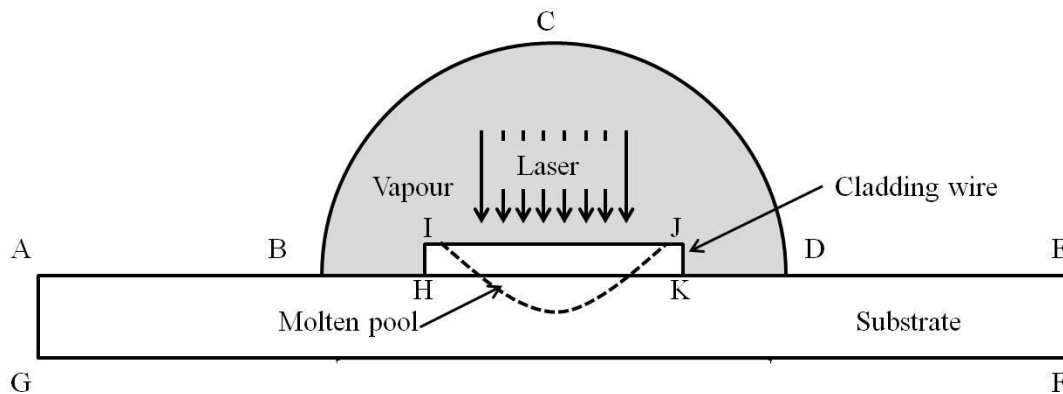


Figure 3.8: Schematic representation of the 2D cross section model

As shown in Figure 3.8, for simplicity a laser flat wire cladding model is set up in here, where boundary BCD is treated as the outflow of the vapour phase; and the boundaries of

the substrate AB, DE, EF, FG and GA are simply treated as wall condition with a thermal insulation property. Meanwhile, the L/V interface is defined as BHIJKD. The above governing equations (Equation 3.2, 3.4.1, 3.8 and 3.19) in Section 3.2 are used to describe the general behaviour of this system. In this section, different source terms in those equations to describe different boundary conditions will be given.

A. The mass flux mechanism during evaporation

During evaporation, there is a mass transfer between liquid and vapour phase. Equation 3.17 clearly reveals the influence of evaporation velocity $\overrightarrow{u^{evp}}$ in the interface velocity.

Here $\overrightarrow{u^{evp}}$ can be defined as:

$$\overrightarrow{u^{evp}} = \frac{\dot{m}}{\rho} \quad (3.25)$$

where \dot{m} is the mass evaporation rate.

To link the mass loss term with the mass conservation equation and level set equation, Equation 3.2 can be firstly modified into the following form:

$$\frac{\partial \rho}{\partial \Phi} \frac{\partial \Phi}{\partial t} + \nabla \cdot (\rho U) = 0 \quad (3.26)$$

The $\frac{\partial \Phi}{\partial t}$ term has already been described by Equation 3.16 and 3.17, simply insert them into Equation 3.26 there is:

$$-\frac{\partial \rho}{\partial \Phi} (U + \overrightarrow{u^{evp}}) \cdot \nabla \Phi + \rho \nabla \cdot U + U \nabla \rho = 0 \quad (3.27)$$

which can be further simplified as:

$$\nabla \rho (-\overrightarrow{u^{evp}}) + \rho \nabla \cdot U = 0 \quad (3.28)$$

i.e.

$$\nabla \cdot U = \overrightarrow{u^{evp}} \frac{\nabla \rho}{\rho} \quad (3.29)$$

By inserting Equation 3.25, a more general form for the mass conservation equation is:

$$\nabla \cdot U = \dot{m} \left(\frac{\rho_l - \rho_v}{\rho^2} \right) \delta(\Phi) \quad (3.30)$$

where l and v represent liquid phase and vapour phase, respectively. The delta function $\delta(\Phi)$ only has value on the L/V interface and it is used to keep the mass transfer term on

the interface only, which has already been explained in previous Section 3.2.2.

Since the L/V interface is smoothed in the current level method, the density on the interface should also be smoothed, as a result:

$$\rho = \rho_v + (\rho_l - \rho_v)\Phi \quad (3.31)$$

The vapour density is varied with temperature and pressure and can be calculated using the following equation:

$$\rho_v = \frac{pM}{RT} \quad (3.32)$$

where M is the molecular weight (kg/mol), R is the universal gas constant.

On the other hand, by inserting Equation 3.17 and 3.25, the level set equation (Equation 3.19) can also be rewritten in the following form:

$$\frac{\partial \Phi}{\partial t} + U \cdot \nabla \Phi + \dot{m} \left(\frac{1 - \Phi}{\rho_v} + \frac{\Phi}{\rho_l} \right) \delta(\Phi) + r_0 \nabla \cdot (\Phi(1 - \Phi)\vec{n} - e_f \nabla \Phi) = 0 \quad (3.33)$$

Now all parameters in governing equations 3.30 and 3.33 have been identified except the mass evaporation rate \dot{m} . It could be defined from the molecular view. According to the Hertz-Knudsen equation, in the state of thermodynamic equilibrium between liquid and vapour, the net evaporation rate J for a liquid-vapour system can be expressed as the difference of absolute rate of evaporation (first term in the right side of Equation 3.34) and back-scattered flux (second term in the right side of Equation 3.34) [118]:

$$J = \frac{1}{\sqrt{2\pi m \Sigma}} \left(\alpha_e \frac{p_{sat}(T)}{\sqrt{T}} - \alpha_b \frac{p_v}{\sqrt{T_v}} \right) \quad (3.34)$$

where m is the mass of single molecule (unit kg), Σ is the Boltzmann constant, α_e and α_b are defined as the evaporation and back-scattered flux coefficient, respectively. $p_{sat}(T)$ is the saturated vapour pressure at T . However, in a normal situation of laser processing, the back-scattered flux is very small compared with the evaporation flux and therefore the recondensation phenomenon is neglected, i.e. α_b is thought as 0. Moreover, the coefficient α_e can be simplified as 1 [112]. As a result, one can achieve the equation for mass evaporation rate as follow:

$$\dot{m} = mJ = \sqrt{\frac{m}{2\pi\Sigma}} \frac{p_{sat}(T)}{\sqrt{T}} = \sqrt{\frac{M}{2\pi R}} \frac{p_{sat}(T)}{\sqrt{T}} \quad (3.35)$$

Since the saturated vapour pressure $p_{sat}(T)$ equal to the atmospheric pressure p_0 at its liquid-vapour equilibrium temperature, therefore $p_{sat}(T)$ can be calculated using the Clausius-Clapeyron equation, which describes the relationship of vapour pressure and temperature of liquid/vapour system at equilibrium state. In this case, at any temperature the saturated vapour pressure $p_{sat}(T)$ can be calculated from:

$$\ln\left(\frac{p_0}{p_{sat}(T)}\right) = -\frac{ML_v}{R}\left(\frac{1}{T_{lv}} - \frac{1}{T}\right) \quad (3.36)$$

i.e.

$$p_{sat}(T) = p_0 \exp\left(-\frac{ML_v}{RT} \frac{T - T_{lv}}{T_{lv}}\right) \quad (3.37)$$

where L_v is the latent heat of evaporation with the unit of J/kg and T_{lv} is the liquid-vapour equilibrium temperature (the boiling point).

B. Force conditions in different phases and interfaces

In the three phase system, the force applied on the L/V free surface is the primary factor that determines the surface morphology of the molten pool. Those forces can be expressed using the source term in the governing momentum conservation equation. Generally, according to the phase stage, the S_m in Equation 3.4.1 consists of four main parts:

$$S_m = S_{mg} + S_{md} + S_{mt} + S_{mr} \quad (3.38)$$

where S_{mg} , S_{md} , S_{mt} and S_{mr} represents the gravity term, S/L phase transition term, surface tension term and recoil pressure term, respectively.

- The gravity term S_{mg} – which includes the net gravity effect and a buoyancy force. The buoyancy force is a result of density variation due to temperature gradient in the liquid. Although to simply the model the density for the individual phase is assumed as constant, it is still valuable to introduce the buoyancy force into the force term. The general expression of S_{mg} is:

$$S_{mg} = \rho g \beta (T - T_l) - \rho g \quad (3.39)$$

where β is the thermal expansion coefficient and the buoyancy term $\rho g \beta (T - T_l)$ only works when $T > T_l$.

- The S/L phase transition term S_{md} – this has already been explained and expressed as a dumping factor in Equation 3.20.

- The surface tension term S_{mt} – different from the previous two terms, the surface tension force is not a body force and only applied on the L/V interface. In the direction normal to the interface, the surface tension denotes to a capillary effect, which acts as a restoring force determined by both the surface curvature and surface tension. Considering the surface curvature as Γ , the capillary force term can be expressed as:

$$S_{mt}^n = \Gamma \gamma \cdot \vec{n} \quad (3.40)$$

Where Γ and \vec{n} are expressed in Equation 3.14; γ is the surface tension. For the steel melt, it can be calculated based on its sulphur content %S (normally the surface tension of liquid stainless steel decreases with increasing sulphur content) [119]:

$$\gamma = 1840 - 0.4(T - T_l) - 0.056T \ln \left\{ 1 + (0.68\%S) \exp \left(\frac{28798}{T} - 8.5647 \right) \right\} \quad (3.41)$$

For the HDPE melt, γ is achieved according to Wei's experiment as [120]:

$$\gamma = (44.34 - 0.046T) * 10^{-3} \quad (3.42)$$

In the tangential direction, a shear force due to the surface tension gradient is generated, which is known as the thermo-capillary force or Marangoni force. Since the surface tension is depended on the temperature, the Marangoni term can be written as:

$$S_{mt}^t = \frac{\partial \gamma}{\partial T} \nabla T \cdot \vec{t} \quad (3.42)$$

To restrict the surface tension term on the L/V interface, a smoothed Delta function needs to be incorporated into Equation 3.40 and 3.42, therefore:

$$S_{mt} = \left(\Gamma \gamma \cdot \vec{n} + \frac{\partial \gamma}{\partial T} \nabla T \cdot \vec{t} \right) \delta(\Phi) \quad (3.43)$$

- The recoil pressure term S_{mr} – during high intensity laser processing, an extra force is

formed due to melt evaporation and it is known as recoil pressure. The recoil pressure is believed as the primary mechanism of L/V interface deformation during keyhole welding. It is applied in the normal direction of the of L/V interface and according to Semak [104] its value reach to 0.55 of the saturated vapour pressure $p_{sat}(T)$. As a result:

$$S_{mr} = (0.55p_{sat}(T) \cdot \vec{n})\delta(\Phi) \quad (3.44)$$

C. Energy source on the L/V interface

In this study, different laser beam irradiance distributions (S_{el}) were applied on the L/V free surface, which is treated as the input energy. Meanwhile, the energy loss also occurs in the form of surface convection (S_{ec}) and radiation (S_{er}). Moreover, during evaporation, extra heat is lost due to mass flux (S_{ee}), as a result there is:

$$S_e = S_{el} - (S_{ec} + S_{er} + S_{ee}) \quad (3.45)$$

where S_{el} , S_{ec} , S_{er} and S_{ee} represents the laser energy term, thermal convection term, thermal radiation term and evaporation heat loss term, respectively.

- The input laser energy term S_{el} – two different energy distribution are applied in the current model: the original Gaussian distribution and the Pedestal distribution, which are shown in Figure 3.9:

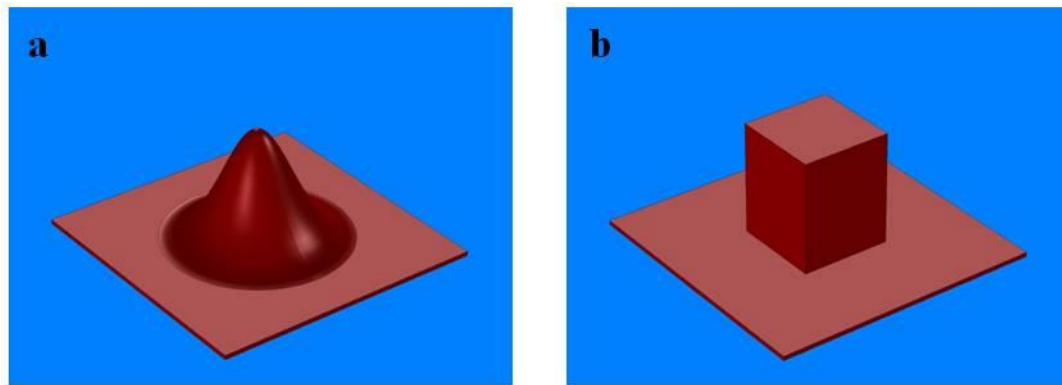


Figure 3.9: Laser profile of (a) Gaussian distribution; (b) uniform Pedestal distribution

For a 1D Gaussian beam, if the energy absorptivity is η and beam radius is assumed as a , which means the power density at $x=a$ equals to $1/e^2$ of the maximum power density P_m . As a result, the Gaussian beam can be written as:

$$E = \eta P_m \exp\left(-\frac{2x^2}{a^2}\right) \quad (3.46)$$

In this work, the model is simplified as 2D in the x - y plane and a 2D cross-section heat source is used. The stationary Gaussian beam distribution is shown in Figure 3.10.a; however since the laser beam has a velocity in z direction; the 2D cross-section heat profile is actually time dependant. If one simply takes time into account, the stationary source will be extended to a line source, the total input energy distribution over a pulse length is figured out in Figure 3.10.b, which is no longer the same Gaussian shape as shown in Figure 3.9.a and therefore obviously incorrect.

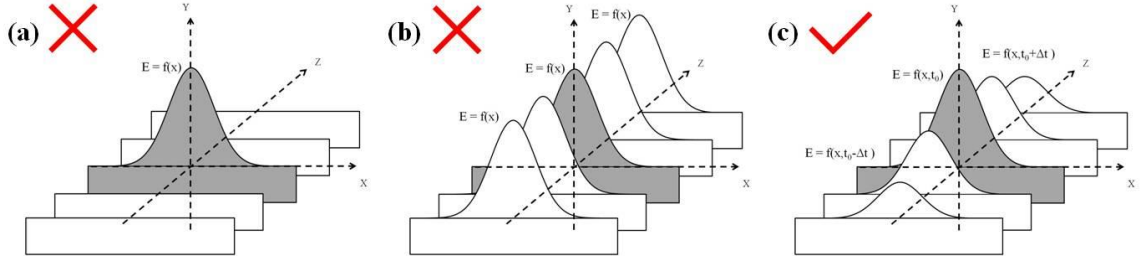


Figure 3.10: The comparison between a (a) stationary; (b) line source and (c) time-dependant Gaussian energy distributions on a 2D substrate

The real heat source model for the 2D case should be a function of both location and time, as shown in Figure 3.10.c, where the variation of P_m with time also obeys the Gaussian distribution. If assume the beam scanning velocity as u_s , the maximum power density P_m at specific time t can be expressed as:

$$P_m = \frac{2P}{\pi a^2} \exp\left(-\frac{2(u_s t - a)^2}{a^2}\right) \quad (3.47)$$

where P is the overall power of the beam with a unit of W/m^2 .

By inserting Equation 3.47 in to 3.46, a general function for the Gaussian heat source can be expressed as follow:

$$S_{el} = E\delta(\Phi) = \eta \frac{2P}{\pi a^2} \exp\left(-\frac{2x^2}{a^2}\right) \exp\left(-\frac{2(u_s t - a)^2}{a^2}\right) \delta(\Phi) \quad (3.48)$$

where $\delta(\Phi)$ is used to make sure the heat source is only applied on free surface.

Meanwhile, since the Pedestal beam has a uniform energy distribution, its 2D cross-section profile is not varied with time. Therefore a simple step function can be used to represent it:

$$S_{el} = E\delta(\Phi) = \begin{cases} \eta \frac{P}{4a^2} \delta(\Phi) & -a \leq x \leq a \\ 0 & x < -a \text{ and } x > a \end{cases} \quad (3.49)$$

- The thermal convection term S_{ec} and radiation term S_{er} — they are results of the heat loss from the processed material to the surrounding phase. They can be expressed using the following equations:

$$S_{ec} = h_c(T - T_{vapour})\delta(\Phi) \quad (3.50)$$

$$S_{er} = \Sigma\varepsilon(T^4 - T_{vapour}^4)\delta(\Phi) \quad (3.51)$$

where h_c , Σ and ε represent the thermal convection coefficient, Boltzmann constant and thermal emissivity, respectively. T_{vapour} is the average temperature of the vapour phase, which is considered as the room temperature in this work.

- The evaporation heat loss term S_{ee} – during the evaporation, energy will loss due to the mass flux from liquid to vapour, thus S_{ee} is a easily calculated from \dot{m} and latent heat of evaporation.

$$S_{ee} = \dot{m}L_v\delta(\Phi) \quad (3.52)$$

3.4 Model verification cases and simulation conditions

According to above descriptions, the final governing equations and source terms are obtained and concluded in Table 3.1.

Table 3.1: Governing equations and source terms used in the model

| Governing equation | | Source terms | | |
|-----------------------|--|---|----------|--|
| Mass conservation | $\nabla \cdot U = \dot{m} \left(\frac{\rho_l - \rho_v}{\rho^2} \right) \delta(\Phi)$ | | | |
| Momentum conservation | $\rho \left(\frac{\partial U}{\partial t} + U \cdot \nabla U \right) = \nabla \cdot \sigma + S_m$ | $S_m = S_{mg} + S_{md} + S_{mt} + S_{mr}$ | S_{mg} | $\rho g \beta (T - T_l) - \rho g$ |
| | | | S_{md} | $-C \frac{(1 - f_L)^2}{(f_L^3 + b)} U$ |
| | | | S_{mt} | $\left(\Gamma \gamma \cdot \vec{n} + \frac{\partial \gamma}{\partial T} \nabla T \cdot \vec{t} \right) \delta(\Phi)$ |
| | | | S_{mr} | $(0.55 p_{sat}(T) \cdot \vec{n}) \delta(\Phi)$ |
| Energy Conservation | $\rho c_p \frac{\partial T}{\partial t} + \rho c_p U \cdot \nabla T = \nabla \cdot (k \nabla T) + S_e$ | $S_e = S_{el} - (S_{ec} + S_{er} + S_{ee})$ | S_{el} | <i>Gaussian:</i> $\eta \frac{2P}{\pi a^2} \exp\left(-\frac{2x^2}{a^2}\right) \exp\left(-\frac{2(u_{st}-a)^2}{a^2}\right) \delta(\Phi)$ |
| | | | | <i>Pedestal:</i> $\begin{cases} \eta \frac{P}{4a^2} \delta(\Phi) & -a \leq x \leq a \\ 0 & x < -a \text{ and } x > a \end{cases}$ |
| | | | S_{ec} | $h_c (T - T_{vapour}) \delta(\Phi)$ |
| | | | S_{er} | $\Sigma \varepsilon (T^4 - T_{vapour}^4) \delta(\Phi)$ |
| | | | S_{ee} | $\dot{m} L_v \delta(\Phi)$ |
| Level set equation | $\frac{\partial \Phi}{\partial t} + U \cdot \nabla \Phi + \dot{m} \left(\frac{1 - \Phi}{\rho_v} + \frac{\Phi}{\rho_l} \right) \delta(\Phi) + r_0 \nabla \cdot (\Phi(1 - \Phi) \vec{n} - e_f \nabla \Phi) = 0$ | | | |

This project is investigating laser additive manufacturing process of integrated 3D circuit board, therefore the model is set up to predict the laser-material interactions at different beam profiles. The material used in the substrate manufacturing is high density polyethylene (HDPE), which has a very small gap between melting and boiling temperatures therefore not ideal for model verification. As a result, a cladding model based on 316L stainless steel is designed first and the result is used to compare with the experiments, which were carried out by Nick Goffin from Loughborough University using a Coherent Everlase S48 CO₂ laser (continuous-wave). Meanwhile, a keyhole welding sample based on mild steel is also prepared. All the simulation cases are designed and listed in Table 3.2.

Table 3.2: Five different cases in the simulation

| No. | Material | Substrate dimension | Input laser beam | Cladding/welding model |
|-----|----------------------|---|------------------|------------------------|
| A | 316L stainless steel | Flat wire: (0.3mm*2mm) on a flat substrate (1mm*14mm) | Gaussian beam | Conduction cladding |
| B | 316L stainless steel | Flat wire: (0.3mm*2mm) on a flat substrate (1mm*14mm) | Pedestal beam | Conduction cladding |
| C | mild steel | Flat substrate (3mm*4mm) | Gaussian beam | Keyhole welding |
| D | HDPE powder | Flat substrate (1mm*4mm) | Gaussian beam | Conduction welding |
| E | HDPE powder | Flat substrate (1mm*4mm) | Pedestal beam | Conduction welding |

Meanwhile, the material properties and laser processing parameters for those cases are shown Table 3.3. One should notice that since the HDPE is in powder form, part of its properties are calculated using the classical mixing theory, i.e.

$$N = N_{PE}V\%_{PE} + N_{AIR}V\%_{AIR} \quad (3.53)$$

where N represents properties of power, including density, heat capacity, latent heat of fusion, latent heat of evaporation and thermal conductivity. V represents the volume fractions of HDPE and air in a close-packing of equal spheres model, as shown in Figure

3.11 and V_{PE} is therefore calculated as 74.1%.

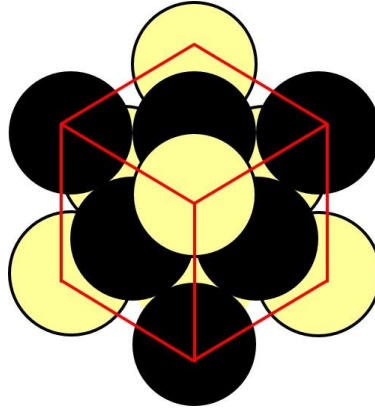


Figure 3.11: An example of close-packing of equal spheres model (face-centred cubic)

Table 3.3: Material properties and processing parameters used in the simulation

| Name | Symbol | Unit | Case A | Case B | Case C | Case D | Case E |
|---|---------------|----------------------|----------------------------|-----------|----------------------------|-----------|----------------------------|
| Material properties | | | | | | | |
| Density of liquid | ρ_l | kg/m ³ | 8000 [130] | | 7850 [142] | | 580 [145] |
| Heat capacity of solid | C_{ps} | J/(kg·K) | 500 [130] | | 780 [142] | | 1926 [145] |
| Thermal conductivity | k | W/(m·K) | 18 [130] | | 50 [142] | | 0.36 [145] |
| Thermal expansion coefficient | β | 1/K | 1.6*10 ⁻⁵ [130] | | 1.17*10 ⁻⁵ [91] | | 1.2*10 ⁻⁴ [145] |
| Dynamic viscosity of liquid | μ | Pa·s | 0.006 [101] | | 0.006 [101] | | 126 [145] |
| Convective heat transfer coefficient | h_c | W(m ² ·K) | 80 [101] | | 80 [101] | | 50 [145] |
| Surface radiation emissivity | ε | / | 0.4 [101] | | 0.4 [101] | | 0.84 [143] |
| Latent heat of fusion | L_f | J/kg | 2.7*10 ⁵ [105] | | 2.7*10 ⁵ [105] | | 1.8*10 ⁵ [145] |
| Latent heat of evaporation | L_v | J/kg | 6.4*10 ⁶ [105] | | 6.4*10 ⁶ [105] | | 3.6*10 ⁵ [145] |
| Solidus temperature | T_s | K | 1648 [130] | | 1755 [112] | | 383 [145] |
| Liquidus temperature | T_l | K | 1674 [130] | | 1813 [112] | | 407 [145] |

| | | | | | | | | |
|---|----------|-----------|--------------------------------------|------------|--------------------------------------|--|------------------------|--------|
| Liquid-vapour equilibrium temperature | T_{lv} | K | 2900 [94] | | 3100 [112] | | 623 [145] | |
| Laser absorptivity of the material | η | / | 0.2 [100] | | 0.2 [100] | | 0.8 [89] | |
| Surface tension coefficient | γ | N/m | Equation 3.41 S% = 0.03% [101] | | Equation 3.41 S% = 0.05% [101] | | Equation 3.42 [120] | |
| Universal gas constant | R | J/(K·mol) | 8.314 | | | | | |
| Boltzmann constant | Σ | J/K | 1.38*10 ⁻²³ | | | | | |
| molecular weight | M | kg/mol | 0.056 | | | | 0.028 | |
| CO ₂ Laser processing parameters | | | | | | | | |
| Beam radius parameter | a | mm | 1 | 1 | 0.15 | | 1 | 1 |
| Standard laser power | P | W | 260 300 | 260 300 | 500 | | 2 4 | 2 4 |
| Laser scanning speed | u_s | mm/s | 1.6 | 1.6 | 10 | | 10 | 10 |

Note: according to Tsuchiya's research [140] the thermal degradation product of HDPE includes different types of alkanes and alkenes; here it is simply assumed as ethylene

The geometry for cladding model has already been indicated in Figure 3.8 and in the welding model the original interface was assumed a straight line. Moreover, the whole model was divided into several computational domains due to different physics needed. The CFD domain near the centre of the model is using a higher number of finite element and degrees of freedom. The mesh visualisations for both the cladding and welding models are indicated in Figure 3.12, where the former one consists of about $1.1 \cdot 10^4$ triangular elements and $1.6 \cdot 10^5$ number of degrees of freedom; the latter one consists of $9.2 \cdot 10^3$ triangular elements and $1.4 \cdot 10^5$ number of degrees of freedom.

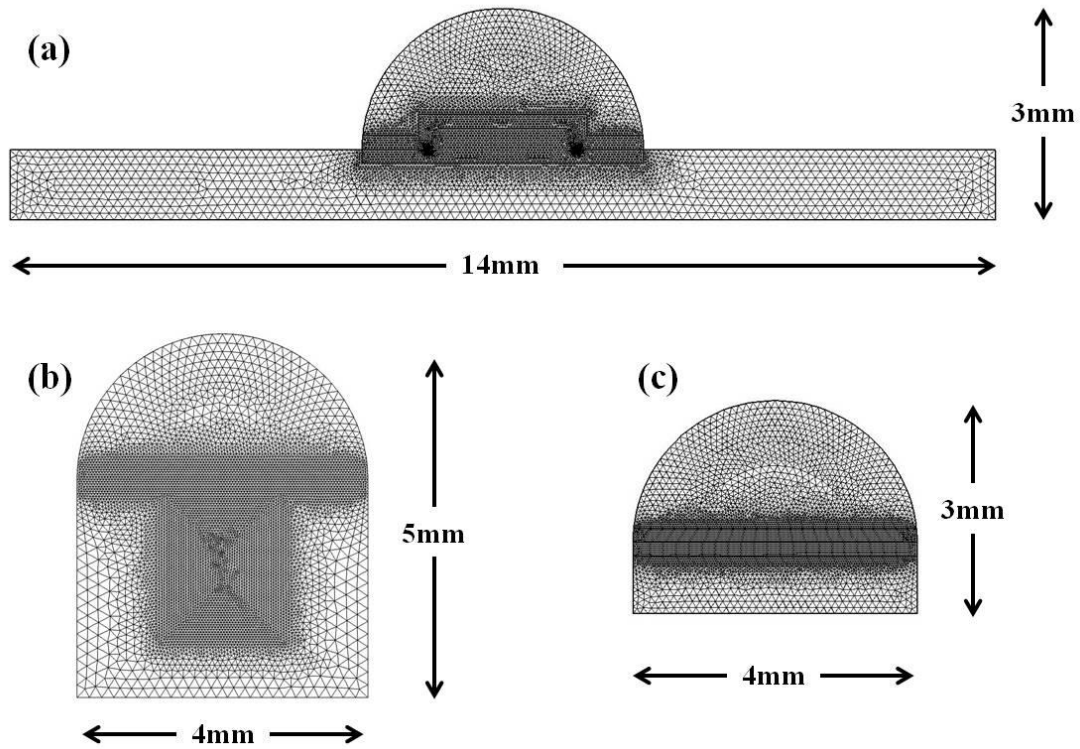


Figure 3.12: Model mesh for (a) cladding: Case A and B; (b) keyhole welding: Case C; (c) conduction welding: D and E

In order to quantify the level of accuracy of the model, the final molten pool image achieved from simulation was compared to the sample image achieved from experiments. The image registration process was selected to align different images into one coordinate system in this work. The goal of image registration is to map points in one image (target image) to the corresponding points in another image (reference image) [146]. According to the common information shared by the features in the two images, the algorithm of image registration can detect points in the target image corresponding to points in the reference image. It then transforms the target image to match the reference image based on point-by-point correspondence [147]. A difference image can therefore be generated, from which the non-overlapping areas are highlighted.

In this work, a program called ImageJ (National Institutes of Health, USA) is used as the image processing software, both the experiment and simulation result images were

imported into it. As shown in Figure 3.13, the geometries of the molten pools were extracted from the original images and they needed further thresholding to be converted to a black and white format. The two images were then registered using an ImageJ plugin program called rigid registration, where the simulation image was selected to transform (target image) and the experiment result was selected as the template (reference image). When registration was completed, a difference image was created with non-overlapping areas shown in white (greyscale = 255) and overlapping areas shown in black (greyscale = 0). The pixels number for each greyscale was quantified from the histogram of the difference image and the similarity can be calculated using Equation 3.54.

$$\text{Similarity (\%)} = \text{Black pixels} / (\text{Black pixels} + \text{White pixels}) \quad (3.54)$$

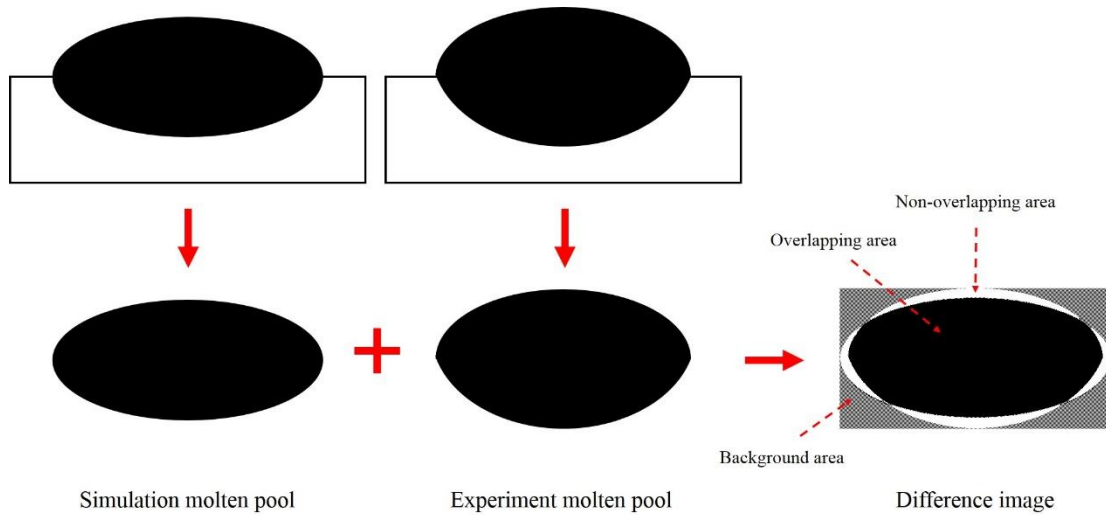


Figure 3.13: Image registration between simulation and experiment molten pool shape

3.5 Laser cladding of 316L stainless steel

3.5.1 Development of the molten pool under Gaussian beam

Figure 3.14 represents the development of the molten pool (black line) when a 260W Gaussian beam is applied, where the temperature field (colour legend) and flow pattern (arrows) are shown.

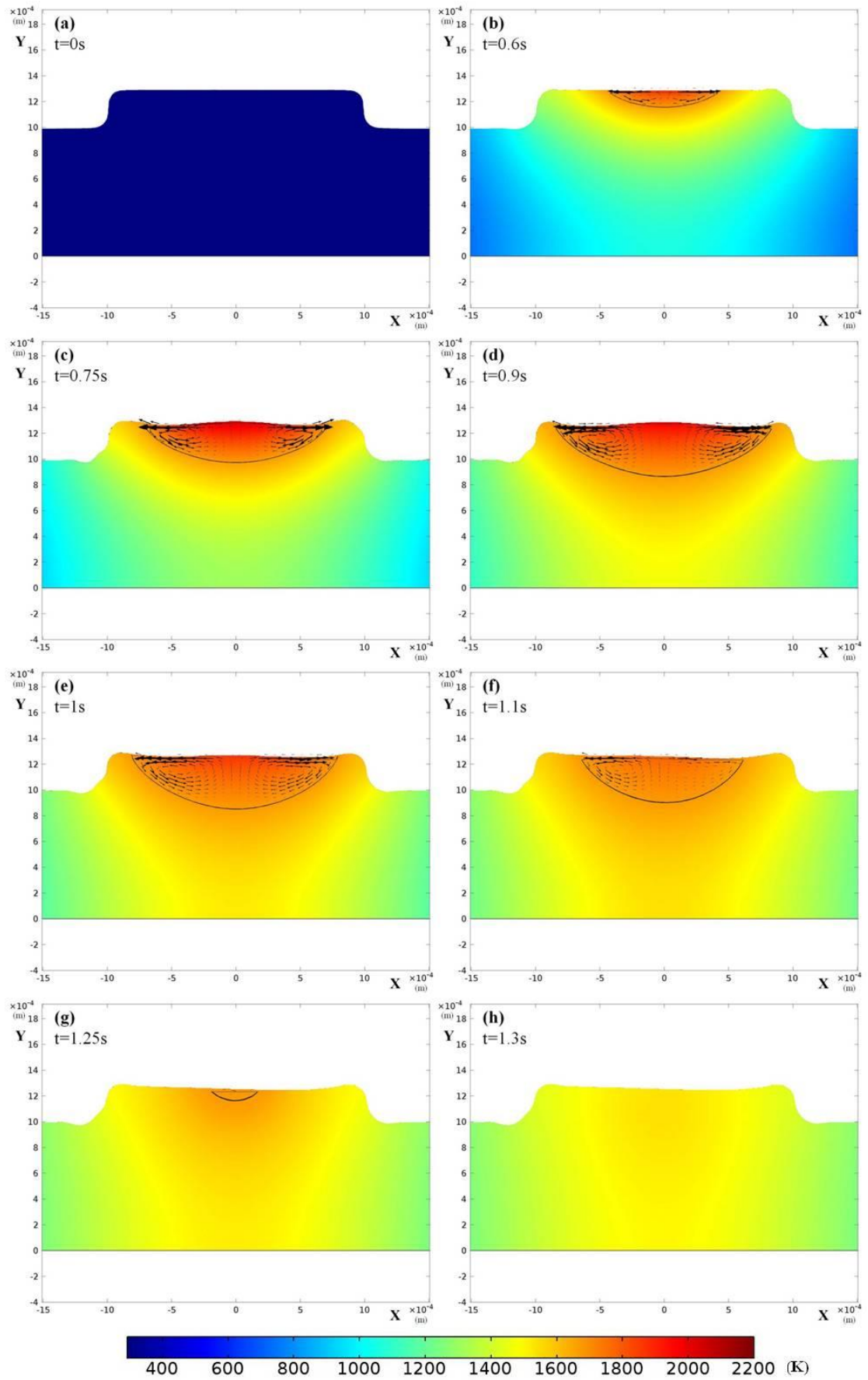


Figure 3.14: Temperature field and fluid flow pattern of the molten pool for case A (260W-1.6mm/s)

At the beginning of the cladding process, the top of the wire is heated and the molten pool is formed at the central region ($t=0.6s$), as a result of the energy distribution of Gaussian beam. Then the molten pool keeps growing in both X and Y axis and the vectors indicate the flow start from the centre to the surrounding regions and after reaching the edge of the molten pool, the flow direction is changed to downward and then goes back to the centre. This kind of circulation is a result of the Marangoni effect, which is generated by the surface tension gradient of the fluid. Normally fluid tends to flow from region with low surface tension to region with high surface tension. And the temperature will have a positive or negative relationship with the surface tension according to the material property. In this case, since 316L stainless steel has low sulphur content (Table 3.3), this temperature coefficient of surface tension is negative and therefore flow will be outward to the low temperature region. Meanwhile, some researchers [121, 122] also reported the welding conditions for a positive coefficient value at the same Gaussian input energy type, which will create a narrower and deeper molten pool due to the flow is reversed to the central region.

It is interesting to notice that as the development of molten pool, the stable state of the free surface is broken and a small ramp is formed at the centre of the wire. Figure 3.15 plots the velocity vectors (u for X axis and v for Y axis) on the L/V interface against radial distance (distance to the central point on X axis), it should be noticed that the oscillations of the curve does not represent the oscillations of the velocity; they are formed because the level set method lacks of numerical stability during free surface tracking. However, one can still find from Figure 3.15 the strongest outward flow appears at the region between the centre and edge of the molten pool and the velocity at the centre point is almost equal to 0. This is a result of the energy distribution of Gaussian beam. From Figure 3.9.a, Gaussian beam has 0 energy gradient in the centre; the gradient keeps increasing along the radial distance and reach the maximum value near the midpoint between centre and edge. A strong Marangoni force is therefore formed in this region and it will further lead a high outward flow velocity. When the fluid reaches the cold solid surface at the edge, its direction will be changed to downward due to gravity. And at the

central bottom region of the molten pool an upward flow is formed under the effect of buoyancy force; although this velocity value (Figure 3.15.b) is quite small compared with that in X axis (Figure 3.15.a), it is still strong enough to overcome the gravity effect since the high temperature gradient in that region. Eventually, the melt will ‘stack’ at the centre and creates a small ramp.

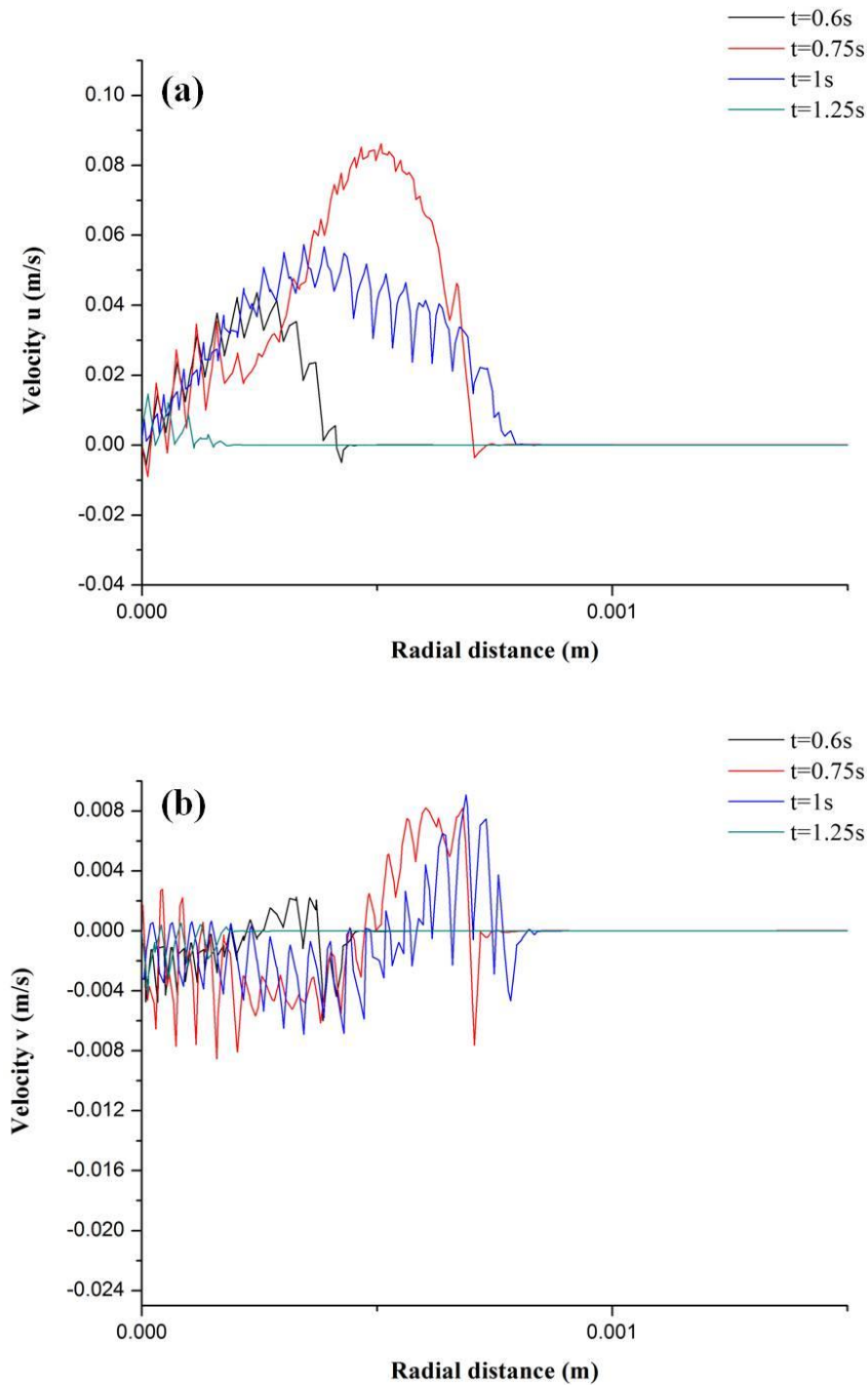


Figure 3.15: Velocity vectors (a) u and (b) v on the L/V interface of case A (260W-1.6mm/s)

From the parameters in Table 3.3, it is easy to calculate at $t_{total}=a/u_s=1.25s$ a complete beam is scanned over the substrate, i.e. the heating is stopped. However, due to the Gaussian energy distribution, the input energy intensity reaches its maximum value at $t_{max}= t_{total}/2=0.625s$. As a result, one can find out from Figure 3.14 the molten pool maintains its size during $t=0.9s$ to $t=1s$ and then the size keeps decreasing; at $t=1.25s$ the substrate is almost fully frozen. This kind of reduction can also be observed from the velocity plots in Figure 3.14. However, one should also notice that after cooling ($t=1.3s$) the wire is not fully melted at this condition, where the edge still keeps its original shape.

3.5.2 Comparison between the Gaussian and Pedestal cladding

If a Pedestal energy distribution is applied on the cladding material, the development of the molten pool is exhibited in Figure 3.16, where a circulation flow similar to the Gaussian cladding case is formed. However, the geometry of the cladding wire is eventually changed from rectangular to half-cycle after the processing, which is different from Gaussian case. To explain this, the temperature distributions on the L/V interface at different times are plotted in Figure 3.17.

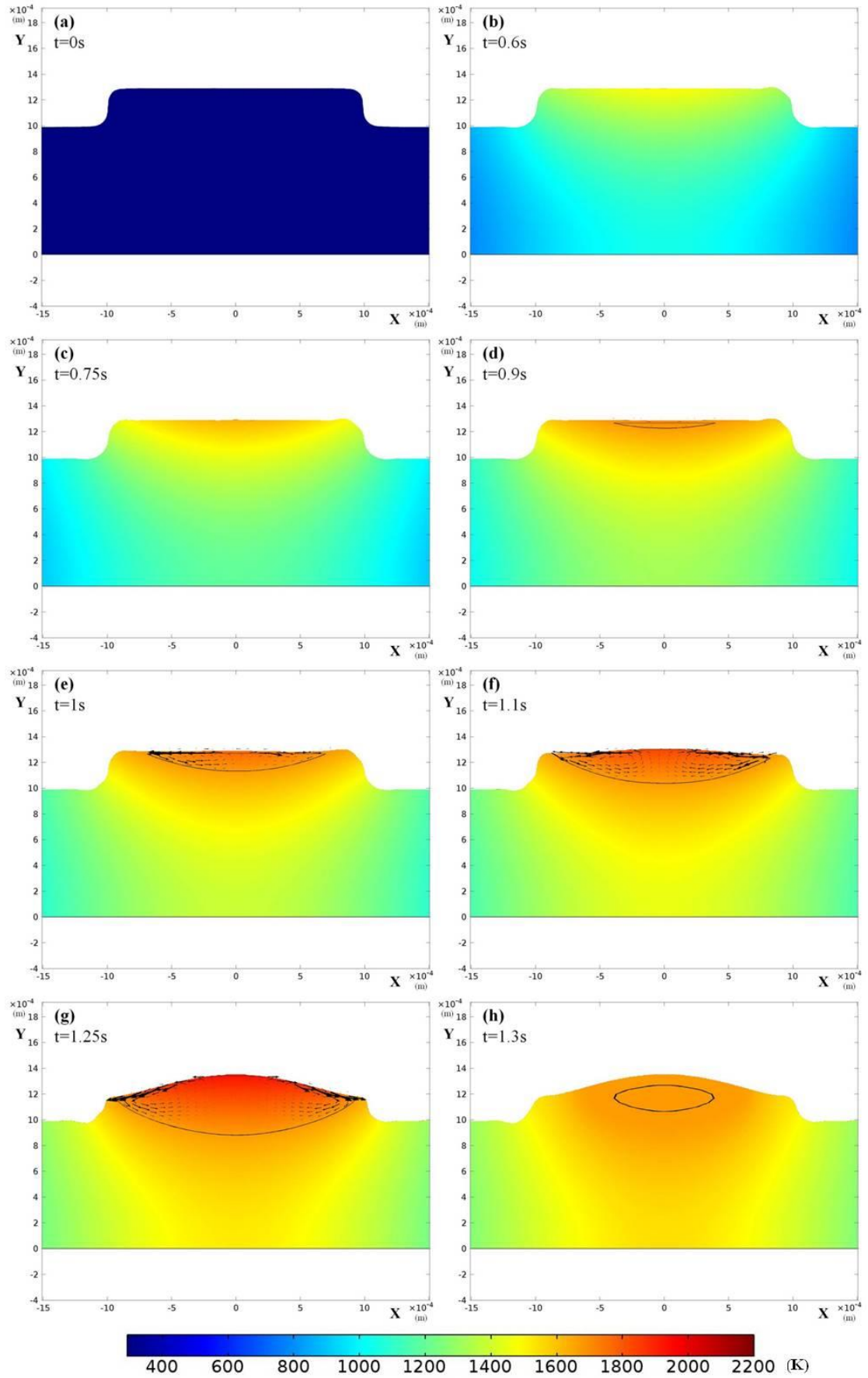


Figure 3.16: Temperature field and fluid flow pattern of the molten pool for case B (260W-1.6mm/s)

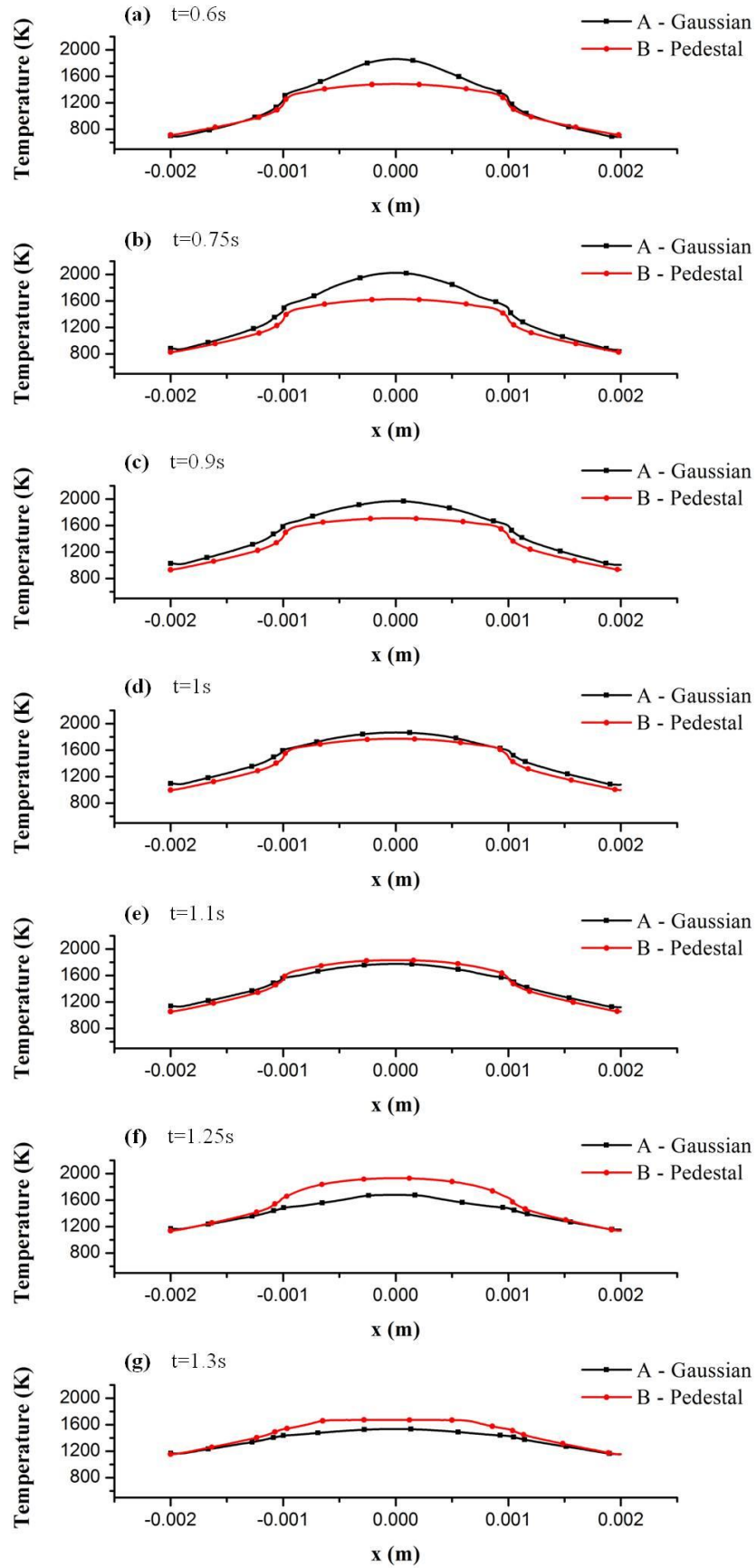


Figure 3.17: Temperature distribution on the L/V interface for case A and B (260W-1.6mm/s)

Obviously, at the start of the heating process, the Pedestal case has a more uniform temperature distribution compared with the Gaussian case but the value at edge is still lower than the centre, because of the direct heat loss in that region. Meanwhile, due to the low temperature gradient, the thermo-capillary force for the Pedestal case is very small and therefore the Marangoni flow is weak, which can be further indicated from the velocity vector plots of case B in Figure 3.18, where the oscillations also represent the instability of the numerical model. Compared with the Gaussian beam case (Figure 3.15), the velocity value in X axis is quite small and until the end of heating process ($t=1.25s$) a large value can be observed; but it is still only half of the maximum value in Gaussian case. This will lead a more stable flow inside the molten pool in the Pedestal case. However, the situation for velocity in Y axis is totally different, where for the Gaussian case it is almost 0 during the whole process but for the Pedestal case, a strong flow to the $-Y$ direction is formed near the edge of the wire. This is the reason for the wire deformation during the processing. The uniform temperature distribution in Pedestal cladding will lead a melting of the whole wire simultaneously, not via a ‘centre – edge’ heat conduction model like the Gaussian case. The wire geometry will therefore transfer to a half-circular shape as a result of capillary force.

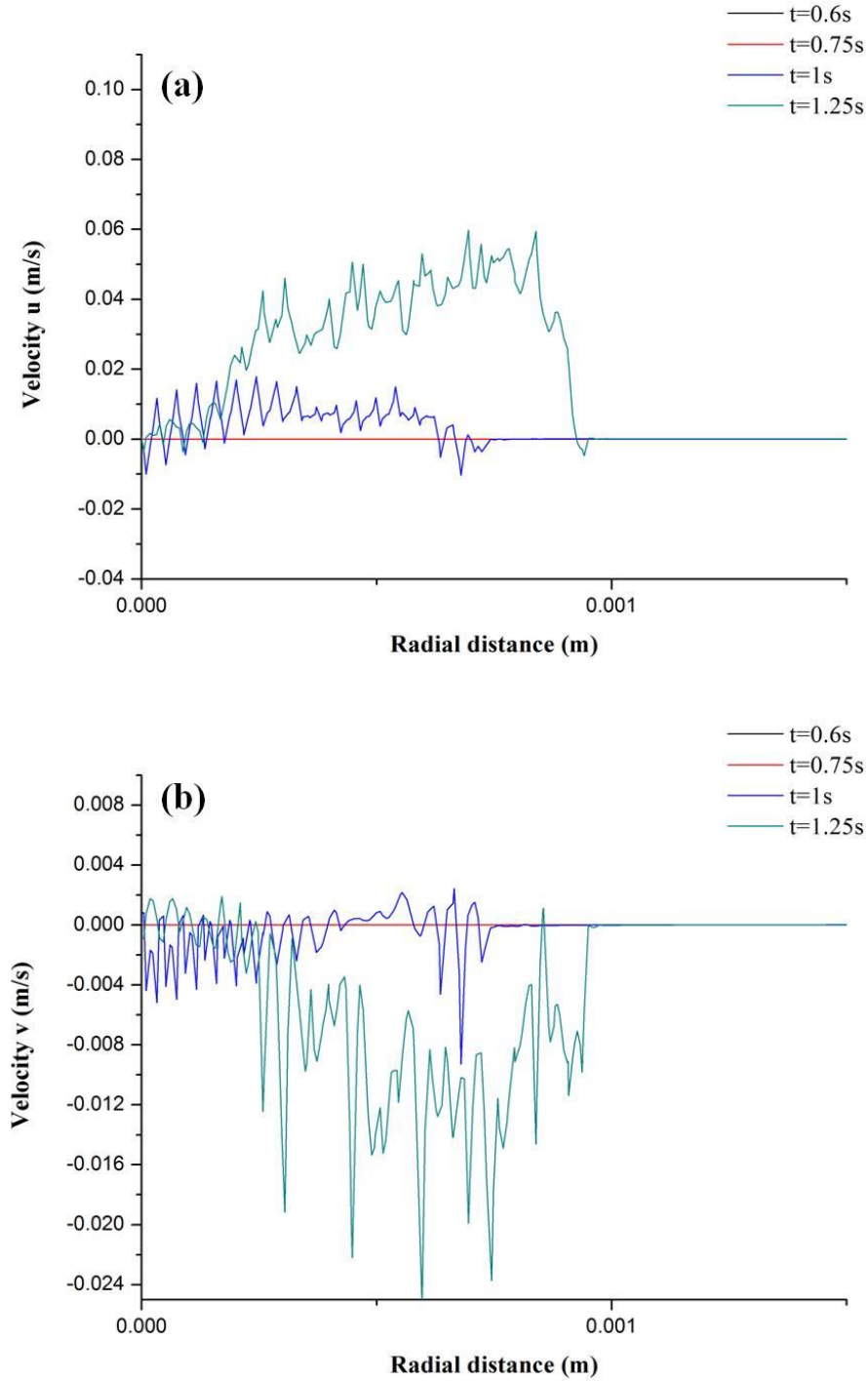


Figure 3.18: Velocity vectors (a) u and (b) v on the L/V interface of case B (260W-1.6mm/s)

One may also notice that (Figure 3.17) as time increases, the temperature difference between the two cases is getting smaller and at $t=1.1s$, the two curves nearly coincide with each other. The detailed temperature variations with time on the central point of the interface are plotted in Figure 3.19. According to previous discussion a Gaussian beam

heating process can be divided into 3 steps:

- 0-0.625s, as the scanning is carried out, the temperature keeps increasing due to the increased beam intensity, which will reach its maximum value at $t=0.625$ s.
- 0.625-1.25s, after the peak intensity passes the substrate, at the early stage the temperature will not decrease with the beam intensity but keep an equilibrium state until the heat loss rate exceeds the heat input rate; then it starts decreasing;
- 1.25-1.5s, there is a significant decreasing of temperature near $t=1.25$ s because laser is switched off; after this, the heat loss rate is also reduced and meanwhile heat stored in the lower region inside the molten pool will transfer up to the surface to compensate the energy loss, as a result the temperature decreasing rate is reduced.

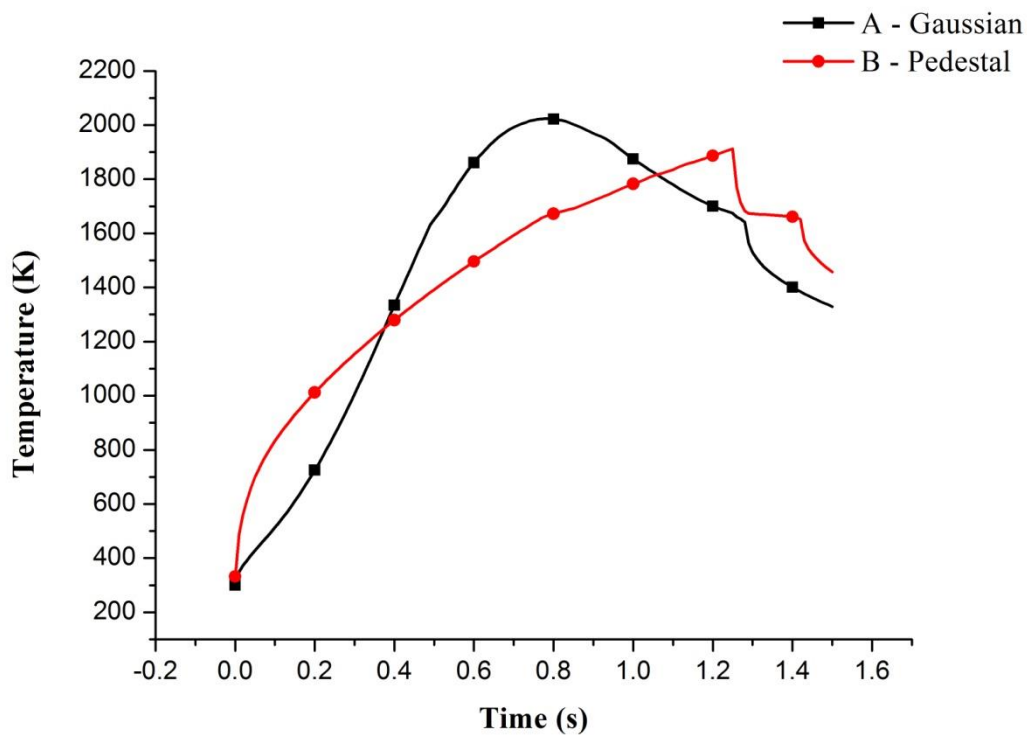


Figure 3.19: L/V interface central point temperature variation with time for case A (260W-1.6mm/s) and B (260W-1.6mm/s)

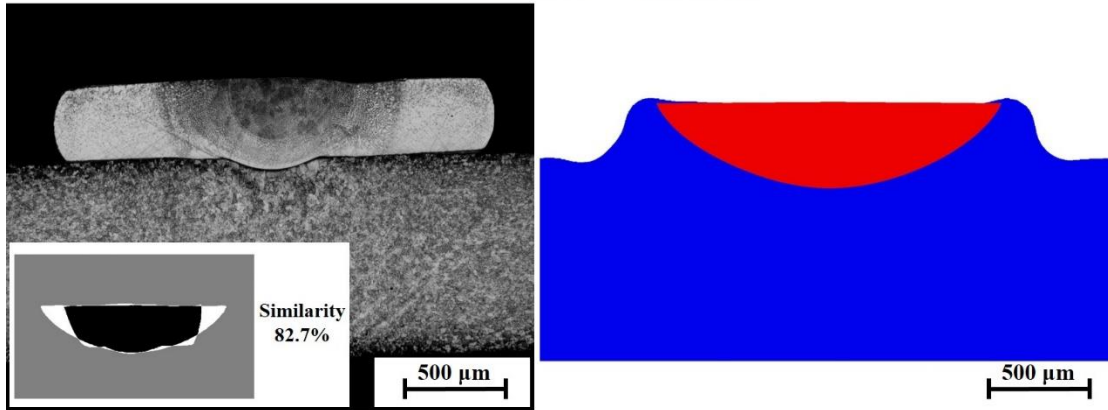
However, the situation for the Pedestal beam is different, which includes two general steps:

- 0-1.25s, at the early stage the Pedestal case has a higher temperature than Gaussian case but will be exceeded by Gaussian case at $t=0.5s$; due to its intensity distribution the Pedestal beam will always keeps a constant input energy until the whole pulse is scanned over. This will lead an increasing of the surface temperature and eventually exceeds Gaussian case again at $t=1.1s$.
- 1.25-1.5s, a significant decreasing in temperature is also observed in Pedestal case, but it is followed by an equilibrium state and then decreases again. This is also a result of the compensating energy from lower region but much stronger than the Gaussian case. After the solidification of surface region a molten pool is still exist in the core of the wire, which is also indicated in Figure 3.16.h.

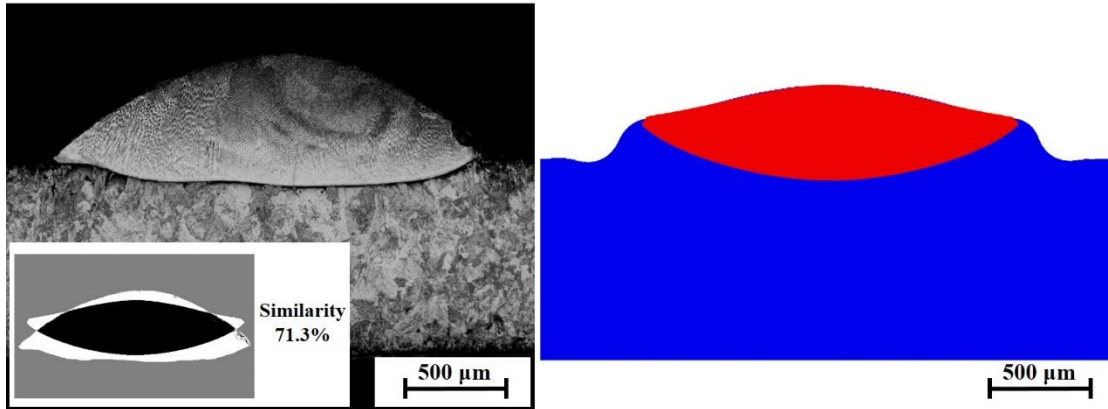
The maximum temperatures for the two cases is about 2000K, which is far below the boiling point of the 316L stainless steel (2900K). Therefore although the evaporation is considered in those models, the mass loss rate is very small and they only exhibit a ‘conduction welding’ type process.

The experiments at the same conditions (with two different powers 260W and 300W, scanning speed 1.6mm/s) are carried out and the cross-section images of the 316L stainless are prepared using optical microscopy. Meanwhile, a 300W laser cladding model is generated for Pedestal case. The direct comparison between the simulation and practical works are shown in Figure 3.20, where the similarity are calculated using the method described in Section 3.4.

(a) Gaussian 260W – 1.6mm/s



(b) Pedestal 260W – 1.6mm/s



(c) Pedestal 300W – 1.6mm/s

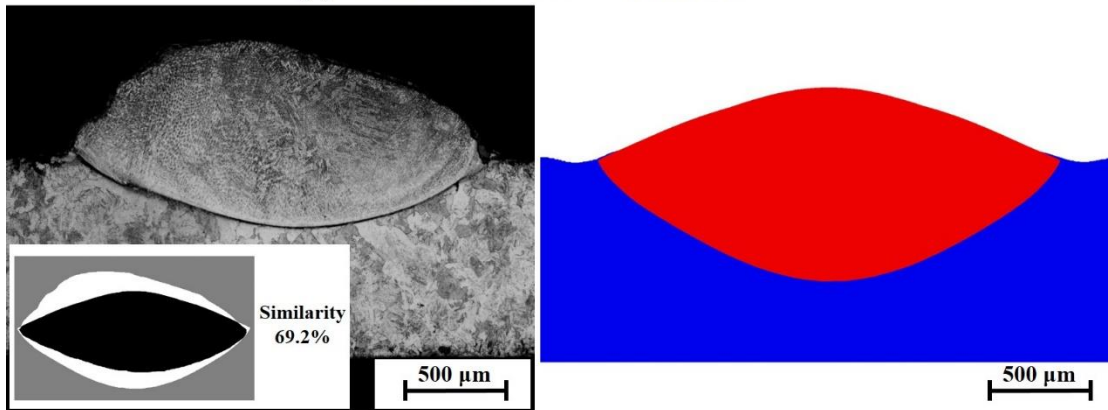


Figure 3.20: Comparison between simulation and practical molten pool geometries for laser cladding at different conditions

The molten pool geometry for the simulation are calculated by projecting the molten pool edges at all relative times on the final $t=1.5\text{s}$ plane. According to the comparison, the similarity between the predicted molten pool geometries and those achieved from the

experiments are as high as 70-80%. However, differences between them can also be observed:

- The molten pool depth from the simulation is higher than the experiment result in every case.
- The wire edges of the Pedestal 260W case are fully melted in experiment but not in the simulation.

This phenomenon is a result of the thermal resistance layer between the wire and substrate material. Although in practical work a roller is used to make sure the wire is closely contact with the substrate, a thin layer of air is still exist between them. Therefore the efficiency of heat flux across this layer is quite low compared with direct heat conduction in a single material phase. However, in the simulation this thermal resistance layer is ignored due to concerns of simplification. Hence in modelling energy is much easier to flow down and generate a deeper molten pool but it is more likely to be ‘trapped’ in the steel wire in experiments, therefore even at a low input power case (Pedestal 260W), the edge of the wire can be melted in practical work.

However, the current model still clearly represents the cladding conditions at different beam irradiance distributions and indicates the advantage of the Pedestal beam. At 260W, wire processed by Gaussian beam keeps its original shape since the molten region is only restricted in the centre; however, the Pedestal beam can overcome the high heat loss rate at the edge of the wire and fully melt it; meanwhile the two parts are well bonded with a small mixing zone. If a higher energy (300W) is applied, the molten pool penetration depth is significantly increased and a larger mixing zone is formed. For industry the size of the mixing zone should be well designed to provide best adhesive property.

3.6 Laser keyhole welding of mild steel

3.6.1 Keyhole formation and development

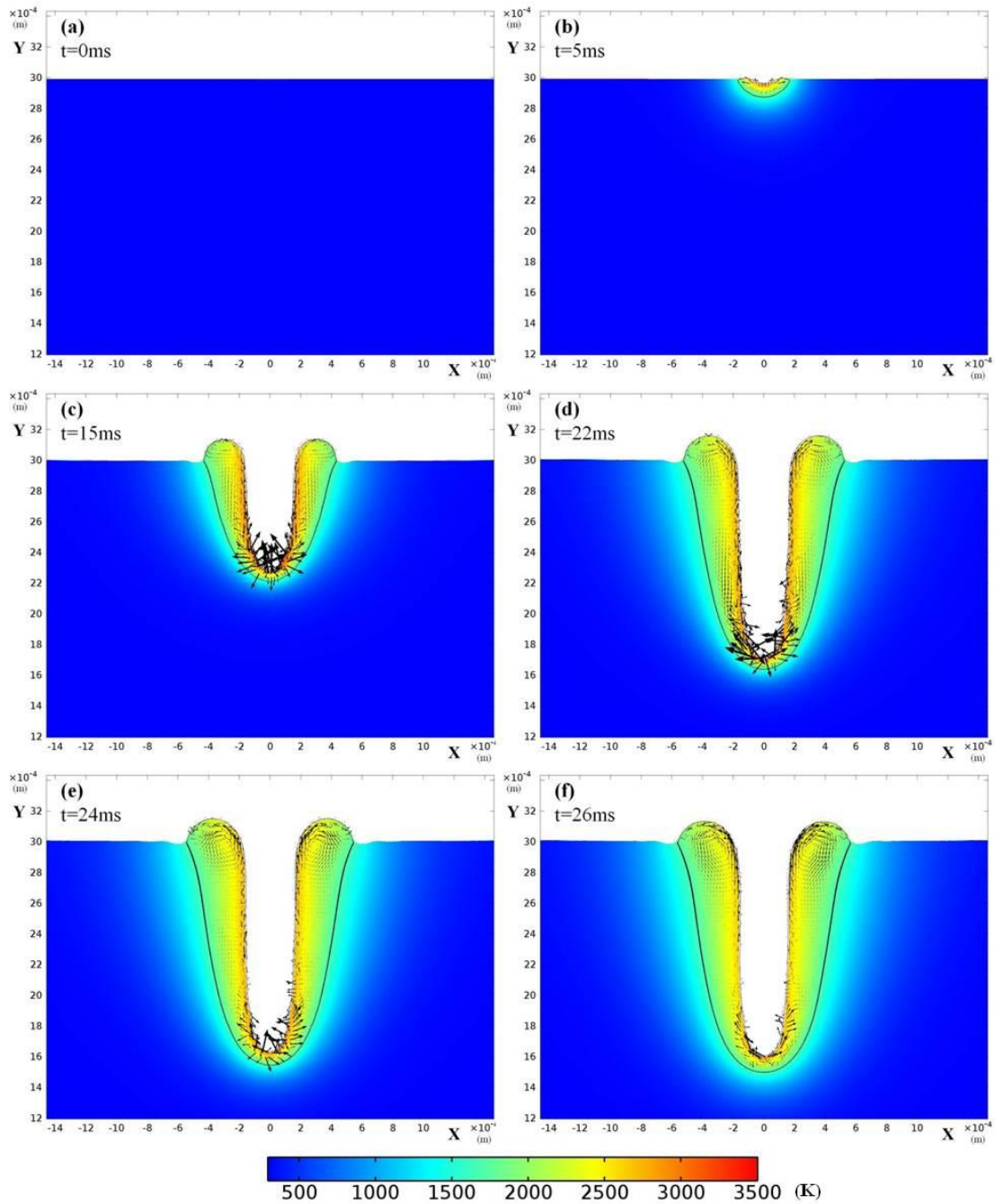


Figure 3.21: Temperature field and fluid flow pattern of the molten pool during the keyhole development in case C (500W-10mm/s)

Figure 3.21 represents the development of the keyhole at a high laser power intensity

condition (case C), where the temperature field and velocity vectors are given. At the very beginning of the heating ($t=5\text{ms}$), a small molten pool is formed but its development behaviour is different from that in the conduction welding/cladding cases; there is no circulation flow and therefore no ramp is formed in the centre of the substrate. However the melted material will be depressed and propagate into deeper region ($t=15\text{ms}$). The thickness of the molten pool (distance from the un-melted material to the nearest L/V free surface) is very low during the whole process of the keyhole development and at the bottom of the keyhole, the lowest thickness appears. Meanwhile, the velocity vectors indicate a strong upward flow is formed along the keyhole surface, which keeps pulling the liquid material out of the keyhole and increase its depth. Moreover, at the top of keyhole, a circulation flow is generated and flow direction is changed to downward. According to previous discussion, the upward flow near keyhole surface could be a result of Marangoni shear force and the downward flow near the solid material surface could be a consequence of the gravity and buoyancy force. However, those forces are not strong enough to enable such a ‘drilling’ process and therefore the evaporation mechanism is used to explain this phenomenon.

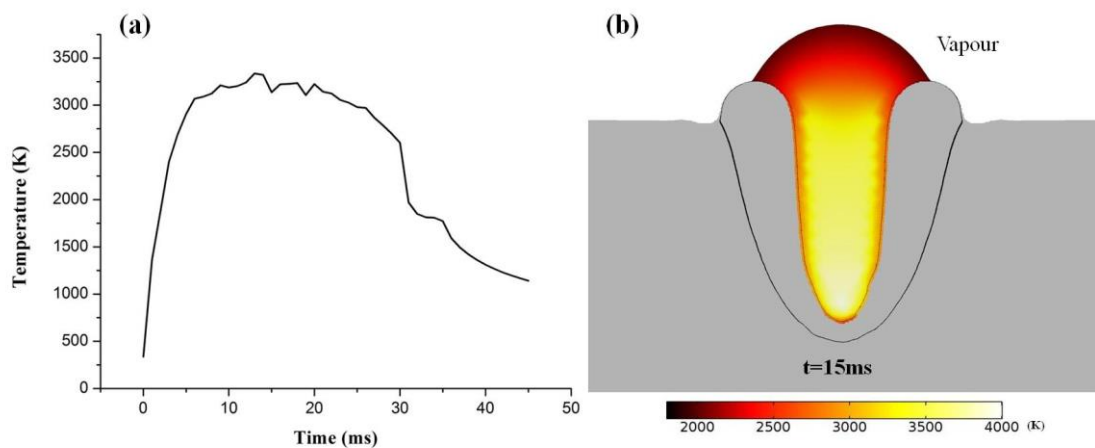


Figure: 3.22: (a) L/V interface central point temperature variation with time for case C (500W-10mm/s) and (b) surrounding vapour temperature field at $t=15\text{ms}$

From the L/V interface central point temperature history plot in Figure 3.22.a, the surface temperature will rapidly reach up to the boiling temperature (3100K) of mild steel and

then oscillating near that point. During evaporation, the generated metal vapour will be trapped inside the keyhole and it will absorb the laser energy directly. The temperature of the vapour phase increased rapidly due to its low heat capacity, as indicated in Figure 3.22.b, where a 4000K vapour temperature can be observed. The hot vapour could be the secondary heat source during keyhole formation since it will heat up the surrounding keyhole walls via radiation. As a result, although the intensity of Gaussian beam starts decreasing after $t=15\text{ms}$, the keyhole wall temperature can still keep stable until $t=30\text{ms}$.

Moreover, although the evaporation occurs at any temperature above the melting point, its rate is quite low and cannot be directly observed (case A and B) until reaching the boiling temperature. The mass loss due to evaporation is one reason for the keyhole propagation but as indicated in Figure 3.23, the total propagation velocity (in Y axis) on the interface central point is quite high when compared with mass evaporation velocity.

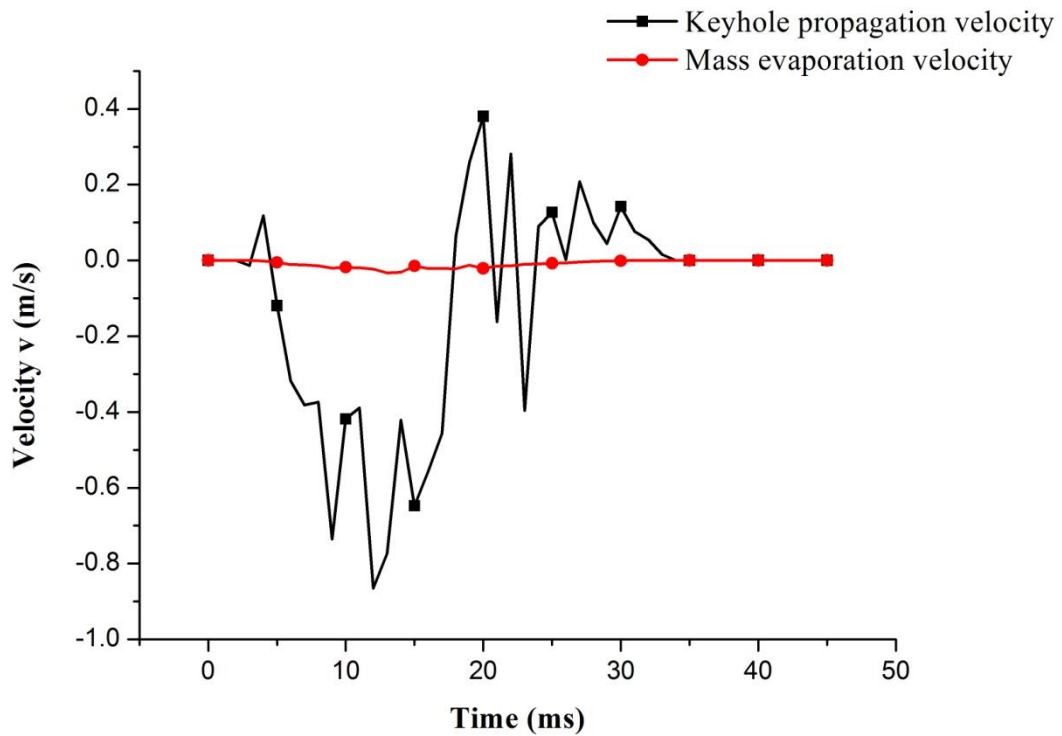


Figure 3.23: L/V interface central point velocity in Y axis variation with time for case C (500W-10mm/s)

Except the mass loss from liquid to vapour phase, the evaporation will also generate a strong pressure on the normal direction of keyhole surface and pushing down the molten layer to the solid metal, which is called recoil pressure and believed as the primary force for keyhole propagation. Since the Gaussian beam has majority of its energy at the centre, it has the highest temperature in that region and therefore strongest recoil pressure. As a result, the melted material is forced to flow up and leaving the thinnest molten layer at the centre. However, one may also notice that the propagation velocity of keyhole keep decreasing and after $t=18\text{ms}$ there is a period of oscillation, which indicates the keyhole propagation has been blocked.

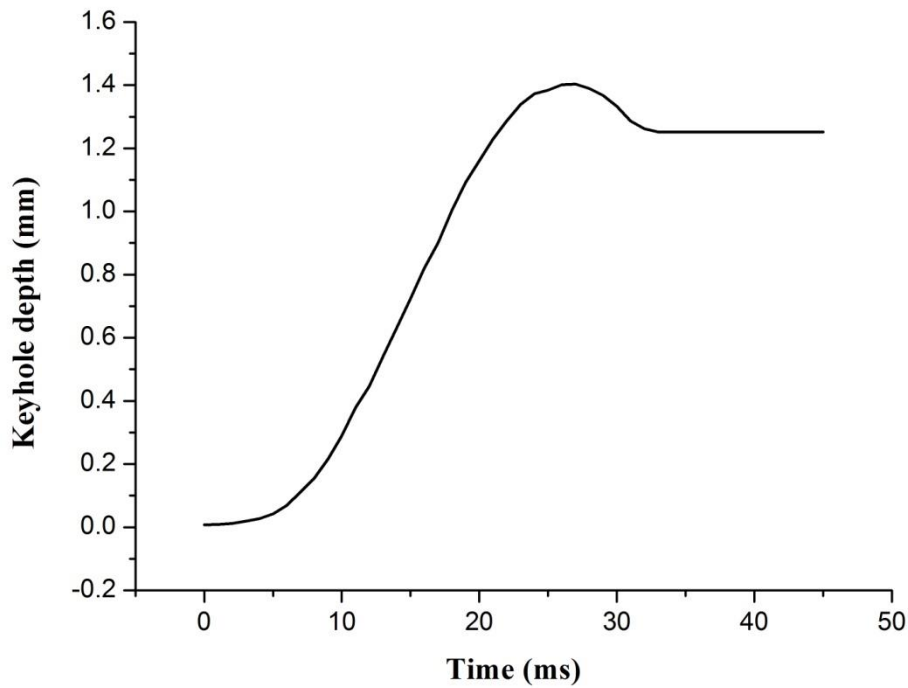


Figure 3.24: Keyhole depth variation with time for case C (500W-10mm/s)

The keyhole depth against time is plotted in Figure 3.24. Obviously after reaching maximum, the depth of keyhole remains stable and does not change significantly. Two extra forces are applied on the melted layer except the recoil pressure and Marangoni force: the gravity generated hydrostatic force and curvature generated capillary force. They will make the flow downward to prevent the keyhole formation. The directions of

those forces are shown in Figure 3.25. Although the recoil pressure force keeps increasing as the keyhole deepens, the hydrostatic force increased more rapidly in the reverse direction. Therefore it is very difficult for the keyhole to keep pumping the fluid upward. Meanwhile, since after the peak intensity of Gaussian beam scanning over the modelled plane, the input energy is reduced and the surface is heated by hot vapour in the keyhole, the temperature gradient along the keyhole surface is reduced and therefore the Marangoni force. As a result, the upward flow is reduced as well. Moreover, although a downward flow is generated by capillary force, it is too small to be considered during the keyhole formation period.

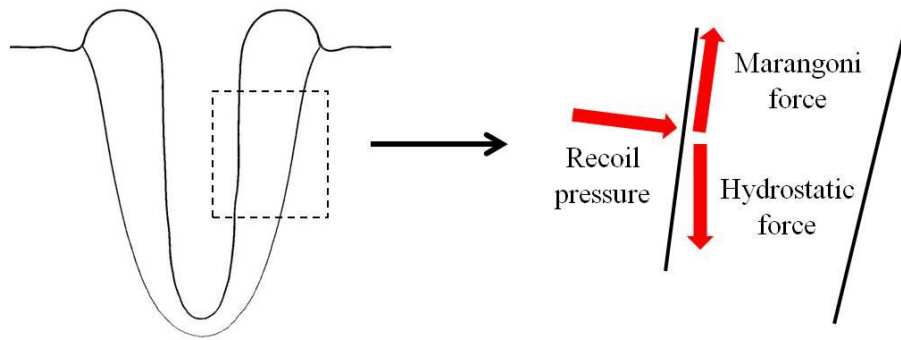


Figure 3.25: Directions of three forces on the keyhole surface

3.6.2 Keyhole collapse and solidification

Figure 3.26 represents the keyhole collapse and solidification process. From the keyhole depth plot in Figure 3.24, it is interesting to notice that the collapse starts at about $t=28\text{ms}$, where the laser is shut off at $t=30\text{ms}$. Due to the low input energy intensity after $t=28\text{ms}$, the temperature of the substrate is unable to keep stable at the boiling point (Figure 3.22.a); therefore the recoil pressure disappears very quickly. Meanwhile, as described before the Marangoni force is also quite small at this time. The hydrostatic force and surface tension became the primary force for keyhole evolution and it will pull the liquid downward to fill back the keyhole. However, since most liquid is maintained in the upper region of the keyhole, the thin layer of liquid in the bottom region is less mobile. Therefore the velocity near the upper region is larger in Figure 3.26 and this part collapses

faster than the bottom region. As a result a ‘bottle-like’ keyhole structure with a narrow neck is formed. It has been reported in some works [101, 110, 111] if the keyhole is sufficiently deep a vapour cavity will be generated; but in this case, it does not have sufficient time for porosity to form. Moreover, from a temperature view the bottom region solidifies much quicker than the upper region, which is also believed as a result of the quantity of liquid; it will lead a low heat capacity and fast heat conduction rate in the bottom region.

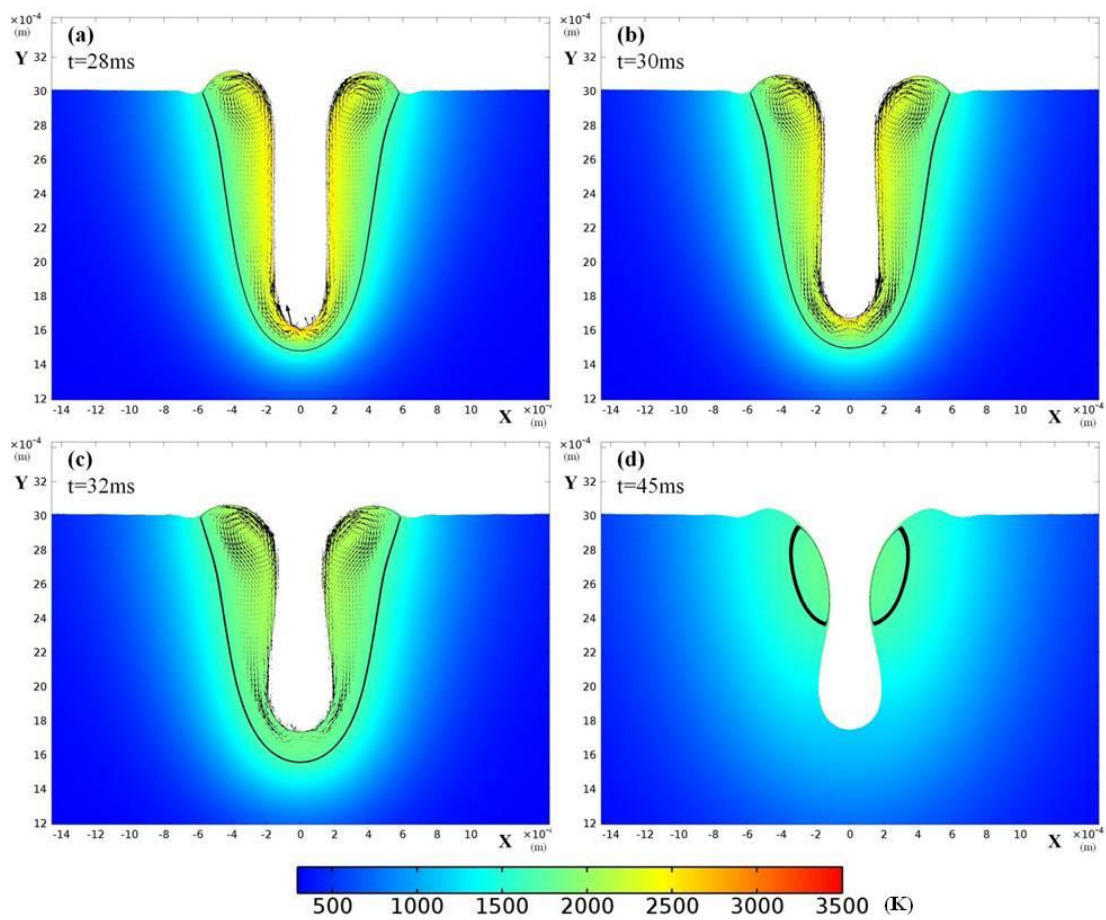


Figure 3.26: Temperature field and fluid flow pattern of the molten pool during the keyhole collapse in case C (500W-10mm/s)

3.7 Laser melting of HDPE powder

The temperature field and flow pattern of the molten pool at $t=0.18s$ during a laser

melting of HDPE substrate (case D and E) are indicated in Figure 3.27. It is interesting to notice that the flow condition for the Gaussian case is similar to the metal cladding case (case A), i.e. a circulation flow is found inside the molten pool and a small ramp is formed. However, in the Pedestal case, only an outward flow from the centre of the substrate can be observed and the L/V interface keeps stable during the laser processing. As described before, the Marangoni effect is the driven force for fluid flow in a conduction welding case; but due to the uniform energy distribution, this force is quite small in Pedestal case, especially for materials with high viscosity such as HDPE melt, therefore the surface velocity in case E is quite low and the circulation flow is unable to be created.

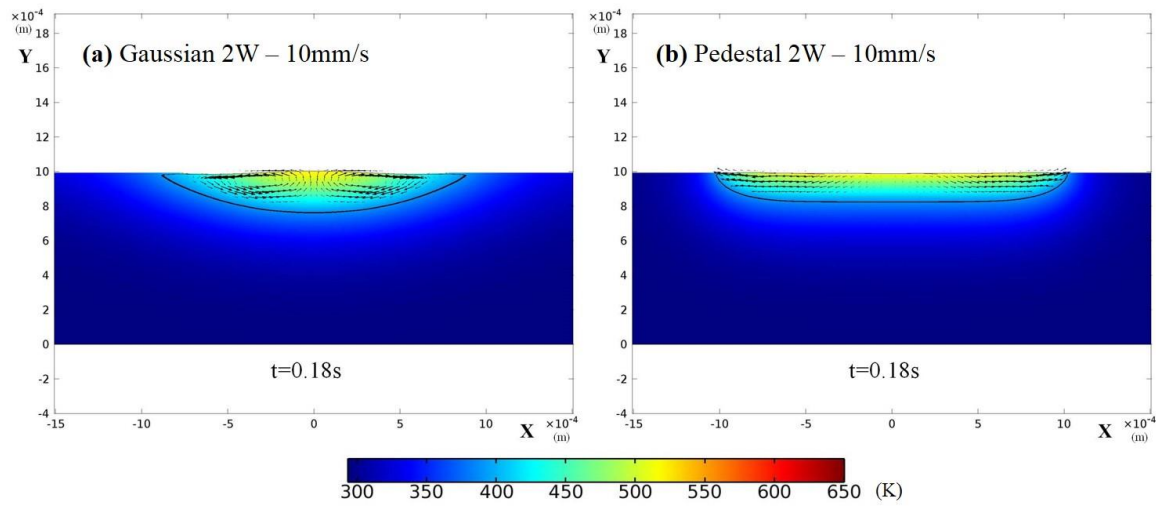


Figure 3.27: Temperature field and fluid flow pattern of the molten pool for (a) case D (2W-10mm/s) and (b) case E (2W-10mm/s)

Moreover, the comparisons between final molten pool size and relative experiment results are shown in Figure 3.28. The experiments were carried out at the same conditions. During this process, the HDPE powder (HMPE75A, Goonvean Fibres) was deposited in a self-made powder bed and a CO₂ laser (Coherent Everlase S48) with linear scanning programme (2W, 10mm/s) was used to create a melted track on it. The track was then sliced using a scalpel and the prepared cross-section was observed using Scanning Electron Microscope (SEM, Leo 440, Carl Zeiss).

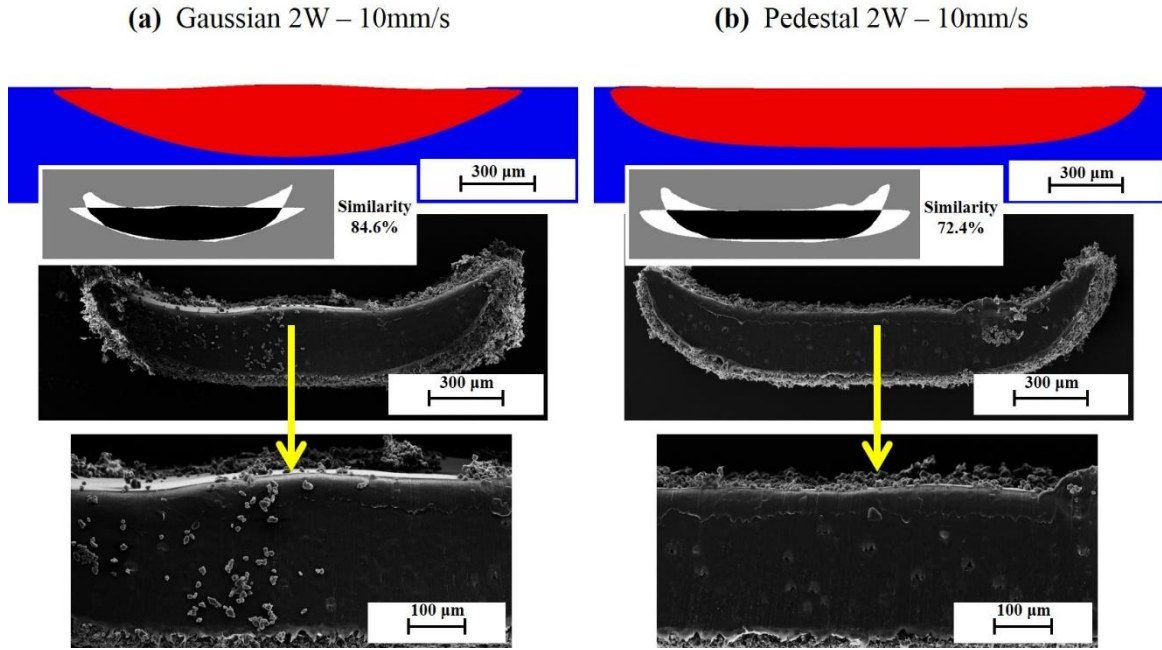


Figure 3.28: Comparison between simulation and practical molten pool geometries for laser melting of HDPE at 2W-10mm/s

The predicted ramp at the central region of the Gaussian case can be observed from the sample cross-section image, where a flat surface was achieved in the centre of Pedestal product. However, the two beams both created curved surfaces, where the edges were warped upward. This phenomenon maybe generated by three reasons:

- The material used in experiments is in powder form and after melting consolidation occurs and a dense phase will be generated; as described before, the volume content of solid part in a close-packing model is 74.1%, which indicates the top surface of the deposited powder will significantly move downward after melting. However, at the edge the degree of particle melt is lower and therefore the powder consolidation is slighter. In simulation the substrate was assumed as bulk material thus the surface is nearly flat;
- During laser processing, the edges of melted track tend to warp due to non-uniform cooling, however its mechanism is not considered in the simulation;

- Material evaporation might be another reason but it has already included in the current model, Figure 3.29 represents the final molten pool geometries for the two beams at an input power of 4W, clearly evaporation occurs in both of the two cases. For the Gaussian beam a bowl shape groove is created; however for the Pedestal beam the front of the slot is still flat, which is similar to the experiment result at 2W. This indicates that for a Pedestal beam, the effect of evaporation on the product surface morphology is equivalent to that of powder consolidation, i.e. a flat surface will always be generated even at an overheating condition. This kind of morphology stability is a significant advantage for Pedestal beam.

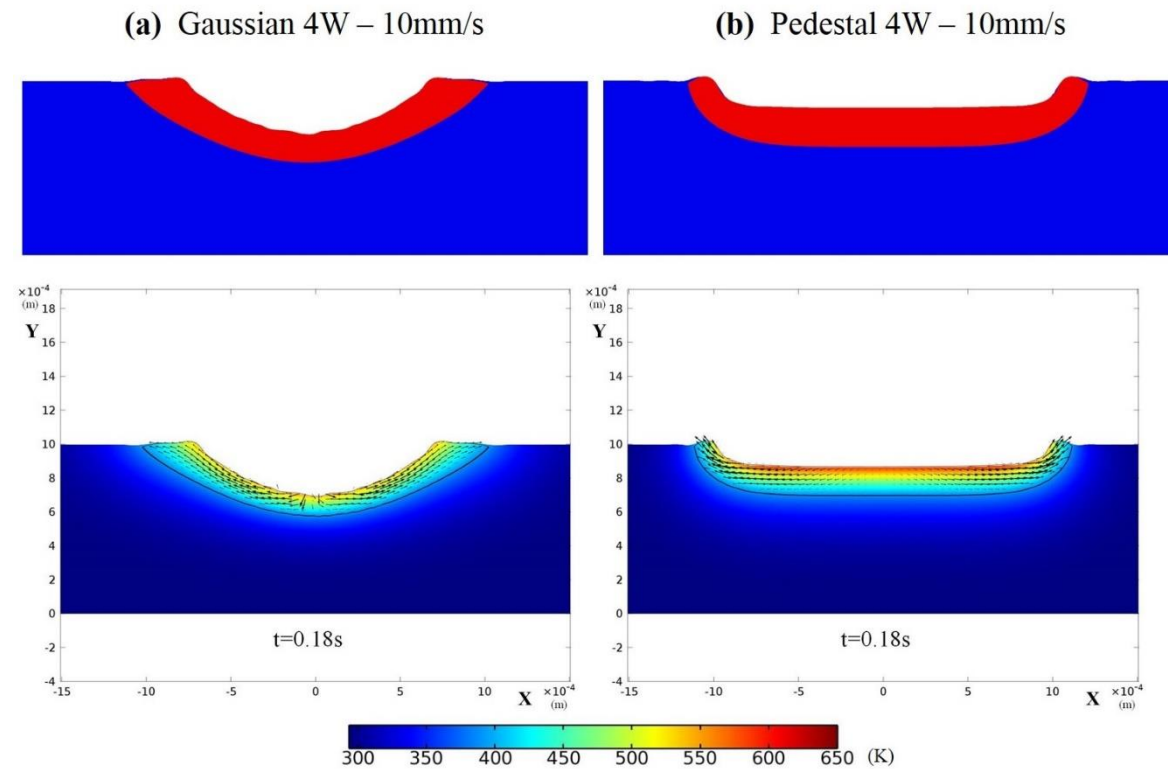


Figure 3.29: Molten pool geometries, temperature field and fluid flow pattern for laser melting of HDPE at 4W-10mm/s

3.8 Summary

In this chapter it addresses the research question in Section 1.2: ‘Can we establish a mathematical model to predict the heat distributions and flow pattern during laser

processing with different beam irradiance distributions?’ by establishing a laser welding/cladding model where two types of beam irradiance distributions – Gaussian and Pedestal are involved:

- The heat transfer, fluid flow and phase transition of 316L stainless steel and HDPE powder were investigated. In the simulation, the evolution of solid/liquid interface was tracked using ‘enthalpy-porosity’ method and the evolution of liquid/vapour interface was tracked using ‘level-set’ method. Extra force and energy source terms are considered in this work, which includes gravity, Marangoni force, capillary force, recoil pressure, buoyancy force, thermal convection and radiation.
- In laser wire cladding of 316L stainless steel cases, an outward flow from the centre to the edge was generated due to Marangoni force. This force was stronger in Gaussian beam than Pedestal beam, since it was mainly determined by the temperature gradient, where the Pedestal beam had a more uniform temperature distribution on the wire. Moreover, in Gaussian beam majority of the energy was in the central part therefore the wire cladding was incomplete; but in Pedestal beam at the same laser processing condition, the wire was fully melted. The simulation results had been verified by relative experiments and the differences were reported: the neglected thermal resistance layer between wire and substrate in the simulation work makes the energy easier to flow down and generate a deeper molten pool.
- In laser keyhole welding of mild steel case, the recoil pressure generated by evaporation was found as the primary force for keyhole development. Keyhole depth oscillation was also reported as a result of equilibrium between recoil pressure and hydrostatic force on the keyhole wall. When heating was stopped, recoil pressure disappeared and keyhole collapse was observed under the effect of hydrostatic force.

In this chapter it also addresses the research question in Section 1.2: ‘Does the redistribution of input energy provide a means of controlling/improving the properties of

the resultant polymeric part?’ by establishing a laser melting of HDPE model and demonstrating the controlled product geometry using Pedestal beam:

- In laser melting of HDPE powder cases, the powders were represented using bulk material and their consolidation during melting is unable to simulate; as a result difference were found between the simulation and experiment. However, the model still indicated the circulation flow inside the HDPE molten pool, which will generate a small ramp in the centre in Gaussian case; and the flat surface will always be achieved in Pedestal case even if evaporation occurs.

CHAPTER 4: LASER MELTING OF HIGH DENSITY POLYETHYLENE POWDER

This chapter details the experimental results of laser melting of HDPE powder. A self-made powder bed system is used for powder deposition; a CO₂ laser with galvo scanning system and Gaussian beam output is used as the energy source. The influence of laser input power, scanning speed, scan spacing are investigated. Tensile test is used to measure the mechanical properties of samples and SEM is used to investigate the microstructure. The melting and solidification process of HDPE powder is observed using hot-stage microscope and the temperature variation during laser scanning is monitored using IR thermal camera. Meanwhile, specific thermal analysis using DSC is carried out to reveal growth of spherulites and formation of imperfect crystalline in HDPE.

4.1 Experimental procedure

4.1.1 Powder deposition and laser melting method

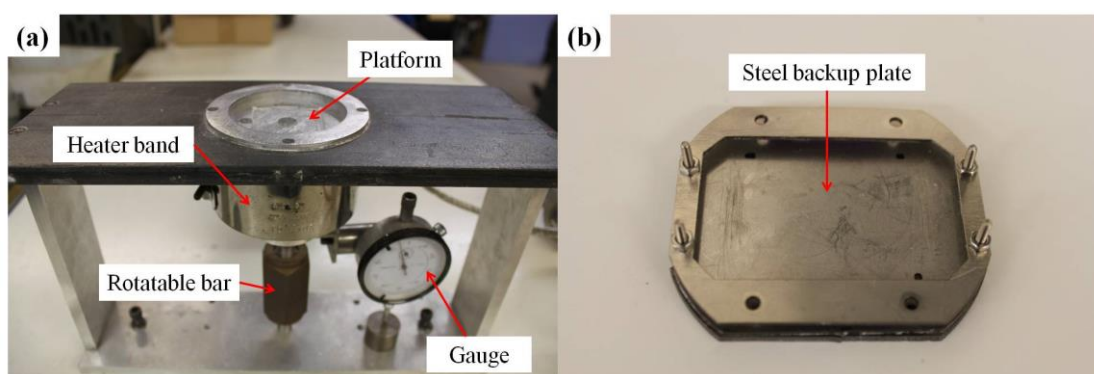


Figure 4.1: Structure of (a) the powder bed and (b) steel backup plate

Figure 4.1.a is a self-made powder bed with a heater band as a post processing tool. The central part is an adjustable platform which is surrounded by an immovable wall. The movement of the platform is controlled by a rotatable bar and the displacement can be read through a gauge, with a minimum value of 10 μ m. An external temperature controller

is used to maintain the temperature of the heater band.

In this work, the HDPE powder (HMPE75A, Goonvean Fibres) was used as received, with an approximate particle size of 12~22 μm . To deposit the powder, a HDPE plate is first generated using the same material by compression moulding, with the purpose of providing a support structure to resist warping force during laser melting. To prevent the plate from bending, a steel backup plate with screws is manufactured as displayed in Figure 4.1.b.

During deposition, the supporting plates were first placed on the powder bed and the initial distance between HDPE plate surface and the steel wall surface was set as 150 μm . Then HDPE powder was spread across the base plate using a spreader artificially, followed by a compressing action to make the powder layer more solid. The Gaussian beam (Synrad Firestar 100W CO₂ laser, wavelength 10.6 μm with a pulse width modulation of 20kHz) was then used to scan across the powder selectively; after generating one melted layer, the platform was moved down 150 μm and another layer of powder was deposited on the finished part again. When the multi-layer sample is built up, the residual powder was blow away and the supporting plates were heated up to 70°C for 10min, with the purpose of removing thermal residual stress inside the sample. Finally, the sample was separated with the HDPE plate using a blade. During the laser melting process, an infrared (IR) thermal camera (Thermovision A40m, FLIR) was set up to monitor the surface temperature of the sample at a recording rate of 50 fps; the emissivity of HDPE white powder was set as 0.9. However, since the wavelength of CO₂ laser (10.6 μm) is in the spectral range of the thermal camera (7.5-13 μm), a Wide Band Passes filter (SWBP-8486-000816, Northumbria Optical Coating Ltd) was selected to block the 10.6 μm beam. The system is indicated in Figure 4.2 and the calibration process of the thermal camera is shown in Appendix A.

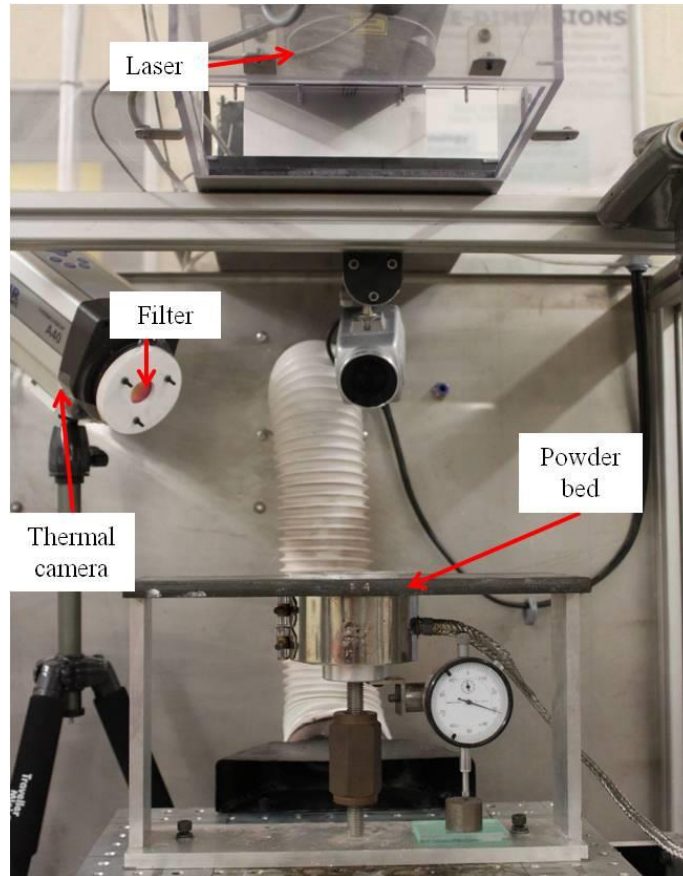


Figure 4.2: Setting up an IR thermal camera with a filter

4.1.2 Sample preparation and characterisation

To demonstrate the mechanical property of the generated sample at different conditions, a tensile bar shape raster scanning programme (42mm*10mm, Figure 4.3) was set up, with a sample thickness of 10 layers. The influence of input power, scanning speed and raster scan spacing are investigated and the selected processing conditions are listed in Table 4.1; at each condition 3 tests were carried out. The prepared samples were then applied on a tensile test machine (Instron 3369) with a constant elongation rate of 5mm/min. And a compression moulded tensile bar using the same material is prepared as the reference.

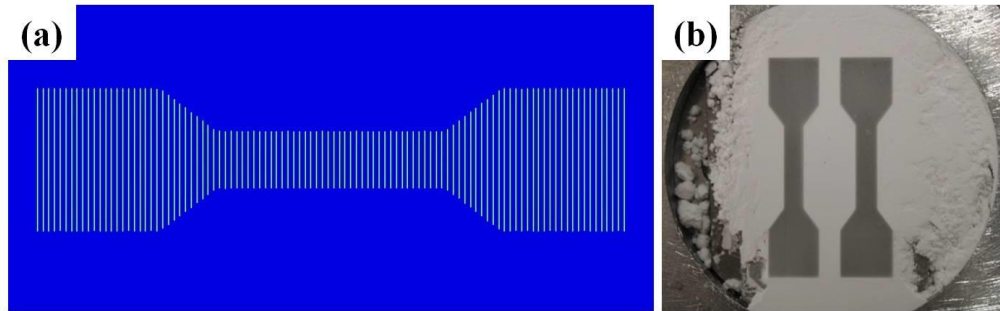


Figure 4.3: (a) Tensile bar raster scanning programme and (b) product shape during manufacturing

Table 4.1: Selected laser processing conditions for tensile test

| | |
|---------------------------------|-----------------------------------|
| Input power (W) | 7, 8, 9, 10, 11, 12, 13 |
| Scanning speed (mm/s) | 160, 180, 200, 220, 240, 260, 280 |
| Raster scan spacing (mm) | 0.1, 0.2, 0.3 |

Note: in this chapter the sample nomenclature is as follow: ‘beam type (G for Gaussian) – power – scanning speed – scan spacing’, e.g. G-10-240-0.2

For each condition in Table 4.1, a rectangular shape (10mm*5mm) sample with 5 layers is also manufactured, which is used to identify its microstructure. Two ways (shown in Figure 4.4) for preparing the cross-section of samples are used in this work: slicing the specimen using a scalpel; or immerse it in the liquid nitrogen and then cut is as a brittle material. After that, the prepared cross-section specimens were observed using a SEM (Leo 440, Carl Zeiss).

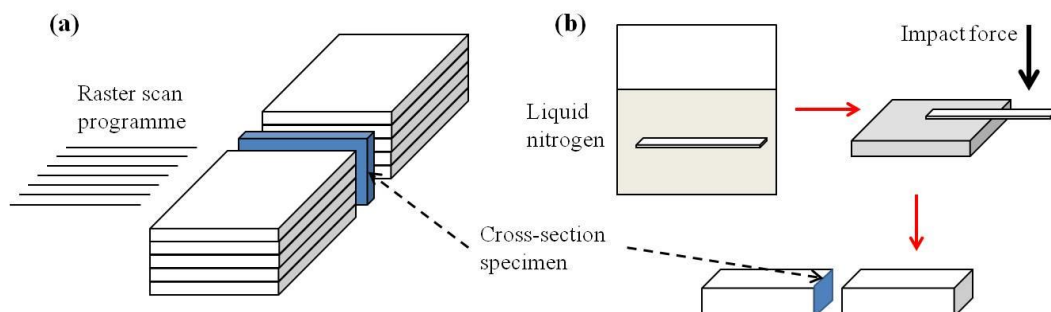


Figure 4.4: Preparation of the specimen for microstructure characterisation: (a) scalpel cutting; (b) liquid nitrogen cutting

The thermal property of the material was also investigated, where a hot stage microscopy (Mettler Toledo FP82HT) was used. The samples were prepared by spreading a very small amount of HDPE powder on plain glass slides and then covered with a glass slip. Too much powder will lead overlapping of particles in the viewing area therefore need to be avoided. The sample melting/cooling and flow situation were then observed at a constant heating/cooling rate of 10°C/min. For each prepared sample in Table 4.1, a DSC test was carried out with the following general procedure:

- Heating from 20°C to 180 °C at a rate of 20°C/min;
- Isotherm at 180 °C for 1min;
- Cooling from 180°C to 40 °C at rate of 20°C/min and 5°C/min;
- 2nd heating starts from 40 °C to 120 °C at a rate of 20°C/min.

4.2 Tensile test and sample microstructure analysis

4.2.1 The influence of input laser power

To completely indicate the shape of the manufactured tensile bar, a normal 60° view and special top view with a light source from the bottom are selected. The sample variation with input power at constant scanning speed (240mm/s) and scan spacing (0.2mm) is represented in Figure 4.5, where the beam type is Gaussian.

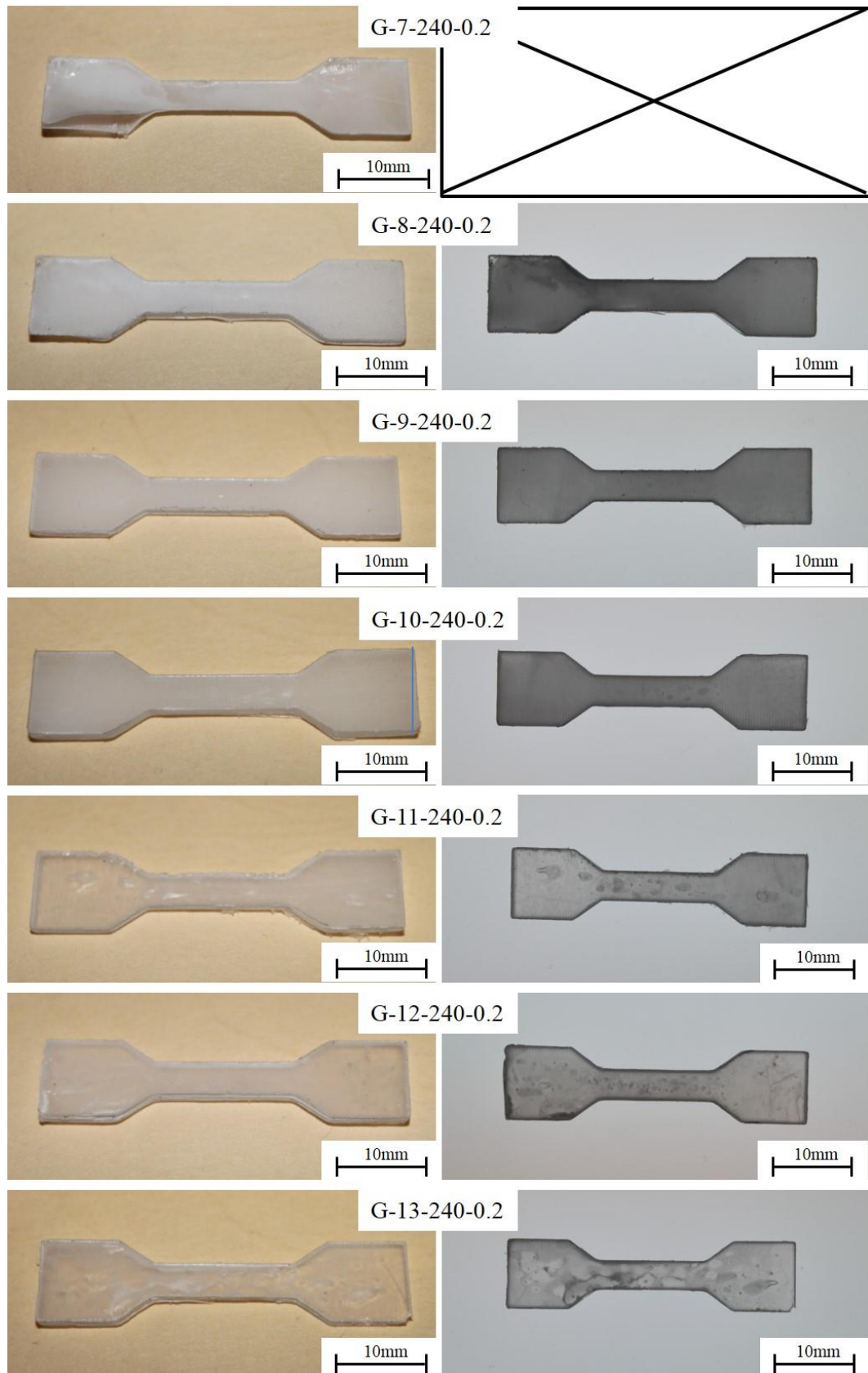


Figure 4.5: 60° view (left) and top view (right) of the tensile bar samples at different input power for series G-X-240-0.2

At a low power (7W), the heat is unable to penetrate through the current powder layer thickness and therefore the adhesive property between different layers is quite weak. Only a 3-layers sample can be manufactured at this condition. As the power increasing (8-10W), the product shape becomes more desirable and the increased thickness makes it opaque. Moreover, if a higher input power (11-13W) is applied, the sample becomes transparent and a lot of bubbles are observed as a result of thermal degradation.

The stress against strain plots for all samples listed in Table 4.1 are shown in Appendix B. According to it, the tensile strength (maximum stress value) and elongation at break (E_{ab} , maximum strain value before break) at different input power are plotted in Figure 4.6, where the black points and lines represent 3 individual laser melting samples and their average value; red lines represent average value of compression moulding samples, respectively.

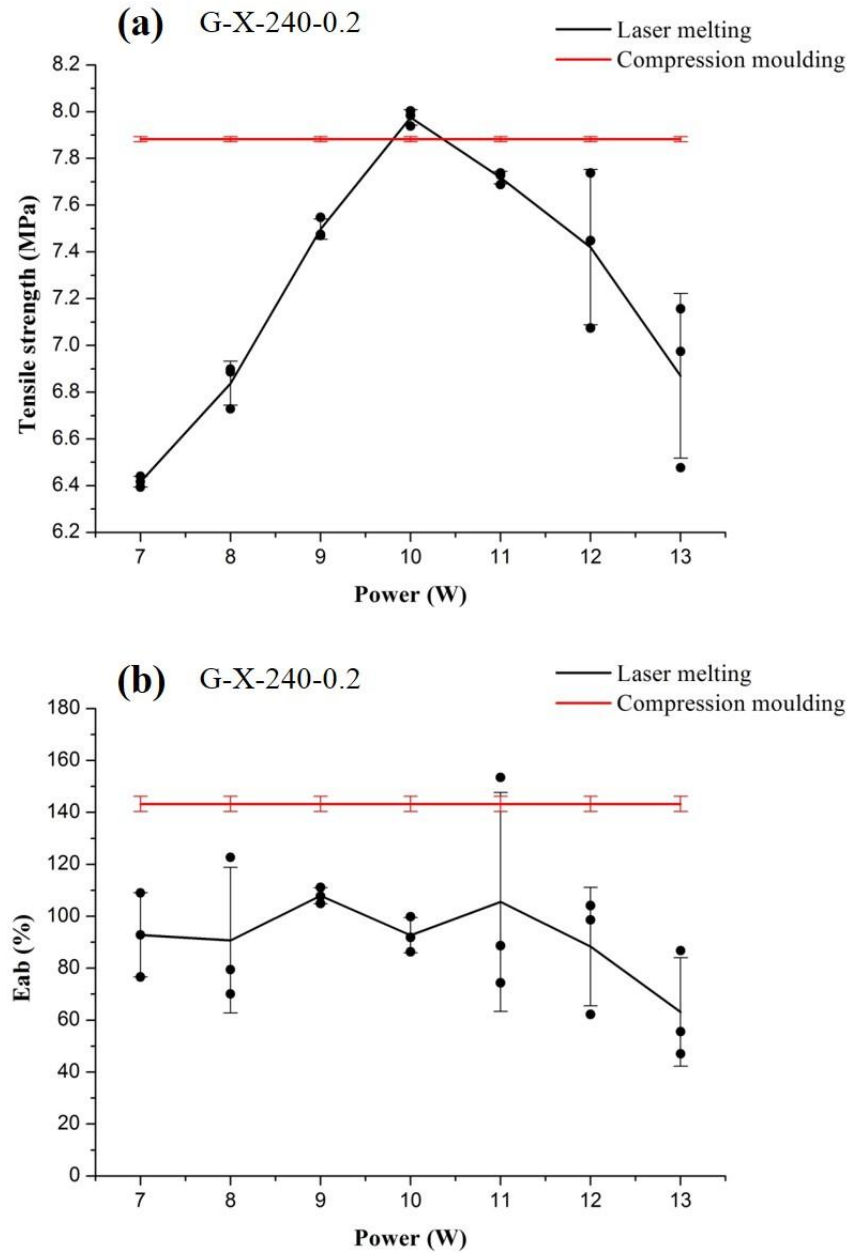


Figure 4.6: Sample series G-X-240-0.2 variation with input power (a) tensile strength and (b) Eab

Clearly, the values of both tensile strength and Eab of the laser manufactured samples are comparable with the compression moulded one at some conditions. For the tensile strength curve, a maximum value is found at $P=10W$ and below it the tensile strength will keep increasing with the input power; then a continuous reduction can be observed if P is higher than $10W$. However, for the Eab curve, no obvious trend can be found and the standard deviation value is quite large. To reveal the reason of Eab variation, the stress

against strain curves at G-11-240-0.2 are selected and plotted in Figure 4.7.

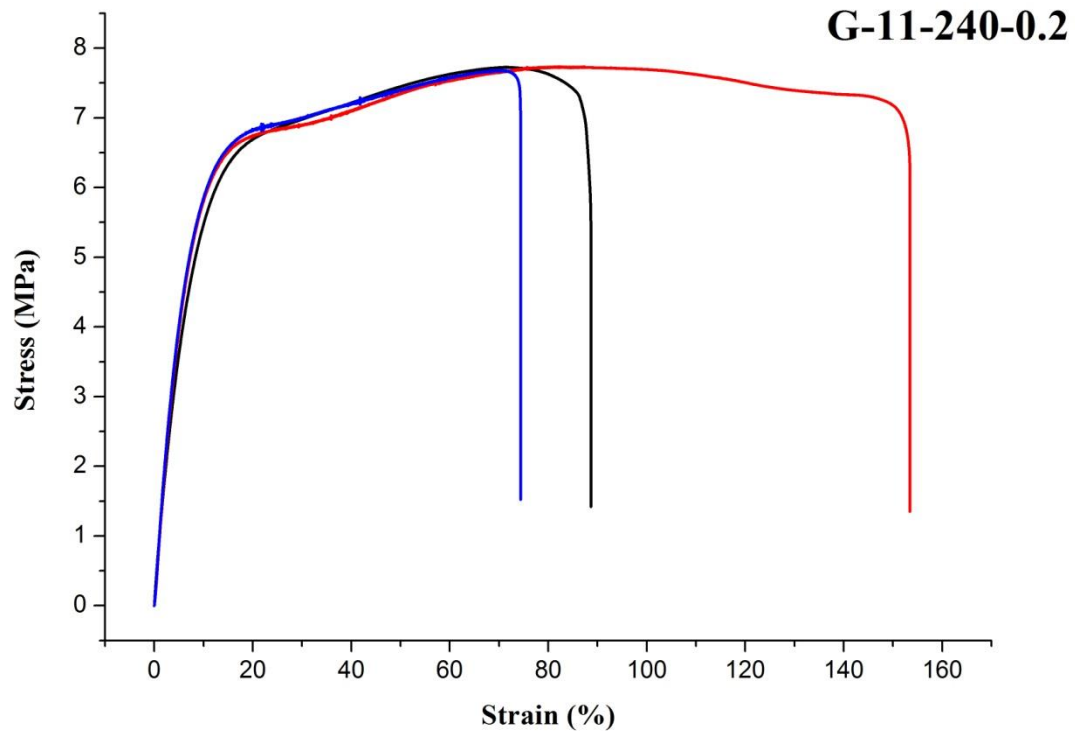


Figure 4.7: Stress-strain plots for sample G-11-240-0.2

The first typical situation is represented by the red curve, which is known as a ‘ductile deformation’, i.e. a linear elastic deformation will occur first until the material reach its yielding point, and then the cross section of the sample is continually decreasing – which is so called necking. During necking stage, the sample will deform quickly and therefore the applied load is constant; as a result, cracks will appear and propagate and it will further lead localised stress concentration, eventually the material will break. Another typical situation is represented by the black/blue curve, which is similar to the red one at the beginning but suddenly break down after reaching its maximum stress value. As one can observe from the photography of the manufactured samples, a large amount of degradation bubbles are formed inside the tensile bar, which will be a location for stress concentration during the tensile test and fracture will attempt to occur in this region. Since the Eab value is mainly determined by those bubbles and they are formed randomly even at the same processing conditions, the samples exhibit irregular Eab values. However, this doesn’t have significant influence in the sample tensile strength since break

normally occurs after sample yielding.

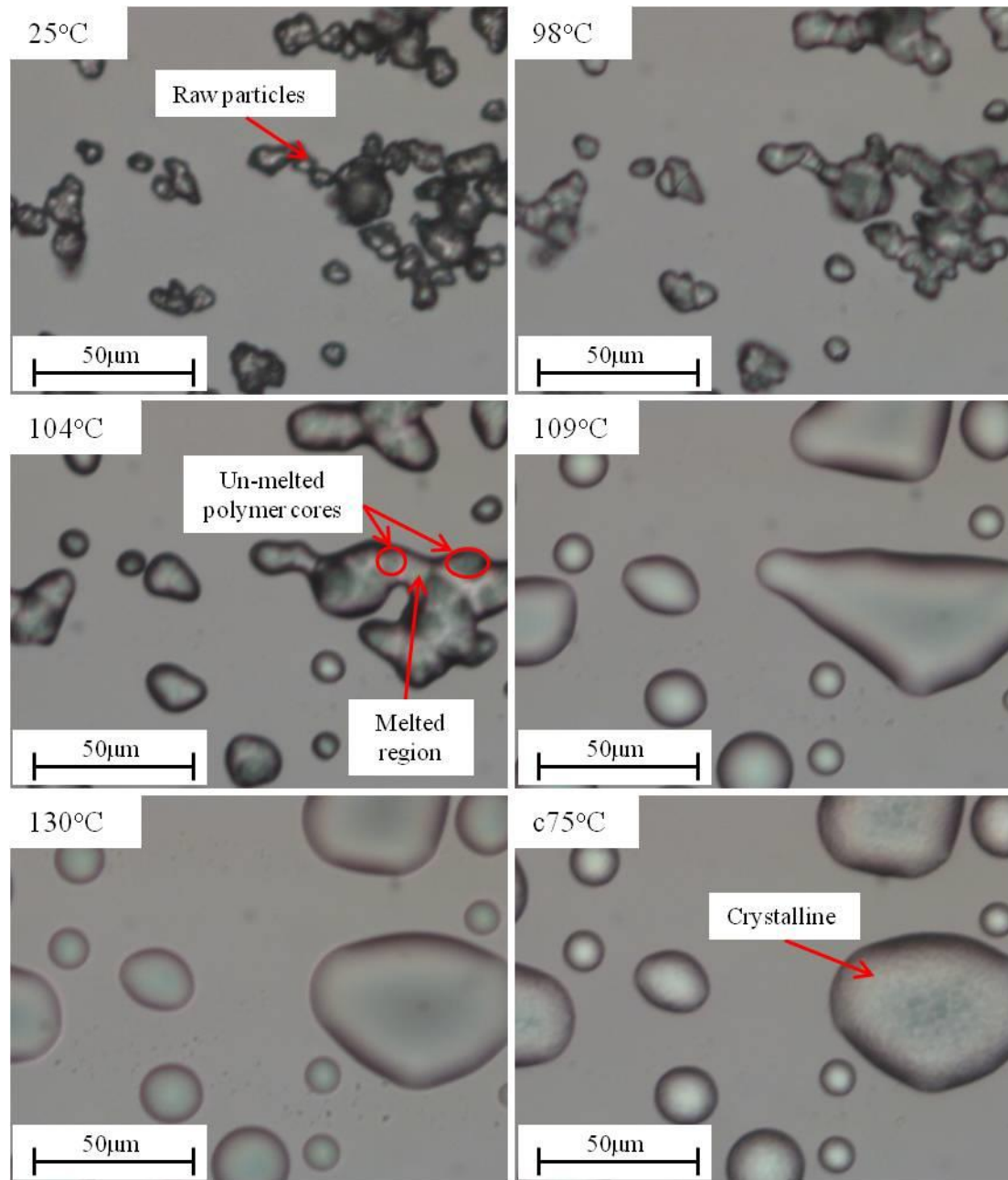


Figure 4.8: Powder particle melting/cooling situation ('c' in the last figure represent 'cooling')

During laser powder processing, since the penetration depth of CO₂ laser is quite low, only the top surface of the deposited powder will absorb the energy directly and the rest part is only heated up by thermal conduction. Therefore the melting will firstly occur from the powder particle surface, which has already been discussed by previous researchers [123, 124]. Figure 4.8 represents the powder melting/cooling situation

achieved from the hot stage microscopy. Clearly, when the raw powder is heated up to 98°C, the outer layer of PE particles is melted and the particles can therefore be divided into two regions: the melted surface region and the un-melted core. As the temperature increasing, the melted region keeps propagating until the whole particle is melted. Meanwhile, the melt starts flowing as a result of surface capillary force and eventually forms a spherical shape. During the cooling stage, the generating of crystalline is found on the surface of the sample. However, if the provided energy is not high enough to fully melt the original powder, a residue of polymer core is formed in the final product, which has been schematic represented in Figure 4.9.

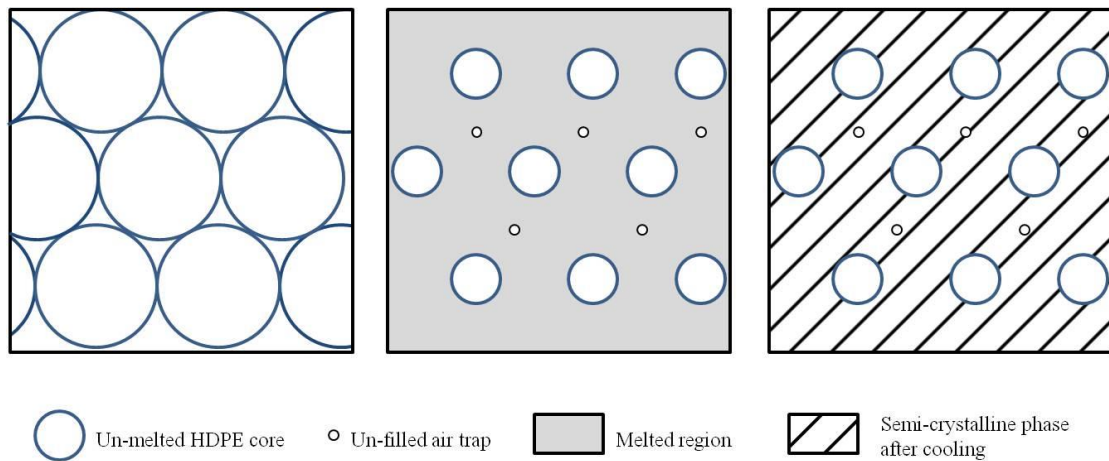


Figure 4.9: Schematic representation of the particle phase transition during a heating/cooling process

To demonstrate the microstructure of the laser processed sample, the SEM cross-section images at G-10-260-0.2 are listed in Figure 4.10, which includes both the scalpel cut and liquid N₂ cut samples. Obviously, the former technology can generate a clean transversal surface but damage the bubbles; while the latter one can keep the original bubble shape due to quenching but the surface is very rough.

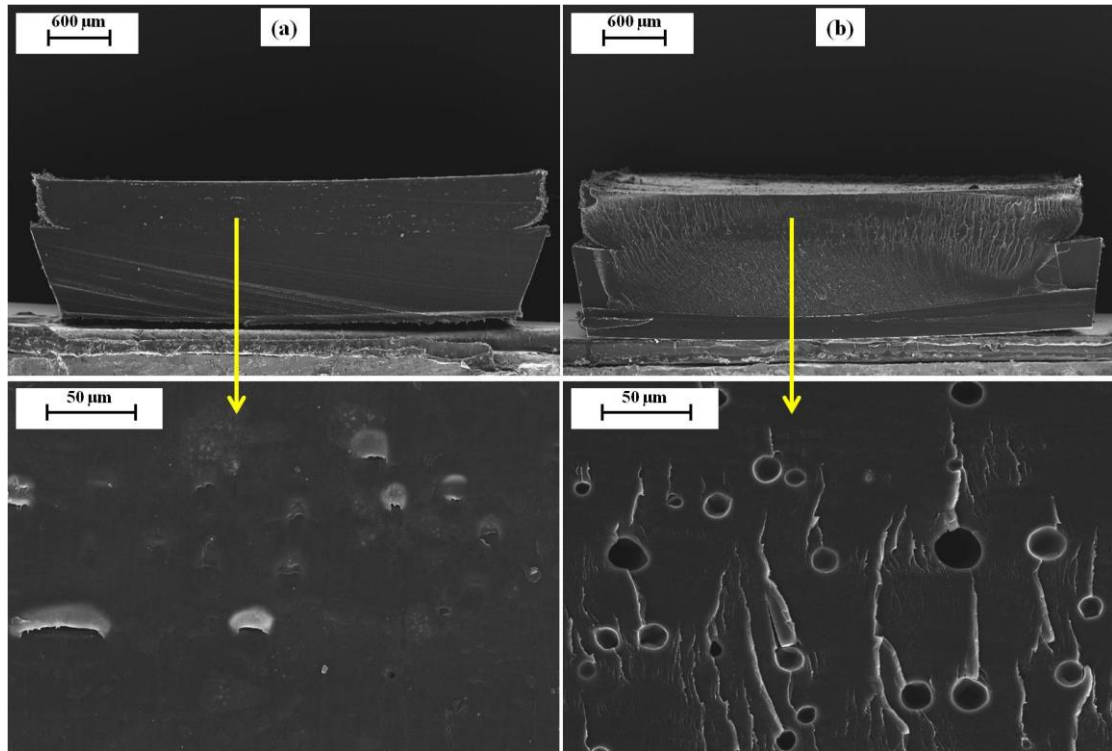


Figure 4.10: The SEM cross-section images of (a) scalpel cut and (b) liquid N₂ cut for G-10-260-0.2

The scalpel cut sample in Figure 4.10.a indicates the laser melted HDPE layer is well-bonded with the substrate. The liquid N₂ cut one in Figure 4.10.b further reveals the bubbles have regular spherical shape and their diameters are about 10μm. They are believed to be the entrapped air voids as described in Figure 4.9. They can keep a spherical shape in the melted HDPE matrix due to surface tension. From Figure 4.11, where the cross-section of samples generated at different input powers are exhibited; at a low input power, the low degree of particle melting (DPM) restricts the flow of the molten pool and a large amount of unfilled air traps are formed. However, if the input power is high enough, the increased temperature will generate a fully melted phase and the fluid viscosity will decrease. The density difference between the air and fluid will extrude those air traps out of the molten pool and generate a dense product. As a result, before reaching the fully melted phase, a positive relationship can be found between the tensile strength and input power (Figure 4.6.a). However, excess energy will not make the product any more dense if it is already fully melted, but lead thermal degradation of the polymer. It will further generate degradation vapour bubbles inside of the product, as shown in Figure 4.11.c. Those degradation bubbles are much larger than the air traps and

they will also reduce the tensile strength of the generated sample.

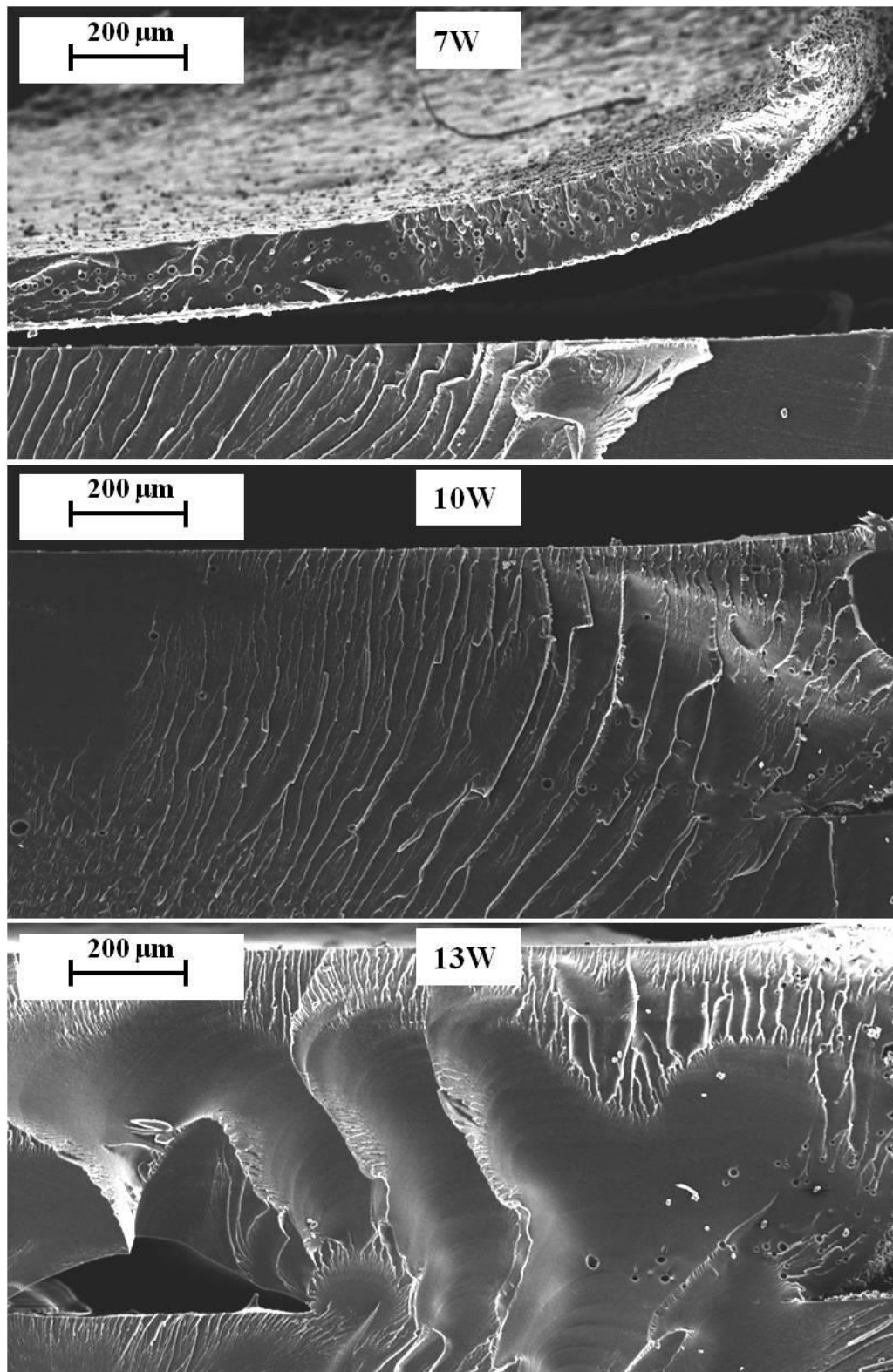


Figure 4.11: The SEM cross-section images of sample series G-X-240-0.2

4.2.2 The influence of scanning speed

Figure 4.12 represents the influence of scanning speed in the product at a constant input power (10W) and scan spacing (0.2mm), which has the similar trend of the input power, i.e. as the decreasing of scanning speed the sample have better transparency but more degradation bubbles. Meanwhile, the spatial resolution is decreased if too much energy is applied (G-10-160-0.2).

The results of the relative tensile test are shown in Appendix B and the tensile strength and Eab values against scanning speed are plotted in Figure 4.13, which is also similar to the input power case. Therefore the two parameters can be thought as having equivalent effect on the DPM of the sample.

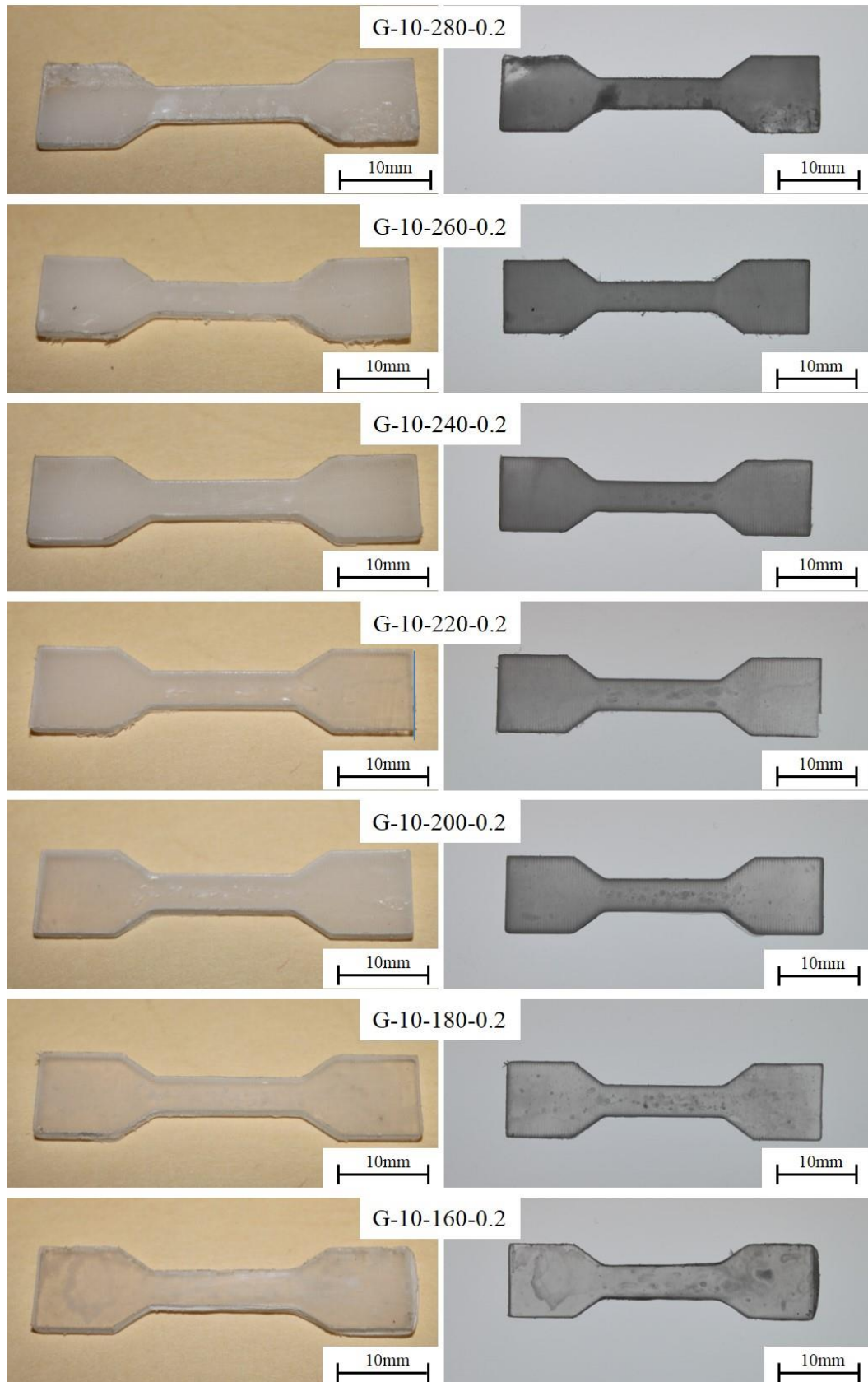


Figure 4.12: 60° view (left) and top view (right) of the tensile bar samples at different scanning speed for series G-10-X-0.2

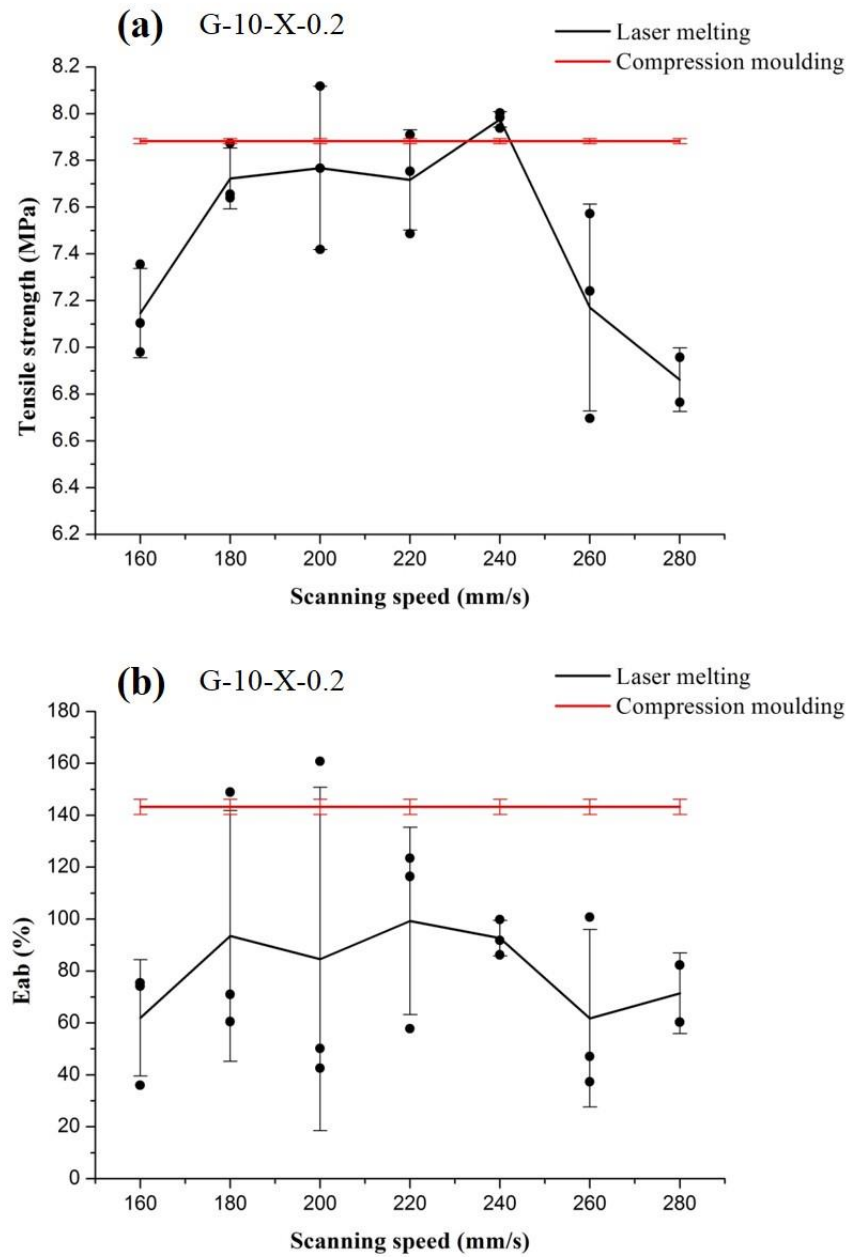


Figure 4.13: Sample series G-10-X-0.2 variation with scanning speed (a) tensile strength and (b) Eab

Figure 4.14 shows the cross-section microstructures of sample at different scanning speeds, which further confirm the formation of air traps which described in the input power variation cases.

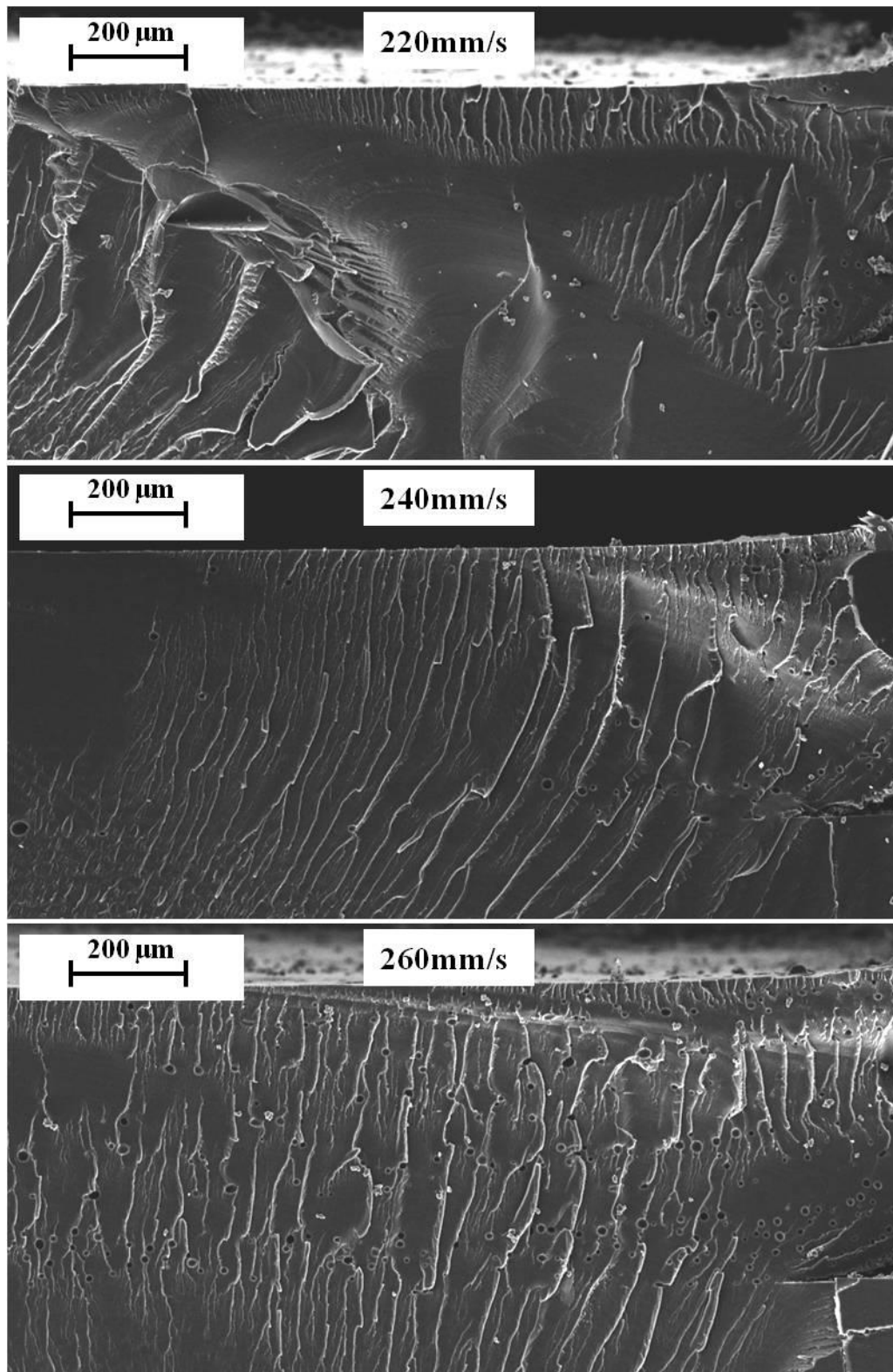


Figure 4.14: The SEM cross-section images of sample series G-10-X-0.2

4.2.3 The influence of scan spacing

To demonstrate the influence of scan spacing in the product properties, G-10-240-0.2 is selected as a standard sample. Simply adjust the spacing value to 0.1 and 0.3 will increase/decrease the input energy dramatically therefore the scanning speed is also adjusted to enable an ‘equivalent energy’ condition.

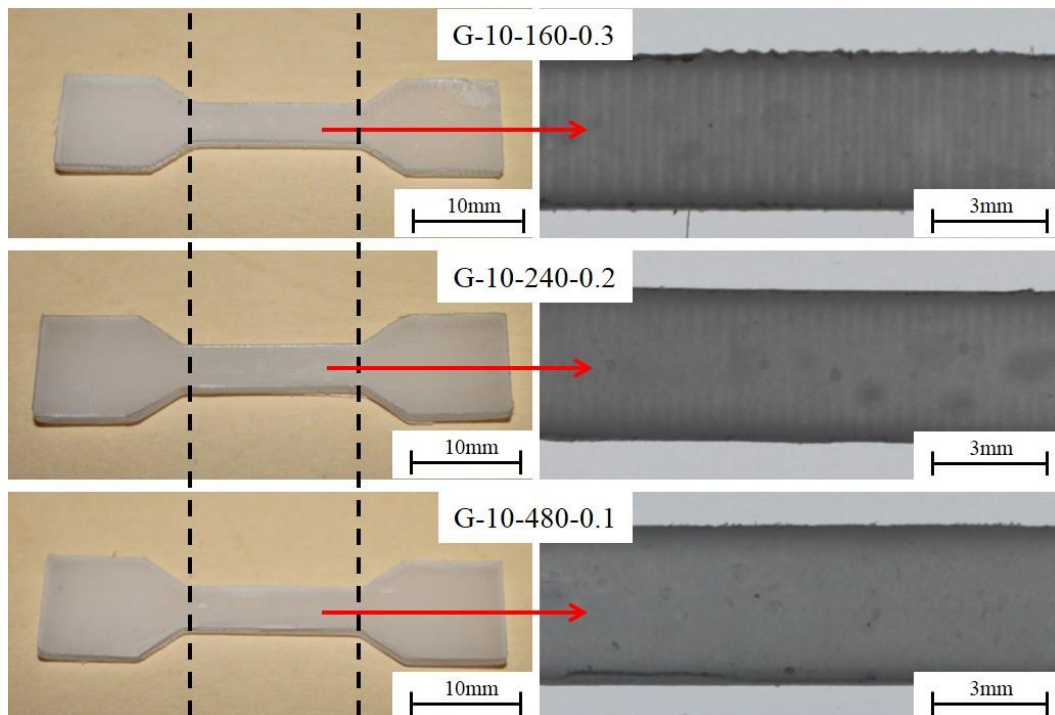


Figure 4.15: 60° view (left) and top view in the central region (right) of the tensile bar samples for series G-10-X-X

Figure 4.15 compares sample G-10-160-0.3, G-10-240-0.2 and G-10-480-0.1. They exhibit similar appearance but it is interesting to notice that the on the sample surface a series of straight lines which parallel to the scanning direction are formed. According to previous discussion in Section 3.7, these lines are formed due to powder consolidation during laser melting. As illustrated in Figure 4.16, a lower scan spacing value will reduce the distance between two adjacent lines and make the surface smoother. Meanwhile, the sample tensile strength and E_{ab} are shown in Figure 4.17. And due to the similar input energy for those three cases, the variations of the two plots are very small.

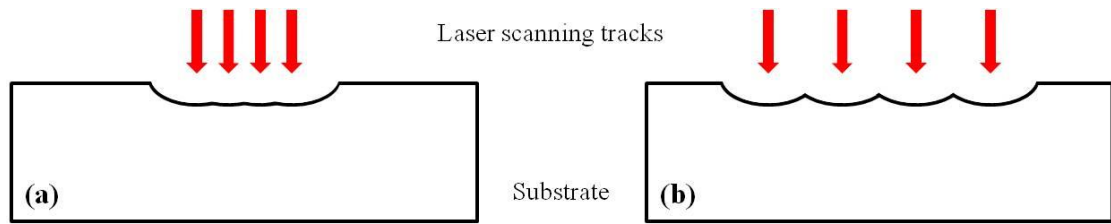


Figure 4.16: Schematic representations of surface lines formation during raster scan (a) low scan spacing; (b) high scan spacing

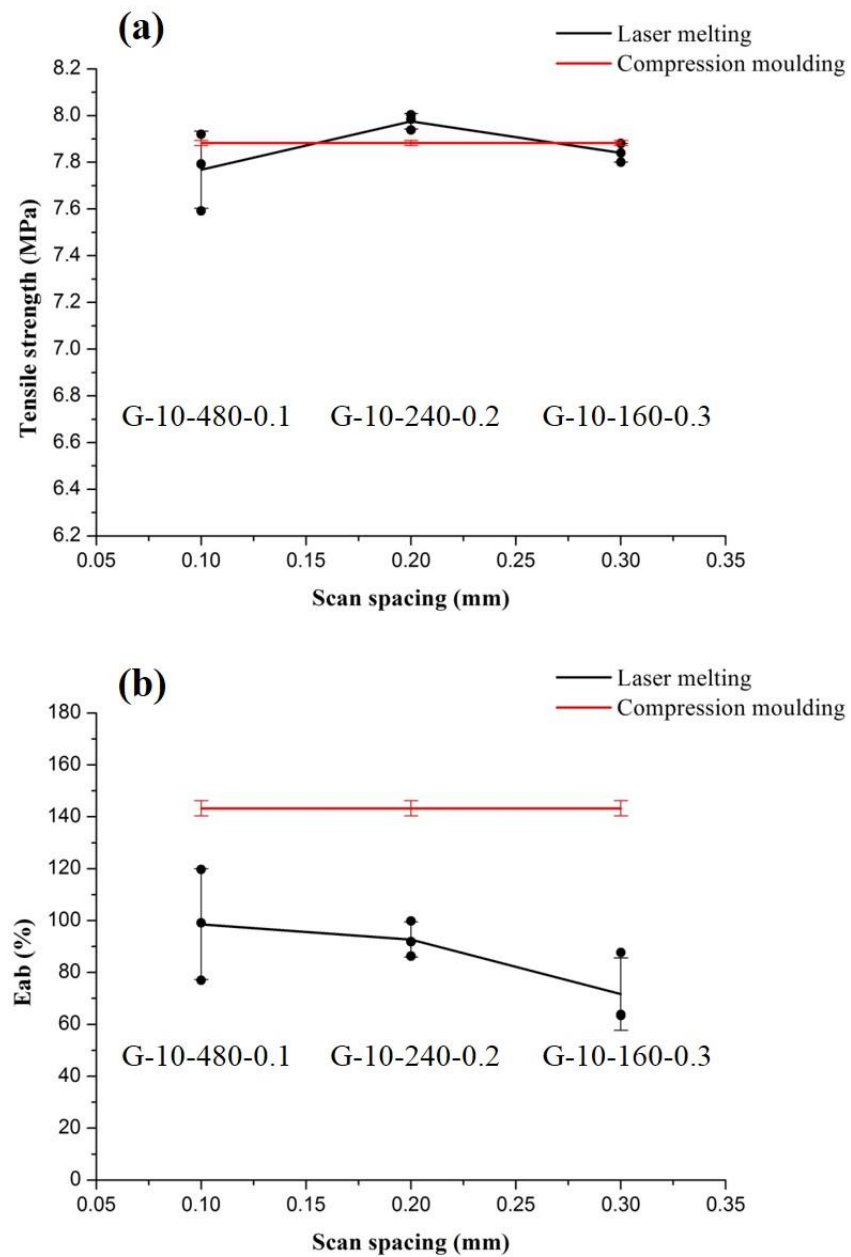


Figure 4.17: Sample G-10-480-0.1, G-10-240-0.2 and G-10-160-0.3 (a) tensile strength and (b) Eab

4.3 Thermal analysis

4.3.1 Temperature measurement using IR camera

The temperature pattern of the tensile bar sample G-10-240-0.2 during laser melting is shown in Figure 4.18, where the temperature values were calibrated using Appendix A.

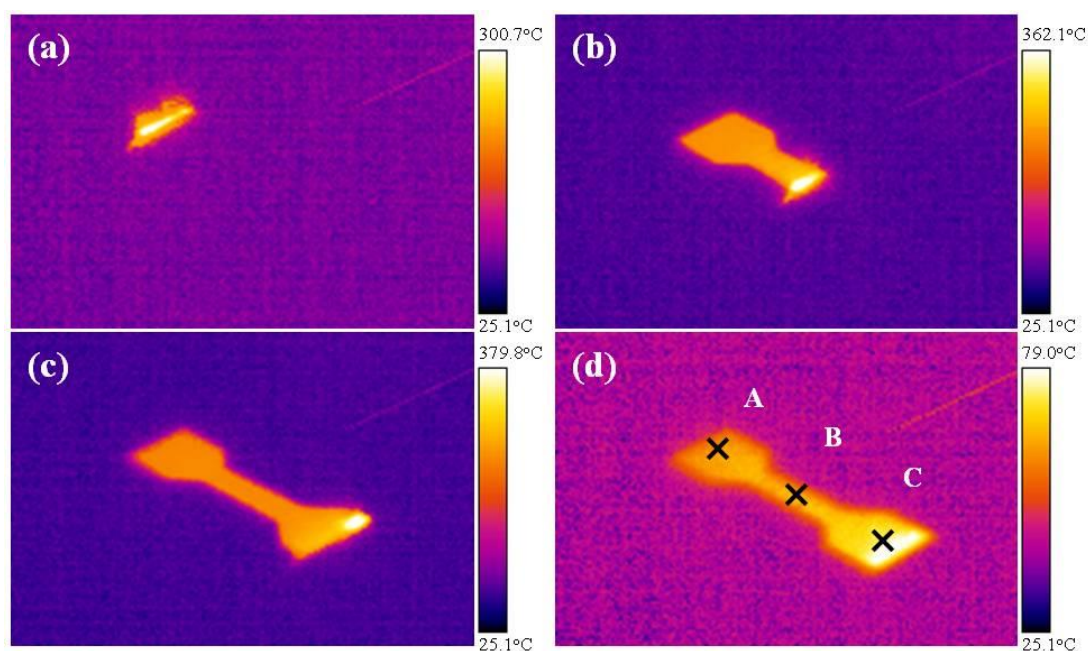


Figure 4.18: Temperature patterns of sample G-10-240-0.2 at (a) $t=0.68s$, (b) $t=3.18s$; (c) $t=5.64s$; (d) $t=6.88s$

The scanning track is clearly exhibited in Figure 4.18 and after laser melting, a precise tensile bar shape is generated. Moreover, Figure 4.19.a reveals the temperature against time plots for point A, B and C at G-10-240-0.2 and Figure 4.19.b reveals the point A temperature comparison between G-10-240-0.2 and G-12-240-0.2. Obviously, the HDPE powder has been heated up to 300-500°C from room temperature in a very short period of time, and then quickly drop back to 100°C. The time for such a ‘pulse’ is only about 0.3s and it is interesting to notice that the temperature has undergone an oscillation period after reaching the maximum value. Since the scan spacing is 0.2mm, which is smaller than the beam diameter 0.3mm, an overlapping region is generated between two adjacent

scanning tracks. As a result, for a specific point, it will be directly treated by the laser several times and this will lead an oscillation in its temperature. Meanwhile, after dropping to about 100°C during the cooling stage, the heat loss rate dramatically decreased and a ‘temperature tail’ is formed in those plots. Figure 4.19.b further confirms a 12W input power can heat the substrate to about 600°C and this will easier make the HDPE degrading.

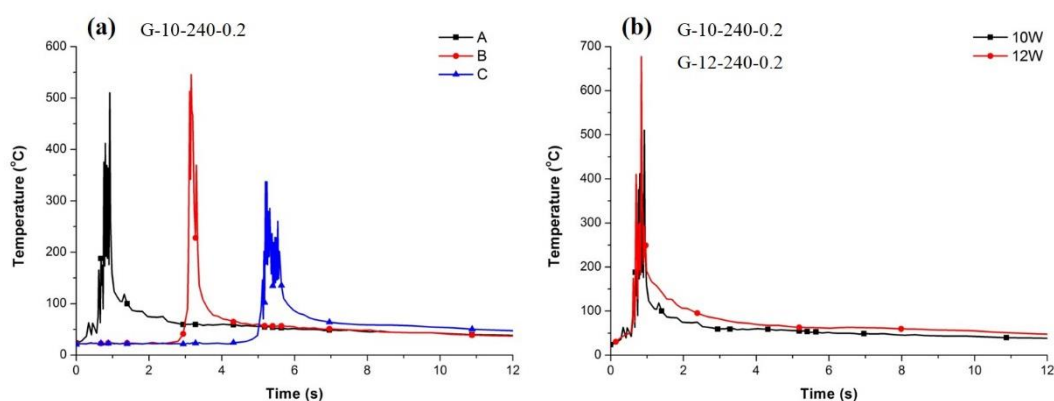


Figure 4.19: Temperature variation with time for (a) points A, B and C of sample G-10-240-0.2; (b) points A of sample G-10-240-0.2 and G-12-240-0.2

4.3.2 Thermal tests using DSC

The results of the DSC tests are indicated in Figure 4.20, where the input power and scanning speed are selected as two variables; the raw power and compression moulding samples are also included.

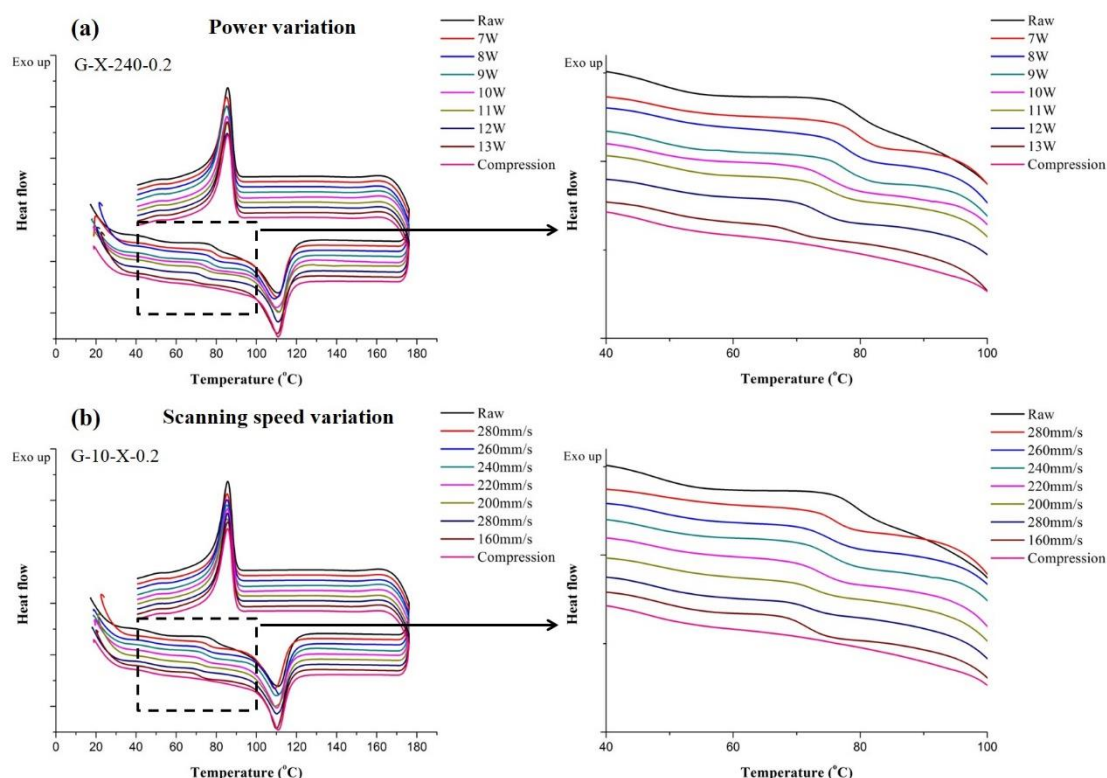


Figure 4.20: Plots of DSC tests at different conditions: (a) G-X-240-0.2 series and (b) G-10-X-0.2 series

For each curve, it consists of two peaks and baselines, according to the standard for thermal analysis [125], a straight base line in DSC result (e.g. 130°C~170°C) represents a constant heat capacity of the sample; the downward and upward peaks represents endothermic and exothermic thermal behaviours for the 2nd order phase transition, respectively (e.g. melting, crystallisation). Moreover, the area of the peak is a result of enthalpy variation. In Figure 4.20, the endothermic peak appears at about 110°C during heating is the melting peak and the exothermic peak at 85°C during cooling is the crystallisation peak.

HDPE is known as a semi-crystalline plastic and it consists of both the crystalline and amorphous phases, which can be confirmed directly from the hot-stage microscopy results in Figure 4.8. The raw powder is semi-transparent but after melting the polymer is changed to amorphous phase and this will provide transparency for the sample; however,

when it is cooling down, the polymer chains starts arrange themselves in an ‘orderly’ manner and form the crystalline structure. This will cause the refraction of light and make sample opaque. In linear polymers such as HDPE, the crystallisation starts from a nucleus, where the chains firstly align in a ‘crystalline lamellae’ form, and then grow to all directions. This will eventually generate a spherical aggregate, i.e. a ‘spherulite’, as shown in Figure 4.21.

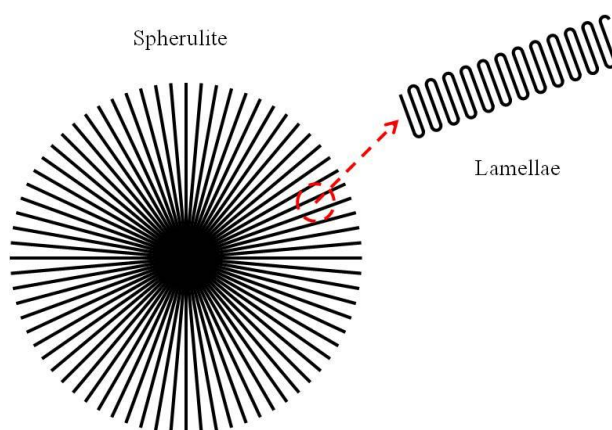


Figure 4.21: Structure of a spherulite

It is interesting to notice that the locations of the melting and crystallisation peaks for different cases are similar to each other. However, the melting peak is very broad and near its onset point a small ‘ramp’ is visible, this ‘ramp’ is similar to a 1st order phase transition ‘ramp’ (e.g. glass transition) and its location is varied with the input power and scanning speed. To reveal its location more clearly, the 1st order derivative of the curves (from 40°C to 100°C) in Figure 4.20 are calculated and shown in Figure 4.22.

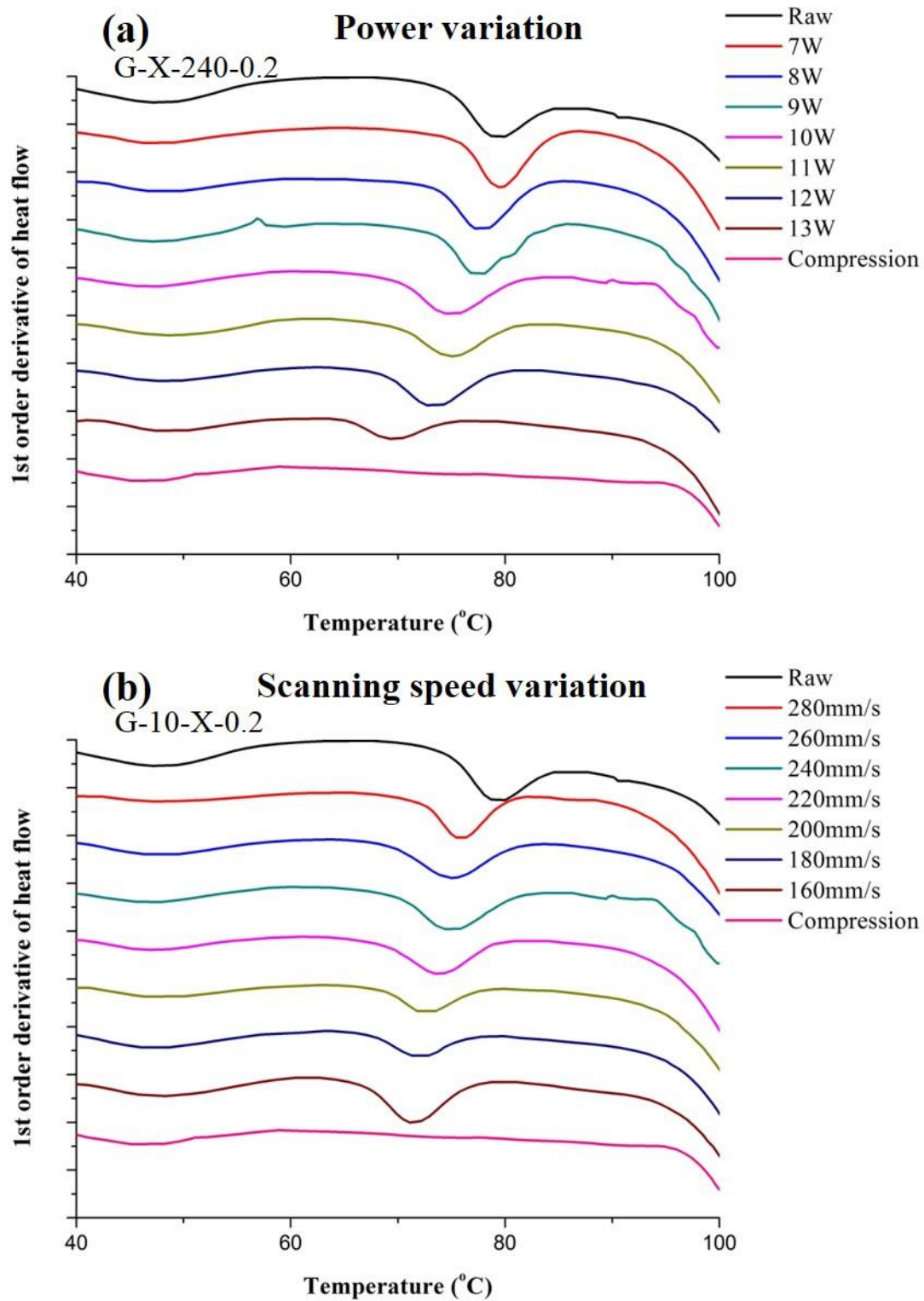


Figure 4.22: 1st order derivative of the heat flow against temperature at different conditions: (a) G-X-240-0.2 series and (b) G-10-X-0.2 series

Obviously, as the increasing of input power or decreasing of scanning speed, the location

of ‘ramp’ shifts towards the low temperature direction. And for a compression moulding sample, no ‘ramp’ can be observed but a straight line with nearly constant gradient is exhibited on the original DSC curve. Menczel et al [126] reported the similar phenomenon in their annealing test of low density polyethylene. In their test, the samples were annealed at different temperatures first, then quenched to -80°C and re-heated for the DSC analysis. They found as the annealing temperature increasing, the location of the ‘ramp’ is moving to a high temperature direction; meanwhile, the ‘ramp’ is actually revealed as a peak when the annealing temperature is high enough, as indicated in Figure 4.23. This has been treated as a result of crystal perfection during heat treatment. At a specific annealing temperature, the imperfect crystalline with a melting temperature lower than the annealing temperature will melt and form perfect crystals, which have a higher melting point. Therefore the onset of melting point will increase with the annealing temperature and a small melting peak is formed.

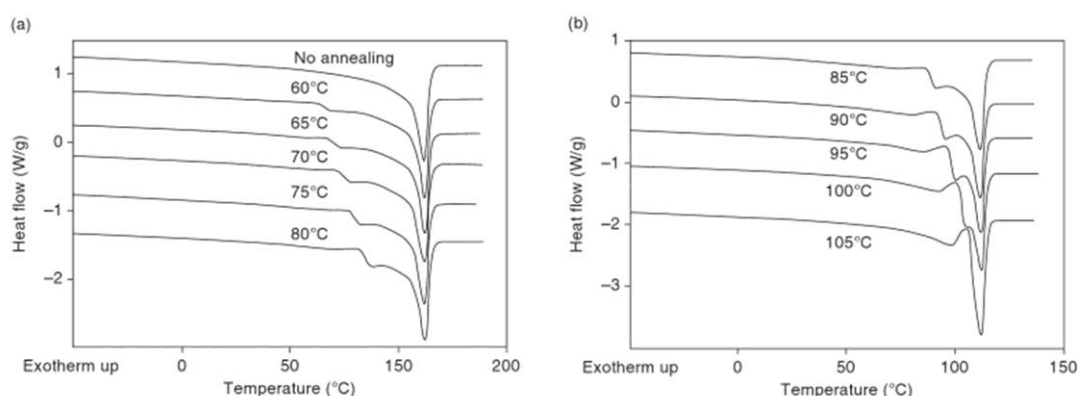


Figure 4.23: Melting curves of LDPE after varies annealing heat treatment plotted by Menczel et al [126]

The DSC plot of compression moulding sample in Figure 4.20 is similar to the no annealing sample in Figure 4.23, which means it contains imperfect crystalline with a wide range of melting temperature based on Menczel’s theory. To reveal the formation of the imperfect crystalline, extra ‘heating-cooling-2nd heating’ DSC tests were carried out, and the cooling rate was controlled at $20^{\circ}\text{C}/\text{min}$ and $5^{\circ}\text{C}/\text{min}$. Figure 4.24 plots the 2nd heating curves for samples at different cooling rates. Obviously, a slow cooling ($5^{\circ}\text{C}/\text{min}$)

will lead a boarder melting peak, i.e. more imperfect crystalline with low melting temperatures.

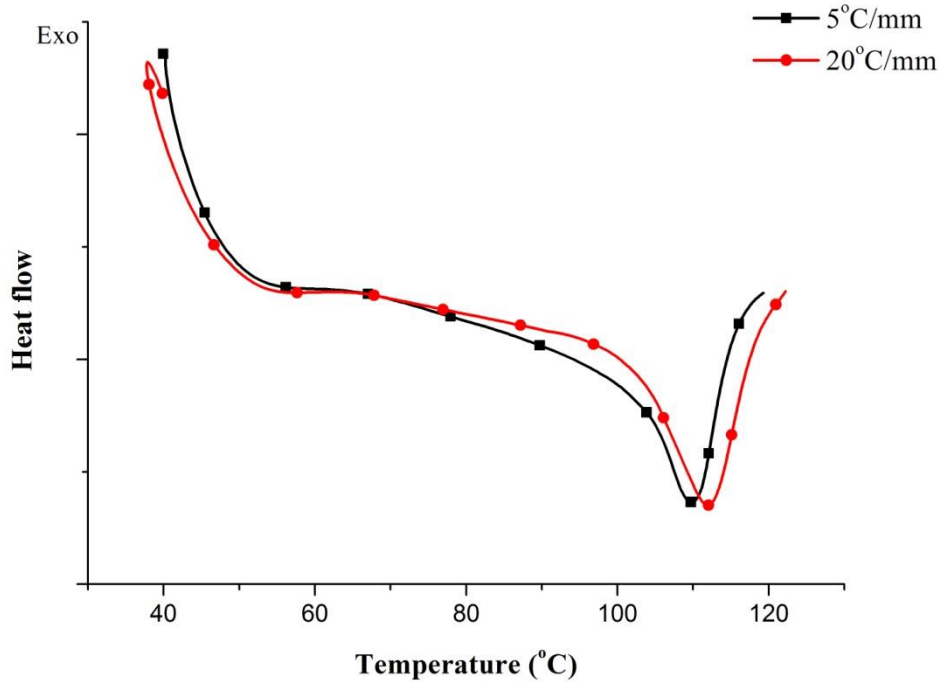


Figure 4.24: 2nd heating of HDPE sample cooling at different rates

Considering the growth of spherulite, it starts from a nucleus and propagates along all spatial directions. The propagation will be terminated if two spherulite boundaries meet with each other and due to the spherical shape, some spherulites do not have sufficient spaces to grow and this will lead the formation of tiny spherulites with low melting temperature, i.e. the imperfect crystalline. It has been proved that a fast cooling will generate a large amount of small spherulites while a slow cooling will generate less but larger spherulites [127]. As illustrated in Figure 4.25.a, larger spherulites are easier to generate imperfect spherulites since they have less nucleation sites and more ‘extra spaces’. Pakula’s experiment [128] further verified this hypothesis; they measured the spherulites sizes of LDPE at different cooling rates (by putting the LDPE melt in water bath at different temperatures) and found that a rapid cooling can generate a more uniform size distribution, as shown in Figure 4.25.b.

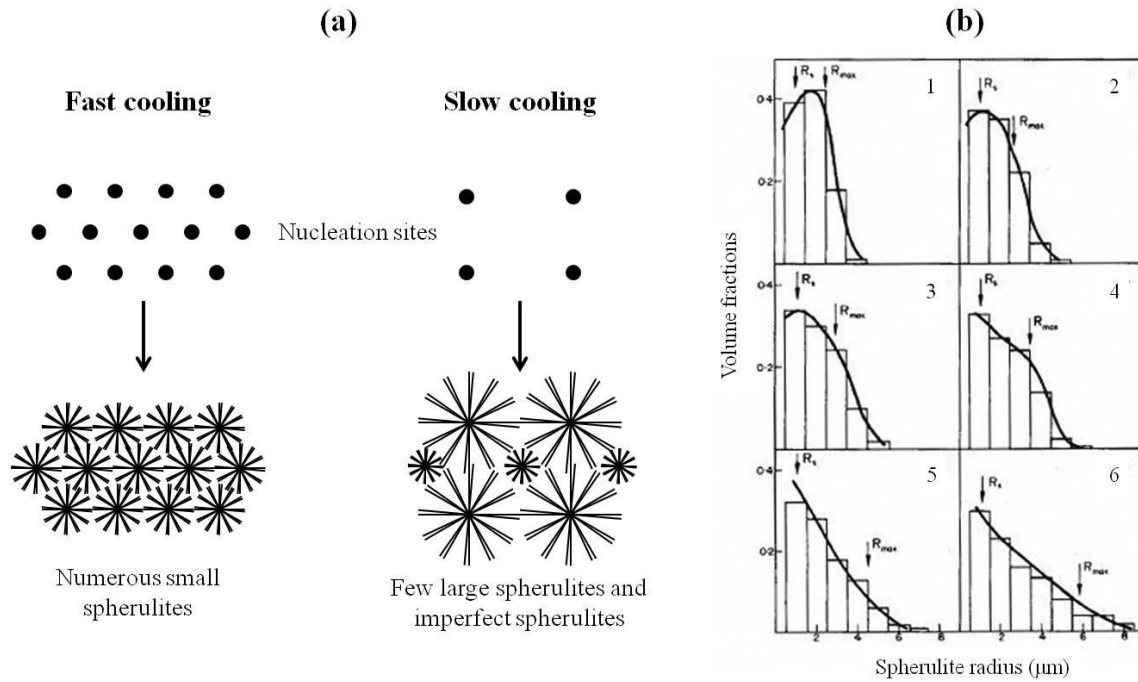


Figure 4.25: (a) Illustration of spherulites growth at fast/slow cooling rate and the formation of imperfect spherulites; (b) Pakula's [128] spherulites distribution measurement at different cooling rate, where from 1-6, the water bath temperature was setting as 0, 25, 50, 70, 80, 90°C

Back to the laser melting process, from Figure 4.22 the raw powder has a 'ramp' at about 77°C, which indicates it has been annealed at this temperature during the manufacturing process. This has been confirmed by the material supplier, where a certain amount of heat is generated during powder grinding and the temperature is about 70°C [129]. The increased input energy during laser melting will lead the shifting of 'ramp' towards low temperature region, which can be explained from two aspects:

- A low input energy cannot fully melt the HDPE powder therefore the product is a mixture of raw powder part and recrystallisation part. The recrystallisation part is similar to the compression moulding sample and has imperfect crystalline with a wide range of melting temperature. As the input energy increasing, the degree of particle melting will increase and this will change the product properties from raw powder phase to recrystallisation phase.

- If the laser energy is high enough to fully melt the powder, the ‘ramp’ still exist on the DSC curve, since the cooling rate for laser treatment is quite high and the rapid cooling will restrict the formation of the imperfect spherulites. However, even if reaching the fully melted state, increasing the input energy will keep making the ‘ramp’ shift towards low temperature direction, which is believed as a result of different cooling rate at different input energy. As revealed by the temperature plots at different input power in Figure 4.19.b, the time consumption for recrystallisation (from 100°C to 60°C) of 12W case (3.82s) is larger than that of 10W case (1.62s), which indicates a high input energy will lead a low cooling rate during recrystallisation stage. A high input energy will increase the overall temperature of the substrate and therefore it has a high energy compensate rate during the cooling stage. As a result, the low cooling rate will contribute to the formation of imperfect spherulites, which will generate the melting ‘ramp’ at low temperature.

4.4 Summary

In this chapter it addresses the research question in Section 1.2: ‘Can we generate fully dense polymeric components as the circuit substrate?’ and ‘Can we make use of different polymers such as high density polyethylene (HDPE) which presently thought of as unsuitable for laser additive manufacturing?’ by making fully dense HDPE components using laser additive manufacturing technology and investigating their properties at different processing conditions:

- The mechanical properties (tensile strength and elongation at break) of the laser manufactured samples were comparable with the compression moulding sample since a fully dense product is produced.
- During laser melting, at low input energy (low power or high scanning speed), the HDPE powder was partially melted and a lot of air-traps were observed in the product, which had low tensile strength. As the input energy increased, the degree of particle

melting was increasing and therefore the tensile strength increased. However, excessive input energy would lead evaporation of the HDPE and boiling were generated. Moreover, a 'line pattern' was found on the sample and this pattern was more obvious at high scan spacing conditions. It is believed as a result of powder consolidation during laser scanning.

- The thermal analysis according to DSC and IR camera revealed the crystallisation mechanism during laser processing. A 2nd order phase transition 'ramp' was observed from the DSC curve and it indicated the solidified sample consisted of perfect crystalline (large spherulites) and imperfect crystalline (small spherulites). The raw powder had lowest small spherulite content due to the thermal treatment. The rapid cooling during laser melting will lead a uniform spherulite size distribution and therefore less small spherulites than compression moulding sample. At high laser input energy, a high degree of particle melting and low cooling rate would be generated; and they would lead more small spherulites in the sample.

CHAPTER 5: LASER CURING OF SILVER PASTE

This chapter details the experimental procedures and results for the fabrication of silver paste on both glass and HDPE structure using laser direct writing technology. This has enabled the direct writing of 3D small circuit boards when discrete electronic components are included into the writing process. In this chapter, the laser beam was reconstructed by HOE to a Pedestal energy distribution. During silver paste curing, the deposited material was scanned by laser beam, using different input powers and scanning speeds. The DSC and TGA tests of the paste were used to identify its thermal properties. The resistivity of the conductive track was measured by 4-point probe technique; meanwhile, the surface topography and cross-section microstructure were investigated by 3D surface measurement technique and SEM, respectively. And the formation of the bubbles during laser curing process was observed by high speed camera. Moreover, the manufacturing of a flexible timer circuit board was also demonstrated using silver paste and HDPE substrate.

5.1 Experimental procedures

5.1.1 Silver paste investigation

The laser curing was carried out on the silver paste (C2050712D58) from Gwent Group, UK with a solid content was 58%. The thermal properties of the paste were investigated by Differential scanning calorimetry (DSC, TA Instruments, DSC 2010) and Thermo-gravimetric Analysis (TGA, TA Instruments, SDT 2960). The DSC test started from room temperature and ended at 300°C, with a heating rate of a 10°C/min; while the TGA was carried out under the atmosphere of argon at a heating rate of 10°C/min.

Meanwhile, the Fourier Transform Infrared spectroscopy (FTIR, Shimadzu, FTIR-8400S) was used to identify the material of the matrix. The FT-IR reflection mode was selected:

the silver paste was first dissolved in methanol and then extracted the silver flakes using vacuum filtration; then the filtrate was dried overnight to allow the methanol to evaporate and then the residue was spread on a glass film, which was followed by curing at 80°C for 1h; the glass film was applied on an Attenuated Total Reflection (ATR) accessory and then scanned by FT-IR. Moreover, another glass film without any matrix on it was used as the reference.

5.1.2 Paste deposition and curing

To investigate the curing mechanism, a stencil printing method was applied and glass films (75mm*25mm) were selected as the substrate, each film was chemically cleaned using acetone and then dried in air. A brass stencil (thickness – 200 microns) with an internal portion (1.3mm*45mm) was placed on the glass film and the silver paste was deposited on the substrate through the stencil using a blade. This process is indicated in Figure 5.1.a.

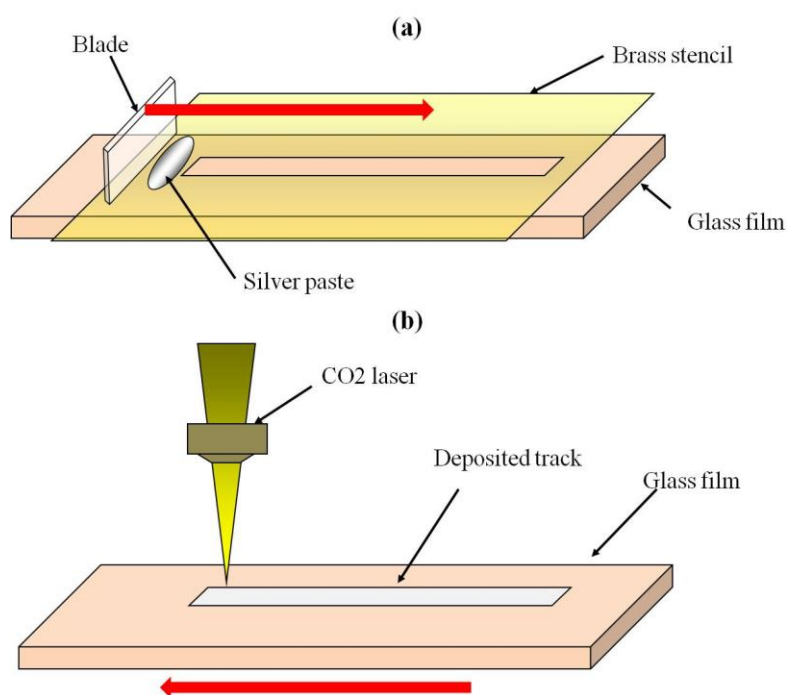


Figure 5.1: (a) Stencil printing method and (b) laser curing of deposited silver paste

The finished part was dried in air for 2 hours and then fixed to the Computer Numerically Controlled (CNC) table. A CO₂ laser (Coherent Everlase S48, wavelength 10.6 microns) with a coaxial focussing head was used to scan over the deposited track. A linear substrate translation path was created in Alphacam Systems (CAD/CAM package). The path data was uploaded to the laser control unit via RS232 connection. The velocity of CNC table can then be changed using the Fanuc by modifying the control programme. The laser was set as a pulsed mode and its power was monitored by an internal meter and controlled by varying the pulse length and frequency. Compressed air was used as the assist gas, which exit directly from the nozzle. The laser curing process was shown in Figure 5.1.b.

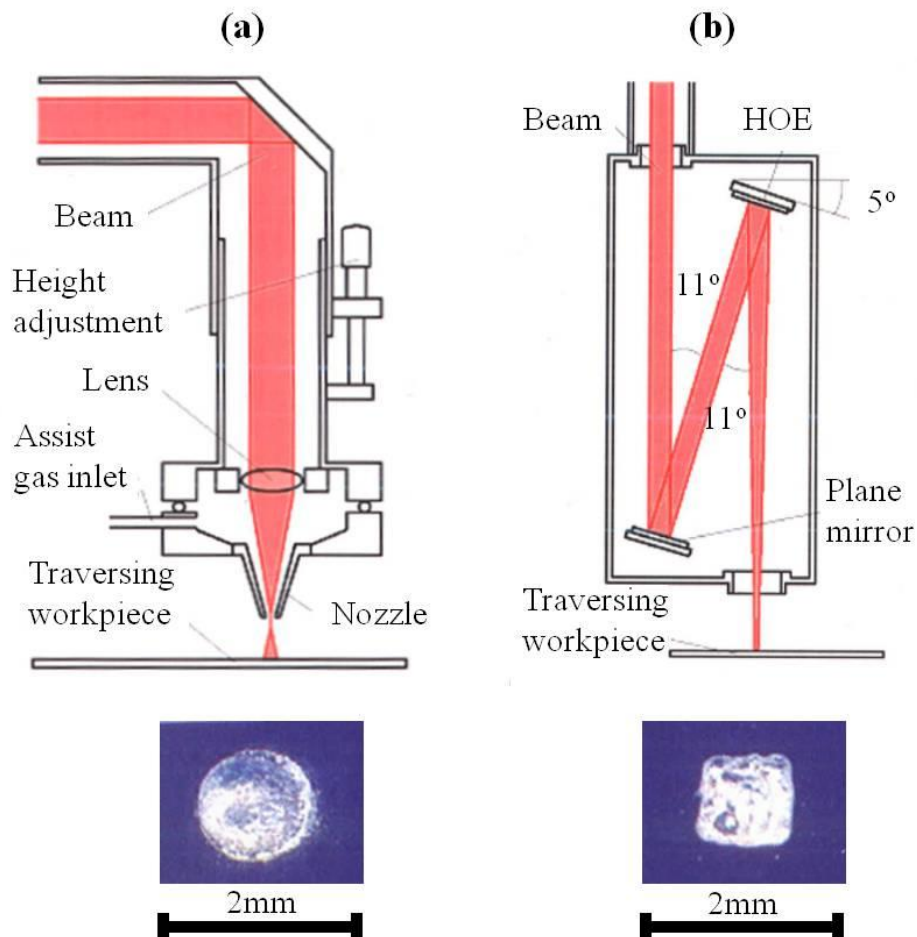


Figure 5.2: Beam construction for: (a) Gaussian irradiance distribution; (b) HOE modified distribution

Both Gaussian beam and HOE modified beam were used in the investigation. During

Gaussian beam construction, the focus distance of the lens is set at 1mm below the nozzle exit first and the beam spot size is therefore adjusted by raising the focussing head (Figure 5.2.a). The beam modification for a CNC system is indicated in Figure 5.2.b, where a beam path based on reflection is designed. And the distance from the nozzle exit to the paste is usually set in the range of 8-10cm. In the HOE test, the Gaussian beam was also converted to a Pedestal beam irradiance distribution, as introduced in Chapter 3. A burn print test was carried out by Kell [81], where a single pulse of 0.1s was shot on a piece of Perspex. The achieved prints are shown in Figure 5.2, the diameter of the Gaussian beam is about 1.25mm and the length of Pedestal beam is about 1.25mm.

In the curing process, the input power and scanning speed were the controllable parameters. Considering the energy loss during light transfer, the real input power was usually smaller than the setting value. The real power was measured using laser energy meter (Coherent, Labmax-Top 10W). Moreover, oven test at 150°C for 0.5h was also selected as a comparison. The processing details are list in Table 5.1.

Table 5.1: Laser and oven curing conditions

| Laser curing | |
|-----------------------|------------------------|
| Input powder (W) | 1.5,1.9, 2.3, 2.7, 3.1 |
| Scanning speed (mm/s) | 0.1, 0.3, 0.6, 1, 2, 3 |
| Oven curing | |
| Temperature (°C) | 150 |
| Time (h) | 0.5 |

Note: in this chapter the sample nomenclature is as follow: ‘beam type (G for Gaussian and P for Pedestal) – power – scanning speed’, e.g. G-2.3-1

5.1.3 Characterisation

The characterisation techniques include visual observation, cross-section microstructure observed by SEM (Carl Zeiss (Leo), 1530 VP), surface morphology achieved by 3D surface profiler (Alicona, InfiniteFocus), thermal property characterised by DSC and electrical resistivity measured by 4 point probe technique. Meanwhile, a high speed camera (Photron Fastcam SA1.1) was used to monitor the laser curing process (recording rate 500 fps) and the whole established system is shown in Figure 5.3.

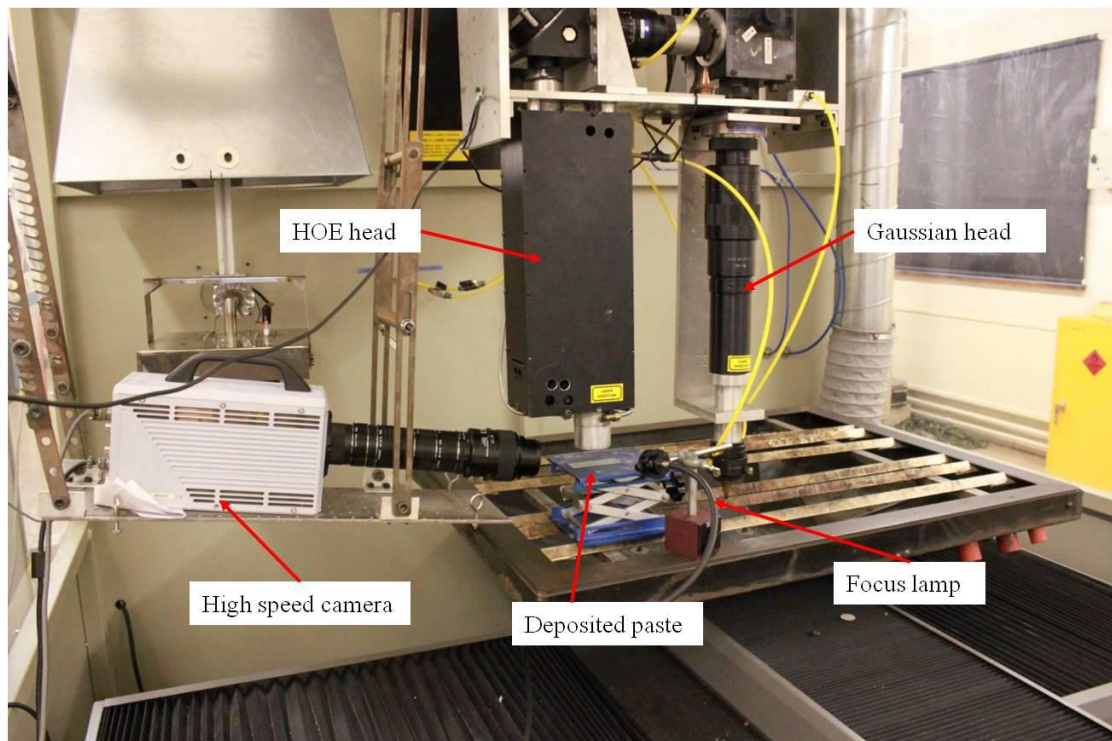


Figure 5.3: Laser curing system with both Gaussian and HOE head

Moreover, in the preparation of the SEM specimens, glass substrate which had a cured silver paste track on its surface was cut into two pieces in the middle using a glass cutter.

The 4-point probe technique is indicated in Figure 5.4: four metal tips which had uniform spacing, s were arranged in line and contacted with the surface of samples. A fixed current I is applied on the two outer probes and the voltage between the two inner probes were measured as V . If the thickness of the deposited layer t is small enough, i.e. $t \ll s$,

the resistivity R_e can be expressed as:

$$R_e = \frac{V}{I} * \frac{A}{l} \quad (5.1)$$

where A is the cross-section of the measured sample and l is the distance between two inner probes.

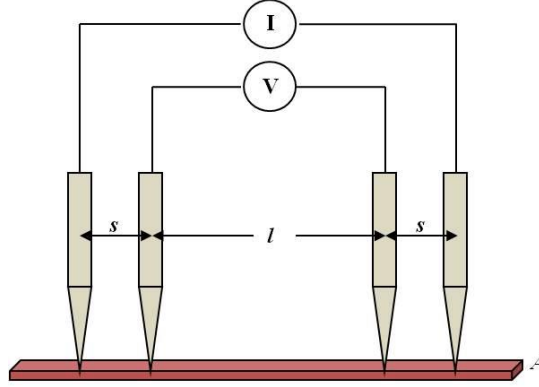


Figure 5.4: Schematic representation of 4 point probe

5.2 Paste characterisation results

The FT-IR results for silver paste sample and glass film reference are shown in Figure 5.5; the peaks appear at 3308.99, 2932.86, 1658.84, 1522.85, 1440.87, 895.96, 754.19 and 619.17 1/cm, where peak 895.96 and 754.19 are results of glass substrate. Based on the FT-IR spectrum references, the matrix should be kind of non-aromatic polyamides, which has its typical peaks at 3100~3400 for NH_2^+ and NH_3^+ , and a fingerprint peak region at 1450~1750 for $-\text{CO}-\text{NH}-$ [144].

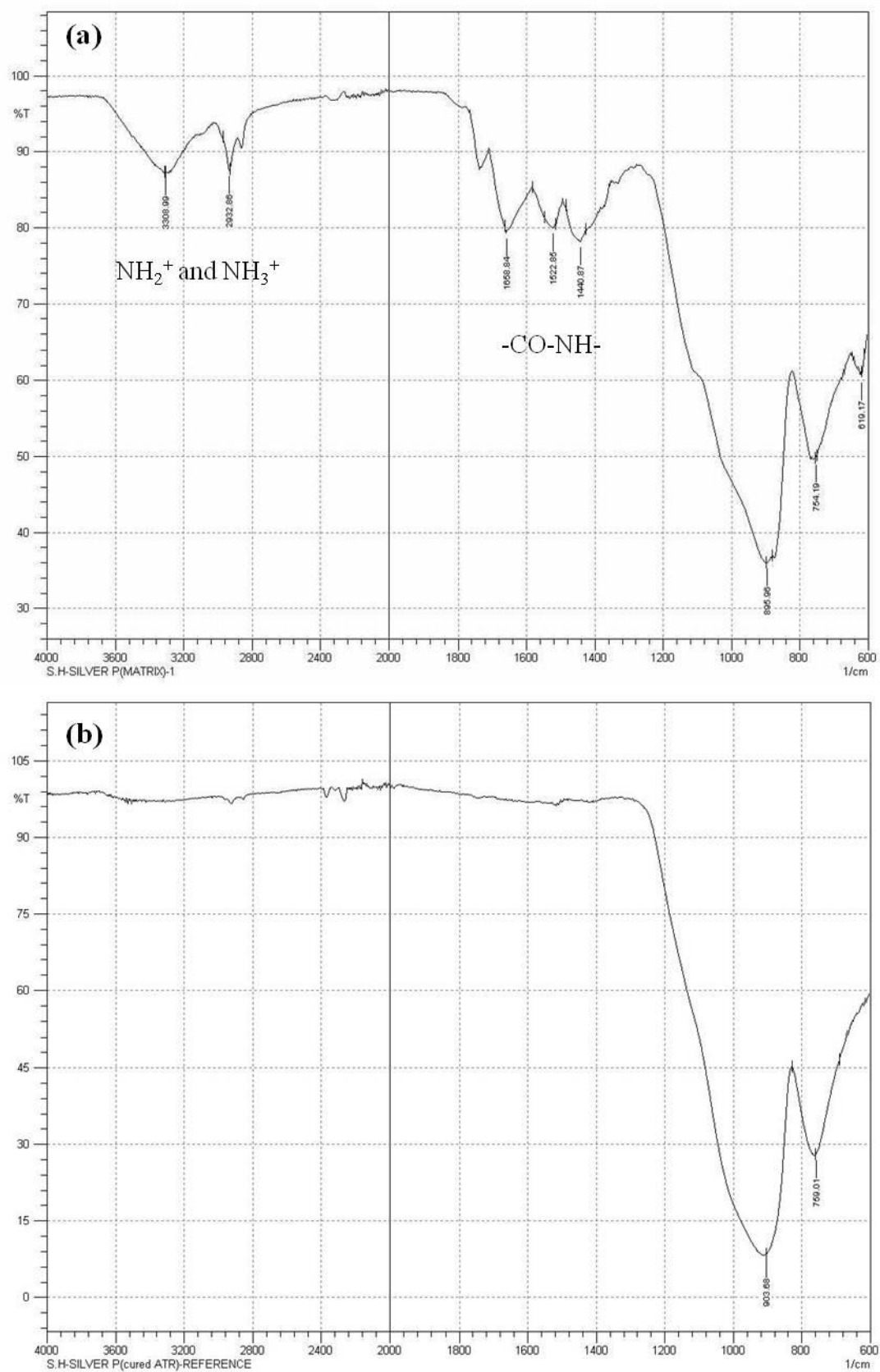


Figure 5.5: FT-IR patterns of (a) paste matrix on glass film and (b) glass film

The result for TGA test is shown in Figure 5.6, which can be divided into several steps based on its weight loss profile:

- 20°C~90°C, a stable state without any weight loss;
- 90°C~230°C, the continuous weight loss may come from the evaporation of trapped solvent in paste composite, the solvent could be the either catalyst or lubricant and the total weight loss is about 24%;
- 230°C~380°C, stable;
- 380°C~460°C, the decomposition of thermoset polymer, 14% in weight
- 460°C~800°C, the polymer burning residues and silver flakes are about 62% in weight.

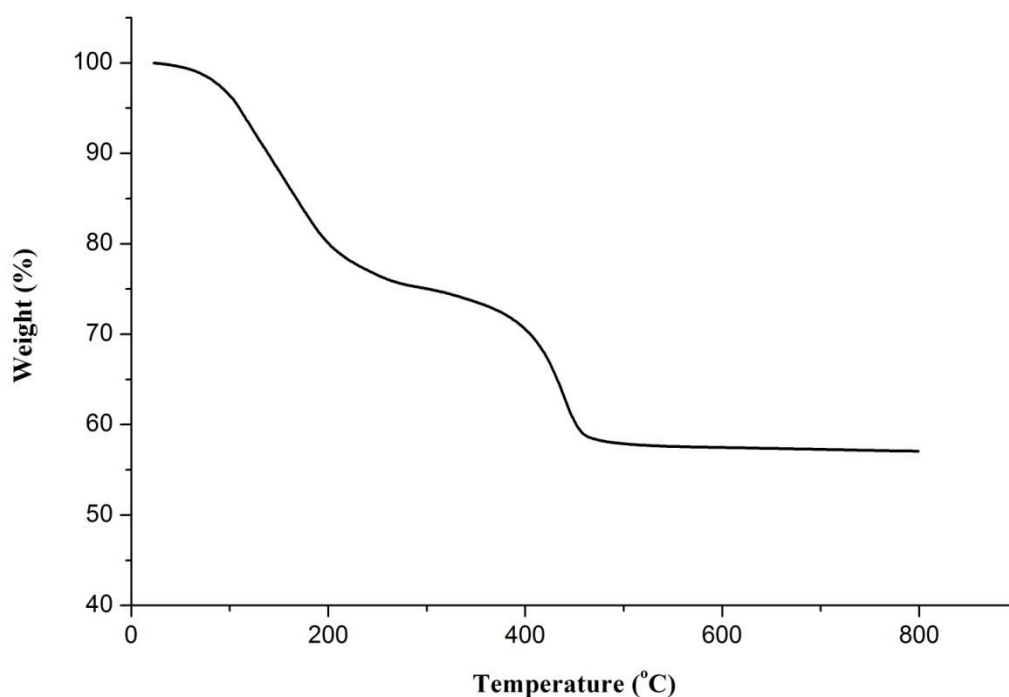


Figure 5.6: TGA curve of the silver paste (from room temperature to 800°C, at a heating rate of 10°C/min)

Based on that, the silver paste can be treated as a three-component system: silver flakes, amide oligomers (high viscosity) and the unknown liquid (low viscosity). To further identify the thermal properties of the paste, the DSC curves of the paste before and after

laser curing are exhibited in Figure 5.7.

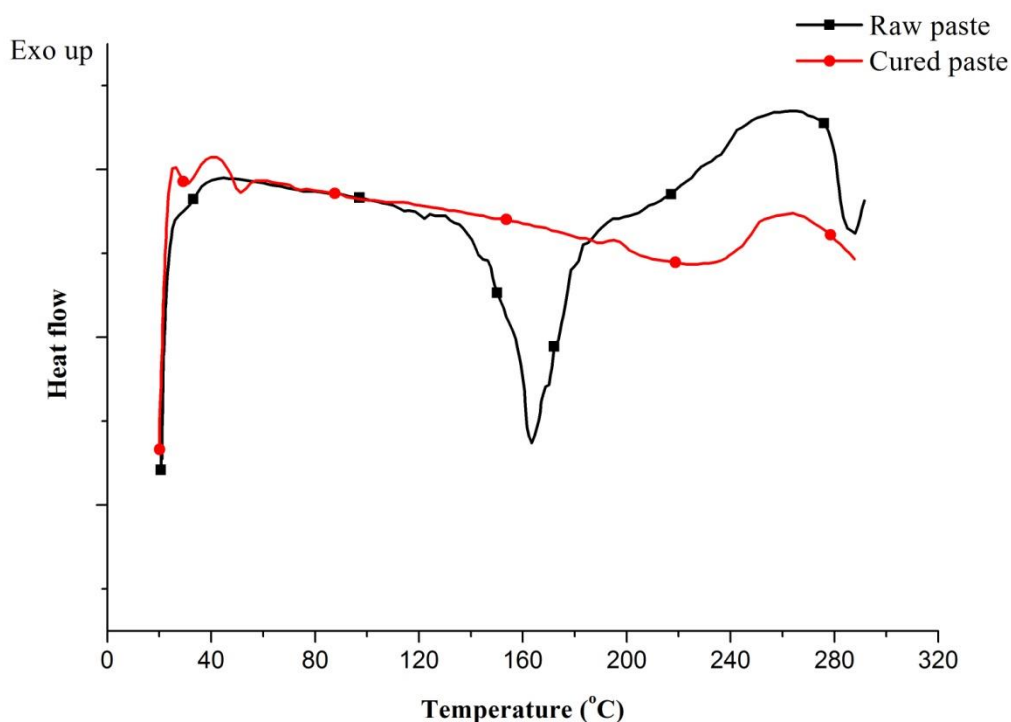
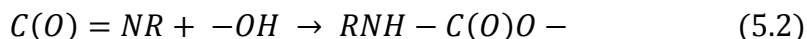


Figure 5.7: DSC results of the silver paste before and after HOE laser curing (P-2.3-1)

From Figure 5.7, before laser curing, the raw paste shows an endothermic peak at the range of 138°C to 182°C, which is a result of solvent evaporation; then a broad exothermic peak is observed from 210°C to the end of the run, which is supposed to be a representation of the polymerisation process of the resin oligmers or monomers. For the typical thermoset amide chain propagation process, i.e. the polymerisation of urethane, the following reaction occurs:



The C=N double bonds (energy 615kcal) and an O-H bond (459kcal) are converted to a C-O (358kcal), a C-N (305kcal) and a N-H (386kcal) [131], as a result the enthalpy variation is -25kcal, which indicates that the polymerisation should be an exothermic process. Actually, not just for polyurethane, most of the polymerisation will release energy.

After laser curing, the endothermic peak disappears and only a small exothermic peak is observed, which indicates that the liquid is fully evaporated but the amide resin is not fully cured at a condition of P-2.3-1.

5.3 Electrical resistivity measurement

To calculate the resistivity of the cured track, its cross-section area is firstly calculated: from the cross-section profile of oven cured sample measured by Alicona (Figure 5.8), the area A is calculated as 0.0875mm^2 and the length l is 40mm . For laser cured samples, although the cross-section is difficult to calculate due to bubbling, the actual functional area is similar to the oven cured one.



Figure 5.8: the cross-section profile of oven cured sample at 150°C for 0.5h

The calculated resistivity values of the sample at different curing conditions are list in Table C.1 in Appendix C. And variation of resistivity against input power and scanning speed are shown in Figure 5.9, where the resistivity of bulk silver is known as $1.59 \times 10^{-6} \Omega\text{cm}$.

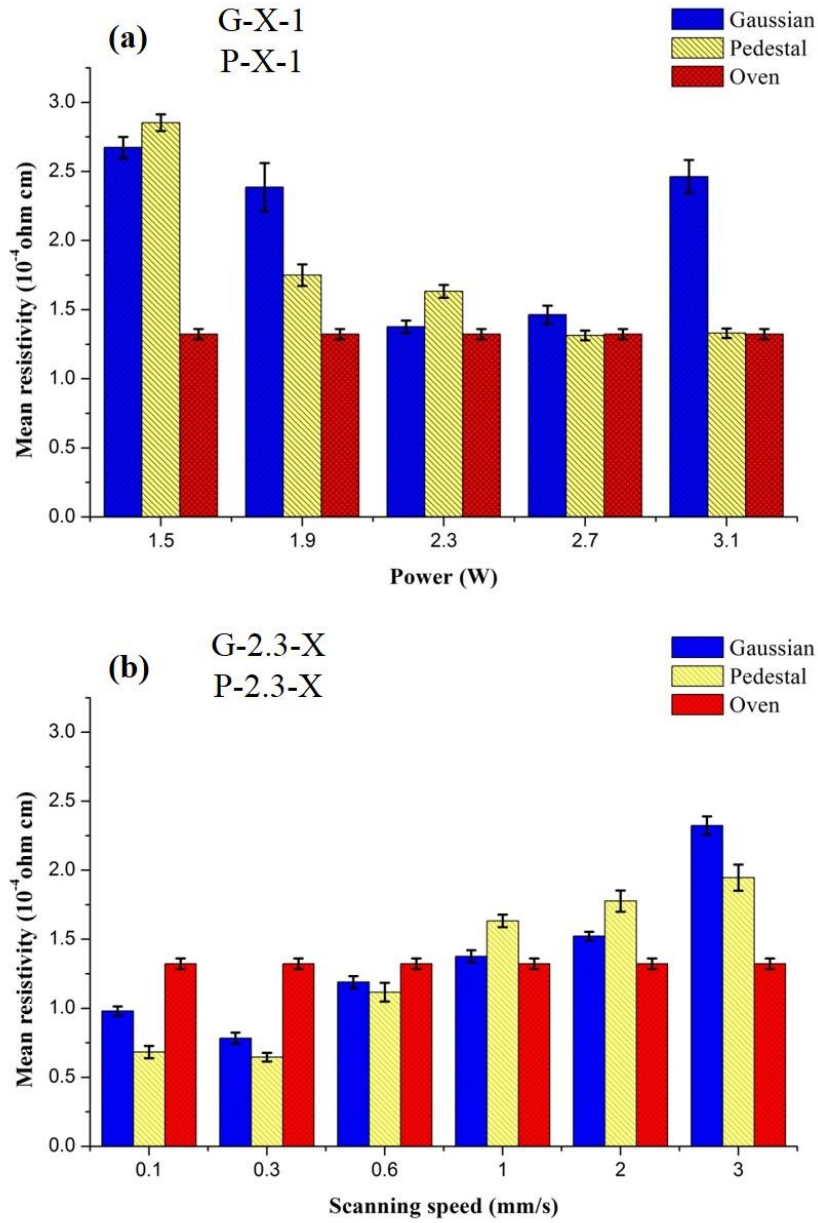


Figure 5.9: Resistivity comparison between Gaussian beam, Pedestal HOE beam and cured sample at: (a) varied input power at constant scanning speed 1mm/s; (b) varied scanning speed at constant input power 2.3W

Two general trends can be observed from Figure 5.9: the resistivity will increase with increased scanning speed or decreased input power. The variation of the resistivity is supposed to be a result of the curing process. Based on the experiment carried out by Lu [25], during thermal curing of conductive adhesive, the volumetric shrinkage of the resin which generated by 3D polymerisation will lead a closer contact between the metal fillers;

therefore, the resistivity of metal-filled paste will keep decreasing when the degree of cure increases. Obviously, a high input power or a low scanning speed will generate a high energy density on the sample, therefore a high degree of cure and low resistivity. Moreover, the Gaussian and Pedestal product have the similar resistivity values in most of the cases but the Gaussian beam exhibit an obvious increasing of resistivity at a high input energy condition (e.g. G-3.1-1). Meanwhile, one may notice that at some conditions, e.g. P-2.3-0.3, the resistivity of laser cured sample is lower than the oven cured one (150°C for 0.5h). To explain those phenomena, it is necessary to analyse the microstructure of the cured sample.

5.4 Morphology and microstructure

5.4.1 A comparison between laser and oven cured samples

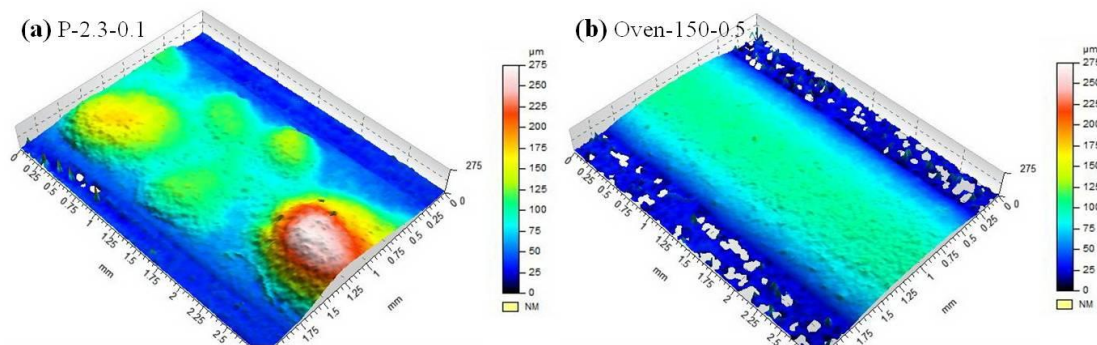


Figure 5.10: The surface morphology of sample (a) P-2.3-0.1 by Pedestal HOE laser; (b) 150°C-0.5h by oven

From Figure 5.10, the sample cured by laser shows a rougher surface and the bubbles can be observed, which is supposed to be a result of the evaporation of the solvent and degradation of polymer in silver paste. Drying in air will lead to solidification of the paste but cannot eliminate the formation of those bubbles.

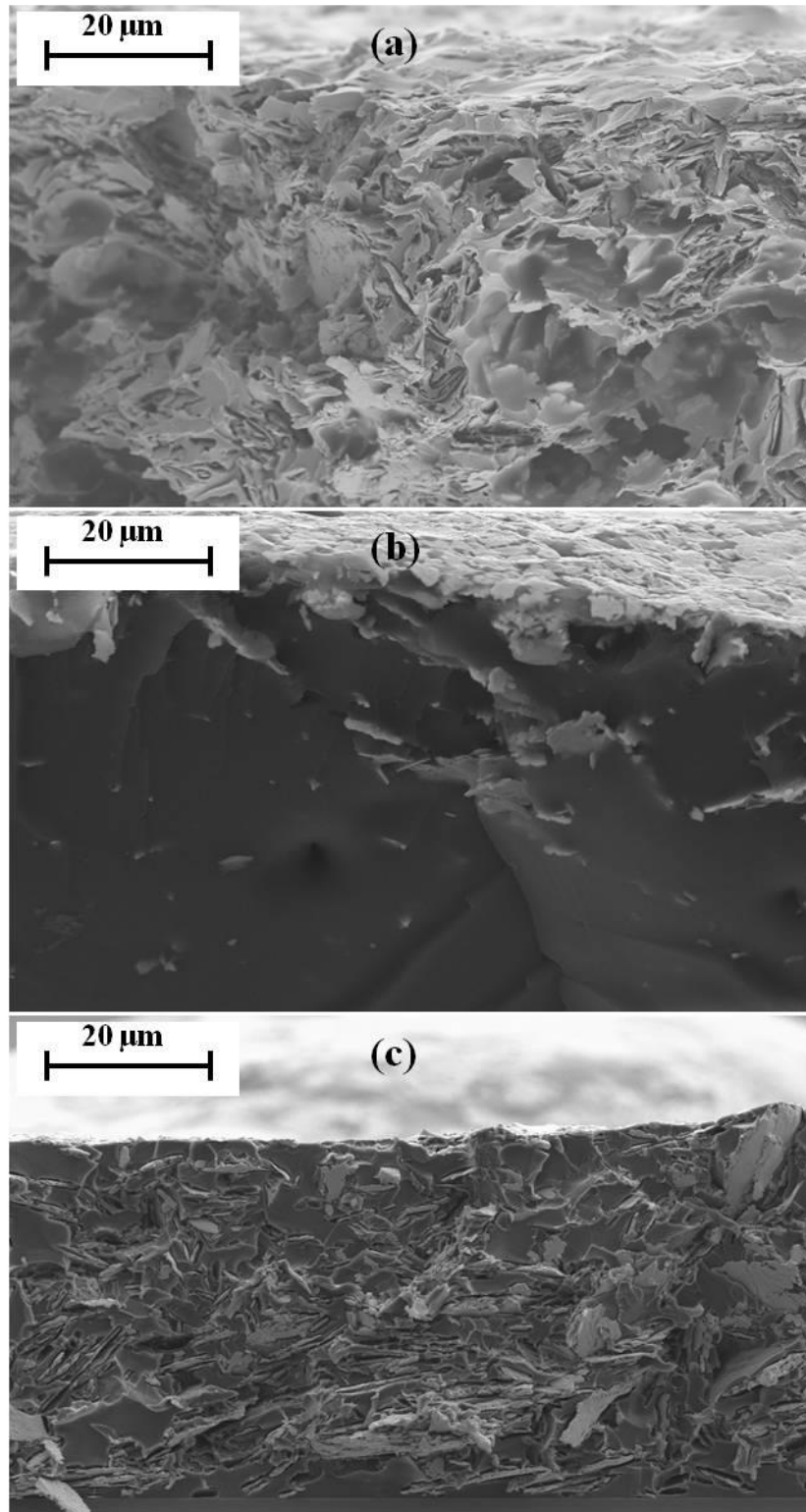


Figure 5.11: The cross-sectional SEM images of: (a) P-2.3-0.1; (b) P-2.3-1 and (c) oven (150°C-0.5h) cured samples

Figure 5.11 represents the SEM images of the transverse plane of conductive tracks. The

porous structure of laser cured sample further confirms that degradation occurs. In the laser-epoxy curing case, the optical penetration depth is only few microns [132]; however the thickness of deposited paste is about $75\mu\text{m}$, as revealed in Figure 5.8. The energy will transfer into the lower region of the track by thermal conduction or convection. As a result, the upper region has a higher temperature and according to its thermal properties (Figure 5.6), the solvent in paste will start evaporating at about 138°C . When this solvent evaporation occurs in the lower region, the upper region may reach its polymerisation temperature, i.e. about 210°C and cross-linking between oligomers occurs, which will further lead to the solidification of the upper region and the evaporated vapour is therefore sealed in the track, eventually bubbles are generated. However, during the conventional oven curing, since the heat transfer among the paste is more uniform and curing rate is much lower; there is sufficient time for those vapours to escape from the track and no obvious bubbles formed.

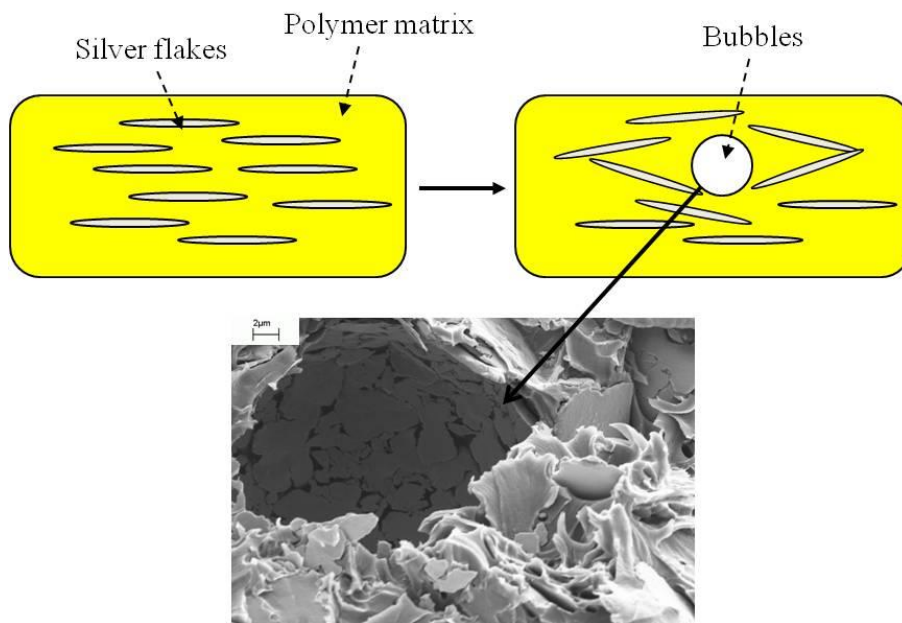


Figure 5.12: The reduction of distance between silver flakes during polymer degradation in laser curing, the SEM image was achieved at P-2.3-0.3

Although this bubbling phenomenon during laser curing is a drawback on sample morphology, it is still worth to notice that the measured resistivity of the P-2.3-0.1 sample

($0.68 \times 10^{-4} \Omega \text{cm}$) is lower than that cured by oven ($1.32 \times 10^{-4} \Omega \text{cm}$). As shown in Figure 5.12, during the bubbles formation, the generated volume force will push the nearby silver flakes away and this process will reduce the distance between different silver flakes and therefore decrease the resistivity.

At high speed scanning condition (P-2.3-1, Figure 5.11.b), an agglomeration of silver flakes on top surface can be observed. For thermoset material, there are two opposing effects on its viscosity during curing – the increasing of temperature will decrease the viscosity while the cross-linking will increase it. Cross-linking is actually a thermodynamic process and it is determined by both temperature and time. Therefore one may observe a small reduction of viscosity at the beginning time of epoxy curing process. Since laser is a rapid heating source, this kind of viscosity reduction should be amplified and the fluid flow is able to occur during this process. As introduced in the simulation part, the fluid flow can be controlled by different beam irradiance distribution. Because of Marangoni and gravity effect, the flow pattern inside the processed polymer matrix should be similar to that of the molten pool in Section 3.5.1, i.e. the uncured polymer tend to flow away from the centre and then form a circulation flow in the matrix. Although a complete circulation flow may not be formed before the epoxy is cured, this will still become the driving force for the movement of the silver flakes. And as a result, those flakes will agglomerate at some positions and a silver flake layer can be generated.

5.4.2 The influence of laser input power and scanning speed

Figure 5.13 indicates the surface morphology of the laser cured samples at varied input power (d, e, f, g, h) and scanning speed (a, b, c, d). Obviously, as the scanning speed increases, the size of the generated bubbles decreases but the surface roughness increases, i.e. a large amount of small bubbles are generated at high scanning speed. Meanwhile, it is interesting to notice that the variation of sample surface morphology with input power is not obvious but the sample height is increased with the input power.

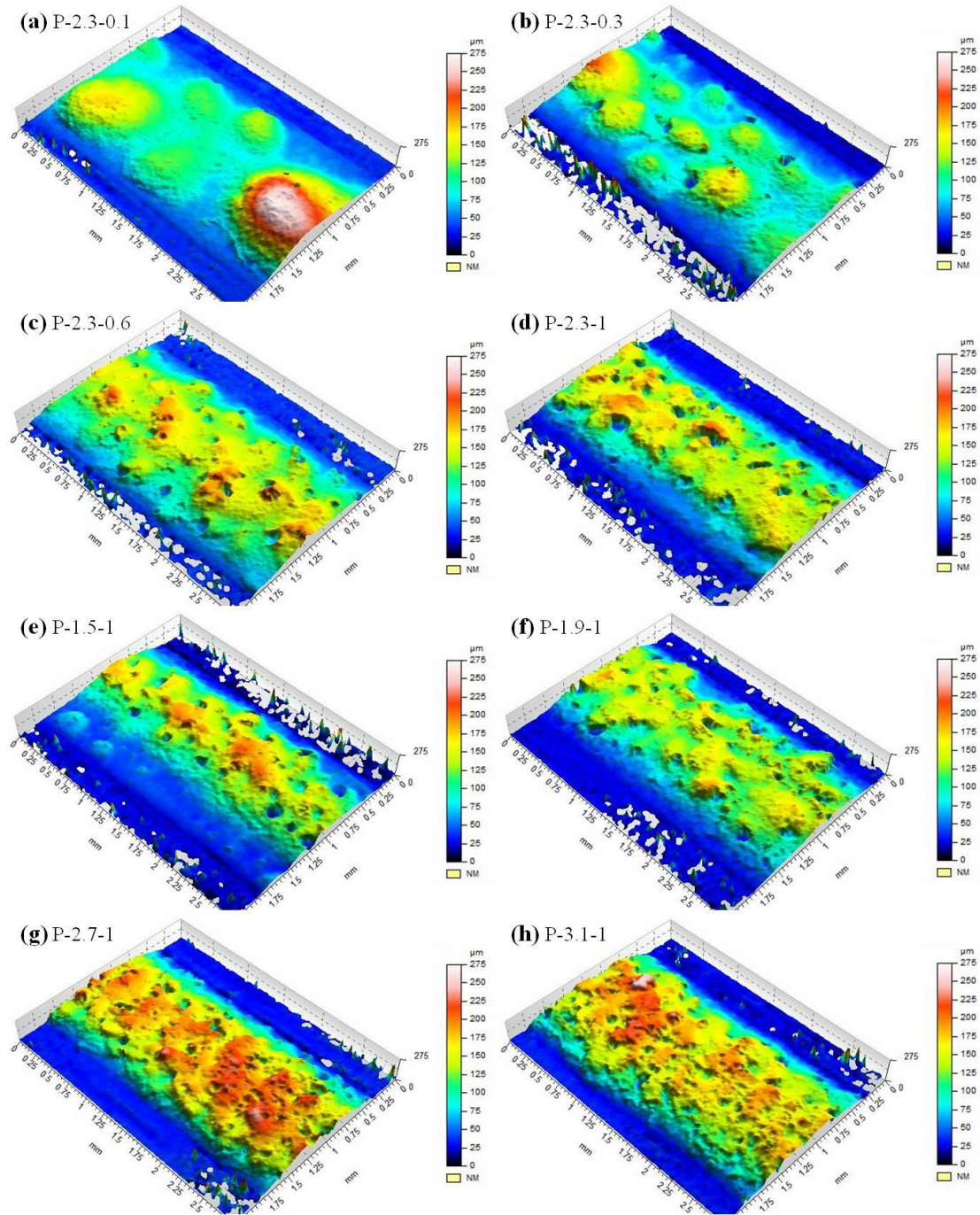


Figure 5.13: Surface morphology measured by Alicona for samples: (a) P-2.3-0.1, (b) P-2.3-0.3, (c) P-2.3-0.6, (d) P-2.3-1, (e) P-1.5-1, (f) P-1.9-1, (g) P-2.7-1, (h) P-3.1-1

To indicate the mechanism of the above phenomenon, the high speed camera was used to capture the formation process of bubbles and the result for a low scanning speed and high scanning speed case are indicated in Figure 5.14. The bubbles are obviously formed from the bottom region of the deposited track. If a laser is applied on the track, from a transverse plane view, the surface region will quickly be cured and form a rigid layer; the

evaporated solvent just below this rigid layer will generate the original bubbles, which have small size but large amount. At a low scanning speed, heat will continuous conduct into the deeper region of the track and more solvent will be evaporated; therefore bubbles will keep growing and even merge with each other sometimes. Eventually several large bubbles are be formed. However, if the scanning speed is high, there is no sufficient time and vapour source for the original bubble to grow and therefore their size are very small.

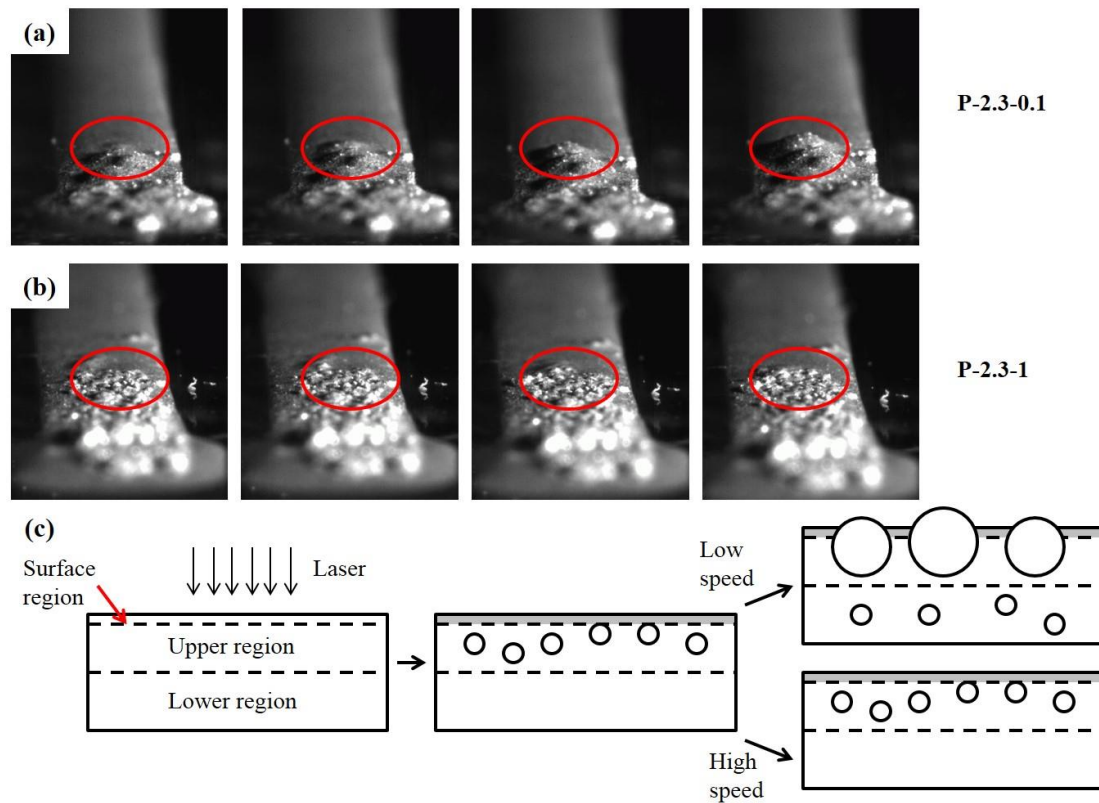


Figure 5.14: Images achieved from high speed video for samples: (a) P-2.3-0.1; (b) P-2.3-1 and (c) the mechanism of bubble growth at different scanning speeds

Moreover, different from the scanning speed, the sample surface morphologies at different input power are similar to each other, since the variation of total input energy for the power series (e.g. P-1.5-1 and P-3.1-1) is quite small compared with that for the scanning speed series (e.g. P-2.3-0.1 and P-2.3-1). However, a high power can still generate more bubbles inside the paste and therefore lead a larger product height.

In the experiment, it is found that an input power higher than 3.1W will lead a damage of the deposited track during laser curing, as shown in Figure 5.15. Since epoxy is naturally thermal insulator, the heat conduction has low efficiency; the surface region will be over-heated at a high input power and thus degradation occurs. Although a low scanning speed also provide a high total energy but the there is sufficient time for the energy to flow down.



Figure 5.15: Direct comparison between an undamaged track (a) P-2.3-1 and damaged track (b) P-3.1-1

5.4.3 A comparison between Gaussian and HOE beam cured samples

Figure 5.16 shows the difference between Gaussian beam and Pedestal beam cured samples, at an input power of 2.3W and different scanning speeds. Obviously, for all conditions, the laser induced thermal ejection is more serious in Gaussian beam cases. According to the discussion in the simulation part, the Marangoni effect is believed as the primary reason for this phenomenon. The Gaussian beam will generate a higher Marangoni force due to its higher temperature gradient compared with the Pedestal beam, which will lead an outward fluid flow from the silver track centre to the edge region; during this process, the thermal ejection is easier to occur. Meanwhile, one may notice the track damage appears only in the Gaussian cases although the input energy is same, which can be explained by the energy distribution of the two beams. The Gaussian beam has the majority of the energy in the centre, and it will lead to an over-heating of the epoxy in that region and producing thermal degradation.

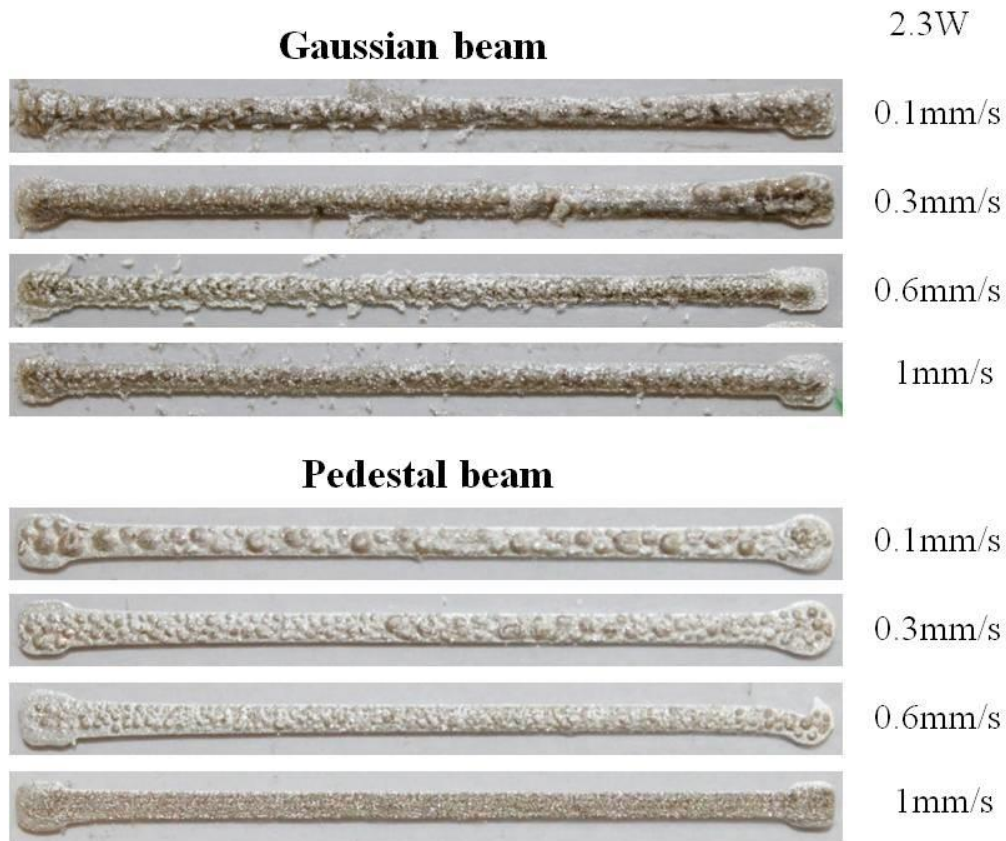


Figure 5.16: Photography of laser cured samples at 2.3W and different scanning speeds using Gaussian and Pedestal beam

According to above discussion, it needs a suitable input energy value (Pedestal, 2.3W-1.6mm/s from current work) to achieve the best preformation of the silver track from both electrical conductivity and morphology. Insufficient energy cannot fully cure the paste and will lead to a high resistivity; the energy can be increased by providing higher input power or lower scanning speed. It is found that by using a Gaussian beam, the silver track will be damaged if the input power is higher than 2.3W or scanning speed is lower than 0.6mm/s, which is believed as a result of over-heating in centre of the track. The Pedestal beam exhibits a more stable curing process due to its uniform energy distribution. However, if a very low scanning speed ($<0.3\text{mm/s}$) is selected, large bubbles are formed and this should be avoided in further manufacturing.

5.5 Building a 2D flexible circuit system

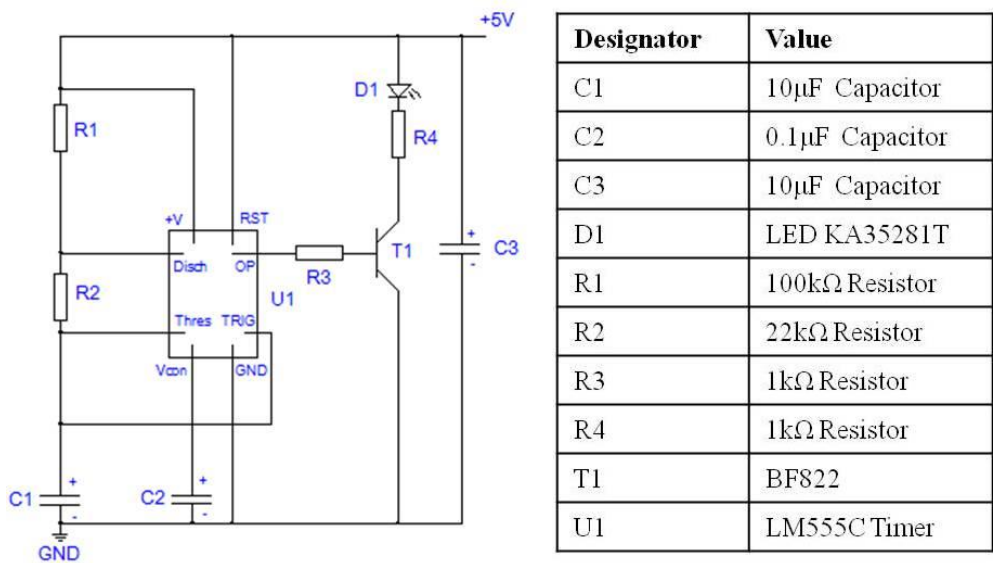


Figure 5.17: Schematic of timer circuit and list of different electronic components

In this part, a 2D timer circuit on a flexible HDPE substrate was manufactured, where the basic circuit schematic is shown in Figure 5.17. When a voltage of 5V is applied, the LED is supposed to flash at a constant frequency.

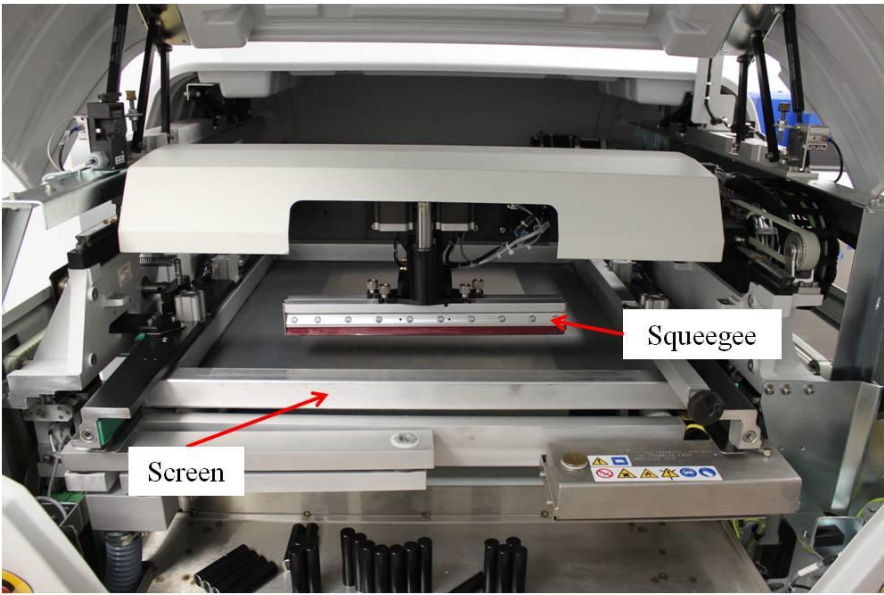


Figure 5.18: The screen printing system used in the timer circuit pattern deposition

During the manufacturing process, the substrate was manufactured using HDPE powder via the technique described in Chapter 4. The substrate includes a compression moulded layer and laser melted layer at a condition of Gaussian beam-10W-240mm/s-0.2mm. The silver paste was then deposited on the substrate using screen printing (265 Horizon, DEK), the screen was designed with a size of 325 mesh and 10 μ m emulsion thickness; meanwhile, to demonstrate a high resolution printing, the width of the deposited line was generated as 0.3mm. The printing system is exhibited in Figure 5.18 and in this work the squeegee pressure and movement speed were set as 10kg and 20mm/s, respectively.

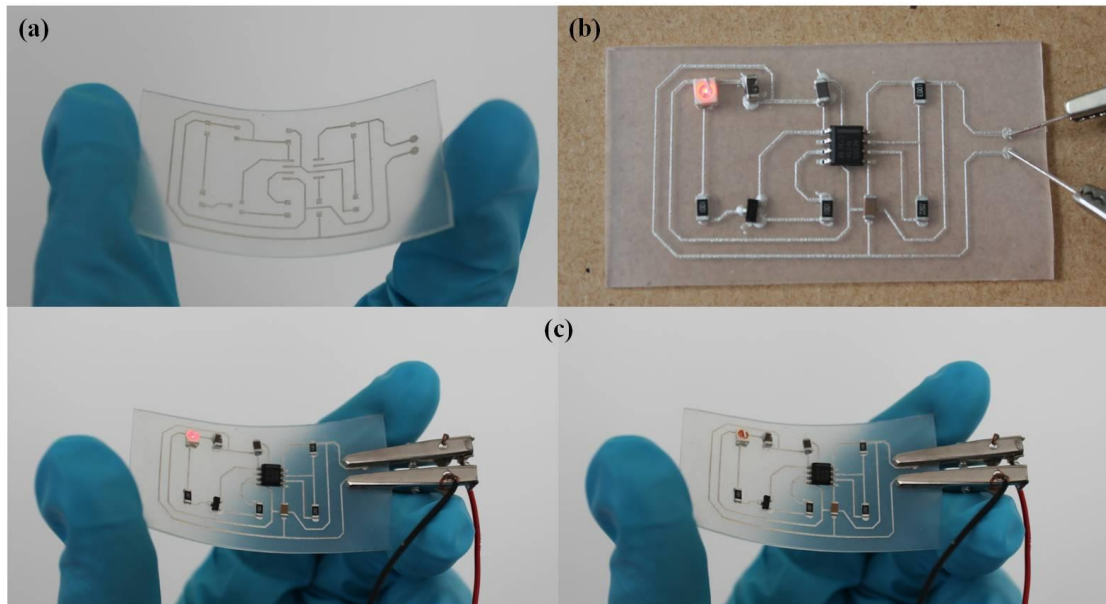


Figure 5.19: (a) Printed timer circuit pattern; (b) original cured circuit with electronic components; (c) bent circuit with electronic components, where LED is flashing

After printing, the deposited silver paste pattern was shown in Figure 5.19.a. During the curing process, although the Pedestal HOE beam demonstrate a better control in sample propety in previous discussion, its minimal size has been limited to 0.5mm due to the current beam reconstrction technology [133]. As a result, a Gaussian beam with a focus diameter of 0.3mm is used as the curing source and the scanning conditon was set as 1.5W, 10mm/s. This selective laser processing enables a curing of silver paste without damege the HDPE substrate. Different components was joined on circuits according to extra silver paste, which is then heated at 80°C for 0.5h with the purpose of soldering.

The final product was exhibited in Figure 5.19.b, where a 5V voltage is applied. Moreover, due the flexible nature of the HDPE substrate, the finished part can be bent while the LED is still working, as shown in Figure 5.19.c.

5.6 Summary

In this chapter it addresses the research question in Section 1.2: ‘Can we use laser to generate conductive circuits which have similar or improved performance compared with convectional?’ by laser curing of silver paste on both glass and HDPE substrate in a very short time and the sample demonstrating a lower electrical resistivity compared with the oven cured one.

- The low electrical resistivity for laser cured sample was a result of reduction of distance between different flakes during bubble formation. The bubbles were generated by the solvent evaporation in the lower region of the paste, where the vapour was sealed in the paste due to the polymerisation of the upper region. Meanwhile, the silver flakes agglomeration could also be observed, which was believed as a result of epoxy flow before curing.

In this chapter it also addresses the research question in Section 1.2: ‘Does the redistribution of input energy provide a means of controlling/improving the properties of the resultant conductive circuits?’ by reconstructing Gaussian beam to Pedestal beam and comparing the morphology and microstructure of cured tracks between the two cases:

- Compared with Gaussian beam, the Pedestal beam could reduce the laser induced thermal ejection since it had a uniform energy distribution, where the Marangoni effect was weak and flow was stable. Moreover, at a high input energy, Gaussian beam was easier to lead thermal degradation on the paste due to the over-heating in centre.

In this chapter it also addresses the research question in Section 1.2: ‘Can we generate 2D

circuit on flexible substrate using laser curing?’ by generating a 2D flexible circuit board using silver paste:

- A timer circuit pattern was fabricated on a HDPE substrate, which was followed by laser curing and electronic component deposition. A flexible circuit was generated and its conductivity kept stable during a simple bending test. However, the circuit pattern was generated by screen printing, which was only applicable in 2D; to manufacture a 3D circuit system, it is necessary to find a new deposition method and suitable conductive material.

CHAPTER 6: LASER MELTING OF COPPER/HDPE POWDER MIXTURE

This chapter details the experimental results of laser melting of copper/HDPE powder mixture. A HOE based galvo scanning system was set up to reconstruct the Gaussian laser beam to Pedestal beam. A burn print test was used for beam profile characterisation. During the laser melting process, the following conditions were included in this research: copper/HDPE ratio; laser input power and scanning speed; single track scanning and raster scanning programme; Gaussian beam and Pedestal beam reconstructed using HOE. The resistivity and microstructures of melted tracks were investigated by 4-point probe and SEM, respectively. Hot-stage microscope was used to reveal the copper particle movement in a melted HDPE matrix and IR thermal camera was used to monitor the temperature variation during the laser melting. A 3D embedded circuit system was manufactured in the current work, with the HDPE as substrate and copper/HDPE mixture as the conductive track. This circuit system is used to demonstrate the additive layer manufacturing of dissimilar materials.

6.1 Experimental procedure

6.1.1 Set up HOE based galvo scanning system

The basic laser scanning system consists of a Gaussian laser source and a galvo scanner. The modification was carried out by introducing an extra HOE optic in the beam path, the new system is illustrated in Figure 6.1.

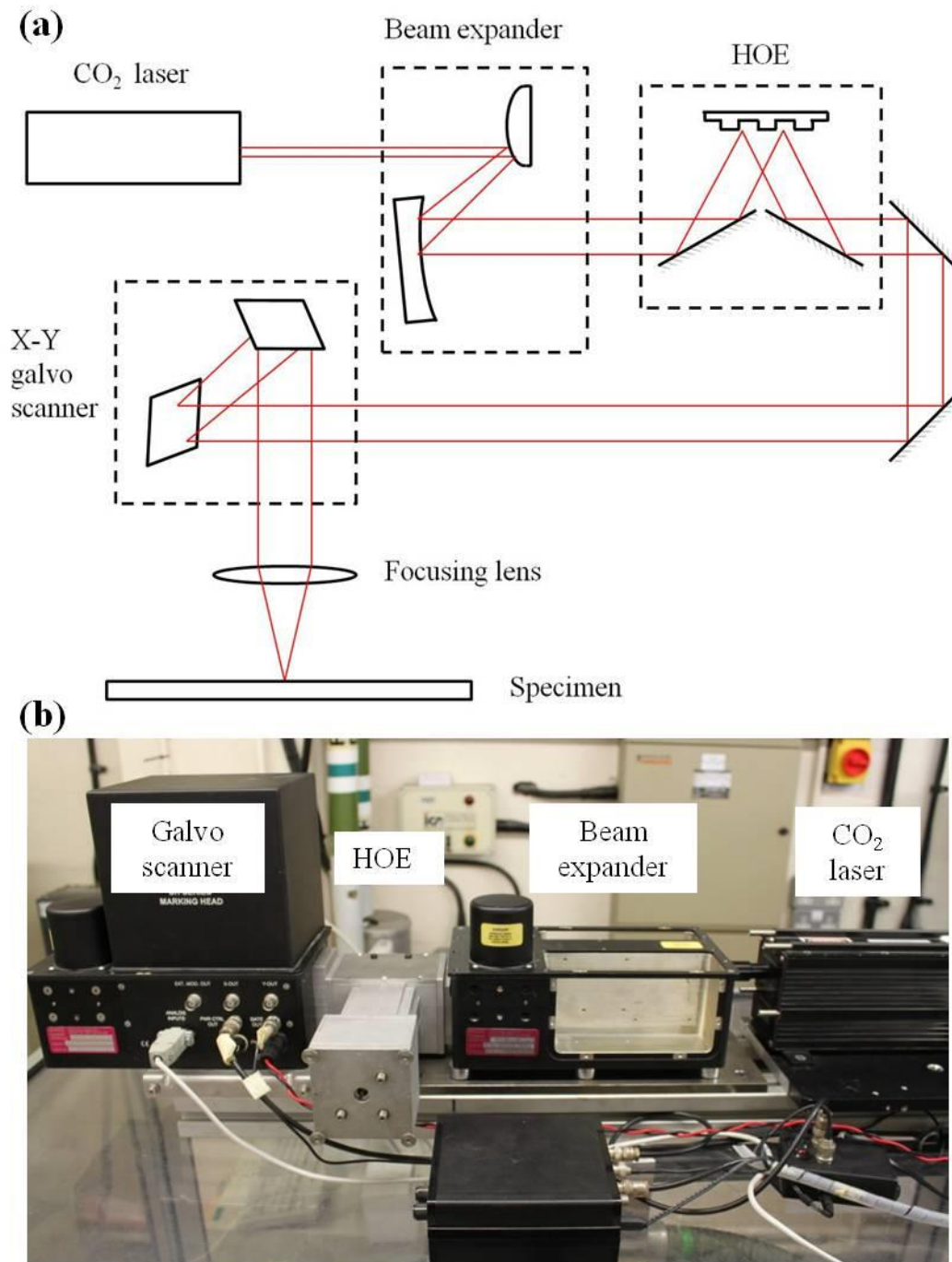


Figure 6.1: (a) Schematic representation and (b) setting up of the HOE galvo scanning laser

- The CO₂ laser is Synrad 10W (Synrad Inc);
- The beam expander uses 2 spherical mirrors to establish a beam reflection system, as shown in Figure 6.2.a; the expander ratio is 3X;
- The HOE is placed in a self-generated box, where two reflection mirrors mounted on the adjustable platforms were used to collimate the beam, as shown in Figure 6.2.b;

- The galvo scanner consists of two reflection mirrors, which are used to control the beam movement in X and Y axis, as shown in Figure 6.2.c.

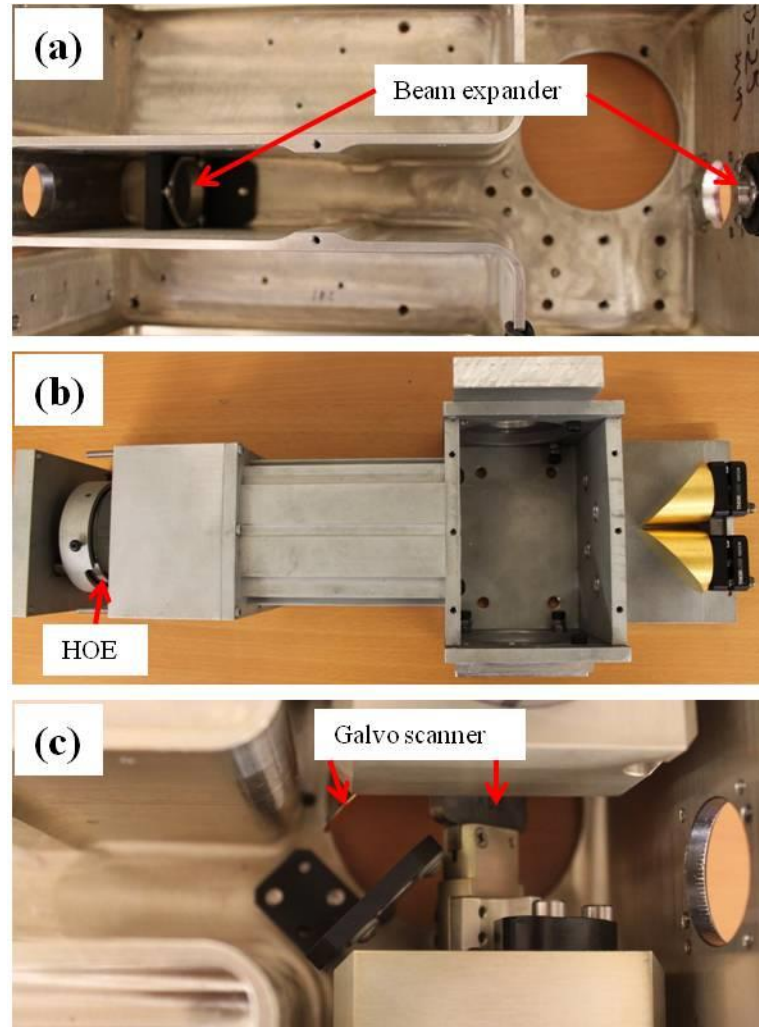


Figure 6.2: Internal structures of (a) 3X beam expander; (b) HOE box; (c) galvo scanner

6.1.2 Laser beam profile characterisation

After beam alignment, burn prints test for both Gaussian beam and constructed Pedestal beam was carried out. A single pulse of 8W and 5ms was shot on a piece of Poly(methyl methacrylate) (PMMA) and the beam prints are shown in Figure 6.3. Plastic will be melted and the flow will ‘distort’ the print, however, it still indicates outlines for the two beam irradiances. To further indicate the beam intensity distributions, the 3D profile of the prints are measured using surface profiler (Alicona, InfiniteFocus).

- The Gaussian burn print has a high depth in the centre, which indicates its high energy intensity in this region.
- One should also notice that the constructed Pedestal beam consists of three high intensity ‘spots’ and it is not ideal square, since the designed beam size is too small to keep a high resolution.

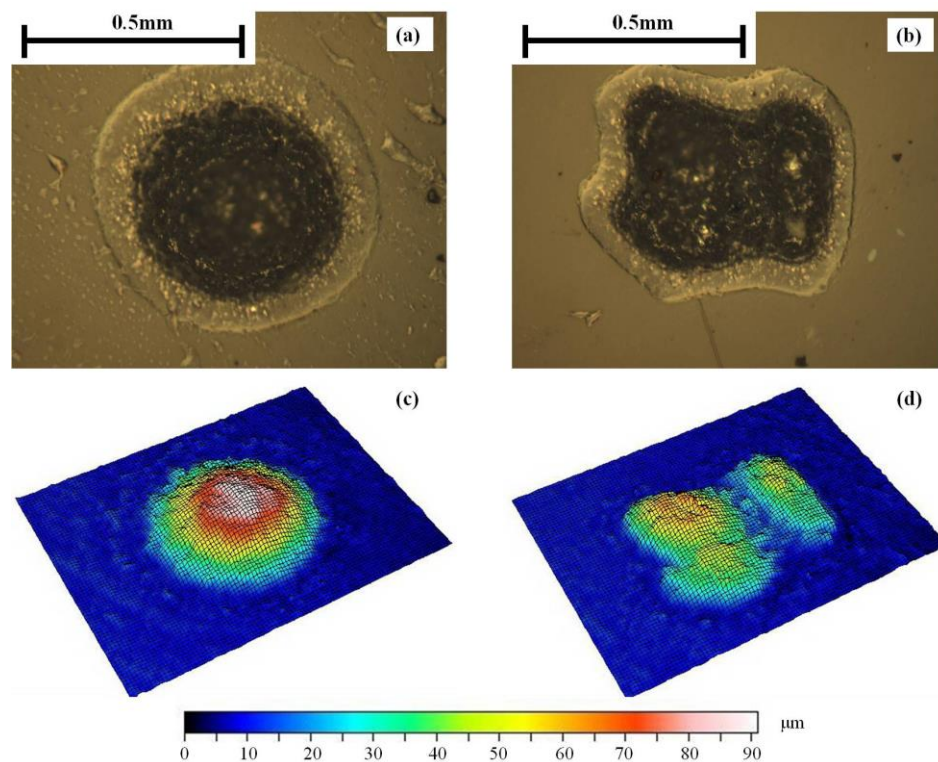


Figure 6.3: (a) Burn print for Gaussian beam; (b) burn print for Pedestal beam achieved from galvo scanning system; (c) burn print 3D profile for Gaussian beam; (d) burn print 3D profile for Pedestal beam

To characterise the beam stability in stand-off height (distance from workpiece to focusing lens), a series burn print tests were carried out with positive and negative stand-off height. Here the positive means moving the PMMA sheet further away from the focusing lens; negative means moving the PMMA sheet closer to the focusing lens. The datum plane height (focusing length) for the current system is set as 241mm. Moreover, during the galvo scanning process, at different locations on the datum plane the angle of

incident of the beam is different; this may also influence the profile of the reconstructed beam, therefore the burn beams of 4 points with coordinates of $(-20, -20)$, $(-20, 20)$, $(20, -20)$ and $(20, 20)$ on the datum plane are investigated (unit mm). The experiment set-up and results are all exhibited in Figure 6.4.

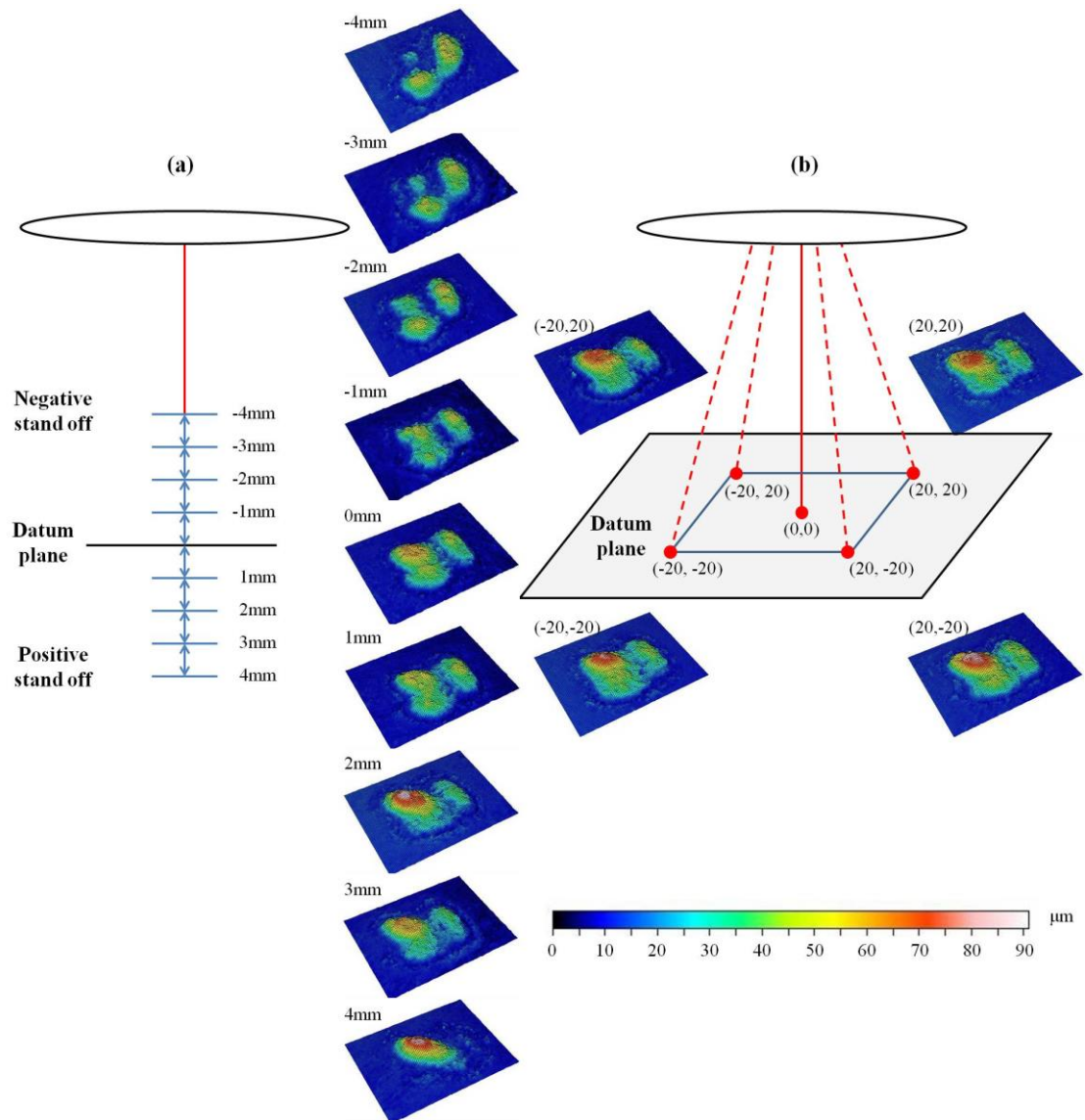


Figure 6.4: 3D burn print profiles of HOE Pedestal beam achieved from (a) stand-off alteration test; (b) spot location alteration test

From Figure 6.4.a, the alteration in stand-off height has significant influence in the beam profile. In the range of $-1\text{mm} \sim 3\text{mm}$, the beam keeps the '3 spots square' shape; a high negative stand-off height will split the beam and a high positive value will concentrate

energy into one single spot. However, no significant variation of the beam profile can be observed during the alteration in spot location on the datum plane, as shown in Figure 6.4.b, which reveals the high robust of HOE system during galvo scanning.

To further characterise the current ‘3 spots’ Pedestal beam, a raster scan programme (10mm*10mm square) is used on the HDPE powder to create a single layer polymer sheet. The experiment set up is similar to that described in Chapter 4 and the processing conditions are: laser power – 8W, scanning speed – 240mm/s and scan spacing – 0.3mm. Both Gaussian and new Pedestal beams are used and the surface profiles of the achieved sample are measured using Alicona. The results are shown in Figure 6.5.

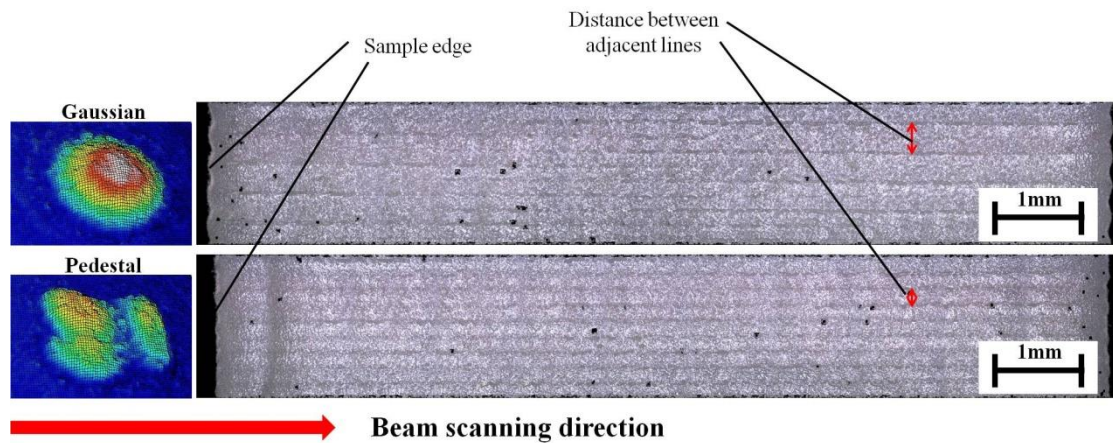


Figure 6.5: Comparison between samples generated by Gaussian and Pedestal beams using the same raster scan programme: 8W-240mm/s-0.3mm

On the sample surface there are a series of straight lines which parallel to the scanning direction. The formation of those lines has already been explained in Section 4.2.3, which is believed as a result of powder consolidation during laser melting. Two differences between the Gaussian case and Pedestal case can be found:

- The distance between two adjacent lines in the Gaussian case is measured as 0.27mm, approximately; which is larger than the value in Pedestal case (0.15mm). Generally, the line represents the scanning a track of the high energy intensity region in a beam. For

Gaussian case, it is the centre therefore the distance between adjacent lines is similar to the scan spacing; for Pedestal case, there are three small high intensity ‘spots’ in the beam therefore more lines will be generated and the distance between adjacent lines is decreased.

- The sample edge is wave-like in the Gaussian case but nearly straight in the Pedestal case, which is believed as a result of beam shape. The Gaussian beam has a round shape therefore the melted HDPE has half-circular shape at its two ends; for Pedestal beam, its square beam shape will generate flat ends, as revealed in Figure 6.6.



Figure 6.6: The edge effect of beam shape during a single track scan

The above characterisation results indicate that the generated laser beam is near square but not an ideal pedestal in energy distribution. Three ‘high intensity spots’ exist in the beam and it will influence the morphology of the processed sample. However, this near-Pedestal beam still exhibits advantages in sample structure control and it will be used in copper/HDPE mixture melting in this chapter.

6.1.3 Copper/HDPE mixture preparation and laser melting process

The micron-copper particles were received from Mr Siyuan Qi and Dr David Hutt at Loughborough University. The raw copper powder (about 20µm in diameter) they used was sourced from Sigma-Aldrich, UK, and a self-assembly-monolayer (SAM) coating of Octadecanethiol (ODT, HS-(CH₂)₁₇-CH₃, Sigma-Aldrich, UK) was used to provide an efficient protection from oxidation for the copper. It should be noticed that the copper oxide was first removed by etching before SAM was deposited and the structure of the

final copper particles is shown in Figure 6.7.

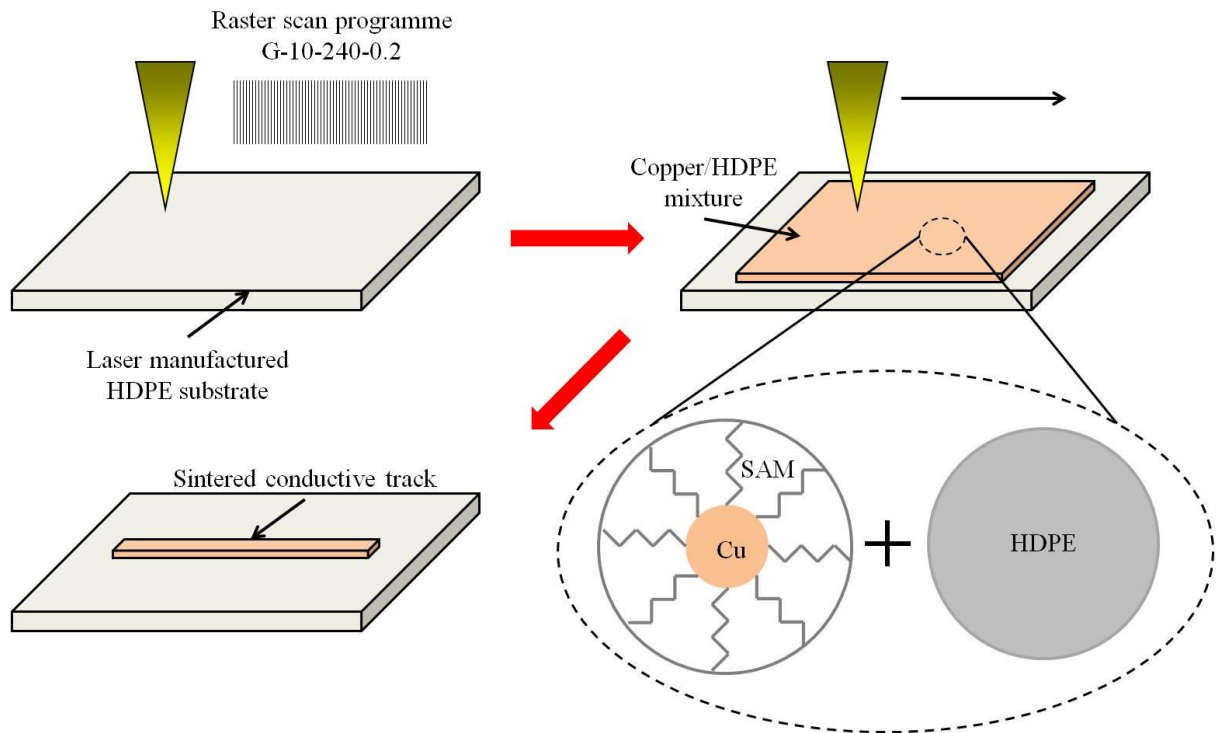



Figure 6.7: Laser melting of copper/HDPE conductive track on a HDPE substrate and the structure of micron-copper particles with SAM coating

The copper particles were then mixed with the HDPE powder (HMHDPE75A, Goonvean Fibres) at the following volume contents of copper (the ratio of the volume of copper particles to the volume of all particles): 30%, 40%, 50%, 60%, 70% and 100%, using a centrifugal mixer (Speed mixer, DAC 150 FVZ-K) at 2000rpm for 2 minutes. The finished material was deposited on a laser generated HDPE substrate (the substrate manufacturing technique is described in Chapter 4) as a layer structure (layer thickness is controlled as 150µm using a powder bed) and then placed under the focus lens of the laser. The whole process is shown in Figure 6.7 and both the Gaussian beam (Synrad Firestar 100W CO₂ laser) and HOE reconstructed Pedestal beam (Section 6.1.1) were used to melt the mixture. Two scanning programmes are selected in current study: the single track scan and raster scan (, 0.2mm width and 0.1mm scan spacing); the detailed conditions are listed in Table 6.1 and during the processing a small plastic box with an Argon supply tube is used to protect the mixture from oxidation. After that, the optimal

condition (G-r-6/4-20-120) was selected to build the multi-layers conductive structure and eventually an embedded 3D timer circuits system was generated.

Table 6.1: Selected laser melting conditions for a single layer conductive track

| Power (W) Scanning speed (mm/s) | 8 | 10 | 15 | 20 | 25 | 30 | 35 | 40 |
|--|---|----|----|----|----|----|----|----|
| 20 | | | | | | | | |
| 40 | | | | | | | | |
| 60 | | | | | | | | |
| 80 | | | | | | | | |
| 100 | | | | | | | | |
| 120 | | | | | | | | |
| 140 | | | | | | | | |

Note: ■ represents G-s-3/7 series; ■ represents G-s-6/4 series, ■ represents G-r-6/4 series and ■ represents P-s-6/4 series; in this chapter the sample nomenclature is as follow: ‘beam type (G-Gaussian or P-Pedestal) – scanning programme (s or r) – copper/HDPE ratio – power – scanning speed’, e.g. G-s-6/4-20-120

6.1.4 Sample characterisation

During this experiment, characterisation of the raw powder mixture and the melted product were both carried out. The X-ray photoelectron spectroscopy (XPS) was used to identify the oxidation conditions of the copper particles [134]. The SEM was used to show the sample morphology. During sample cross section preparation, to prevent unexpected damage, the liquid nitrogen assisted cutting technique described in Chapter 4 was applied. Moreover, the 4 point probe technique was used to measure the resistivity of

the circuit. Meanwhile, the IR thermal camera is also used to monitor the temperature variation during the melting process.

6.2 Raw copper/HDPE mixture characterisation

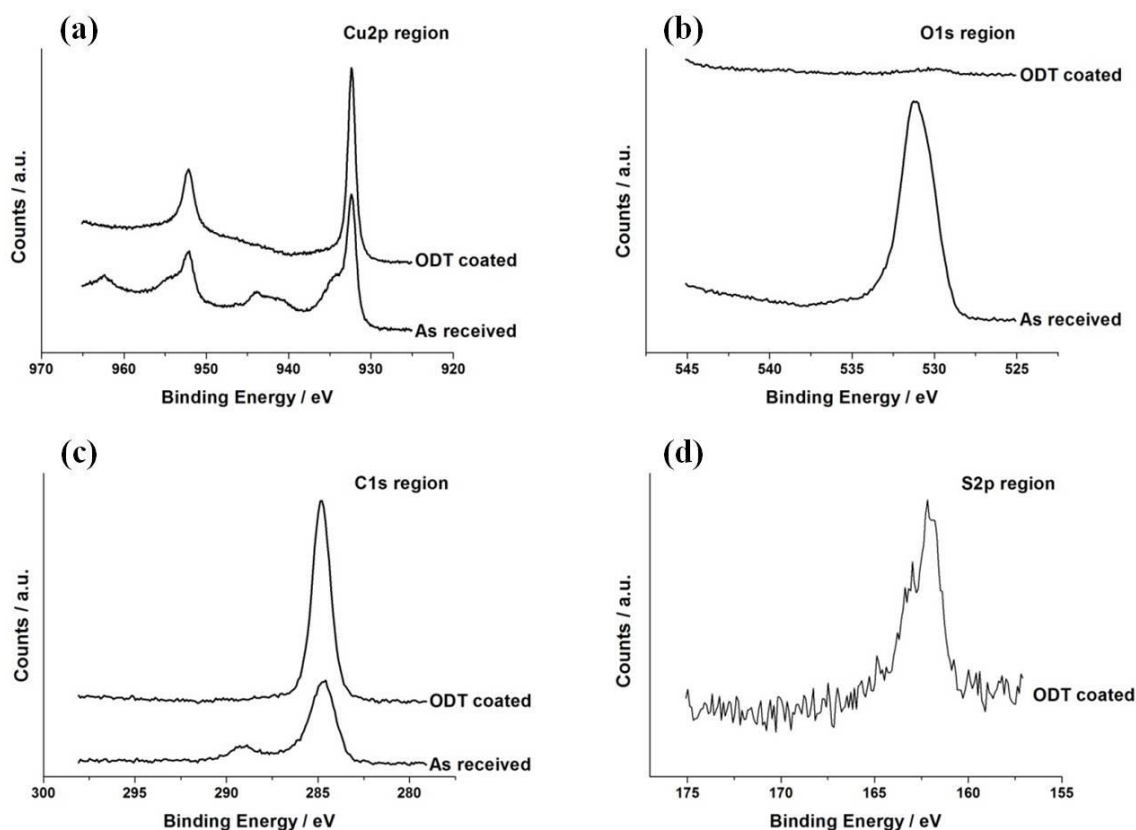


Figure 6.8: High resolution XPS scans for ODT coated and uncoated copper powders at: (a) Cu2p region; (b) O1s region; (c) C1s region and (d) S2p region

The XPS results (received from Mr Siyuan Qi [134]) for the copper powder before and after coating are shown in Figure 6.8: (a) the Cu2p peak (at 923eV) for ODT coated sample is pure and sharp, however for the untreated copper power, it is wide and some satellite peaks can be found near the main peak, which is believed a result of copper oxide; (b) an obvious O1s identification peak (at 531eV) appears in the raw copper but after treatment, this peak no longer exist; (c) for C1s peak, similar to Cu2p, a satellite peak for carbon oxide near the main peak can be observed on the raw copper figure; (d) sulphur is an identification element for the ODT and it can be detected on the coated sample. All

those results indicate that the copper oxide is removed by etching and the SAM is successfully coated on the copper particle, which can protect the copper core from oxidation effectively.

Figure 6.9 is the SEM image of the raw mixture at a copper content of 60%. The particles with a porous surface (marked by white circle) are copper and the rest with a smooth surface are HDPE powders. The copper particles are found well distributed among the HDPE particles.

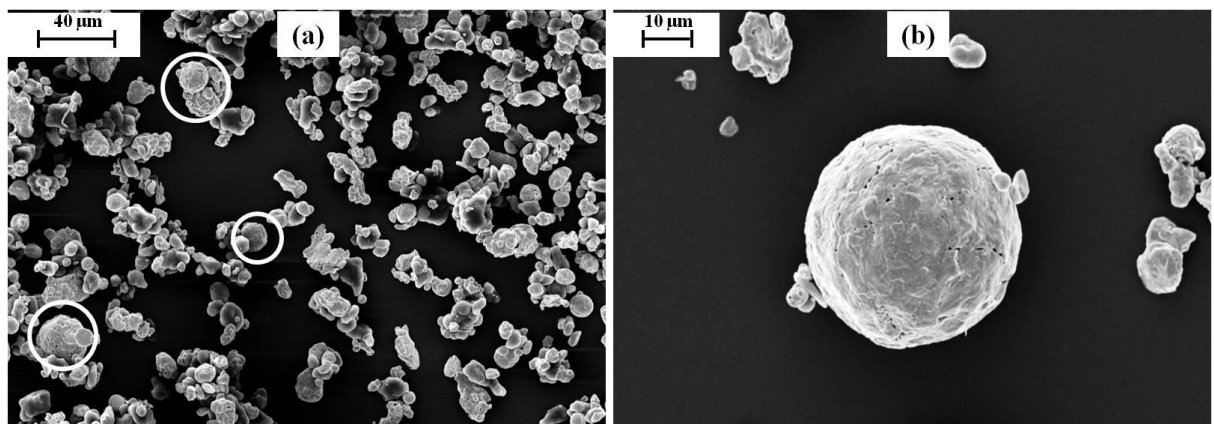


Figure 6.9: (a) copper/HDPE powder mixture (6/4) and (b) pure copper particle

6.3 Electrical resistivity analysis

The resistivity was calculated using Equation 5.1 described in Chapter 5. The sample cross-section area A was obtained directly from the SEM images, where ImageJ (National Institutes of Health, USA) is used. From Figure 6.10, the cross-section is selected as the white region and its area is calculated by the software. The raw data and final achieved resistivity value are listed in Appendix D.

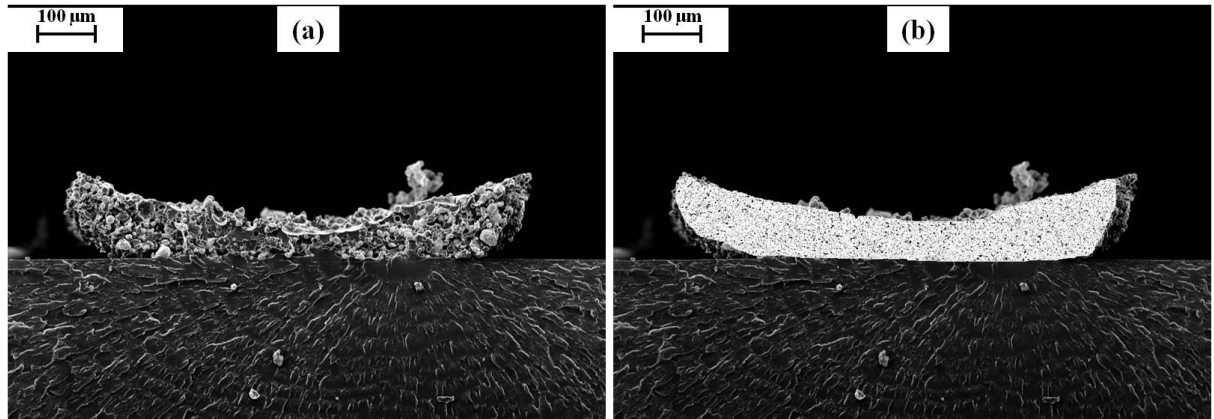


Figure 6.10: Cross-section area calculation using ImageJ for sample G-s-3/7-15-120 (a) raw image; (b) processed image

The influence of input energy (includes the scanning speed and input power) in the product properties are investigated in two conditions: a low copper content series G-s-3/7 and a high content series G-s-6/4. From Figure 6.11, both the two cases exhibit a decreasing of resistivity while scanning speed is reduced. However, after reaching its lowest limit, the resistivity starts increasing for some samples (e.g. G-s-6/4-20), which is believed to be a result of the discontinuous copper phase due to overheating. And when the speed is reduced to 40mm/s, the track lost its conductivity. Meanwhile, the resistivity variation with the input power has the similar trend and the minimal value for G-s-6/4 is found at about 20W, below or above this value the resistivity will keep increasing. Moreover, one should notice that although the G-s-6/4 series exhibit an obvious lower resistivity than the G-s-3/7 series, its lowest value ($1.94 \times 10^{-4} \Omega \text{cm}$, G-s-6/4-20-80) is still more than 100X of that of bulk copper ($1.67 \times 10^{-6} \Omega \text{cm}$).

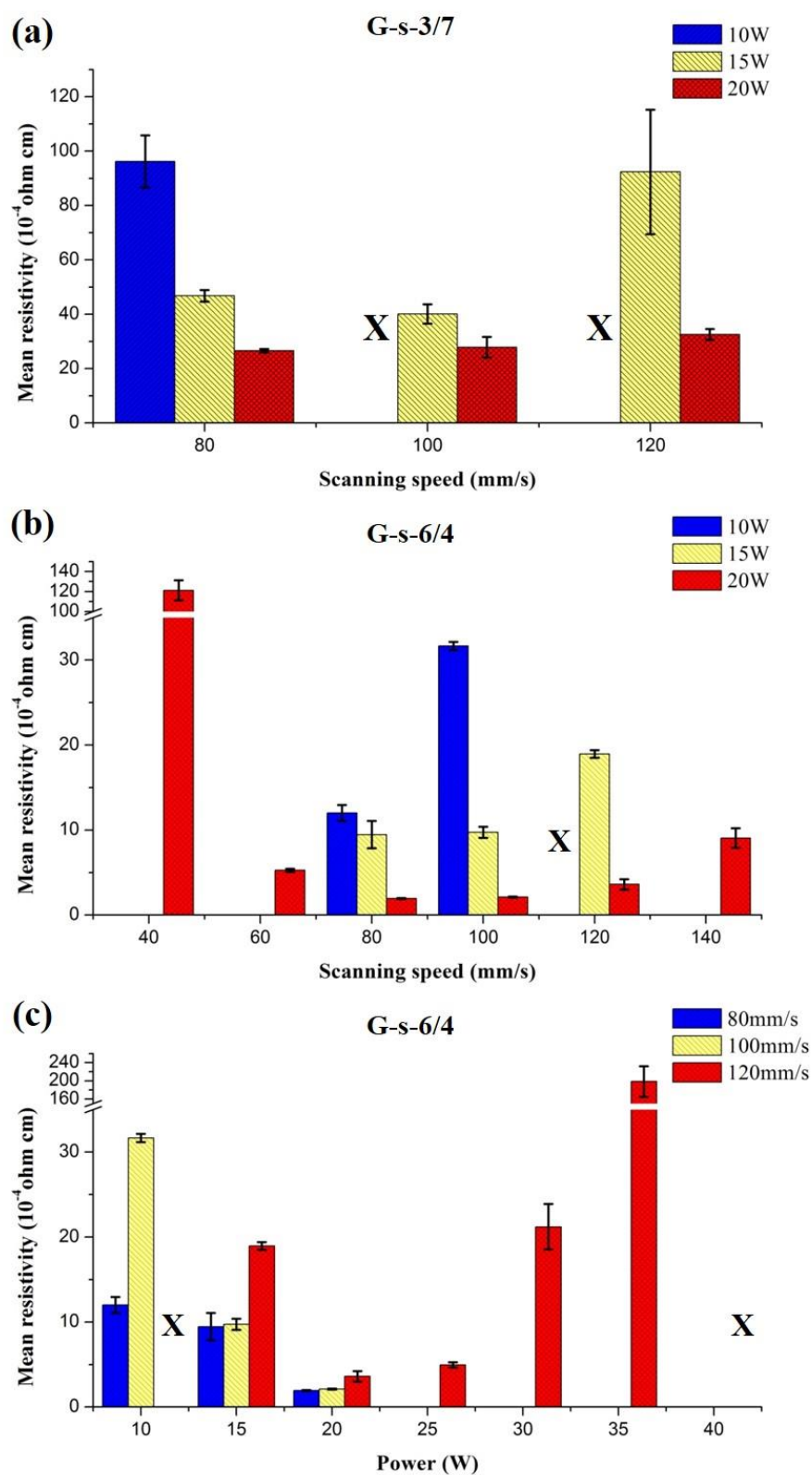


Figure 6.11: Resistivity variation for sample series: (a) G-s-3/7; (b) G-s-6/4 at different scanning speeds; (c) G-s-6/4 at different input powers. The letter 'X' means the sample resistivity value is quite high and can be thought as dielectric

Therefore, the scanning speed and input power should have the equivalent effect in the product resistivity and in some literatures [135, 136, 137] people use a combination of them – energy density (E_d as shown in Equation 6.1) as the energy variable.

$$E_d = \frac{Pl_s}{u_s a} \quad (6.1)$$

where P is input power, l_s is scanning length, u_s is velocity and a is beam width.

However, in this case if one compares the resistivity value between those samples which have the same E_d , e.g. G-s-6/4-20-80 and G-s-6/4-30-120, or G-s-6/4-20-60 and G-s-6/4-40-120; they exhibit an obvious difference in the value, which is believed as a result of conductive track damage when the input power is too high. From a thermodynamic view, if the heat loss rate (conduction, convection and radiation) in the laser processed material is high enough to balance the input energy, the power and scanning speed could be treated as equivalent conditions and energy density could be used directly. However, for material with low thermal conductivity like the mixture in this experiment; a high power – high speed case (G-s-6/4-30-120) will store the energy in the surface layer and further lead an overheating, and the sample resistivity is obviously higher than a low power – low speed case (G-s-6/4-20-80).

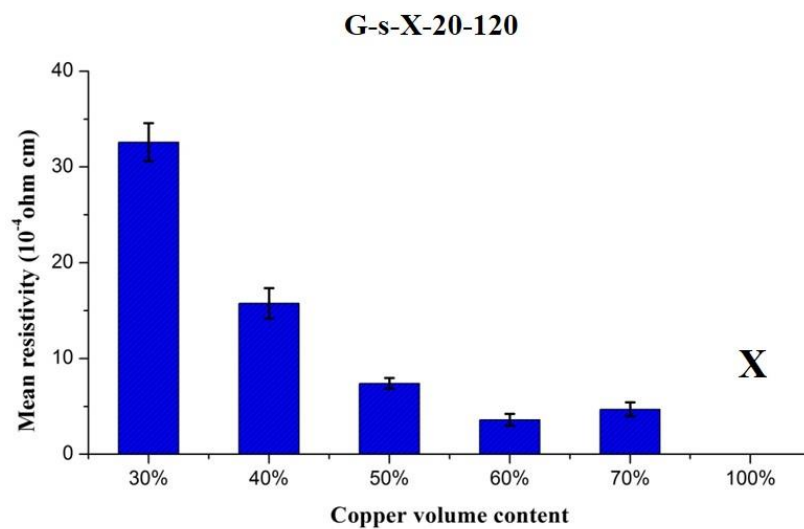


Figure 6.12: Resistivity variation for sample series G-s-X-20-120 at different copper volume content

Figure 6.12 shows the resistivity variation with copper volume content. This ‘volume content’ does not represent the ‘real copper content’ in the mixture, but the copper/HDPE volume ratio; since the mixture is not 100% dense product, the ‘real copper content’ is lower than the listed value. From the chart, a general decreasing trend appears when the volume content is increasing; however, after reaching 60%, the value no longer decreases. Moreover, it also indicates that a pure copper power does not exhibit any conductivity after processing.

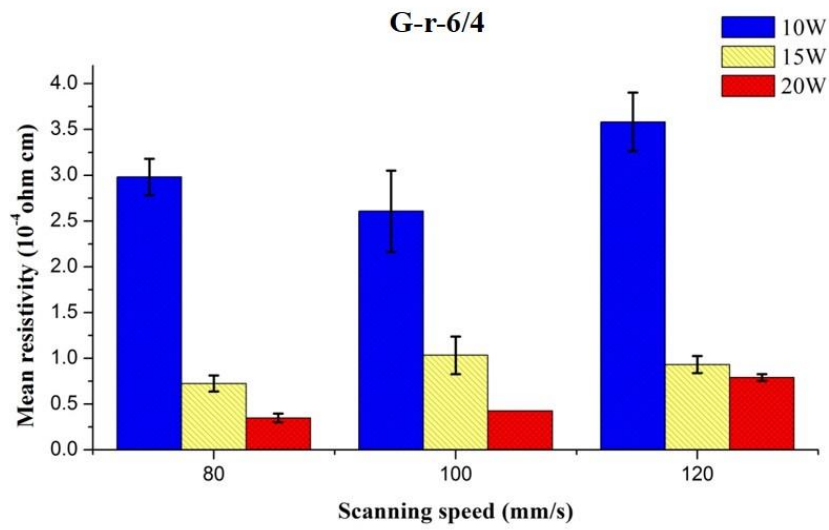


Figure 6.13: Resistivity variation for sample series: G-r-6/4 for raster scanning programme

Figure 6.13 represents the resistivity variation with scanning speed and input power for raster scanning programme, where the value is quite small (can reach to 20X of bulk copper) compared with the single track scanning programme at the same conditions. However, one cannot simply compare the two scanning programmes at the same conditions since the total input energy is different. According to the raster scanning programme (0.2mm width, 0.1mm scan spacing), the laser spot moving distance L can be calculated as:

$$L = 0.2 * \left(\frac{l_p}{0.1} + 1 \right) \approx 2l_p \quad (6.2)$$

where l_p is the length of the programme. And it further indicates that input energy for raster scanning programme is same to the single track programme at a half scanning

speed. Two sets can be found under this rule: G-s-6/4-20-40 ($121.28 \times 10^{-4} \Omega \text{cm}$) versus G-r-6/4-20-80 ($0.35 \times 10^{-4} \Omega \text{cm}$) and G-s-6/4-20-60 ($5.27 \times 10^{-4} \Omega \text{cm}$) versus G-r-6/4-20-120 ($0.79 \times 10^{-4} \Omega \text{cm}$). Obviously, the raster scanning samples still have lower resistivity, which reveals the advantage of this scanning programme.

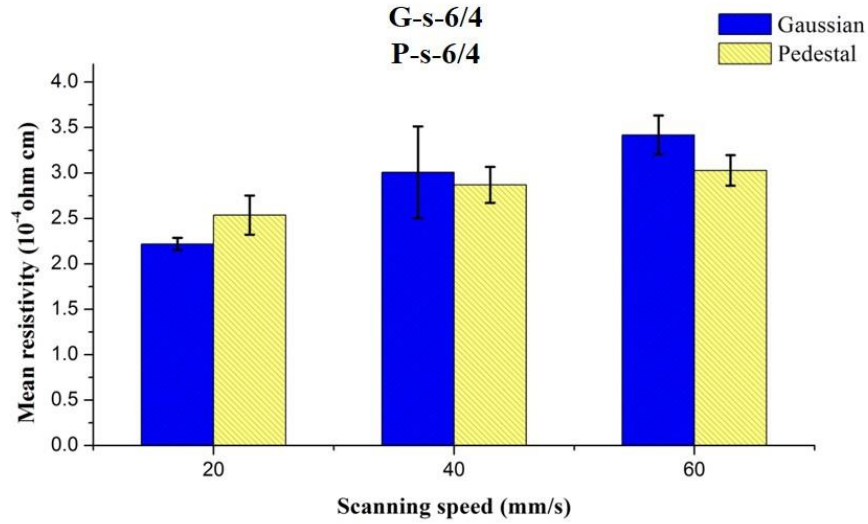


Figure 6.14: Resistivity variation for sample series: G-s-6/4 and P-s-6/4 at constant input power of 8W and different scanning speeds

Figure 6.14 represents the resistivity values of tracks melted at Gaussian beam and Pedestal beam. The maximum output power of the laser used in HOE glavo scanning system is 10W and after beam reconstruction, the real power is measured as 8W. This value is quite low, therefore it is kept as 8W for all tests and only the scanning speed is varied. Meanwhile, a series of Gaussian beam melted samples at the same condition are generated as a comparison. Obviously, for both of the two beams a low scanning speed will lead a low resistivity; however, it is interesting to notice that at 20mm/s, the Gaussian case has a lower resistivity; while at 60mm/s, its value is higher than that in Pedestal case. This indicates the resistivity variation with scanning speed for Pedestal case is smaller than Gaussian case.

6.4 Laser processing mechanism investigation

To explain the above phenomena exhibited in the resistivity measurement part and further reveal the laser processing mechanism, the morphology and microstructure of the sample are investigated in this section.

6.4.1 The investigation of G-s-3/7 series

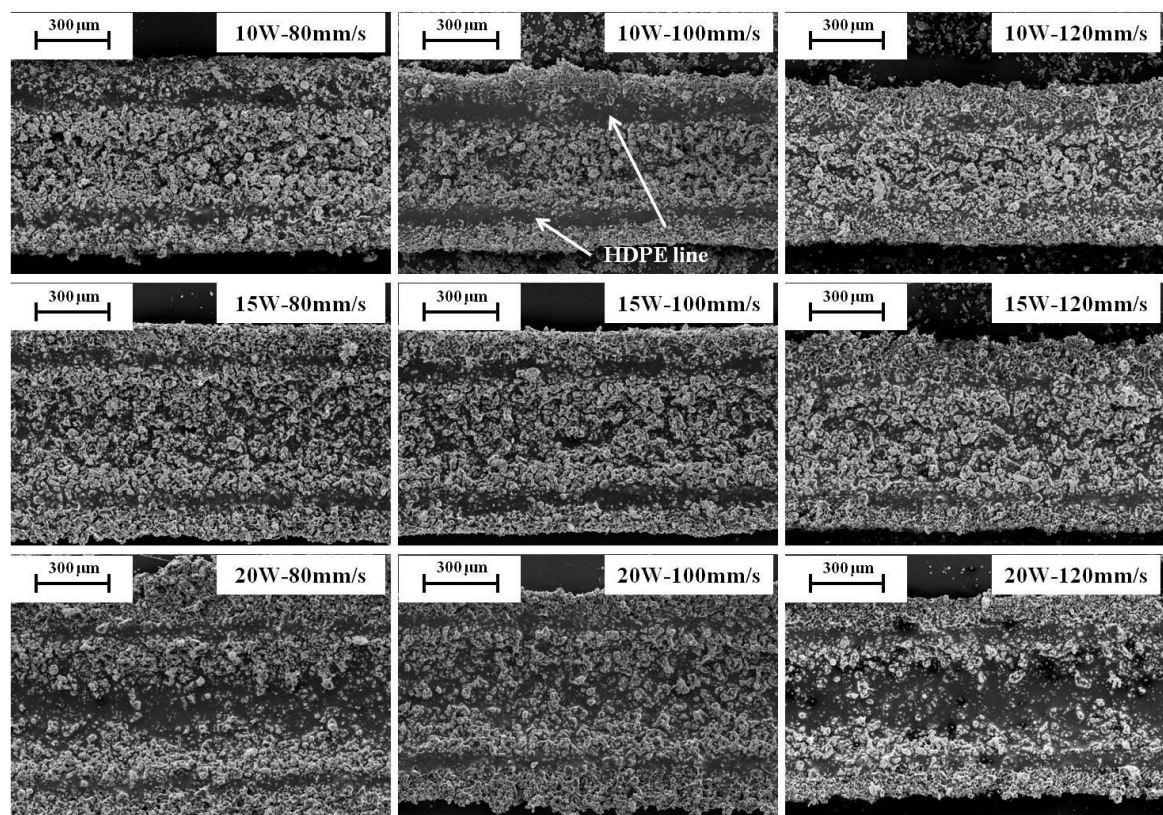


Figure 6.15: Surface morphology of sample series G-s-3/7 achieved by SEM

Figure 6.15 represents the surface morphology of the G-s-3/7 series from a top view. The widths of the melted tracks are measured in Table 6.2. Obviously, a increasing of track width can be found when the input power increases or scanning speed decreases. At low copper content the melting/evaporating of HDPE is the primary phenomenon during the laser processing; therefore a high input energy will melt more HDPE powder and further increase the track width. Meanwhile, on each sample, two bright ‘HDPE lines’ can be

observed near the edge and the distance between them is about 300 μm (similar to the laser spot size 300 μm), which can therefore be thought as the boundary of laser direct processing region.

Table 6.2: Measured widths of sample series G-s-3/7 (unit: mm)

| Power (W) Scanning speed (mm/s) | 10 | 15 | 20 |
|---------------------------------------|------|------|------|
| 80 | 0.78 | 0.88 | 1.06 |
| 100 | 0.68 | 0.81 | 0.87 |
| 120 | 0.64 | 0.74 | 0.79 |

6.4.1.1 Microstructure analysis

Figure 6.16 shows the microstructure of sample G-s-3/7-15-120, which is a good representation of the series G-s-3/7. From its top view; the track can be divided into two zones: the laser direct melting zone in the centre and the heat conduction affected zone in the edge. Considering the nature of Gaussian beam, where majority of the energy is distributed in the centre and normally the location with $1/e^2$ of maximum intensity is used as its spot radius (as shown in Figure 6.16); the HDPE in this region is much easier to be melted and even evaporated, and the residual copper particles will form pillar-like structures (white circles). As a result the thickness in the central region is obviously lower than that in the edge, as observed from the cross-section view. This phenomenon has also been reported in previous Section 3.7, where the laser melting of HDPE powder was investigated from both simulation and experiment parts.

However, in the heat conduction affected zone near the track edge, the energy is transferred from the central part by heat conduction and therefore the value is very low; the HDPE powder can only be melted in this region. Because the volume ratio of the

copper/HDPE is 3/7, where HDPE takes the major part; the copper particles can be thought as immersing into the HDPE matrix, which will generate two HDPE lines on the surface. Moreover, one may also notice that at the track boundary, only a partial melting of the HDPE particles can be observed; and the generated bridge-like structure will stick on the surface of copper particles.

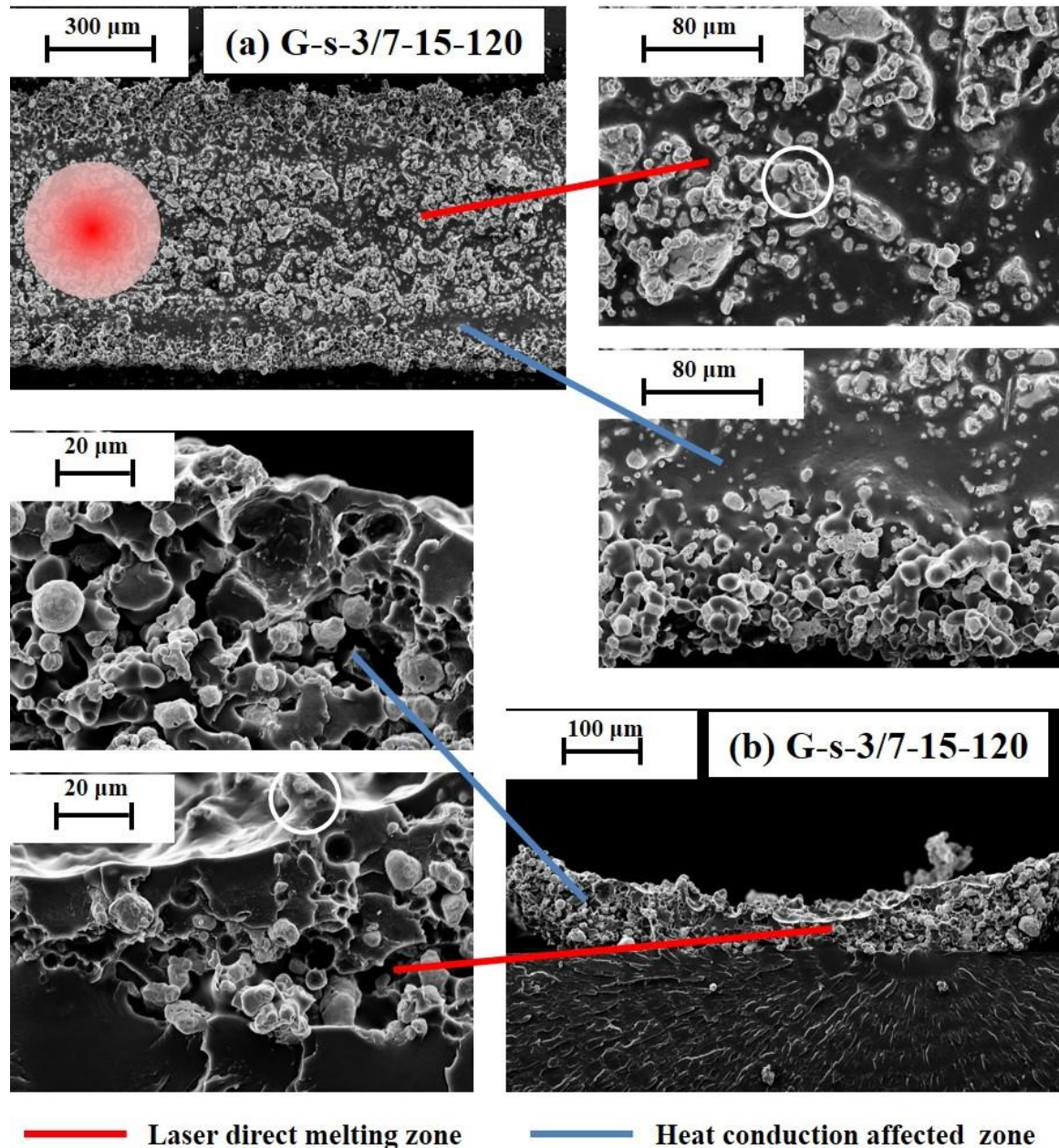


Figure 6.16: Microstructures of sample G-s-3/7-15-120 from: (a) top view; (b) cross-section view

The SEM images further indicate a porous structure is generated after laser processing,

which is believed to have negative influence in the mechanical property of the track. To reveal the formation of the pores, the same raster scanning programme (G-10-240-0.2) used in Chapter 4 for laser melting of pure HDPE is applied on the copper/HDPE (3/7) mixture; the comparison of the pure HDPE and mixture products are shown in Figure 6.17. Obviously, the mixture will generate a product with high porosity while the pure HDPE will generate a fully dense product. As discussed in Section 4.2.1, the dense product is a result of melt flow during the laser melting, which will fill the original spaces among powders. However in the mixture the flow will be blocked by the solid copper particles and only ‘polymer bridges’ are formed between copper particles.

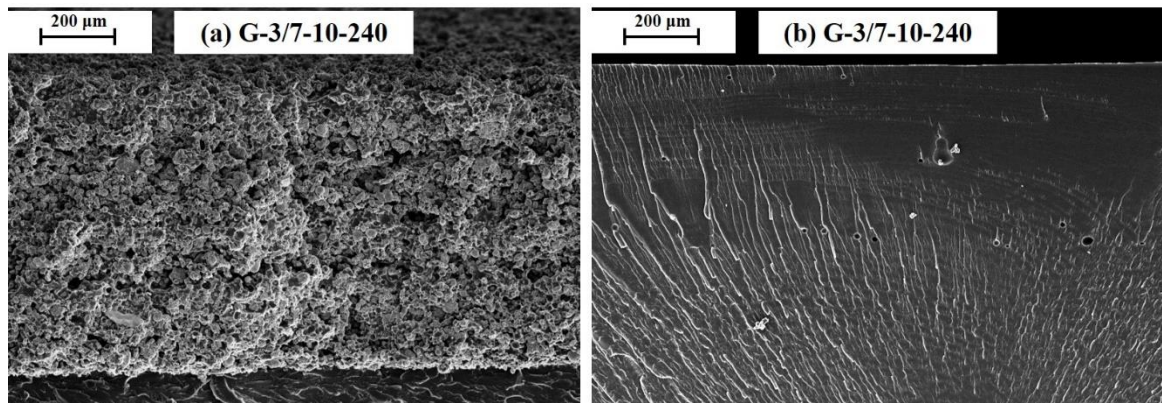


Figure 6.17: Comparison between a 5 layer copper/HDPE mixture (3/7) and pure HDPE sample at the same laser raster processing condition of Gaussian beam, 10W power, 240mm/s scanning speed, 0.2mm scan spacing

The sample microstructure of a high input power case (G-s-3/7-20-120) is shown in Figure 6.18. Obviously, compared with G-s-3/7/15/120, tiny amount of copper particles can be found in the laser direct melting zone and this phenomenon also appears in other high power samples (G-s-3/7-20-100 and G-s-3/7-20-80). This is a result of copper particle movement and can be explained from two aspects:

- The cross-section structure reveals a bowl-shape groove is formed at the central region, which is a result of HDPE evaporation. The force generated from volume expansion during phase transition can push the copper particles away from the centre

region;

- As discussed in Section 3.5, the Gaussian beam will lead a strong Marangoni flow in the melted material, this flow starts from the centre (high temperature) to the edge (low temperature) and the copper particles might flow with the HDPE melt during the laser processing.

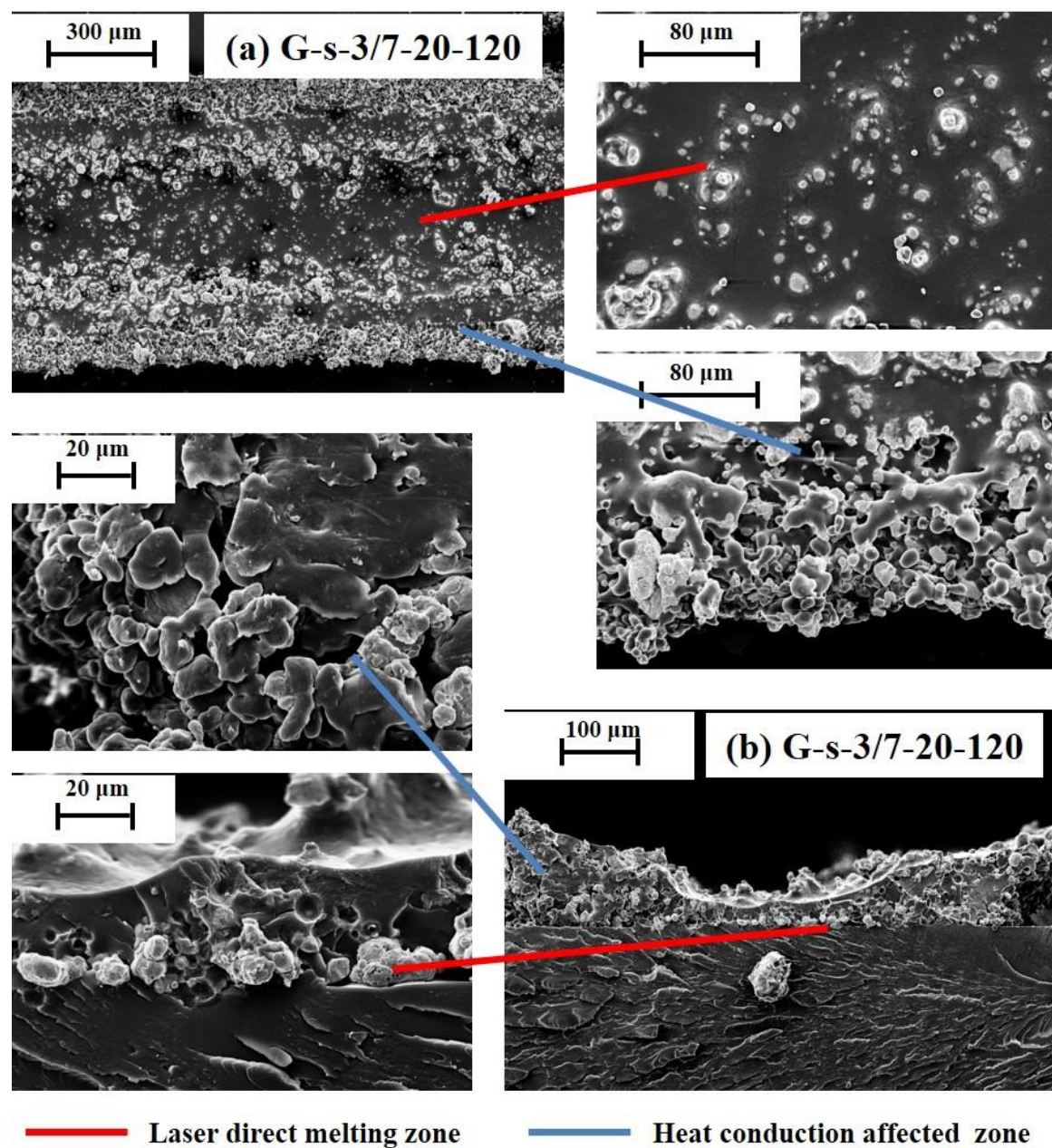


Figure 6.18: Microstructures of sample G-s-3/7-20-120 from: (a) top view; (b) cross-section view

6.4.1.2 The movement of copper particles in HDPE matrix

Figure 6.19 exhibits the melting situation of copper/HDPE (3/7) mixture monitored using hot-stage microscopy, where a constant heating/cooling rate of 10°C/min was applied. At 100°C the melting of HDPE particles occurs and the melted material tends to flow on the glass substrate. This phenomenon has been reported and discussed in the laser melting of pure HDPE in Section 4.2.1 and the driving force of flow is considered as surface tension. Here for the mixture case, the copper particles are found flowing with the HDPE melt. This further confirms the copper particle movement assumption described in the laser processing cases in Section 6.4.1.1. Moreover, during the cooling step in Figure 6.19, the crystalline was found on the surface of HDPE matrix and the copper particles are ‘frozen’ to where they are.

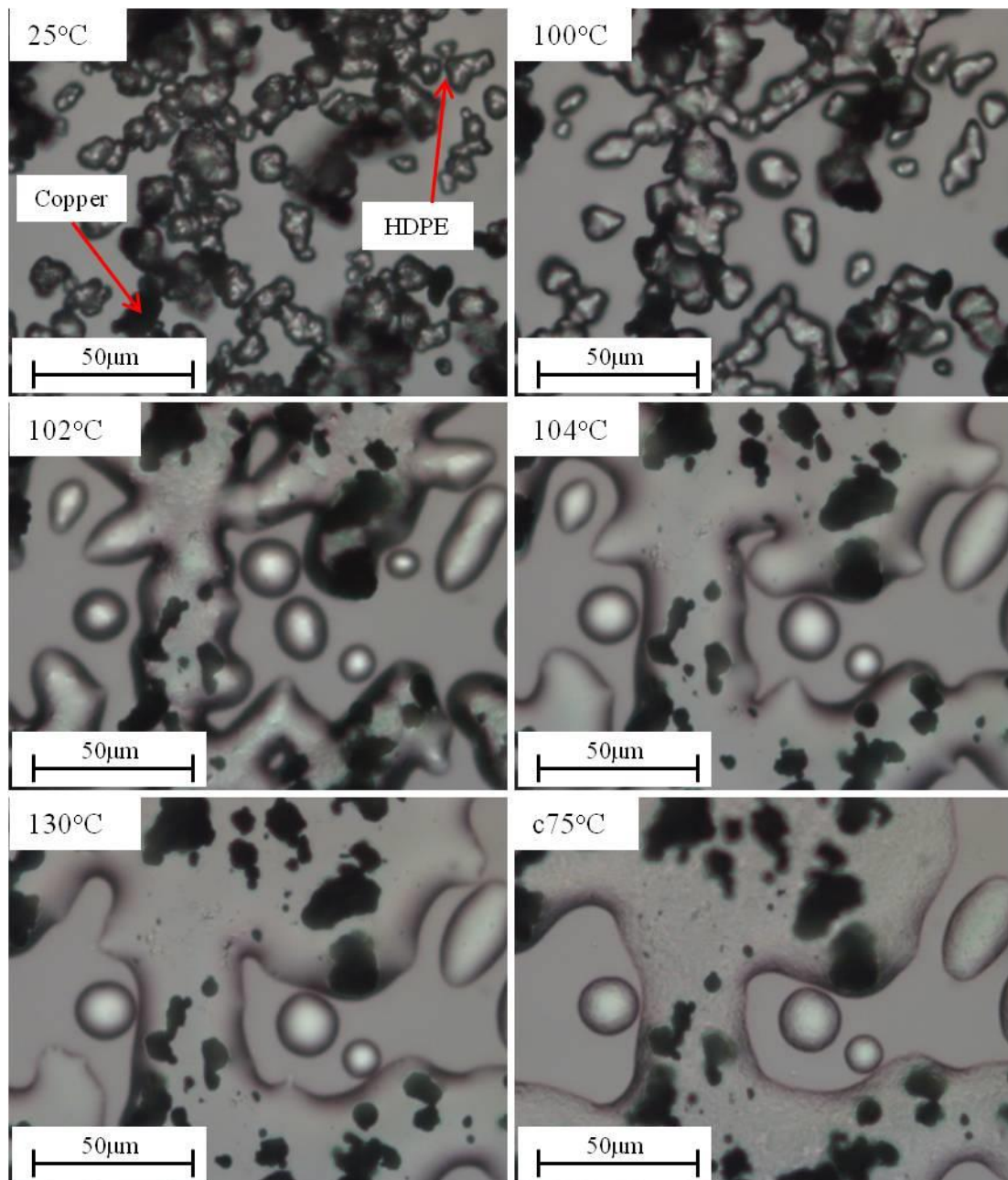


Figure 6.19: Copper/HDPE (3/7) mixture melting/cooling situation ('c' in the last figure represent 'cooling')

It seems the copper particles are immersed in the HDPE matrix and well-bonded with the surrounding polymers from Figure 6.19. However, at a high magnification of the SEM cross-section image of sample G-s-3/7-20-120 in Figure 6.20, it is interesting to find that between the copper particles and HDPE there are small gaps. This should be explained by the surface wetting mechanism and the adhesive force between two materials can be described using Young–Dupré equation:

$$W = \sigma_{LV} * (1 + \cos\theta_A) \quad (6.3)$$

where W is the work for adhesive, σ_{LV} is the interface tension and can be thought as constant in this case, θ_A is the contact angle. At a dispersive adhesive model, i.e. only Van der Waals force is considered; the contact angle provides an inverse measure of adhesive work. However, Laibinis et al [138] measured the contact angle between n-Alkanethiols monolayer coated on copper and non-polar solvent (hexadecane) and find out the values are quite small, i.e. the monolayer is oleophilic. They indicated it is because the n-Alkanethiols chains are all oriented and they expose the low energy methyl surface, which is also non-polar and can be well-wetted by the non-polar solvent. Moreover, for shorter n-Alkanethiols chains where part of the copper will be exposed to the solvent directly, θ is even smaller since copper has a high surface energy, which makes it easy to be wetted by the non-polar solvent.

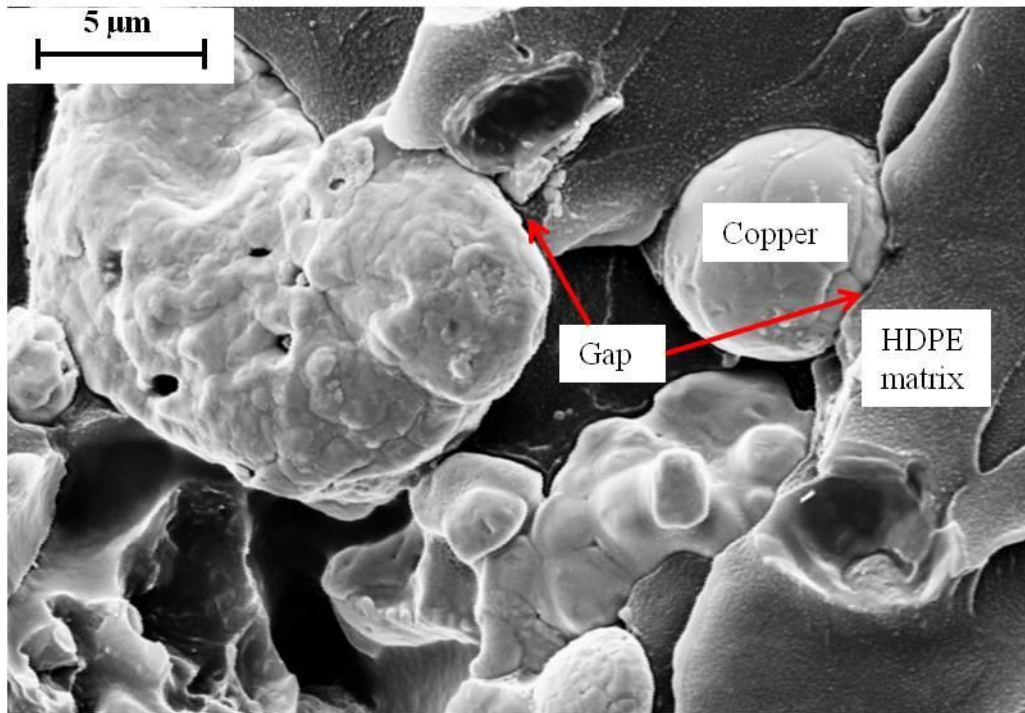


Figure 6.20: High magnification microstructures of sample G-s-3/7-20-120 from cross-section view

Back to the copper/HDPE mixture case, since the HDPE melt can also be considered as non-polar solvent, the contact angle between it and the copper particles (with ODT monolayer) is small. Moreover, the thermal test on the prepared copper particles had

confirmed the ODT will decompose at about 110°C [134]; this value is lower than the melting point of HDPE and it will expose the pure copper surface to the HDPE melt directly. No matter what type of surface it is, the wettability (low θ) between the two materials is high; however since the interaction between the conductor and the HDPE chains is mainly Van der Waals force, which is weak and unstable; the value of interface tension σ_{LV} is small. As a result, during the cooling stage after processing, the crystallisation (Figure 6.19) of HDPE matrix occurs, where polymer chains will orient and fold and leading volume shrinkage. This will break the bonds between copper and HDPE and generate a gap between them.

According to the investigations carried out on the G-s-3/7 series, the conductivity of the tracks is believed as a result of copper particle contact, which is similar to the silver paste as discussed in Chapter 5. This might lead to discontinuities in the conductive phase at some locations and therefore the measured resistivity for the G-s-3/7 series in Section 6.3 is usually quite high (about 1000X of bulk copper). The generated porous structure after laser melting will make the track brittle and as a result the conductive pathway is unstable.

6.4.2 The investigation of G-s-6/4 series

The surface morphology of G-s-6/4 series is shown in Figure 6.21. At low input power and high scanning speed, the sample exhibits a porous structure similar to the G-s-3/7 series. When the input energy is high enough, as marked in sample G-s-6/4-20-60, a ‘bright line’ which is comprised of dendrite structures can be observed in the laser direct melting zone. According to measurement, the width of the ‘dendrite line’ is similar to the laser spot diameter, which is about 300 μm .

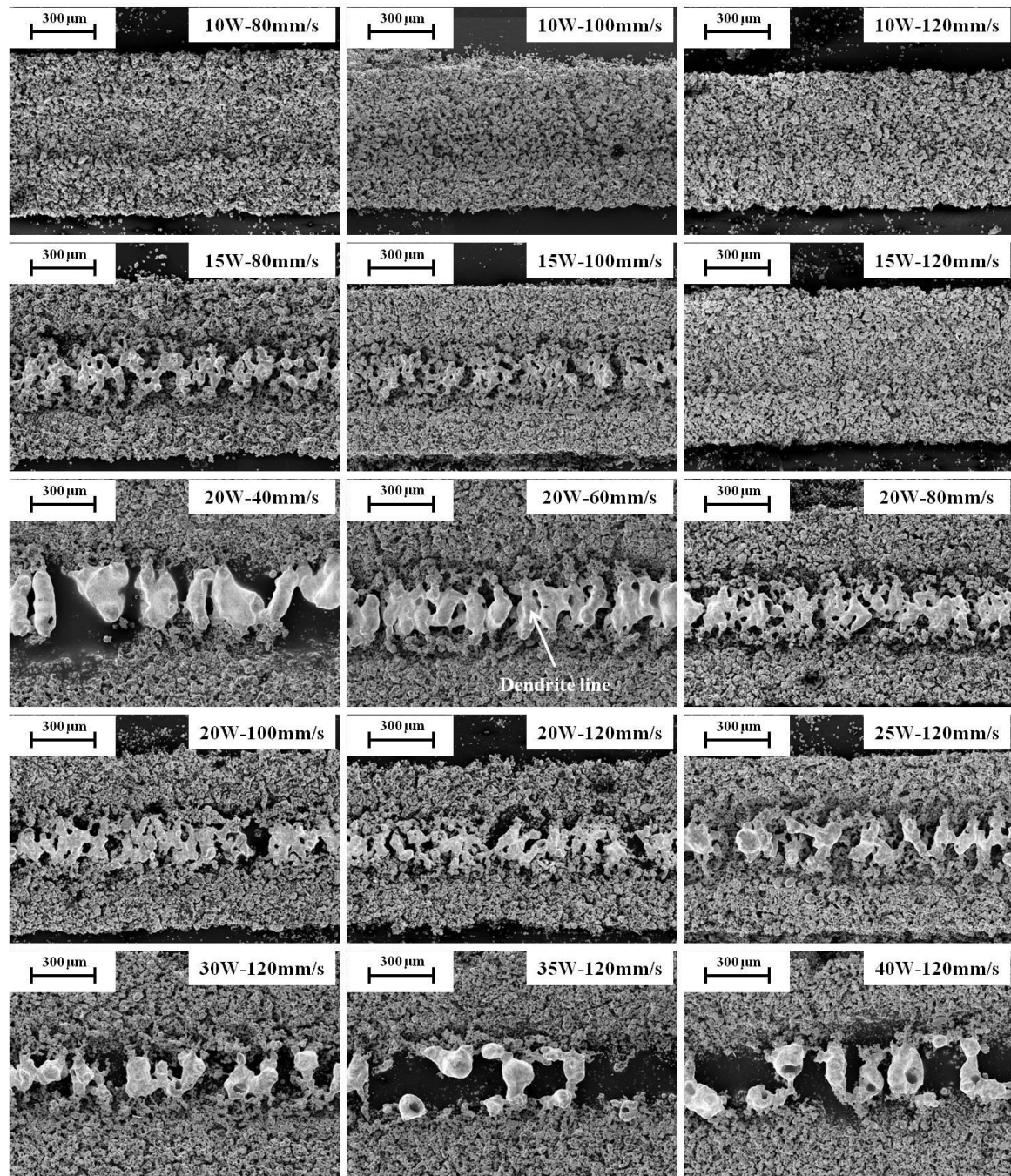


Figure 6.21: Surface morphology of sample series G-s-6/4 achieved by SEM

6.4.2.1 Microstructure analysis

The sample G-s-6/4-20-120 is selected as a representative for those samples with a dendrite line in centre and its microstructure is exhibited in Figure 6.22. Obviously, HDPE have been completely evaporated in the laser direct melting zone and the copper particles have been partially melted to continuous dendrite structures; however, in the

heat conduction affected zone, HDPE are only melted and become the ‘polymer bridge’ between copper particles. Meanwhile, from the cross-section view, it can be found that the central ‘dendrite line’ is separated from the rest part of the track and its bottom region is bonded to the substrate according to HDPE matrix.

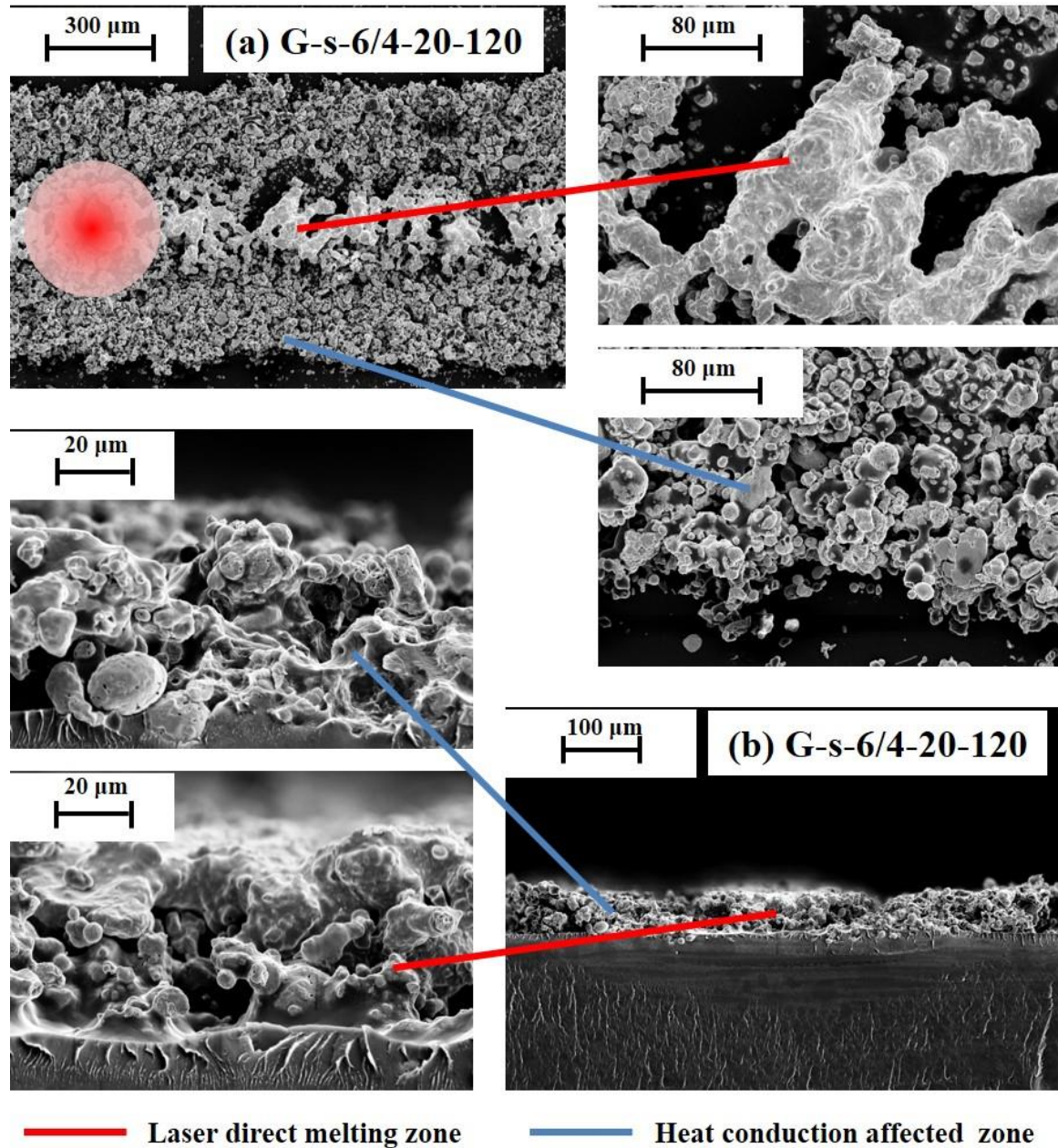


Figure 6.22: Microstructures of sample G-s-6/4-20-120 from: (a) top view; (b) cross-section view

To investigate the melting mechanism, the microstructures of laser direct melting zone and heat conduction affected zone at a high magnification are shown in Figure 6.23. A

large number of crystallites can be observed on the ‘dendrite line’, which is a result of copper particle melting. However, the size of the crystallites is about 2~5 μm and it is quite small compared with copper particle size (20 μm); therefore the melting does not occur on the copper particle scale. From the structure of heat conduction affected zone, where the input energy is insufficient to lead copper melting; it is interesting to find that the copper particle surface consists of many cracks, and they split the particle into some tiny fragments with a size of 2 μm approximately. Those cracks can also be observed on the original copper particle surface as shown in Figure 6.9. Meanwhile, back to the structure of laser direct melting zone, some cores are found at the centre of the crystallites (marked by red circle in Figure 6.23) and they are the residues of the partial melted fragments.

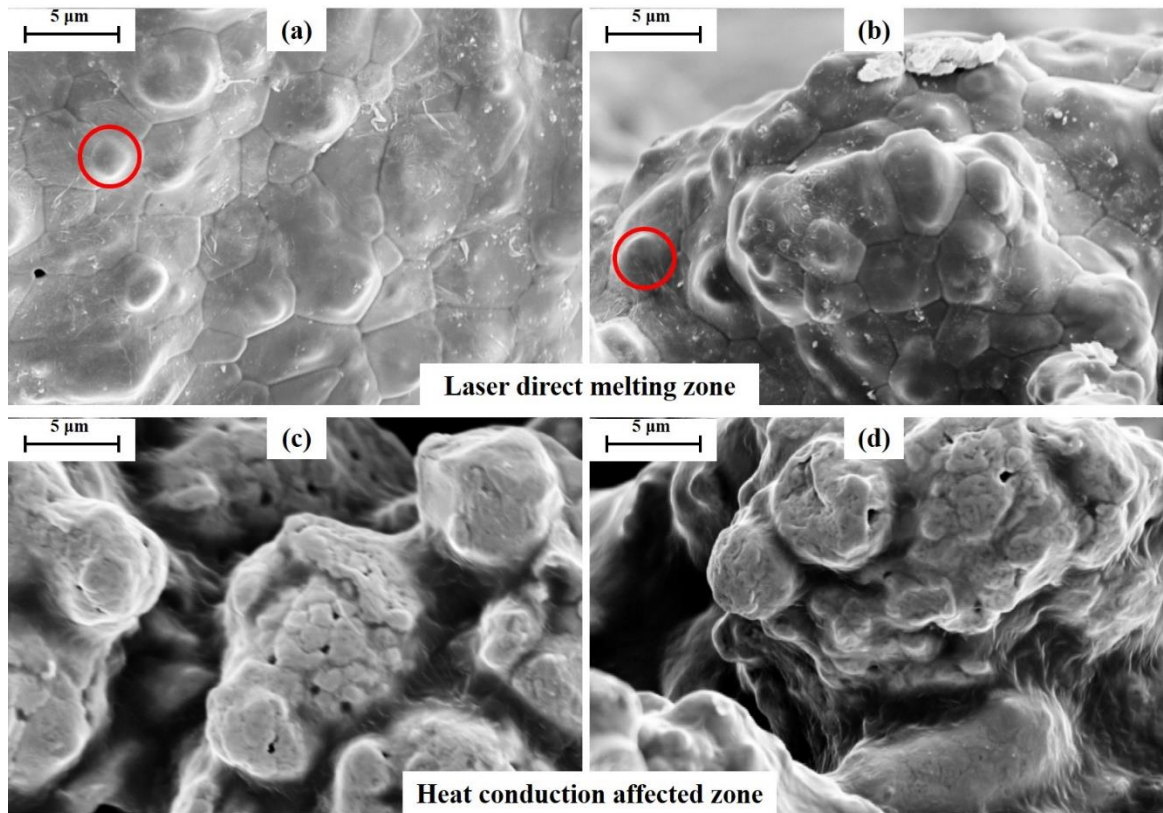


Figure 6.23: High magnification microstructures of sample G-s-6/4-20-120: (a) laser direct melting zone (top view); (b) laser direct melting zone (cross-section view); (c) heat conduction affected zone (top view); (d) heat conduction affected zone (cross-section view)

According to the microstructure analysis, the copper melting process can be illustrated in Figure 6.24. The HDPE particles will be evaporated rapidly in the laser direct melting zone and the residual copper particles will agglomerate. Those particles have been broken into small fragments by cracks and therefore the specific surface area is increased, which indicates they are more likely to be partially melted. During laser processing, melting will firstly occurs on the boundary between different fragments from the same particle or adjacent particles; and a melted surface layer will be formed on the surface of fragments. If the fragment is small enough, a consolidated crystalline phase is generated. Meanwhile, the original cracks and copper particles boundaries become the new grain boundaries. However since some fragments are too large to be fully melted, their residual cores can therefore be observed in the product.

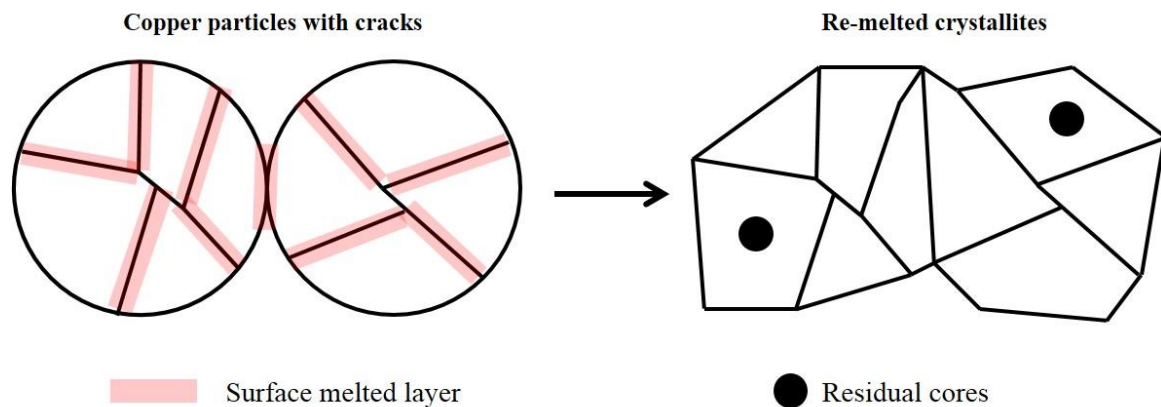


Figure 6.24: Schematic representation of the melting mechanism for the copper particles with cracks

According to the measured resistivity in Section 6.3, the G-s-6/4 series exhibits an obvious lower resistivity compared with the G-s-3/7 series, which can be explained by their melting nature. The copper particles are melted and form a continuous conductive pathway, where the electrons can transfer freely inside of it. The resistance of this continuous phase is much lower than that in the ‘particle contact’ model in G-s-3/7 series, where the conductive pathway is formed by direct or indirect contact between different copper particles, as introduced in Section 6.4.1.

However, if the G-s-6/4 track is processed at a high input energy (e.g. G-s-6/4-40-120), the surface morphology in Figure 6.21 reveals the track has been damaged and the conductive pathway is not continuous. This explains the obviously large resistivity values measured at these conditions in Figure 6.11. As analysed in Section 6.4.1, during the Gaussian beam processing, a high input energy will generate strong Marangoni force on HDPE melt and make more HDPE evaporating, i.e. strong volume force; those forces will generate outward movement of the copper particles and therefore damage the central part of the track.

6.4.2.2 Temperature measurement during laser melting process

Figure 6.25 exhibits the temperature pattern of sample G-s-6/4-20-120 achieved by IR thermal camera, where the temperature values were calibrated using Appendix A.

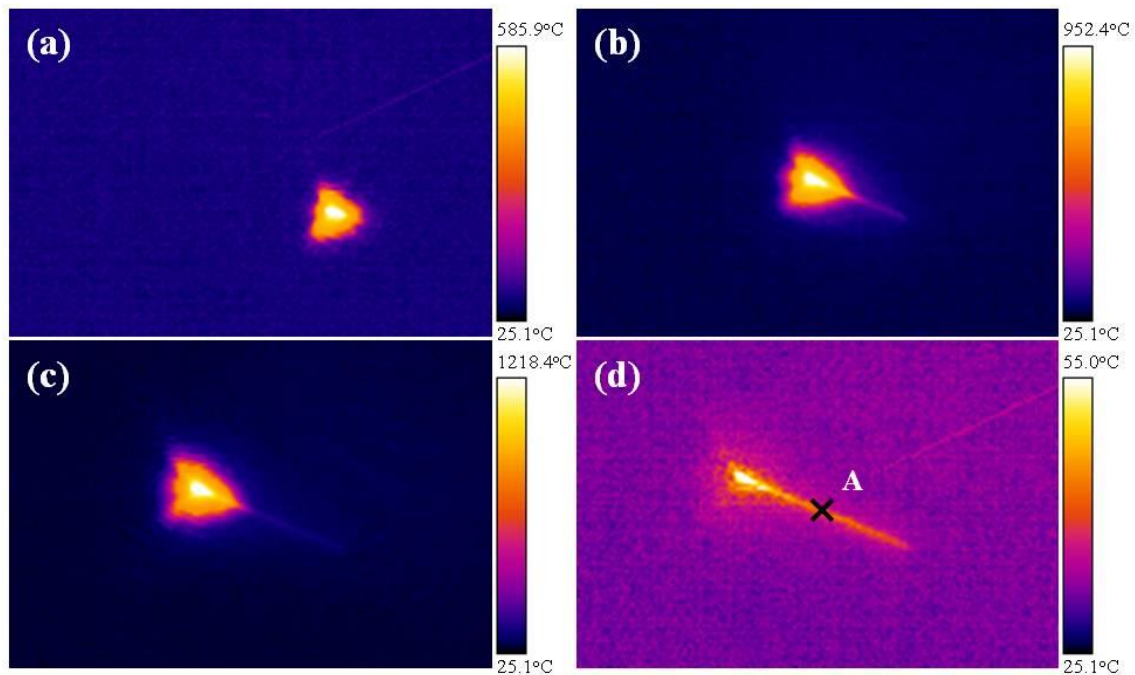


Figure 6.25: Temperature patterns of sample G-s-6/4-20-120 at (a) $t=0.02s$, (b) $t=0.14s$; (c) $t=0.22s$; (d) $t=0.32s$

An obvious linear scanning track can be found in Figure 6.25. During the laser melting

process, the temperature variation of point A is recorded and then plotted in Figure 6.26. Obviously, in a very short period (0.15s), the temperature is increased to about 1300°C and then drops back to room temperature again. The peak value is about 1300°C, which is higher than the melting temperature of copper (about 1080 °C). However, since the time is too short to fully melt the copper, only partial melting occurs and a continuous copper phase will be generated, as described in Section 6.4.2.1. In addition, from the sample cross-section microstructure at the same processing conditions in Figure 6.22.b, one can find that the HDPE substrate (with a melting temperature about 400K) underneath is undamaged when the copper particle is partially melted. This is believed as an important advantage of the laser processing system. In this case, a large amount of energy will be applied on the copper/HDPE mixture layer in a short period; since the metal phase is discontinuous, the thermal conductivity in the mixture is low and majority of the energy will flow to the surrounding environment via surface convection and radiation. The downward energy into the HDPE substrate can only melt the surface and form an adhesion region between the melted copper track and substrate.

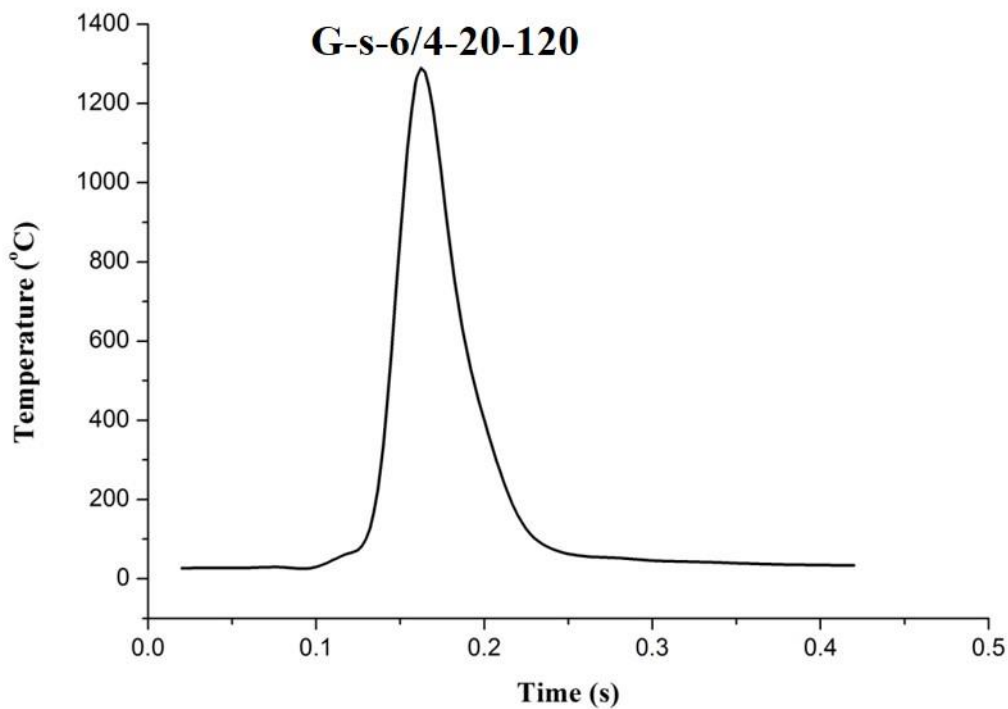


Figure 6.26: Temperature variation with time for track middle points of sample G-s-6/4-20-120

6.4.3 The investigation of G-s series with different copper/HDPE ratios

Figure 6.27 details a series of sample surface morphology at the same laser processing condition (G-s-X/Y-20-120) but with different copper/HDPE ratios. Obviously, at a low copper content, the morphology of the product is mainly affected by the flow and evaporation of HDPE; where a groove is formed at the centre of the track and the copper particles are pushed to the edge. As copper content increasing, the driving force for the copper particles movement is reduced; as a result, a porous sample is generated where the HDPE melts and forms bridge-like structures between copper particles. However, when the copper/HDPE ratio exceeds 5/5, a partially melted copper track can be observed in the laser direct melting zone, which consists of large amount of ‘dendrite’ structures.

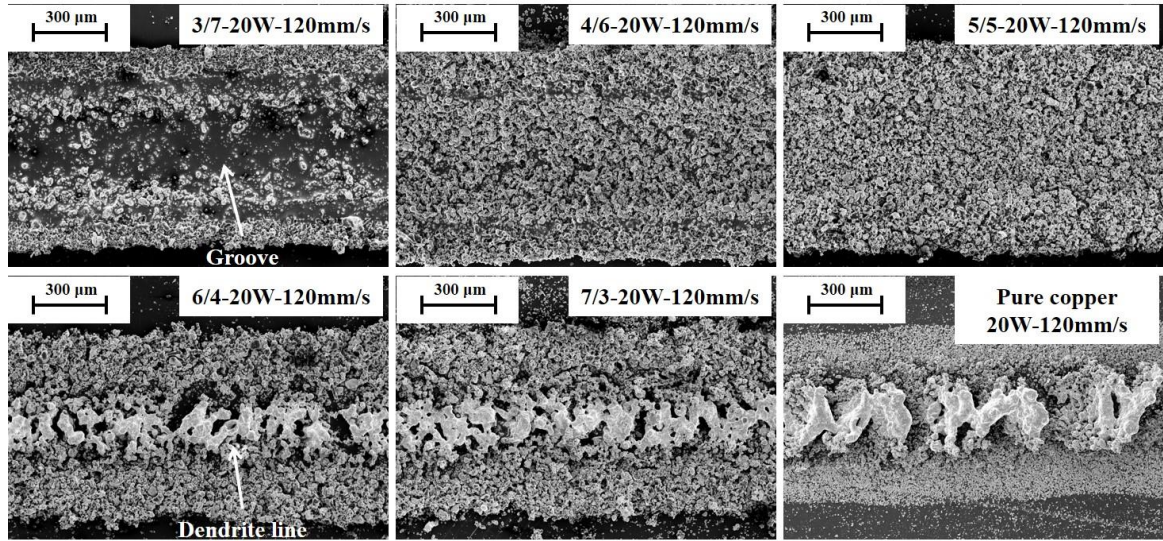


Figure 6.27: Surface morphology of sample series G-s-X/Y-20-120 achieved by SEM

If assume the total input energy during processing is Q , there is:

$$Q = Q_{HDPE} + Q_{Cu} + Q_r \quad (6.4)$$

where Q_{HDPE} , Q_{Cu} and Q_r represent the energy absorbed by HDPE, energy absorbed by copper and energy loss due to reflection, respectively. Generally, the energy absorption for polymers such as HDPE (about 80%) is much higher than that in metals such as copper (about 5%) under a CO₂ laser in this case. As a result if the copper/HDPE ratio is

low, most energy will be absorbed by the HDPE part in the mixture (Q_{HDPE}) and the reflected energy Q_r is small; Q_{HDPE} will further lead the melting and evaporating of HDPE powder and generate strong force for copper particle movement. At this condition, the copper particles cannot be closely packed and therefore melting will not occurs. At a high copper/HDPE ratio case, the energy absorbed by copper particles Q_{Cu} will increase. Moreover, due to the increased copper particle number, a denser copper phase is generated in the mixture, which makes those particles easier to be melted. However, since the energy absorption of copper is low, the overall reflected energy Q_r should be large. To prove it, the thermal image of sample G-s-pure copper-20-120 is achieved by IR camera and the temperature of the middle point of copper track (same location to point A in Figure 6.25.d) is recorded and plotted in Figure 6.28. Although at the scanning parameters, the maximum temperature of the pure copper case ($\sim 850^{\circ}\text{C}$) is obviously lower than that in the G-s-6/4-20-120 case ($\sim 1300^{\circ}\text{C}$) in Figure 6.26; since in the mixture case, energy can be absorbed by HDPE but in the pure copper case most energy will be reflected.

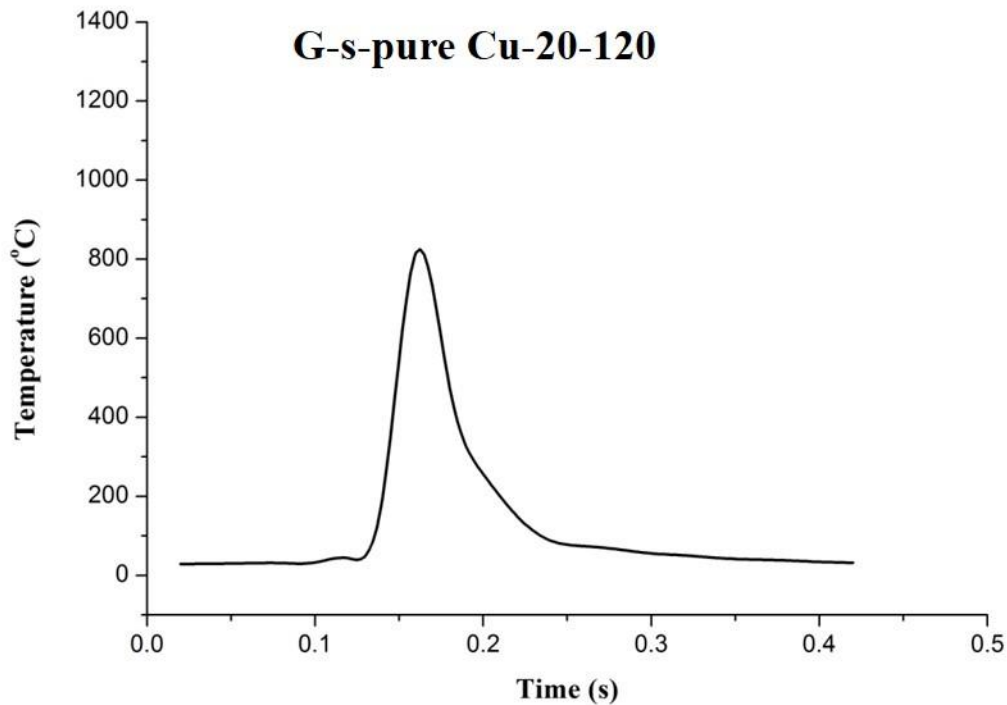


Figure 6.28: Temperature variation with time for track middle points of sample G-s-pure copper-20-120

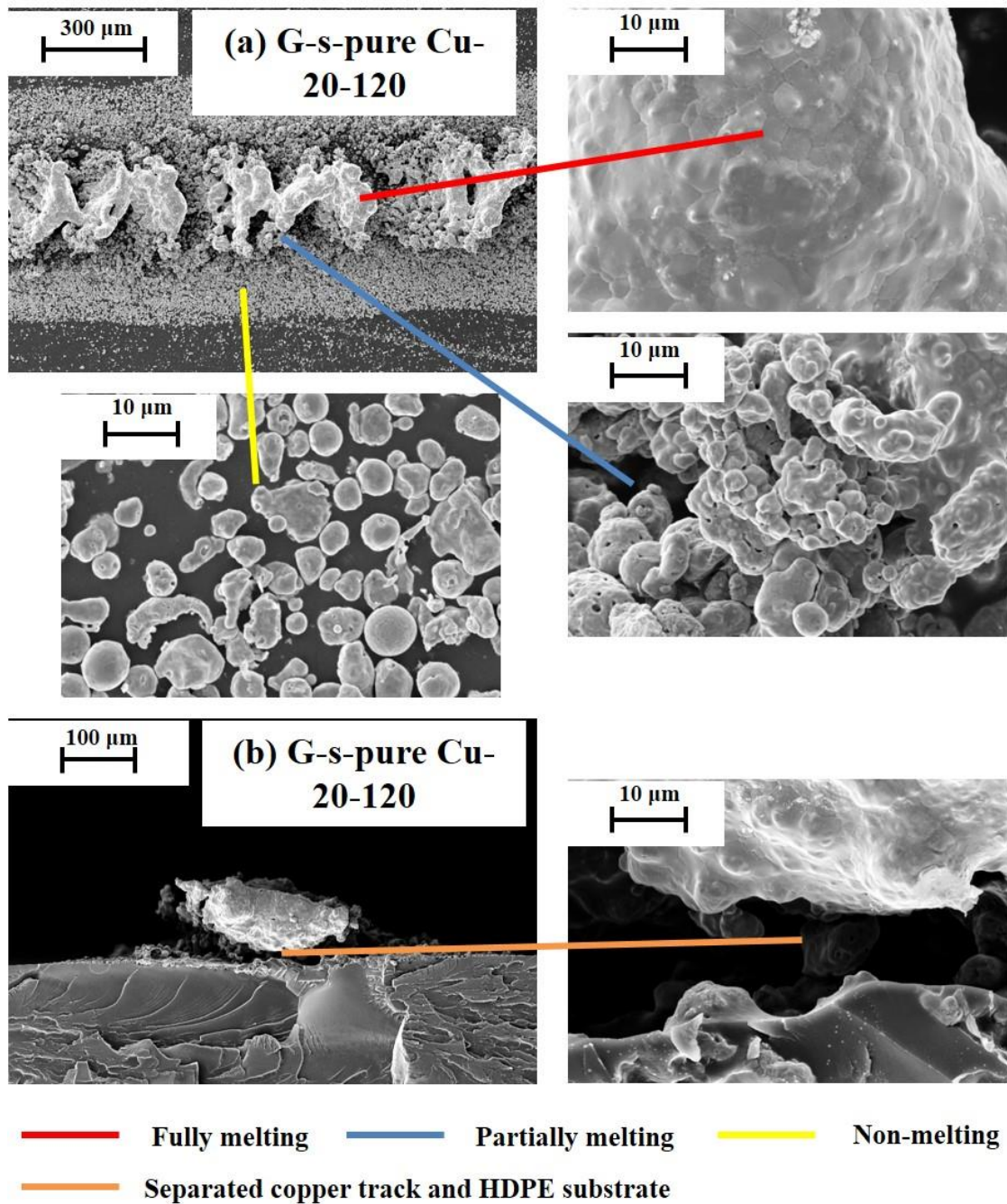


Figure 6.29: Microstructures of sample G-s-pure copper-20-120 from: (a) top view; (b) cross-section view

Although the processing temperature is low, it is interesting to notice from Figure 6.20 the sample G-s-pure copper-20-120 can still be melted. However, the melted track is thought as dielectric according to the resistivity measurement in Section 6.4.3. From the microstructure of G-s-pure copper-20-120 in Figure 6.29, one may notice that from the edge to the centre of the track, the morphology of copper particles changed from

non-melting to partially melting, then to fully melting. However, obvious gaps are found between melted copper phases and the conductive track is therefore discontinuous. The cross-section surface further indicates that part of the melted track is separated from the HDPE substrate. As explained in Section 6.4.1.2, the primary interaction between copper and HDPE matrix is Van der Waals force, which is weak and easily broken down when the shrinkage of HDPE occurs during cooling stage. Therefore during pure copper melting, the adhesion between the melted copper ‘dendrite’ and HDPE substrate is poor and it is easy to achieve a discontinuous copper track at this condition. However, in the copper/HDPE mixture case part of the HDPE powder will be melted and become the supporting structure of the copper ‘dendrite’, which will provide a better adhesion between the copper phase and the substrate. According to above investigations, to achieve the lowest resistivity in the melted track, it is necessary to mix copper powders with HDPE powders and the best copper/HDPE volume ratio is found as 6/4.

6.4.4 The investigation of G-r-6/4 series

The morphology of sample series G-r-6/4 under raster scanning programme is shown in Figure 6.30 and one should notice that the magnification for Figure 6.30 is lower than previous track morphology images in Figure 6.15, 6.21 and 6.27. Moreover, the widths of the tracks are measured and listed in Table 6.3, where the widths for samples melted at same conditions by single track scanning are also included.

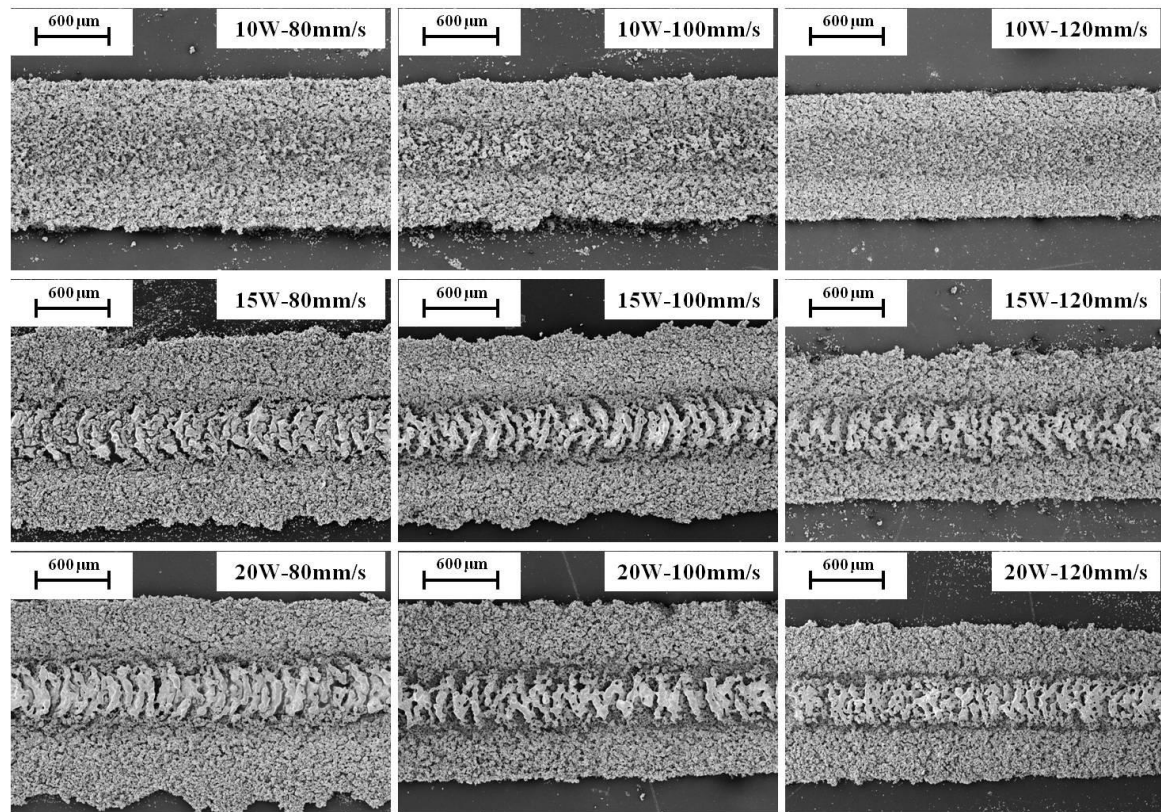


Figure 6.30: Surface morphology of sample series G-r-6/4 achieved by SEM

Table 6.3: Measured widths of sample series G-r-6/4 and G-s-6/4 (unit: mm)

| Power (W) Scanning speed (mm/s) | 10 | | 15 | | 20 | |
|---------------------------------------|---------|---------|---------|---------|---------|---------|
| | G-r-6/4 | G-s-6/4 | G-r-6/4 | G-s-6/4 | G-r-6/4 | G-s-6/4 |
| 80 | 1.20 | 0.76 | 1.51 | 0.79 | 1.61 | 0.93 |
| 100 | 1.16 | 0.65 | 1.41 | 0.77 | 1.42 | 0.82 |
| 120 | 1.01 | 0.62 | 1.20 | 0.73 | 1.26 | 0.75 |

Obviously, at the same condition, the width of the G-r-6/4 sample is larger than that of G-s-6/4. Figure 6.31 is a direct comparison between G-r-6/4-20-120 and G-s-6/4-20-120 at the same magnification; it further indicates the raster scanning programme will generate larger laser melting region. As described before the Gaussian beam has a non-uniform intensity distribution, where the majority of energy is in the centre. As a

result, the copper melting only occurs in the laser direct melting region. For a single track scanning programme, to achieve more melted copper phase, one can either increase the input power or decrease the scanning speed but it will damage the track and increase its resistivity, as explained in the Section 6.4.2. However, during raster scanning a larger region is exposed to the laser and the overall energy distribution on the track surface is more uniform due to the movement of the beam. It will generate larger melted region without damage the track, and the resistivity can therefore be reduced effectively. This raster scanning programme shows the advantages of controlling the input energy distribution during the track melting process. However, since the ‘beam reconstruction’ is achieved by the movement of laser spot, which is an indirect method and only generating approximate uniform energy distribution; the track morphology cannot be controlled accurately and its width is significantly increased.

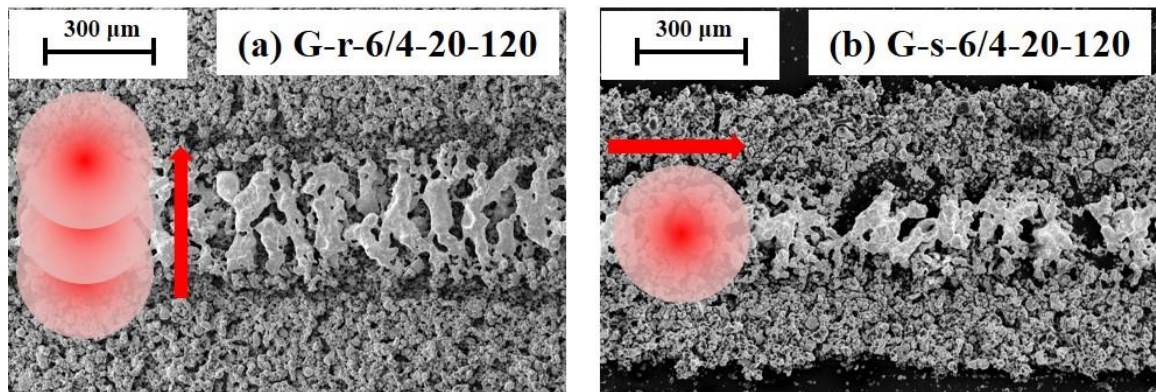


Figure 6.31: Comparison between sample (a) G-r-6/4-20-120 and (b) G-s-6/4-20-120, where the spot and red arrow represent the Gaussian beam and its scanning directly, respectively

6.4.5 The investigation of P-s-6/4 series

Figure 6.32 compares the surface morphology of sample series G-s-6/4 and P-s-6/4 at constant input power of 8W and different scanning speeds. The widths of the tracks are listed in Table 6.4.

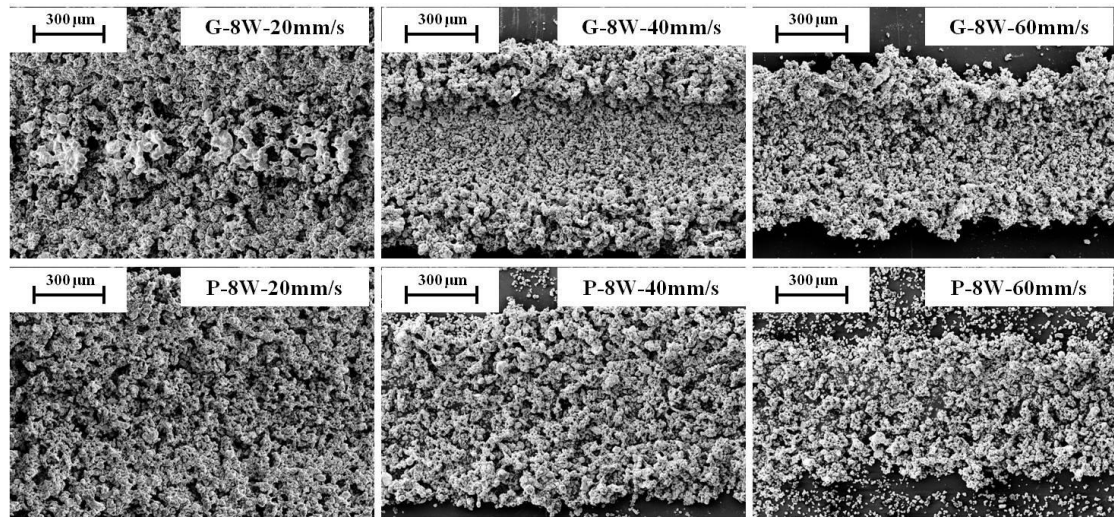


Figure 6.32: Surface morphology of sample series G-s-6/4 and P-s-6/4 at constant input power of 8W and different scanning speeds achieved by SEM

Table 6.4: Measured widths of sample series G-s-6/4 and P-s-6/4 (unit: mm)

| Scanning speed (mm/s) | 20 | 40 | 60 |
|-----------------------|------|------|------|
| Gaussian | 1.13 | 0.88 | 0.67 |
| Pedestal | 1.06 | 0.77 | 0.57 |

From Table 6.4, the widths of the Pedestal cases are smaller than those in Gaussian cases, although the designed Pedestal beam size (0.5mm) is larger than the Gaussian beam $1/e^2$ diameter (0.3mm). According to previous discussion in Section 6.4.1, the width of laser direct melting zone is determined by the beam size, while the heat conduction affected zone is a result of heat transfer in the powder mixture. Due to its energy distribution, the Pedestal beam has a sharp edge and therefore the heat conduction affected zone is smaller than the Gaussian beam. This phenomenon can also be observed directly from the beam prints in Figure 6.3, where the width of the outer ring around the beam print in Pedestal case is much smaller than Gaussian case.

Moreover, at high scanning speeds (60mm/s and 40mm/s), an obvious half-pipe groove can be observed in centre of the Gaussian beam melted tracks, but in Pedestal cases, the

track thickness is nearly uniform. As discussed in Section 6.4.1, a strong outward force is applied on copper particles during Gaussian beam scanning, which is believed as a result of Marangoni force during HDPE melt flow and volume force during HDPE evaporation. However, since Pedestal beam has a uniform energy distribution, the temperature gradient of the melted HDPE is quite low and the Marangoni effect is insignificant; moreover, the central part will not be over-heated and the volume force from HDPE evaporation is also small. This indicates the stability of the Pedestal beam during the scanning process and therefore the sample electrical resistivity for the Pedestal cases is lower than the Gaussian cases at these conditions (Figure 6.14).

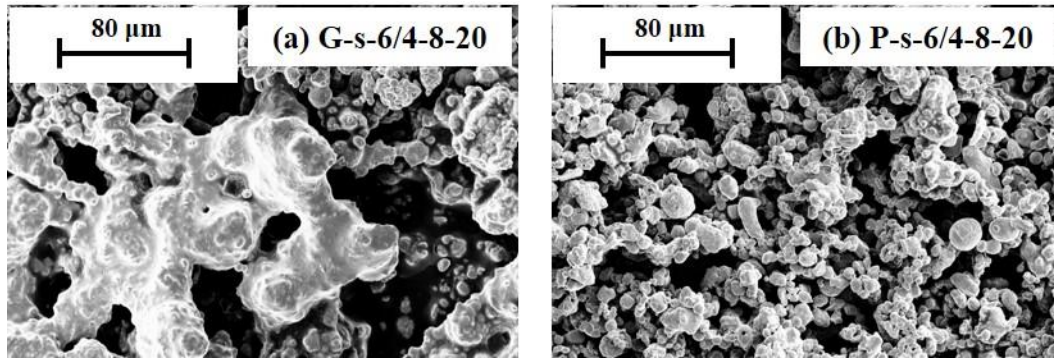


Figure 6.33: Microstructures of laser direct melting zone of sample (a) G-s-6/4-8-20 and (b) P-s-6/4-8-20

If the scanning speed is reduced to 20mm/s, the microstructure of laser direct melting zone for both the Gaussian and Pedestal cases are exhibited in Figure 6.33 with a high magnification. The melted copper ‘dendrite’ can only be observed in the Gaussian case; while in Pedestal case, copper are agglomerated and can be thought as a partially melted state. For Gaussian beam, its central region has higher energy intensity compared with uniform Pedestal beam; as a result for a low input power of 8W, only Gaussian beam can create the melted phase in the centre. This changes the conductive mechanism and therefore the Gaussian cases exhibits a lower resistivity than the Pedestal cases at 20mm/s in Figure 6.14.

The above comparison further indicates the controllability of the sample microstructure

by providing different laser beam irradiance distributions. However, due to the limitation of the current HOE galvo scanning system (low laser power and inaccuracy of real beam profile), the Pedestal beam does not exhibit a significant advantage when compared with Gaussian beam and it needs more investigations in future.

6.5 Additive manufacturing of multi-layer embedded circuit system

6.5.1 Circuit system design

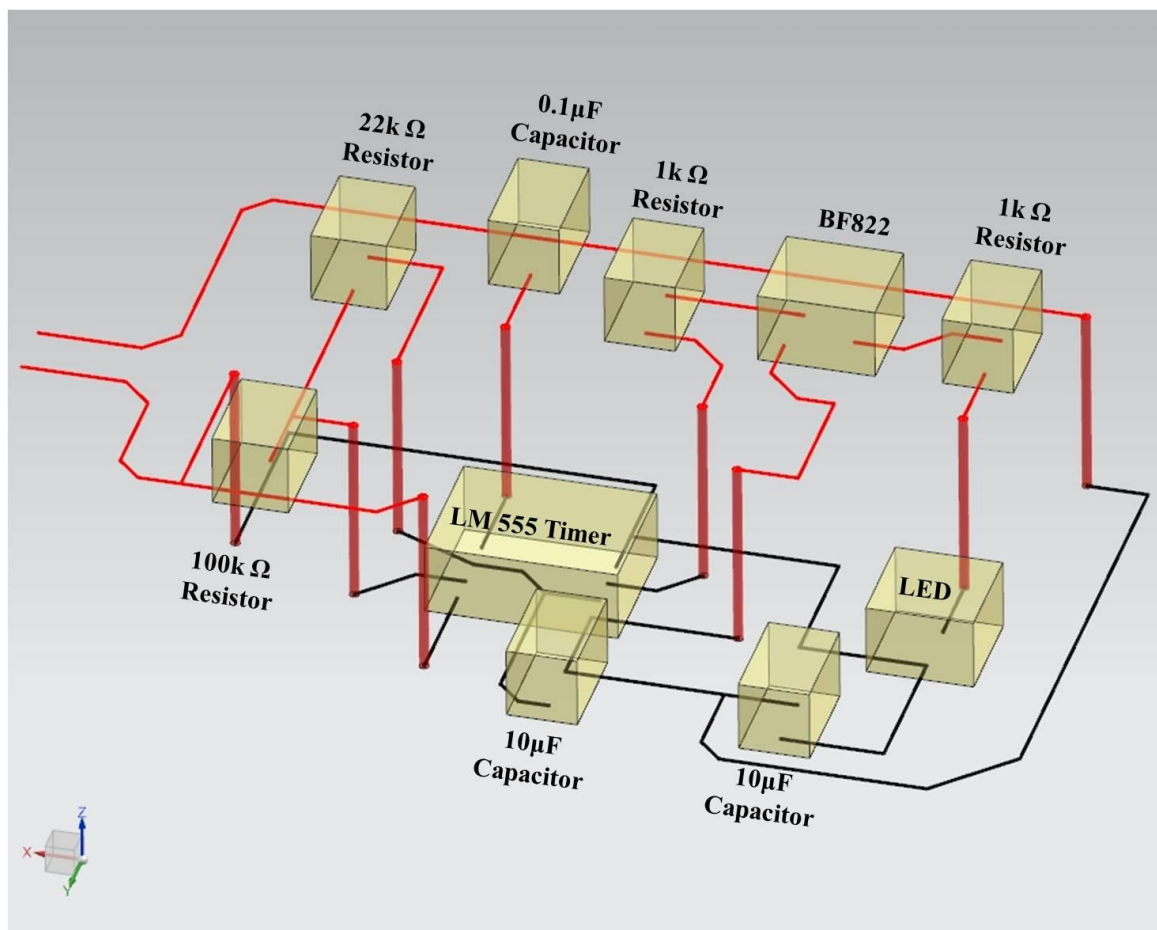


Figure 6.34: schematic representation of 3D embedded circuit system, where the black and red lines are the 1st and 2nd circuit layer; yellow blocks are electronic components

In this section, a double layer circuit board with embedded electronic components is manufactured and tested. The system was designed as a timer circuit and its schematic is

same to the 2D flexible circuit system in the silver paste curing part, as shown in Figure 5.17 in Section 5.5. However, to demonstrate a 3D circuit manufacturing process, the circuit system is divided into two different layers, with several vertical conductive pathways between them as the interconnections. The 3D circuit structure is shown in Figure 6.34.

6.5.2 Additive manufacturing of 3D embedded timer circuits and its performance test

This additive manufacturing process includes two different materials: the HDPE as substrate and copper/HDPE mixture as conductive track, therefore it is necessary to carefully design the laser scanning pattern and material deposition order. Since the Pedestal beam only has a maximum output power of 8W, which is too low to create a melted copper phase; in this section the Gaussian beam is selected. Figure 6.35 indicates the whole process from a transverse view:

- A HDPE substrate is first manufactured using the technology described in Chapter 4, the scanning condition used (including the following HDPE supporting layer) is Gaussian beam, 10W power, 240mm/s scanning speed, 0.2mm scan spacing; then fix the substrate in the self-designed steel backup plate (Figure 4.1 in Section 4.1.1) to prevent thermal warping during laser processing (step 1);
- Deposit the copper/HDPE powder mixture with a ratio of 6/4 using a blade, the layer thickness is set as 150 μ m (step 2);
- Selectively laser melting using programme G-r-6/4-20-120 to create the 1st circuit layer, then blow the unmelted copper/HDPE mixture away (step 3);
- Deposit HDPE powders and selectively laser melting to create the HDPE supporting layer (step 4);
- Design and manufacture multi-layers circuit system and the supporting HDPE structure, the interconnection consists of 5 layers 1mm*1mm melted copper square (step 5);

- Place electronic components in the designed slots and connect them with the copper tracks using silver paste, then move the whole system into a sealed glovebox (with Ar atmosphere) and heat for 0.5h at 80°C, then slowly cool it to room temperature, with the purpose of silver paste curing and thermal residual stress releasing (step 6);

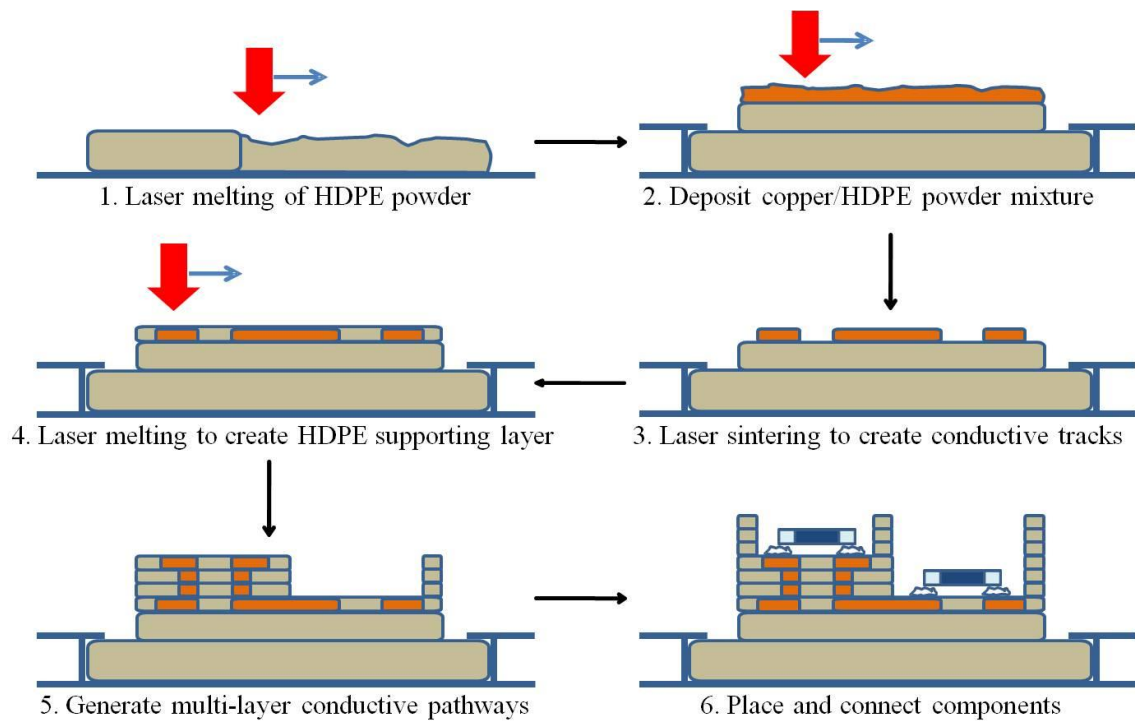


Figure 6.35: The additive manufacturing process of a 3D timer circuits system (transverse view)

Figure 6.36 shows the generated sample at each step, where Figure 6.36.g and h are the sample image with a light source from the bottom. It indicates clearly the existence of two individual circuit layers and the square interconnections between them. The track widths are small enough for them to separate from each other and the sizes of designed slots are suitable for those components.

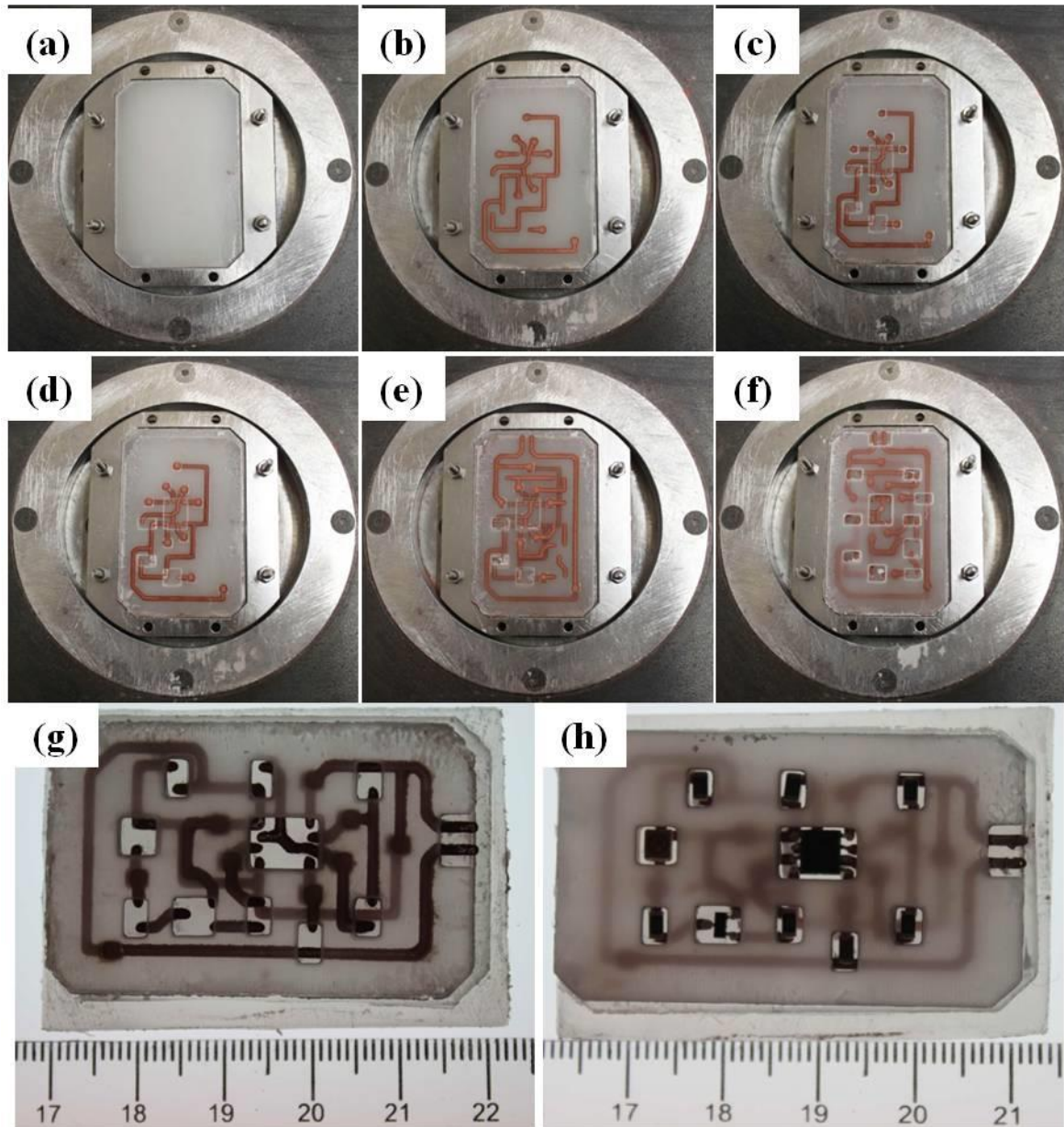


Figure 6.36: Finished sample at each step of the additive manufacturing process

To check the performance of the manufactured circuit board, a voltage of 5V is applied and Figure 6.37 shows the LED flashing conditions, which are acquired from a video at different times. The results indicate the success of the embedded 3D circuit board manufacturing.

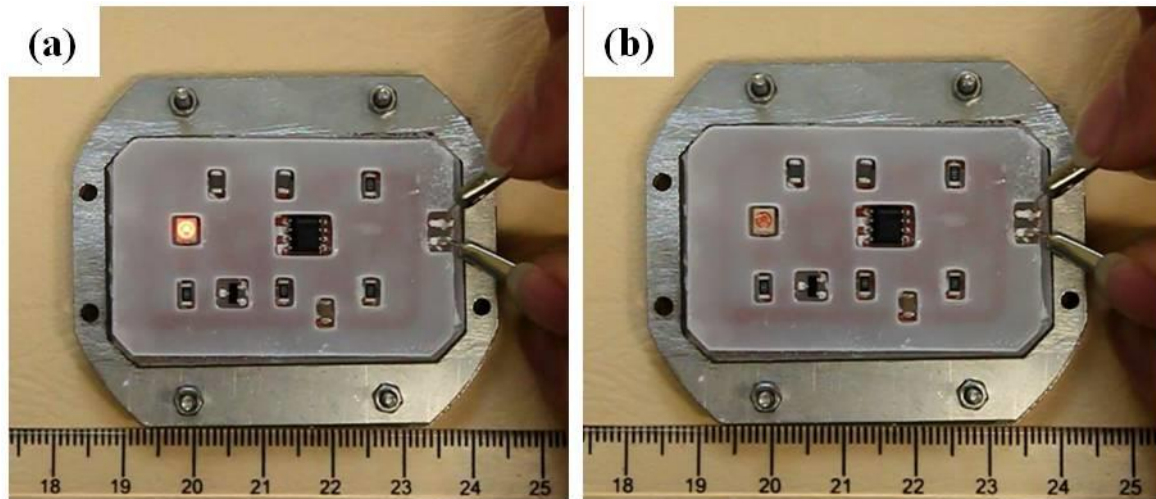


Figure 6.37: Flashing conditions of the LED acquired from a video

6.6 Summary

In this chapter it addresses the research question in Section 1.2: ‘Can we make circuits using low cost copper during laser processing without oxidation?’ by using SAM to protect copper from oxidation and making conductive copper tracks on HDPE substrate:

- The copper/HDPE mixture was prepared in a powder form since it can be incorporated in the powder based laser additive manufacturing process. The copper/HDPE ratio was an important parameter since it determined the track conductive model after laser processing.

In this chapter it also addresses the research question in Section 1.2: ‘Can we use laser to generate conductive circuits which have similar or improved performance compared with convectional?’ by melting copper particles and generating continuous conductive phase at some processing conditions:

- At a copper/HDPE ratio of 3/7 (low copper content), the conductivity is believed as a result of copper particle contact. This will lead discontinuous of the conductive phase at some locations and therefore the measured resistivity for the G-s-3/7 is quite high (1000X

of bulk copper). During laser processing, the HDPE will be melted and evidence indicated the copper particles will flow with the HDPE melt. When a high input energy (high power or low scanning speed) is applied, the HDPE will be evaporated and a porous structure in the track will be generated.

- At a copper/HDPE ratio of 6/4 (high copper content), the copper particles are melted and formed a continuous conductive pathway, where the electrons can transfer freely inside of it. The measured resistivity of this continuous phase (100X of bulk copper) is much lower than that in the ‘particle contact’ model. However, if a Gaussian beam with high input energy is applied, a strong outward movement of copper particles are generated due to the Marangoni force of HDPE melt and volume force of HDPE vapour; therefore the track will be damaged and the resistivity will be significantly increased.

- At a pure copper case, the monitored temperature during laser melting is lower than that for copper/HDPE mixture since the copper has a low absorptivity for CO₂ laser. The conductive phase is discontinuous in pure copper case, which is believed as a result of poor adhesion between copper track and HDPE substrate.

- At a raster scanning programme the overall energy distribution on the surface is more uniform and larger melted region can be generated without damage track. This will effectively reduce the resistivity (20X of bulk copper) but increase the track width. Compared with the ICA (silver paste) cases described in Chapter 5, the melted copper even exhibits a lower resistivity, which is a significant advantage of this innovative copper/HDPE power mixture when used in circuits manufacturing.

In this chapter it also addresses the research question in Section 1.2: ‘Does the redistribution of input energy provide a method of controlling/improving the properties of the resultant conductive circuits?’ by setting up a HOE based galvo scanning laser and comparing the difference between Gaussian and Pedestal beam cases:

- The HOE successfully converts the Gaussian beam to a Pedestal beam, the constructed beam is square but has 3 high intensity spots in its energy distribution. The beam profile keeps constant at different locations in the focusing plane.

- A Pedestal can create a copper track with more uniform thickness compared with the Gaussian beam at the same processing parameters. This is believed as a result of its uniform (nearly) energy distribution, where both outward Marangoni force during HDPE melt flow and volume force during HDPE evaporation are reduced.

- In this chapter it also addresses the research question in Section 1.2: ‘Can we extend the present 2D circuit system to 3D using laser additive manufacturing technology?’ by manufacturing a complete 3D embedded circuit system:

- For the 3D circuit system, the substrate and supporting structure were made from HDPE and the conductive track is made from melted copper. A double layer timer circuit pattern with vertical conductive interconnections is manufactured. During performance test the system works well and it successfully demonstrated a dissimilar material additive layer manufacturing process.

CHAPTER 7: CONCLUSIONS

The main aim of this project was to create a functional 3D PCB system, which included the manufacturing of dielectric substrate and 3D conductive tracks inside of it. Traditional PCB manufacturing was a ‘2D circuit – 3D packing’ process, as discussed in Chapter 2, its main limitation was the low design freedom and large space requirements. Early concept of 3D PCB was moulded circuit board [48] or injected circuit board [47]; they both exhibited limitation in system design and manufacturing and not widely used in industry. The additive layer manufacturing technique developed in recent years provided a new opportunity to manufacture 3D complex structures and therefore, it was a main intention of this study to explore the potential of using laser additive manufacturing in 3D PCB manufacturing.

The secondary major goal in this project was to investigate the material behaviour during laser processing, with the purpose of optimising the product performance. Previous researches mainly focused on the influence of laser parameters, where only the original round beams (Gaussian and Tophat) were adopted. This work introduced the HOE based beam reconstruction technique to achieve different beam profiles, and they were supposed to have different influence in material properties. Meanwhile, the whole laser processing situation was predicted by a FEM model in this work. The detailed conclusions were discussed in the following sections.

7.1 Development of FEM model

Although a lot of mathematic models [100, 150, 106] had been developed to describe laser welding/cladding cases, the influence of beam profiles was rare to be selected as a variable parameter. In this work, the FEM model in Chapter 3 was created based on two different beam profiles: ‘Gaussian’ and ‘Pedestal’, it was then tested and verified using HOE system in practical works. The established model was supposed to help the designer

to optimise the HOE design to gain better control in material properties. This novel production cycle was shown in Figure 7.1, which had not been reported in either laser processing modelling or HOE design part.

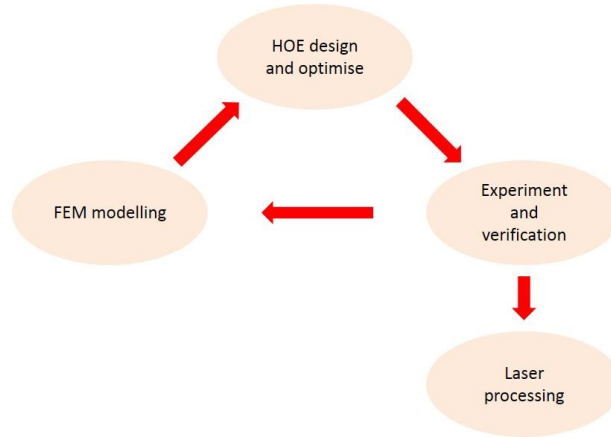


Figure 7.1: The novel production cycle for a FEM assisted HOE design system

The results and main contributions of the modelling work can be summarised as follow:

- In this work, the FEM model included the prediction of temperature field, melt flow and phase transition conditions for both Gaussian and Pedestal beams. The ‘level set’ and ‘enthalpy-porosity’ methods were selected to represent the evolution of liquid/vapour and solid/liquid interface, respectively.
- The 316L steel wire cladding was selected as first model verification case in this work. This work successfully demonstrated during molten pool formation, Pedestal beam led to a weaker outward flow when compared with Gaussian beam. This indicated from theoretical part that the material flow and product geometry were controllable by providing bespoke beam profiles. The simulation and experiment results had high similarity of 70-80%: at a condition of 260W and 1.6mm/s, wire processed by Gaussian beam keeps its original shape since the molten region is only restricted in the centre; however, the Pedestal beam can overcome the high heat loss rate at the wire edge and fully melt the wire. If a higher energy (300W) is applied, the molten pool penetration depth is significantly increased and a larger mixing zone is

formed. However, since the thermal resistance layer between wire and substrate was ignored in simulation work, it exhibited a deeper molten pool.

- The mild steel keyhole welding was another case for model verification. In this part the phase transition from liquid to vapour was exhibited. The recoil pressure generated by evaporation is found as the primary force for keyhole development. Keyhole depth oscillation is also reported as a result of equilibrium between recoil pressure and hydrostatic force on the keyhole wall. When heating is stopped, recoil pressure disappears and keyhole collapse is observed under the effect of hydrostatic force.
- The last verification case of the modelling work was the HDPE powder melting. The modelling work also had a high similarity (70-80%) with the experiment work: at a condition of 2W and 10mm/s, only melting occurred; a small ramp was observed in Gaussian beam case and it represented the circulation flow inside the molten pool; at a condition of 4W and 10mm/s, evaporation occurs; the Gaussian beam will create a bowl shape groove on the sample but Pedestal can still keep the slot front flat. However, since the powder was simplified to a dense material form, its consolidation during laser melting was unable to simulate. As a result samples generated in experiment exhibited a curved surface but the simulation predicted a flat surface.

The current work successful established the model but it did not include the HOE optimisation step in Figure 7.1, which should be added in future works.

7.2 Circuit substrate manufacturing using HDPE powder

The circuit substrate was a dielectric component and suitable to be created using laser additive manufacturing. However, one of the main challenges was the selection of material. Early products such as nylon-12 exhibited high porosity [67] after processing, which was not suitable for conductive material deposition when it was used as a substrate;

and its low Eab (about 15%) [67] also restricted its application in industry. This work successfully developed another material – HDPE in laser additive manufacturing, the main results and contributions in substrate manufacturing can be summarised as follows:

- Commercial laser additive manufacturing process used pre-heating method to avoid sample warpage; however HDPE was thought as unsuitable for this process due to its narrow super-heating region (Section 2.2.3). In Chapter 4, this work adopted a supporting structure technique which is normally used in metal additive manufacturing. The 3D HDPE component could be constructed without bending. It had improved the possibilities for future researchers to expand the potential for the technology to be implemented to a wider range of material applications.
- Fully dense HDPE component was created at a laser processing condition of Gaussian beam, 20W input power, 240mm/s scanning speed, 0.2mm scan spacing (G-20-240-0.2). Its tensile strength (7.97 ± 0.03 MPa) and Eab ($92.7 \pm 6.8\%$) were comparable with those of compression moulding samples (7.88 ± 0.01 MPa; $143.2 \pm 2.9\%$). At low input energy conditions (low power or high scanning speed), the HDPE powder was partially melted and a lot of air-traps are observed in the product, which led to low tensile strength. As the input energy increased, the degree of particle melting (DPM) was increased and therefore the tensile strength increases. However, if excessive input energy was applied, degradation bubbles are generated inside the product and the tensile strength would be reduced.
- Thermal analysis was also carried out in this work and the crystallisation mechanism of HDPE during laser processing was revealed. In this work, a melting phenomenon from particle surface to its core was observed using hot stage microscope, which confirmed a degree of particle melt (DPM) theory during laser additive manufacturing raised by previous research [68], i.e. at low input energy the particle is partially melted and DPM can be used for quantitative analysis.

- The DSC tests in this work exhibited a 2nd order phase transition ‘ramp’ and it was found as an evidence for the existence of imperfect crystalline (small spherulites). As the increasing of input energy, this ‘ramp’ was found shifting towards low temperature direction, which was explained as the increasing of small spherulites in this work. This result indicated DSC could be used as an effective method to analyse the thermal history during laser processing, since this process is too rapid to be recorded by other facilities.

7.3 Circuit manufacturing using silver paste / copper mixture and 3D embedded system fabrication

A lot of different types of conductor were investigated in early researches, such as conductive inks, pastes and particles. In this work, silver paste was firstly selected in this work since it was highly commercialised. However, laser was still a new technique for paste curing and the influence of different beam profiles in product properties had never been investigated. The main results and contribution in laser curing of silver paste were summarised as follow:

- A CNC scanning system was selected in silver paste curing and both Gaussian and Pedestal beams were used as the heating source. By using a Gaussian beam, the silver track would be damaged if the input power was higher than 2.3W or scanning speed was lower than 0.6mm/s, which was believed as a result of over-heating in centre of the track. It would also lead to obvious thermal ejection due to the high Marangoni force, which had been proved in simulation work in Chapter 3. The Pedestal beam exhibited a more stable curing process due to its uniform energy distribution. However, if a very low scanning speed (<0.3mm/s) was selected, large bubbles are formed and this should be avoided in further manufacturing.
- The laser cured silver paste exhibited its lowest electrical ($0.65 \pm 0.03 \times 10^{-4} \Omega \text{cm}$) at Pedestal beam, 2.3W input power, 0.3mm/s scanning speed (P-2.3-0.3); which was

even lower than oven cured sample ($1.32 \pm 0.04 * 10^{-4} \Omega \text{cm}$). The microstructure revealed that during laser curing degradation bubbles were formed and this would reduce the distance between different silver flakes. Considering from both electrical conductivity and sample morphology, the best laser curing condition was P-2.3-1.6 ($1.63 \pm 0.04 * 10^{-4} \Omega \text{cm}$).

- A 2D 555 timer circuit board was manufactured by fabricating silver paste on HDPE substrate, which was followed by laser curing and electronic component deposition. Since both the thin HDPE substrate and cured silver track had an acceptable flexibility, the circuit board could be bended and the system was still working.

However, silver paste was not suitable for 3D deposition by stencil printing or screen printing which were adopted in this project. In other work [53], a micro dispensing technique was selected to create 3D silver paste tracks but it was difficult to integrate it into the laser additive layer manufacturing process. As a result, a powder formed conductor was developed in this work using copper/HDPE mixture. This would make it possible to deposit both the substrate material and circuit material using the same method, as a dissimilar material additive manufacturing process. The first test was Gaussian beam melting of copper/HDPE mixture and its main results and contributions were summarised as follow:

- The copper powder was coated with a SAM and it was used to protect the copper core from oxidation. The copper particles were found well distributed among the HDPE particles after a centrifugal mixing.
- At a low copper/HDPE ratio of 3/7, the lowest electrical resistivity ($26.61 \pm 0.64 * 10^{-4} \Omega \text{cm}$, G-s-3/7-20-80) was even found as >1000 times of pure copper ($1.72 * 10^{-6} \Omega \text{cm}$). At these cases, the conductivity was believed as a result of copper particle contact and therefore quite low. During laser processing, the HDPE would be melted and evidence indicated the copper particles moved with the HDPE

melt. When a high input energy was applied, the HDPE would be evaporated and a porous structure in the track was generated.

- At a high copper/HDPE ratio of 6/4, the electrical resistivity ($1.94 \pm 0.07 \times 10^{-4} \Omega\text{cm}$, G-s-6/4-20-80) during single track scan was found reduced to 100 times of pure copper. The microstructure revealed that melting/partial melting of copper particles occurred without damaging the HDPE substrate. A continuous conductive pathway was formed and electrons can move freely inside it. It was also found that excessive input energy would not help to reduce the resistivity but evaporated HDPE and generated strong volume force, which would eventually damage the melted copper track. If a raster scanning programme was applied, the resistivity ($0.35 \pm 0.04 \times 10^{-4} \Omega\text{cm}$, G-r-6/4-20-80) could be further reduced to 20 times of bulk copper. This programme could create a more uniform overall energy distribution on the surface and created large melted region, as a result, the resistivity was reduced without damage the track. Compared with the silver paste described in Chapter 5, the raster scan cases even exhibited lower resistivity, which was believed as a significant advantage of this innovative copper/HDPE power mixture when used in circuit manufacturing. However, the problem of this programme was the width of the track would be significant increased ($172 \pm 8\%$).
- At a pure copper melting case, the conductive pathway was found discontinuous, as a result of poor adhesion between copper track and HDPE substrate. In addition, the monitored temperature during laser melting was lower than that for copper/HDPE mixture since the copper had a low absorptivity for CO₂ laser.

The raster scanning programme exhibited an advantage in copper particle melting and the Pedestal beam was therefore supposed to have the same benefit but without increasing the width of generated track. In this work, a HOE based galvo scanning laser was set up the main results and contributions can be summarised as follow:

- The idea of combining HOE and galvo scanner together to reconstruct beam profiles at high scanning speed condition in this study had never been reported in any other literatures. The burn print test indicated that the created beam has a square shape but its energy distribution was not an idea pedestal shape, since the designed beam size was too small to keep a high resolution. However, this beam still exhibited high robust during galvo scanning process, i.e. the alteration in spot location on the datum plane had insignificant influence in beam profile.
- By using the Pedestal beam the outward movement of copper particles could be reduced, which was believed as a result of weaker Marangoni force (HDPE melt flow) and volume expansion force (HDPE evaporation). This would lead to lower resistivity of the Pedestal cases at high scanning speeds (8W-40mm/s and 8W-60mm/s). Moreover, the widths of generated track in Pedestal cases were found only $89\pm3\%$ of Gaussian cases. However, at low scanning speed (8W-20mm/s), the Gaussian case was found melted in the central region, while Pedestal case was only partially melted and exhibited higher resistivity.

Although the Pedestal beam had some advantages in copper particle movement control, the current laser source used in the HOE galvo scanning system only had an original output of 10W (8W after beam reconstruction), which was too low to create a fully melted copper phase using Pedestal beam. As a result, considering from both electrical conductivity and track resolution, the best processing condition was G-r-6/4-20-120 (resisitvity $0.79\pm0.03*10^{-4}\Omega\text{cm}$, width 1.26mm).

- This work integrated the additive manufacturing of HDPE supporting structures and copper conductive tracks in one system. A multi-layer 555 timer circuit board with all electronic components embedded in the system was designed and successfully demonstrated. This system worked well during the performance test. This device indicated the opportunities to manufacture functional complex system using additive manufacturing in future.

So now it had been shown that the simulation work can help to design the input laser energy in manufacturing, the spatial control of input energy provided new opportunity to generate materials with designed structures, therefore the mechanical properties, electrical properties and et al. This could now be expanded to generate materials of improved performance over conventionally produced materials. And the additive process could be used to manufacture dissimilar materials system with high complexity.

CHAPTER 8: FURTHER WORK

The previously discussions and conclusions reveal additional questions and opportunities for further innovation. A suggestion of further research is outlined in this chapter.

- **Improvement of the simulation work:** The current model was established on bulk materials, but the material used in additive manufacturing is in powder form. As a result it is unable to simulate some processes such as powder consolidation during melting. To improve the current model, the granular flow mechanism of powder should be included. Moreover, a 3D model could be established to replace the 2D model; it is not difficult to convert 2D to 3D from mathematic view but the computational resource consumption should be carefully concerned. Some simplifications on the model and optimisations on the solver must be used.
- **Improvement of the HOE galvo system:** The constructed beam used in current work is not an idea Pedestal, which is a result of the HOE optic design. The required beam size is too small to keep the output beam profile at high resolution and new design must be made. In addition, the power of the laser source used in the HOE system is too low and a higher laser power should be used in future.
- **Using different beam irradiance distributions:** Using HOE to produce a completely customised beam profile is an effective method to control the product properties. This project used a Pedestal beam but more beam irradiance distributions should be investigated in further work. For instance, during the copper/HDPE conductive track melting, a ‘Rugby Post’ beam with high energy intensity at the edge can be selected to generate force to lead an inward movement of copper particles, which might make a dense copper phase in the centre. During substrate manufacturing, a thermal ramp could be positioned before/after the primary beam to provide a pre-heating/post-heating of the material.

- **Using different materials:** Alternative polymers such as polypropylene, polycarbonate and possibly composites should be investigated as the substrate material, since they may provide a better mechanical property. The conductive track material should still focus on copper but alternative matrix could be used.
- **Generating dense conductive track:** The main challenge of the current copper/HDPE system is its high porosity after partially melting. Possible solutions include using desirable beam profile to control copper particle movement and selecting small particles to generate a fully melting instead of partially melting.
- **Investigating 3D circuit structure:** The current work successful demonstrates the manufacturing process of a 3D conductive system but additional investigation should be carried out in the conductive properties in Z direction. New laser beam profile should be designed to control the interface properties between different conductive layers.
- **Building machine for dissimilar materials additive manufacturing:** Manually powder deposition is used in current work. This could be replaced by CNC system, where the substrate powder is deposited using powder bed and roller; the conductive powder is deposited using powder feeding nozzle. This two deposition process could be integrated into one hybrid system with computer numerical control.

REFERENCES

- [1] Khandpur R.S. (2005) *Printed Circuit Boards: Design, Fabrication, Assembly and Testing*, Tata McGraw-Hill Education, New Delhi
- [2] Günther H. (2008) *Development and Evaluation of Setup Strategies in Printed Circuit Board Assembly*, Springer, Berlin
- [3] Gilleo K. (1996) *Polymer Thick Film*, Van Nostrand Reinhold, New York
- [4] Park B.K., Kim D., Jeong S., Moon J., Sub Kim J.S. (2007). *Direct writing of copper conductive patterns by ink-jet printing*, *Thin Solid Films*, **515**, 7706-7711
- [5] Ko S.H., Pan H., Grigoropoulos C.P., Luscombe C.K., Frechet J.M.J., Poulidakos D. (2007). *All-inkjet-printed flexible electronics fabrication on a polymer substrate by low temperature high resolution selective laser sintering of metal nanoparticles*, *Nanotechnology*, **18**, 345202
- [6] Mun S., Yun S., Jung H., Kim J. (2012). *Sintering condition effect on the characteristics of ink-jet printed silver pattern on flexible cellulose paper*, *International Workshop on Flexible & Printable Electronics*, **12**, e10-e13
- [7] Ko S.H., Pan H., Grigoropoulos C.P., Frechet J.M.J., Luscombe C.K., Poulidakos D. (2008). *Lithography-free high resolution organic transistor arrays on polymer substrate by low energy selective laser ablation of inkjet-printed nanoparticle film*, *Applied Physics A*, **92**, 579-587
- [8] Cui W., Lu W., Zhang Y., Lin G., Wei T., Jiang L. (2010). *Gold nanoparticle ink suitable for electric-conductive pattern fabrication using in ink-jet printing technology*,

- [9] Sanchez-Romaguera V., Madec M.B., Yeates S.G. (2008). *Inkjet printing of 3D metal–insulator–metal crossovers*, *Reactive and Functional Polymers*, **68(6)**, 1052-1058
- [10] Zakariyah S., Conway P., Hutt D., Wang K. Selviah D. (2012). *CO₂ laser micromachining of optical waveguides for interconnection on circuit boards*, *Optics and Lasers in Engineering*, **50**, 1752-1756
- [11] Alwaidh A., Sharp M., French P. (2014). *Laser processing of rigid and flexible PCBs*, *Optics and Lasers in Engineering*, **58**, 109-113
- [12] Kelkar R., Kinzel E.C., Xu X. (2009). *Laser sintering of conductive carbon paste on plastic substrate*, *Optical Engineering*, **48**, 074301
- [13] Cai Z., Li X., Hu Q., Zeng X. (2009). *Laser sintering of thick film PTC thermistor paste deposited by micro-pen direct-write technology*, *Microelectronic Engineering*, **86**, 10-15
- [14] Chung J., Ko S., Grigoropoulos C.P., Bieri N.R., Dockendorf C., Poulikakos D. (2005). *Damage-free low temperature pulsed laser printing of gold nanoinks on polymers*, *ASME*, **127**, 724-732
- [15] Kinzel E.C., Sigmarsson H.H., Xu X., Chappell W.J. (2007). *Laser sintering of thick-film conductors for microelectronic applications*, *Journal of applied physics*, **101**, 063106
- [16] Genetti W.B., Yuan W.L., Grady B.P., O'Rear E.A., Lai C.L., Glatzhofer D.T. (1998). *Polymer matrix composites: Conductivity enhancement through polypyrrole coating of nickel flake*, *Journal of Materials Science*, **33**, 3085-3093

[17] Du Pont product information

http://www2.dupont.com/DuPont_Home/en_US/index.html

[18] Vu K. (2003). *Silver Migration – The mechanism and effects on thick-film conductors*, *Material Science Engineering*, 234

[19] Khanna P.K., Kale T.S., Shaikh M., Rao N.K., Satyanarayana C.V.V. (2008). *Synthesis of oleic acid capped copper nano-particles via reduction of copper salt by SFS*, *Materials Chemistry and Physics*, **110**, 21-25

[20] Yang J., Okamoto T., Bessho T., Satake S., Okido M. (2006). *A simple way for preparing antioxidation nano-copper powders*, *Chemistry Letters*, **35**, 648-649

[21] Engels V., Benaskar F., Jefferson D.A., Johnson B.F.G., Wheatley A.E.H. (2010). *Nanoparticulate copper – routes towards oxidative stability*, *Dalton Trans*, **39**, 6496-6502

[22] Athreya S.R., Kalaitzidou K., Das S. (2010). *Processing and characterization of a carbon black-filled electrically conductive nylon-12 nanocomposite produced by selective laser sintering*, *Materials Science and Engineering A*, **527**, 2637-2642

[23] Yamazaki M., Maekawa I. (1988). *Electroconductive resin paste*, *US patent*, 4,732,702

[24] Martin F.W., Shahbazi S. (1986). *Solderable Conductor*, *US patent*, 4,464,563

[25] Lu D., Wong C.P. (2000). *Effects of shrinkage on conductivity of isotropic conductive adhesives*, *International Journal of Adhesion & Adhesives*, **20**, 189-193

[26] Bigg D.M. (1984). *An investigation of the effect of carbon black structure, polymer*

morphology, and processing history on the electrical conductivity of carbon-black-filled thermoplastics, Journal of Rheology, 28, 501-516

[27] Buffat Ph., Borel J-P. (1976). *Size effect on the melting temperature of gold particles, Physical Review, 13, 2287-2298*

[28] Schmidt M., Kusche R., Issendorff B., Haberland H. (1998). *Irregular variations in the melting point of size-selected atomic clusters, 393, 21*

[29] Kim M.K., Hwang J.Y., Kang H., Kang K., Lee S. H., Moon S.J. (2009). *Laser sintering of the printed silver ink, 2009 IEEE International Symposium on Assembly and Manufacturing, 155-158*

[30] Yung K.C., Wu S.P., Liem H. (2009). *Synthesis of submicron sized silver powder for metal deposition via laser sintered inkjet printing, Journal of Material Science, 44, 154-159*

[31] Perelaer J., Gans B., Schubert U.S. (2006). *Inkjet printing and microwave sintering of conductive silver tracks, Advanced Materials, 18, 2101-2104*

[32] Hou S. (2010). *MSc thesis: Synthesise a nano-copper based ink and use it in conductive pathway formation, Loughborough University, Loughborough*

[33] Khanna P.K. More P., Jawalkar J., Patil Y., Rao N.K. (2009). *Synthesis of hydrophilic copper nanoparticles: effect of reaction temperature, J Nanopart Res, 11, 793-799*

[34] Park S., Chung W., Kim H. (2014). *Temperature changes of copper nanoparticle ink during flash light sintering, Journal of Materials Processing Technology, 214(11), 2730-2738*

- [35] Garrigos R., Cheyssac P., Kofman R. (1989). *Melting for lead particles of very small sizes; influence of surface phenomena*, *Z. Phys. D. – Atoms, Molecules and Clusters*, **12**, 497-500
- [36] Sakai H. (1995). *Surface-induced melting of small particles*, *Surface Science*, **351**, 285-291
- [37] Ko S.H., Chung J., Pan H., Grigoropoulos C.P., Poulikakos D. (2007). *Fabrication of multilayer passive and active electric components on polymer using inkjet printing and low temperature laser processing*, *Sensors and Actuators A*, **134**, 161-168
- [38] Zhang R., Moon K., Lin W., Wong C.P. (2010). *Preparation of highly conductive polymer nanocomposites by low temperature sintering of silver nanoparticles*, *Journal of Materials Chemistry*, **20**, 2018-2023
- [39] Suritski V., Idla K., Opik A. (2004). *Synthesis and redox behavior of PEDOT/PSS and PPy/DBS structures*, *Synthetic Metals*, **144**, 235-239
- [40] Vitoratos E., Sakkopoulos S., Dalas E., Paliatsas N., Karageorgopoulos D., Petraki F., Kennou S., Choulis S.A. (2009). *Thermal degradation mechanisms of PEDOT:PSS*, *Organic Electronics*, **10**, 61-66
- [41] Sele C.W., von Werne T., Friend R.H., Sirringhaus H. (2005). *Lithography-free, self-aligned inkjet printing with sub-hundred-nanometer resolution*, *Advanced Materials*, **17**, 997-1001
- [42] Sirringhaus H., Kawase T., Friend R.H., Shimoda T., Inbasekaran M., Wu W., Woo E.P. (2000). *High-resolution inkjet printing of all-polymer transistor circuits*, *Science*, **290**, 2123-2126

- [43] Lasagni A.F., Hendricks J.L., Shaw C.M., Yuan D., Martin D.C., Das S. (2009). *Direct laser interference patterning of poly(3,4-ethylene dioxythiophene)-poly(styrene sulfonate) (PEDOT-PSS) thin films*, *Applied Surface Science*, **255**, 9186-9192
- [44] Lidzey D.G., Voigt M., Giebeler C., Buckley A., Wright J., Bohlen K., Fieret J., Allott R. (2005). *Laser-assisted patterning of conjugated polymer light emitting diodes*, *Organic Electronics*, **6**, 221-228
- [45] Lai M.F., Li S.W., Shih J.Y., Chen K.N. (2011). *Wafer-level three-dimensional integrated circuits (3D IC): Schemes and key technologies*, *Microelectronic Engineering*
- [46] Lopes A., MacDonald E., Wicker R.B. (2012). *Integrating stereolithography and direct print technologies for 3D structural electronics fabrication*, *Rapid Prototyping Journal*, **18(2)**, 129-143
- [47] Min Y., Olmedo R., Hill M., Radhakrishnan K., Aygun K., Kabiri-Badr M., Panat R., Dattaguru S., Balkan H. (2013). *Embedded Capacitors in the Next Generation Processor*, *ECTC 2013*, 1225-1229
- [48] Gilleo K., Jones D., Pham-Van-Diep G. (2005). *Thermoplastic injection moulding: new packages and 3D circuits*, *ECWC 10 Conference*, S01-3
- [49] Laser direct structuring technology (LDS) for 3 dimensional circuits or molded interconnect devices (MIDs)
<http://www.lpkfusa.com/mid/index.htm>
- [50] Palmer J.A., Summers J.L., Davis D.W., Gallegos P.L., Chavez B.D., Yang P., Medina F., Wicker R.B. (2005). *Realizing 3-D interconnected direct write electronics within smart stereolithography structures*, *International Mechanical Engineering Congress and Exposition 2005 Proceedings*, 14-18

- [51] Medina F., Lopes A.J., Inamdar A., Hennessey R., Palmer J., Chavez B., Davis D., Gallegos P., Wicker R.B. (2005). *Hybrid manufacturing: integrating stereolithography and Direct Write Technologies, Proceedings of the 16th Annual Solid Freeform Fabrication Symposium, University of Texas at Austin*, 39-49
- [52] Navarrete M., Lopes A., Acuna J., Estrada R., MacDonald E., Palmer J., Wicker R. (2007). *Integrated layered manufacturing of a novel wireless motion sensor system with GPS, Proceedings of the 18th Annual Solid Freeform Fabrication Symposium, University of Texas at Austin*, 575-85
- [53] Lopes A.J., MacDonald E., Wicker R. (2012). *Integrating stereolithography and direct print technologies for 3D structural electronics fabrication, Rapid Prototyping Journal*, **18/2**, 129–143
- [54] Pique A., Mathews S.A., Pratap B., Auyeung R.C.Y., Karns B.J. Lakeou S. (2006). *Embedding electronic circuits by laser direct-write, Microelectronic Engineering*, **83**, 2527-2533
- [55] Vasquez M. (2012). *PhD thesis: analysis and development of new materials for polymer laser sintering*, Loughborough University, Loughborough
- [56] Wohlers T. (2003). *Wholers Report 2003, Rapid prototyping, tooling & manufacturing, State Of The Industry, Annual Worldwide Progress Report*, Wohlers Associate Inc. Colorado
- [57] John V. (2003). *Introduction to Engineering Materials 4th Edition*, Palgrave Macmillan, Gosport
- [58] Ion J.C. (2005). *Laser Processing of Engineering Materials: Principles, Procedure*

and Industrial Application, Elsevier Butterworth-Heinemann, Norfolk

[59] Mumtaz K. A. (2008). *PhD thesis: selective laser melting of inconel 625 using pulse shaping*, Loughborough University, Loughborough

[60] Wendel B., Reitzel D., Kuhnlein F., Hulder G., Schmachtenberg E. (2008). *Additive processing of polymer*, *Macromolecular Materials Engineering*, **293**, 799

[61] Gibson I., Shi D. (1997). *Material properties and fabrication parameters in selective laser sintering process*, *Rapid Prototyping Journal*, **3(4)**, 129

[62] Niino T., Haraguchi H., ITAGAKI Y. (2011) *Feasibility study on plastic laser sintering without powder bed preheating*, *Proceedings of the 22th Annual Solid Freeform Fabrication Symposium, University of Texas at Austin*, 17-29

[63] Taha M.A., Yousef A.F., Gany K. A., Sabour H. A. (2012). *On selective laser melting of ultra high carbon steel: effect of scan speed and post heat treatment*, *Mat.-wiss. u. Werkstofftech*, **43(11)**, 913-923

[64] Starr T., Gornet T., Usher J. (2011). *The effect of process conditions on mechanical properties*, *Rapid Prototyping Journal*, **17(6)**, 418-423

[65] Caulfield B., McHugh P., Lohfield S. (2007). *Dependence of mechanical properties of polyamide components on build parameters in the SLS process*, *Journal of Materials Processing Technology*, **182(1)**

[66] Ho H., Cheung W., Gibson I. (2003). *Morphology of properties of selective laser sintered bisphenol-A-polycarbonate*, *Ind. Eng. Chem. Res*, **42(9)**, 1850-1862

[67] Goodridge R., Tuck C., Hague R. (2011). *Laser sintering of polyamides and other*

polymers, *Progress in Materials Science*, **57**, 229-267.

[68] Zarringhalam H., Hopkinson N., Kamperman N., deVlieger J. (2006). *Effects of processing on microstructure and properties of SLS nylon-12*, *Materials Science and Engineering Part A*, **1-2**, 172-180

[69] Gibson M., Higginson R.L., Tyrer J. (2009). *The control of grain size during welding and direct metal deposition using three dimensional time-temperature control provided by holographic beam shaping*, *ICALEO 2009*, 1505

[70] Noden S. (2000). *PhD thesis: applications of diffractive optical elements with high power lasers*, Loughborough University, Loughborough

[71] Gaumann M., Bezencon C., Canalis P., Kurz W. (2001). *Single-crystal laser deposition of superalloys: processing-microstructure maps*, *Acta mater.*, **49**, 1051-1062

[72] Nishimoto K., Saida K., Fujita Y. (2008). *Crystal growth in laser surface melting and cladding of Ni-base single crystal superalloy*, *Welding in the World*, **52**, 64-78

[73] Higginson R.L., Gibson M., Kell J., Tyrer J. (2010). *Weld pool Shaping and microstructural control using novel computer generated holographic optic laser welding of steel and stainless steel*, *Materials Science Forum*, **638-642**, 3673-3678

[74] Fred M.D., Scott C.H. (2000). *Laser beam shaping: theory and techniques*, Marcel Dekker, Inc, New York

[75] Steen W. (1978). *Surface coating using a laser*, *Advances in Surface Coating Technology*, **13-15**, 175-187

[76] Farooq K., Kar A. (1999). *Effects of laser mode and scanning direction on melt pool*

shape, *Journal of Applied Physics*, **85(9)**, 6415-6420

[77] Bianco M., Rivela C., Talentino S. (1994). *On-line surface treatment feasibility of industrial components by means of CO₂ power laser*, *Laser Materials Processing: Industrial and Microelectronics*, **2207**, 53

[78] König W., Kirner P.K. (1994). *Laser surface treatments prolongs tool life*, *Laser Materials Processing: Industrial and Microelectronics*, **2207**, 44

[79] Pinkerton A.J., Li L. (2005). *An experimental and numerical study of the influence of diode laser beam shape on thin wall direct metal deposition*, *J. of Laser Applications*, **17(1)**, 47-56

[80] Safdar S., Li L., Sheikh M.A. (2007). *Numerical analysis of the effects of non-conventional laser beam geometries during laser melting of metallic materials*, *J. of physics & Applied Physics*, **40(2)**, 593-603

[81] Kell J. (2007). *PhD thesis: melt pool and microstructure manipulation using diffractive holographic elements in high power conduction laser welding*, Loughborough University, Loughborough

[82] Babin S.V., Danilov S.V. (1998). *Data preparation and fabrication of DOE using electron-beam lithography*, *Optics and Lasers in Eng.*, **29**, 307-324

[83] Ekberg M., Larsson M., Boller A., Hard S. (1991). *Nd:YAG laser machining with multilevel resist kinoform*, *Applied Optics*, **30(25)**, 3604-3606

[84] Kell J., Tyrer J.R., Higginson R.L., Jones J.C., Noden S. (2012). *Laser weld pool management through diffractive holographic optics*, *Materials Science and Technology*, **28**, 354-362

- [85] Groover M.P. (2007). *Fundamentals of modern manufacturing: materials, processes and systems*, John Willey & Sons Inc, New York
- [86] Schmid M., Amado F., Levy G., Wegener K., (2014). Flowability of powders for selective laser sintering (SLS) investigated by round robin test, Eidgenössische Technische Hochschule Zürich, IWF
- [87] William M.S. (2003). *Laser material processing*, 3rd edition, Springer, London
- [88] Lippert T. (2005). *Interaction of photons with polymers: from surface modification to ablation*, *Plasma Process. Polymer*, **2**, 525-546
- [89] Klein R. (2012). *Laser welding of plastics*, Wiley-VCH, Germany
- [90] Nowakowski K.A. (2005). *Phd thesis: Laser beam interaction with materials for microscale applications*, Worcester Polytechnic Institute, Worcester
- [91] Cho W., Na S., Cho M., Lee J. (2010). *Numerical study of alloying element distribution in CO₂ laser-GMA hybrid welding*, *Computational Materials Science*, **49**, 792-800
- [92] Incropera F.P., Dewitt D.P. (2002). *Introduction to heat transfer*, 4th edition, John Wiley & Sons, New York
- [93] Rosenthal D. (1946). *The theory of moving sources of heat and its application to metal treatments*, *transaction of the American Society of Mechanical Engineers*, **68**, 849-866
- [94] Cho W., Na S., Thomy C., Vollertsen F. (2012). *Numerical simulation of molten pool*

dynamics in high power disk laser welding, Journal of Materials Processing Technology, **212**, 262-275

[95] Brent A.D., Voller V.R., Reid K.J. (1988). *Enthalpy–porosity technique for modeling convection–diffusion phase change: application to the melting of a pure metal*, *Numerical Heat Transfer, Part B: Fundamentals: An International Journal of Computation and Methodology*, **13**, 297-318.

[96] Sajid M. (2010). *PhD Thesis: A contribution towards the numerical study of bubble dynamics in nucleate boiling at local scale using a conservative level set method*, University of Cergy Pontoise, Cergy Pontoise

[97] Zahdel S. (2009) *Thesis: Numerical modelling of fluid interface phenomena*, KTH Computer Science and Communication

[98] Morville S., Carin M., Muller M., Gharbi M., Peyre P., Carron D., Lemasson P., Fabbro R. (2010). *2D axial-symmetric model for fluid flow and heat transfer in the melting and resolidification of a vertical cylinder*, *Proceedings of the Comsol Conference 2010 Paris*

[99] Lee J., Ko S., Farson D., Yoo C. (2002). *Mechanism of keyhole formation and stability in stationary laser welding*, *Journal of Physics D: Applied Physics*, **35**, 1570-1576

[100] Han L., Liou F.W. (2004). *Numerical investigation of the influence of laser beam mode on melt pool*, *International Journal of Heat and Mass Transfer*, **47**, 4385-4402

[101] Zhao H., Niu W., Zhang B., Lei Y., Kodama M., Ishide T. (2011). *Modelling of keyhole dynamics and porosity formation considering the adaptive keyhole shape and three-phase coupling during deep-penetration laser welding*, *Journal of Physics D:*

[102] Tomashchuk I., Sallamand P., Jouvard J.M. (2012). *The modelling of dissimilar welding of immiscible materials by using a phase field method*, *Applied Mathematics and Computation*, **219(13)**, 7103-7114

[103] Koch H., Kägeler C., Otto A., Schmidt M. (2011). *Analysis of welding zinc coated steel sheets in zero gap configuration by 3D simulations and high speed imaging*, *Physics Procedia*, **12**, 428-436

[104] Semak V., Matsunawa A. (1997). *The role of recoil pressure in energy balance during laser materials processing*, *Journal of Physics D: Applied Physics*, **30**, 2541-2552

[105] KI H., Mohanty P.S., Mazumder J. (2002). *Modeling of laser keyhole welding: part I. mathematical modeling, numerical methodology, role of recoil pressure, multiple reflections, and free surface evolution*, *Metallurgical and Materials Transactions A*, **33A**, 1817-1830

[106] KI H., Mohanty P.S., Mazumder J. (2002). *Modeling of laser keyhole welding: part II. simulation of keyhole evolution, velocity, temperature profile, and experimental verification*, *Metallurgical and Materials Transactions A*, **33A**, 1831-1842

[107] Han L., Liou F.W., Phatak K.M. (2004). *Modelling of laser cladding with powder injection*, *Metallurgical and Materials Transaction B*, **35B**, 1139-1150

[108] Wen S., Shin Y.C. (2011). *Comprehensive predictive modelling and parametric analysis of multitrack direct laser deposition processes*, *Journal of Laser Applications*, **23(2)**, 022003

[109] Pang S., Chen L., Zhou J., Yin Y., Chen T. (2011). *A three-dimensional sharp*

interface model for self-consistent keyhole and weld pool dynamics in deep penetration laser welding, Journal of Physics D: Applied Physics, **44**, 025301

[110] Zhou J., Tsai H. (2007). *Porosity formation and prevention in pulsed laser welding, Transactions of the ASME*, **129**, 1014-1024

[111] Tan W., Bailey N., Shin Y. (2013). *Investigation of keyhole plume and molten pool based on a three-dimensional dynamic model with sharp interface formulation, Journal of Physics D: Applied Physics*, **46**, 055501

[112] Courtois M., Carin M., Masson P., Gaied S., Balabane M. (2013). *A new approach to compute multi-reflections of laser beam in a keyhole for heat transfer and fluid flow modelling in laser welding, Journal of Physics D: Applied Physics*, **46**, 503305

[113] Bennon W.D., Incropera F.P. (1987). *A continuum model for momentum, heat and species transport in binary solid-liquid phase change systems - I. Model formulation, Int. J. Heat Mass Transfer*, **30**, 2161-2170

[114] Osher S., Sethian J.A. (1988). *Fronts propagating with curvature dependent speed: algorithms based on Hamilton-Jacobi formulations, J. Comput.Phys*, **79**, 12-49

[115] Desmaison O., Bellet M., Guillemot G. (2014). *A level set approach for the simulation of the multipass hybrid laser/GMA welding process, Computational Materials Science*, **91**, 240-250

[116] Olsson E., Kreiss G. (2005). *A conservative level set method for two phase flow, J. Comput. Phys.*, **210**, 225-246

[117] Harten A. (1977). *The artificial compression method for computation of shocks and contact discontinuities. I. Single conservation laws, Comm. Pure Appl. Math.*, 611-638

- [118] Rahimi P., Ward C.A. (2005). *Kinetics of evaporation: statistical rate theory approach*, *Int.J. of Thermodynamics*, **8(1)**, 1-14
- [119] Su Y., Li Z., Mills K.C. (2005). *Equation to estimate the surface tensions of stainless steels*, *Journal of Materials Science*, **40**, 2201-2205
- [120] Wei H. (2009). *MSc thesis: Surface tension measurement of high density polyethylene and its clay nanocomposites in supercritical nitrogen*, University of Waterloo, Waterloo
- [121] Pierce S.W., Burgardt P., Olson D.L. (1999). *Thermocapillary and arc phenomena in stainless steel welding*, *Welding Research Supplement*, 45-52
- [122] Lu S., Fujii H., Sugiyama H., Tanaka M., Nogi K. (2002). *Weld penetration and Marangoni convection with oxide fluxes in GTA welding*, *Materials Transactions*, **43(11)**, 2926-2931
- [123] Zarringhalam H. (2007). *PhD thesis: investigation into crystallinity and degree of particle melt in selective laser sintering*, Loughborough University, Loughborough
- [124] Shi Y., Li Z., Sun H., Huang S., Zeng F. (2004). *Effect of the properties of the polymer materials on the quality of selective laser sintering parts*, *Journal of Materials: Design and Applications*, **218**, 247-252
- [125] Plaats G. (1992). *The practice of thermal analysis*, Mettler Toledo, AG 11/92 ME-724 412
- [126] Menczel J.D., Prime R.B. (2009). *Thermal Analysis of Polymers, Fundamentals and Applications*, John Wiley & Sons, Inc, New Jersey

- [127] Raff R.A.V., Ahmad A.S. (1970). *Dependence of properties on spherulite size in crystalline polymers*, *Northeast Science*, **44(3)**, 184-205
- [128] Pakula T., Kryszewski M., Soukup Z. (1976). *Determination of spherulite size distribution by small-angle light scattering*, *European Polymer Journal*, **12**, 41-45
- [129] Private conversation with Jake Marshall from Goonvean Fibres Ltd
- [130] Stainless Steel – AISI 316 material data sheet, Goodfellow
<http://www.goodfellow.com/E/Stainless-Steel-AISI-316.html>
- [131] Bond energy data
<http://www.kentchemistry.com/links/Kinetics/BondEnergy.htm>
- [132] Fearon E., Sato T., Wellburn D., Watkins K.G., Dearden G. (2007). *Thermal effects of substrate materials used in the laser curing of particulate silver inks*, *Laser Assisted Net Shape Engineering Proceeding of the LANE 2007*, **5**, 379-390
- [133] Private conversation with Daniel Lloyd from Laser Optical Engineering, the supplier for the HOE optics
- [134] Private conversation with Siyuan Qi from Loughborough University
- [135] Simchi A. (2004). *The role of particle size on the laser sintering of iron powder*, *Metallurgical and Materials Transaction B*, **35B**, 937-948
- [136] Salmoria G., Klauss P., Zepon K. Kanis L. (2013). *The effects of laser energy density and particle size in the selective laser sintering of polycaprolactone/progesterone specimens: morphology and drug release*, *Int J Adv Manuf Technol*, **66**, 1113-1118

- [137] Ho H.C.H., Gibson I., Cheung W.L. (1999). *Effects of energy density on morphology and properties of selective laser sintered polycarbonate*, *Journal of Materials Processing Technology*, **89-90**, 204-210
- [138] Laibinis P.E., Whitesides G.M., Allara D.L., Tao Y., Parikh A., Nuzzo R. (1991), *Comparison of the structures and wetting properties of self-assembled monolayers of n-Alkanethiols on the coinage metal surfaces, Cu, Ag, Au*, *J. Am. Chem. Soc.*, **113**, 7152-7167
- [139] Otto A., Koch H., Vazquez R.G. (2012). *Multiphysical simulation of laser material processing*, *Physics Procedia*, **39**, 843-852
- [140] Tsuchiya Y., Sumi K. (1968). *Thermal decomposition products of polyethylene*, *Journal of Polymer Science: Part A-1*, **6**, 415-424
- [141] Fouassier J.P., Allonas X., Burget D. (2002). *Photopolymerization reactions under visible lights: principle, mechanisms and examples of applications*, *Progress in Organic Coatings*, **47**, 16–36
- [142] Cho J., Na S. (2006). *Implementation of real-time multiple reflection and Fresnel absorption of laser beam in keyhole*, *J. Phys. D: Appl. Phys.*, **39**, 5372-5378
- [143] Emissivity coefficients of some common materials, The Enigneering ToolBox
http://www.engineeringtoolbox.com/emissivity-coefficients-d_447.html
- [144] Sigma-Aldrich (1997). *The Aldrich library of FT-IR spectra*, 2nd edition, Sigma-Aldrich Co., USA
- [145] Martienssen W., Warlimont H. (2005). *Springer Handbook of Condensed Matter*

and Materials Data, Springer, Berlin

[146] Sonka M., Fitzpatrick J.M. (2000). *Handbook of medical imaging, Volume 2 – medical image processing and analysis*, SPIE, Washington

[147] Goshtasby A.A. (2005). *2-D and 3-D image registration: for medical. Remote sensing and industrial applications*, John Wiley & Sons, New Jersey

APPENDIX

Appendix A: Thermal camera calibration

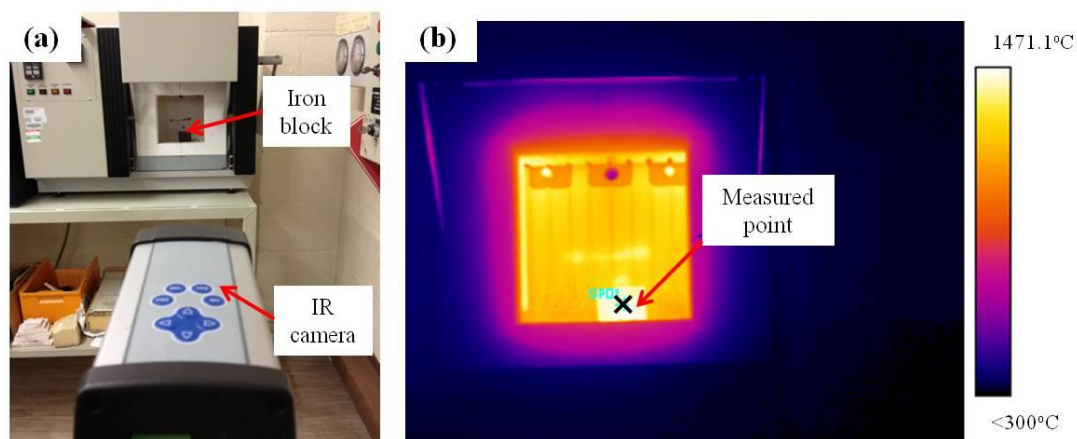


Figure A.1: (a) Setting up of the IR camera calibration system; (b) location of the measured point

The calibration of the IR thermal camera (Thermovision A40m, FLIR) itself was carried out by FLIR System, Inc. This work will only focus on the temperature difference caused by filter system. As indicated in Figure A.1.a, the calibration system was set up by pointing the IR camera to an iron block in a furnace. The block was heated to 1500°C and then cooling in ambient air. The measurement was carried out at the highest recording rate (50 fps) and no filter was applied on the camera lens for the 1st run. After reaching the room temperature the blocked was heated up to 1500°C again for the 2nd run and the filter (SWBP-8486-000816, Northumbria Optical Coating Ltd) was placed in front of the lens. The temperature of the point in Figure A.1.b was extracted for both the two runs and the plot of measured temperature with filter against direct measured temperature is indicated in Figure A.2.

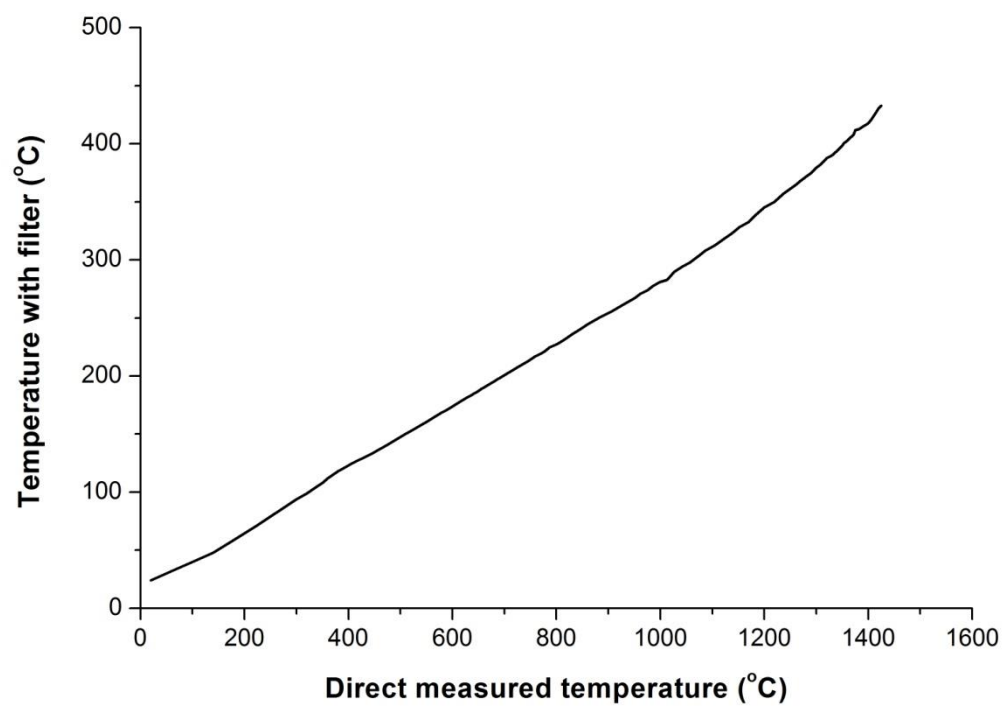
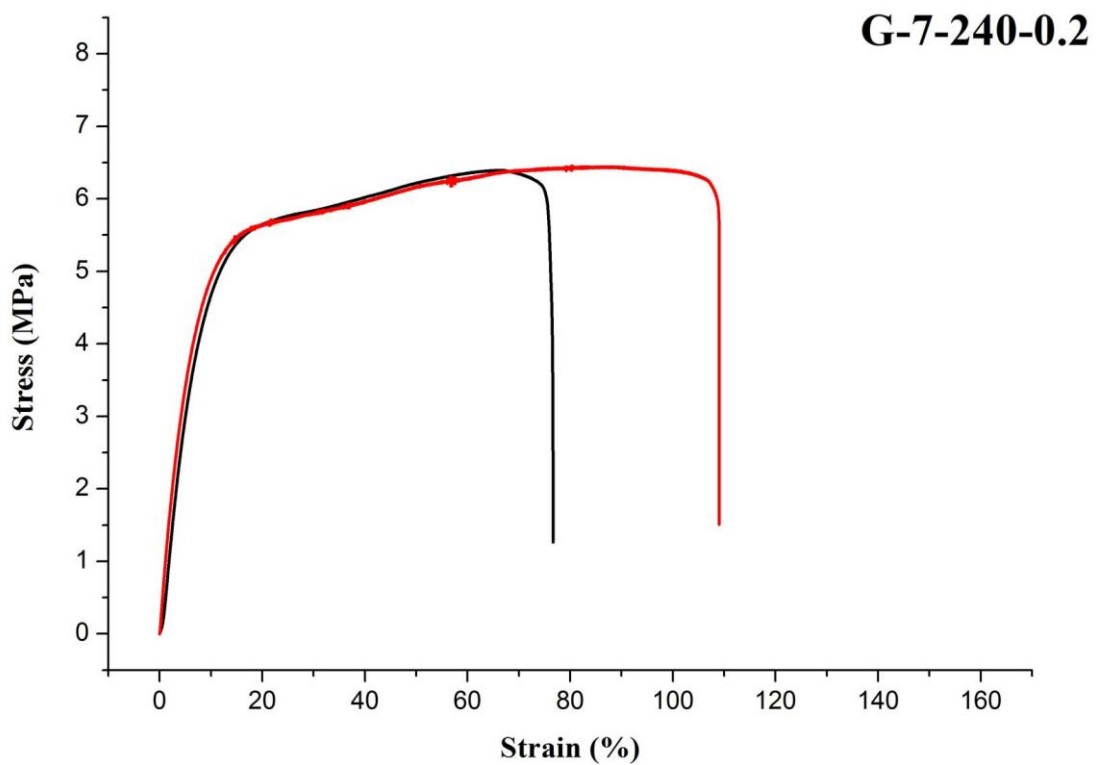
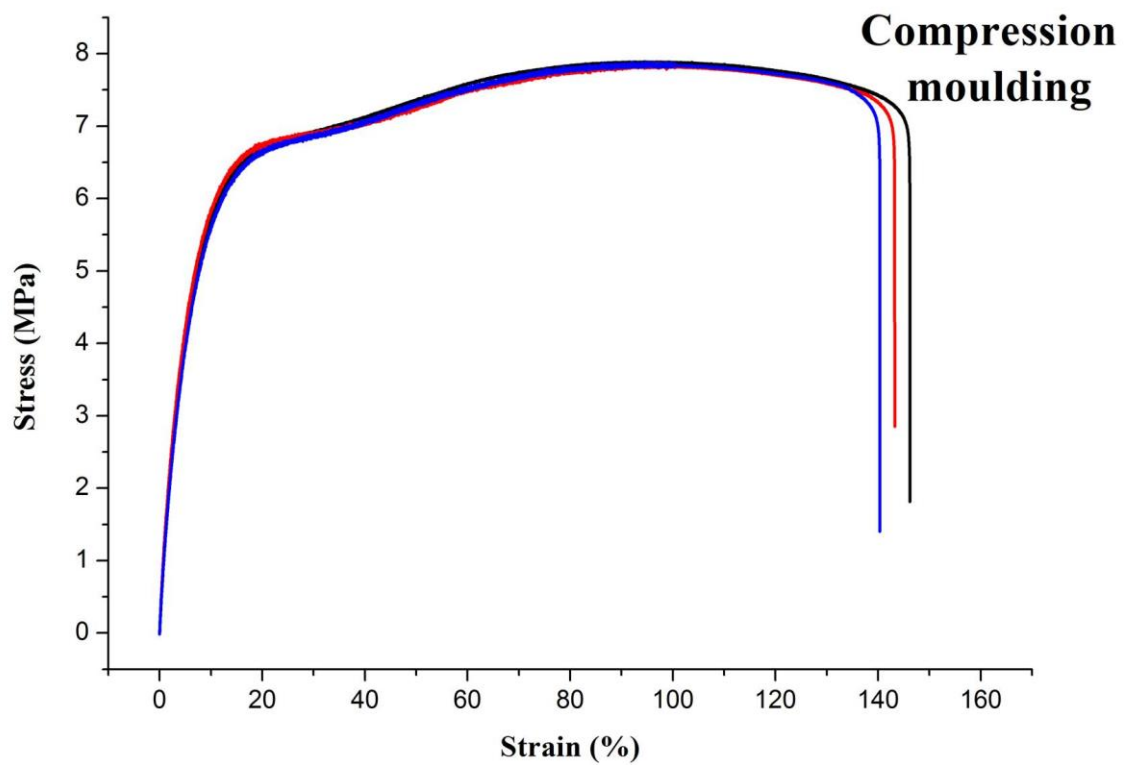
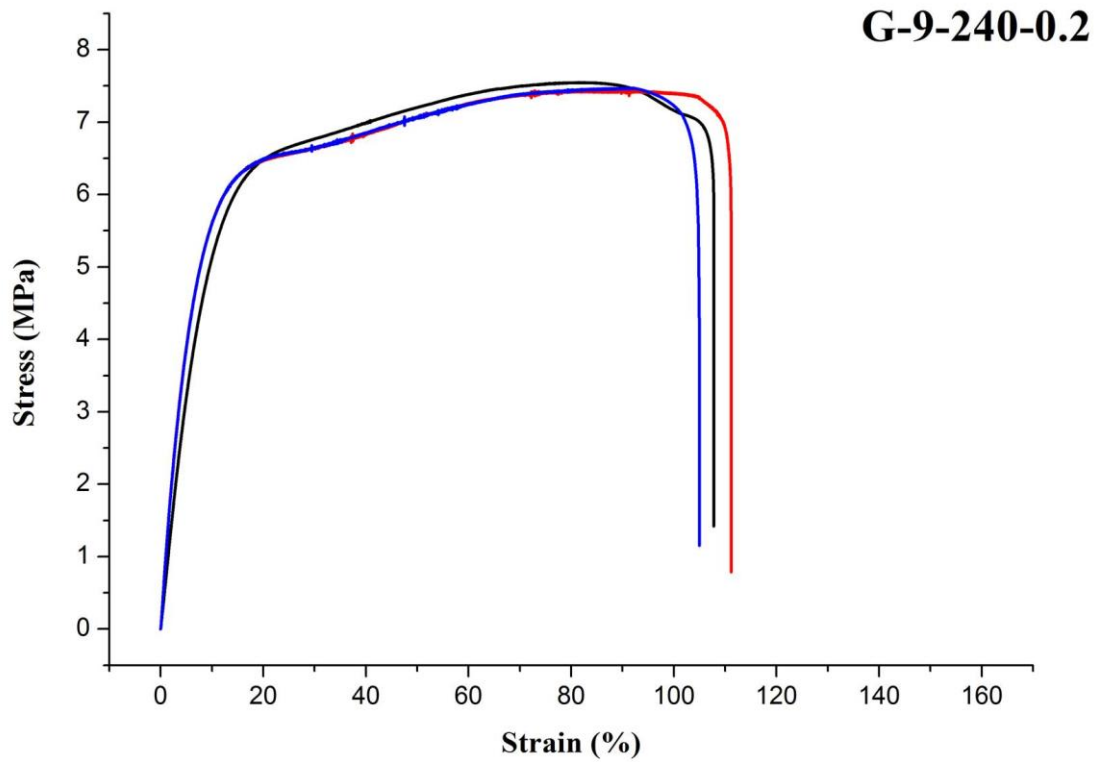
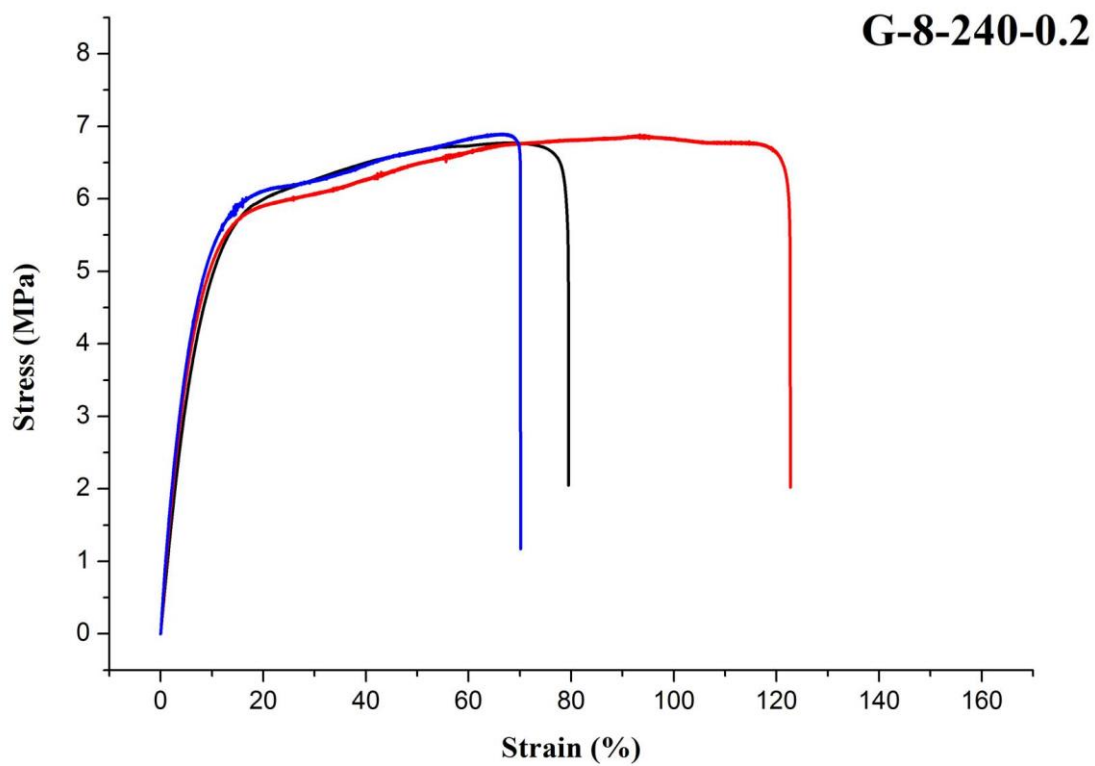
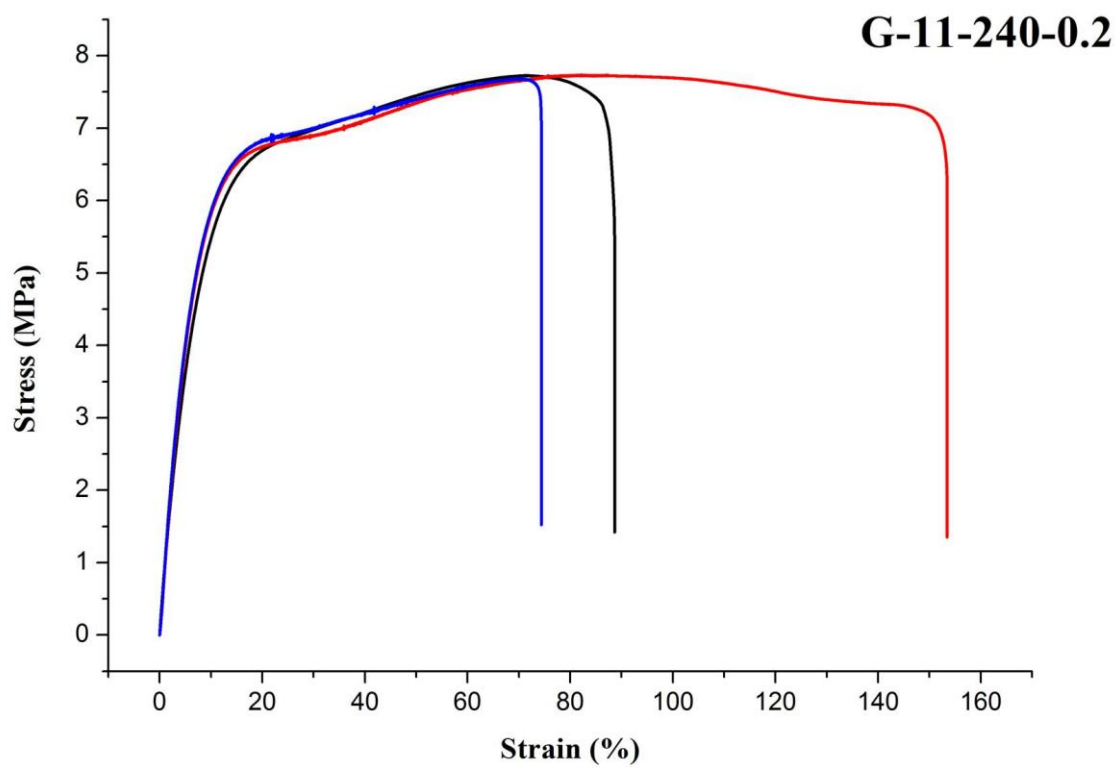
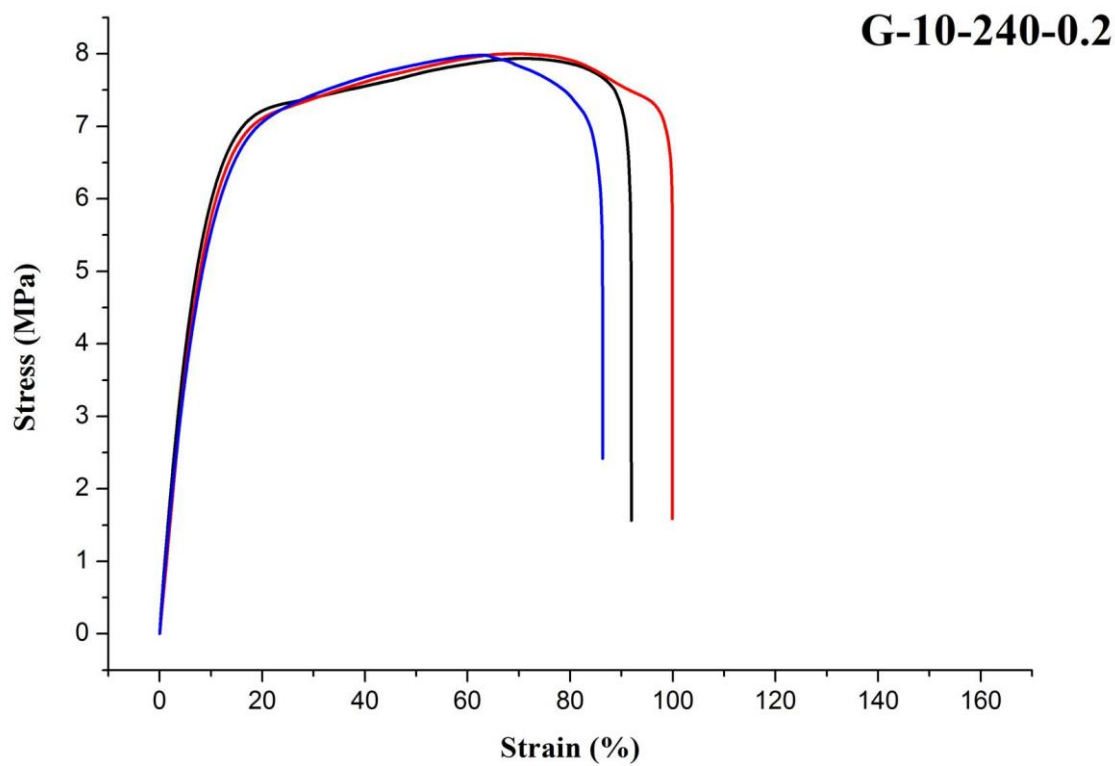


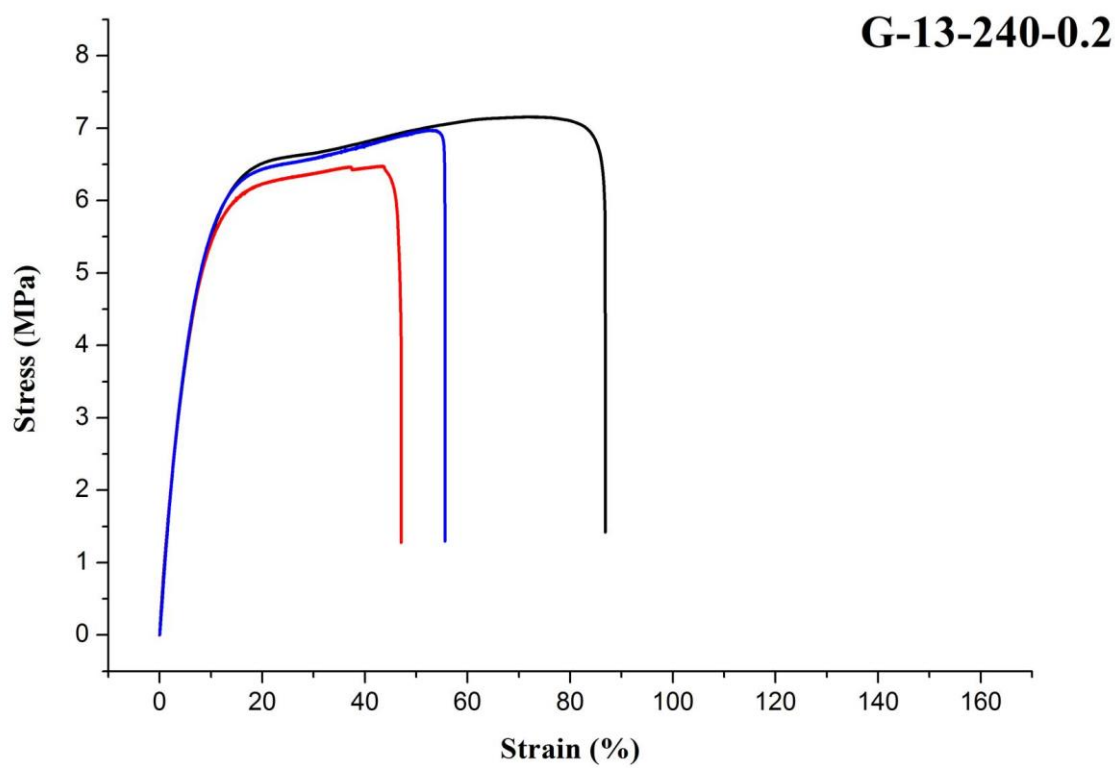
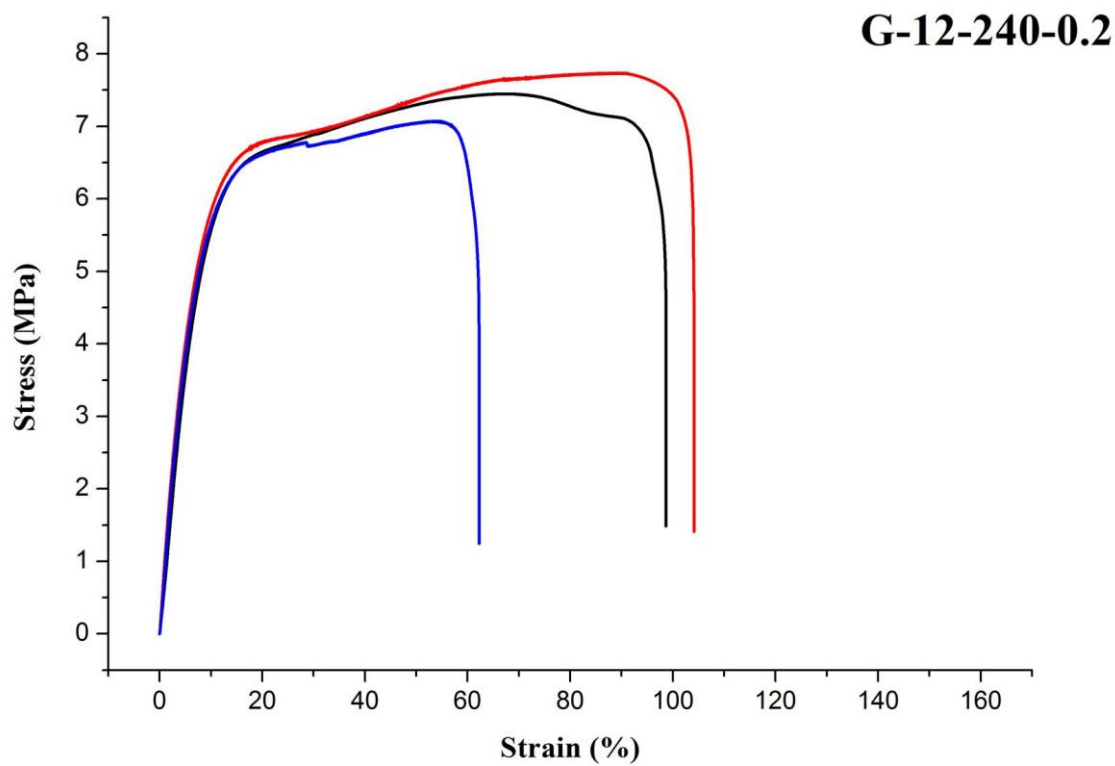
Figure A.2: Calibration plot of temperature with filter against direct measured temperature

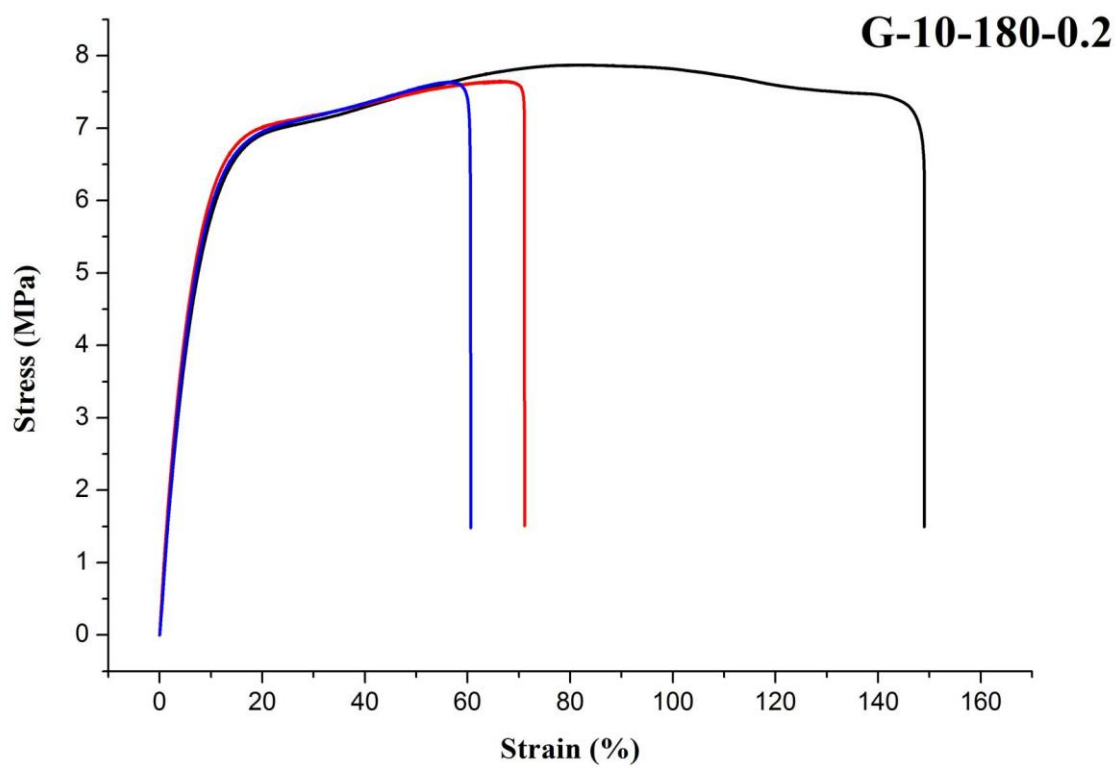
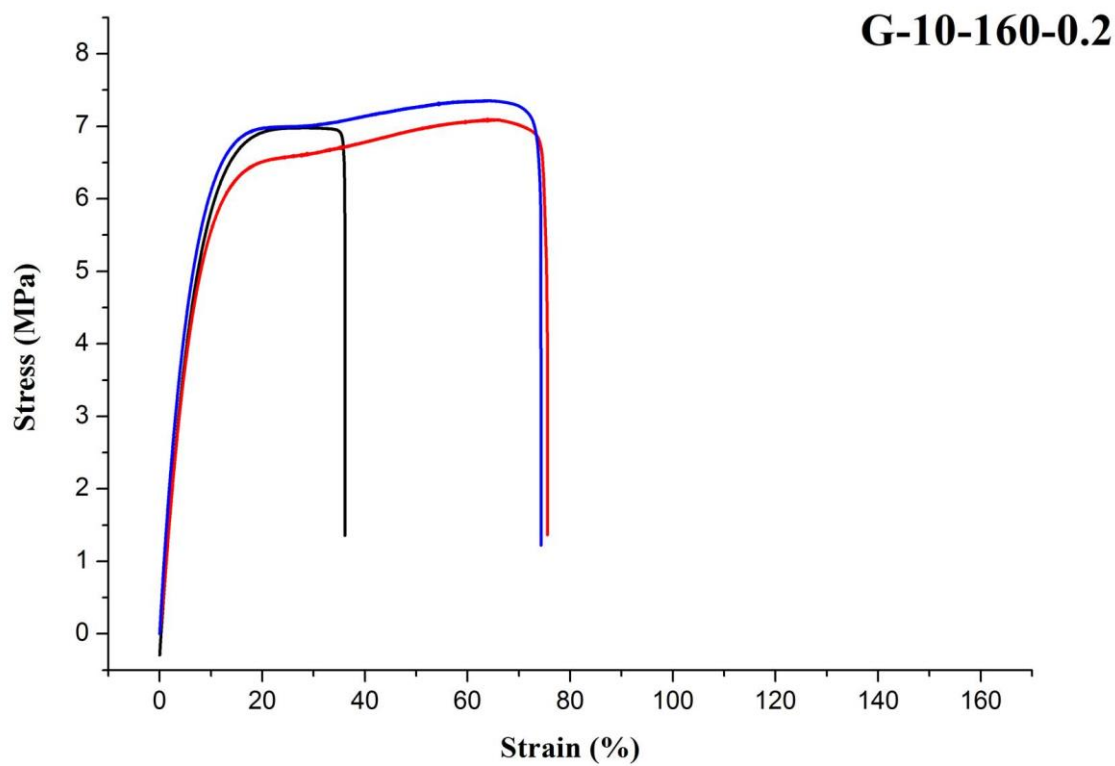
Appendix B: Original stress-strain plots for HDPE tensile test

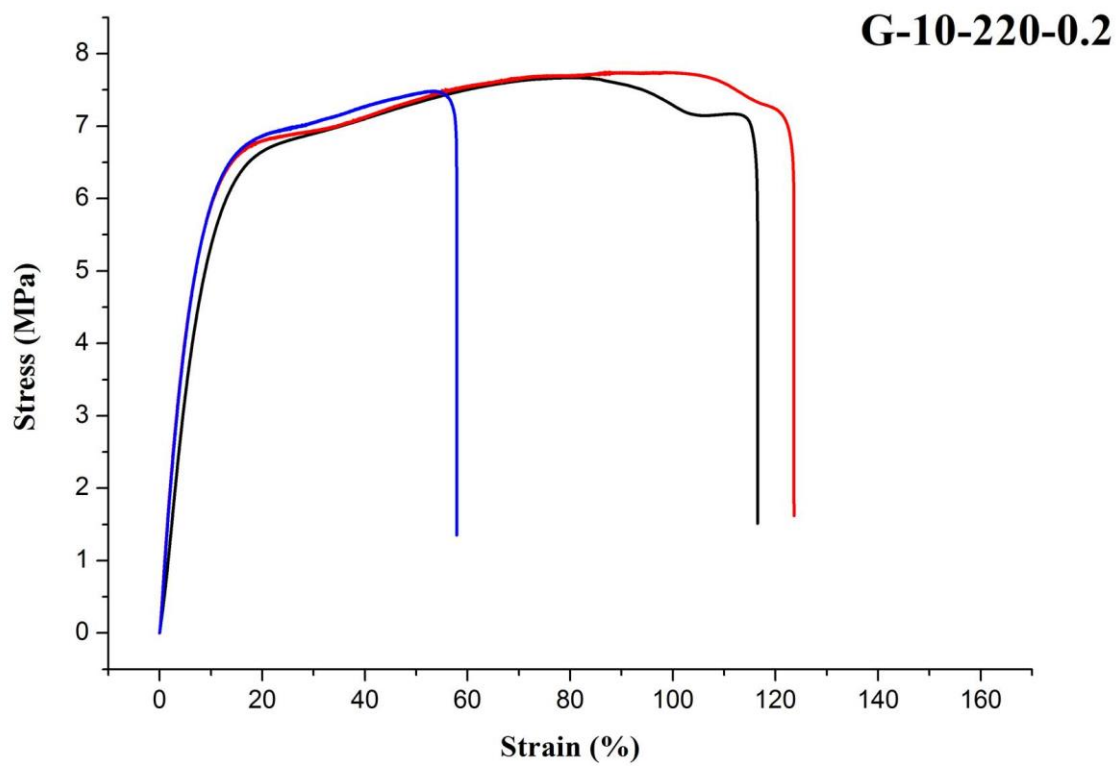
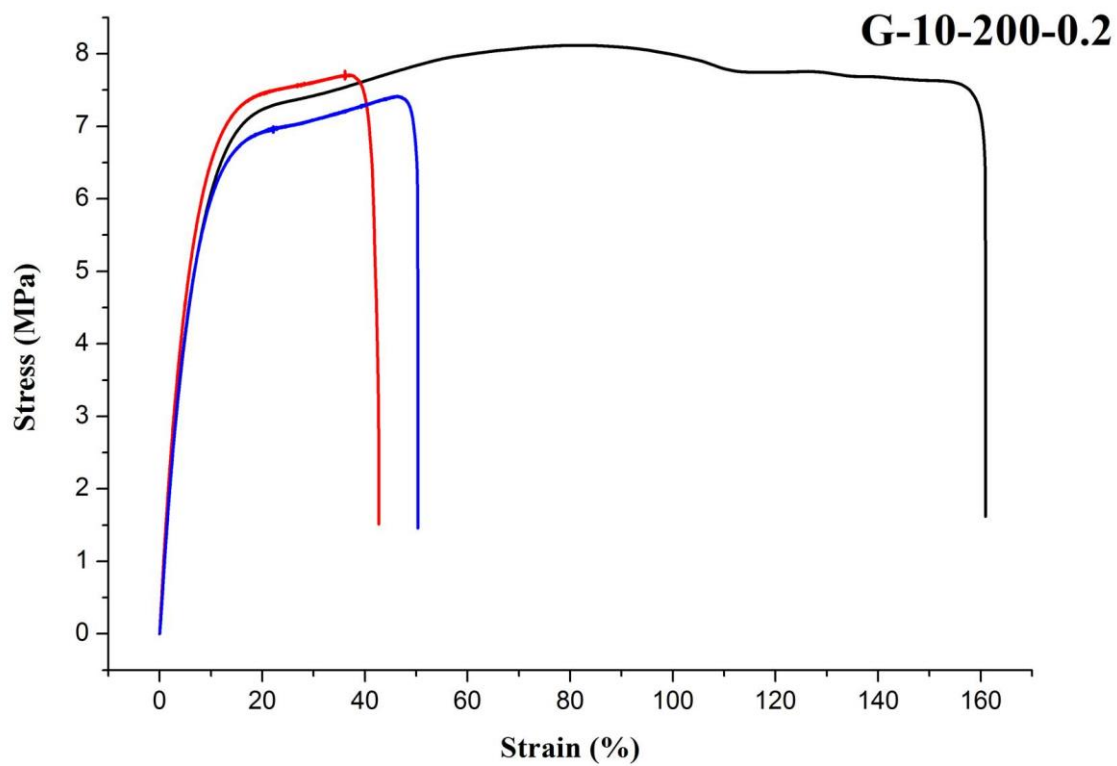


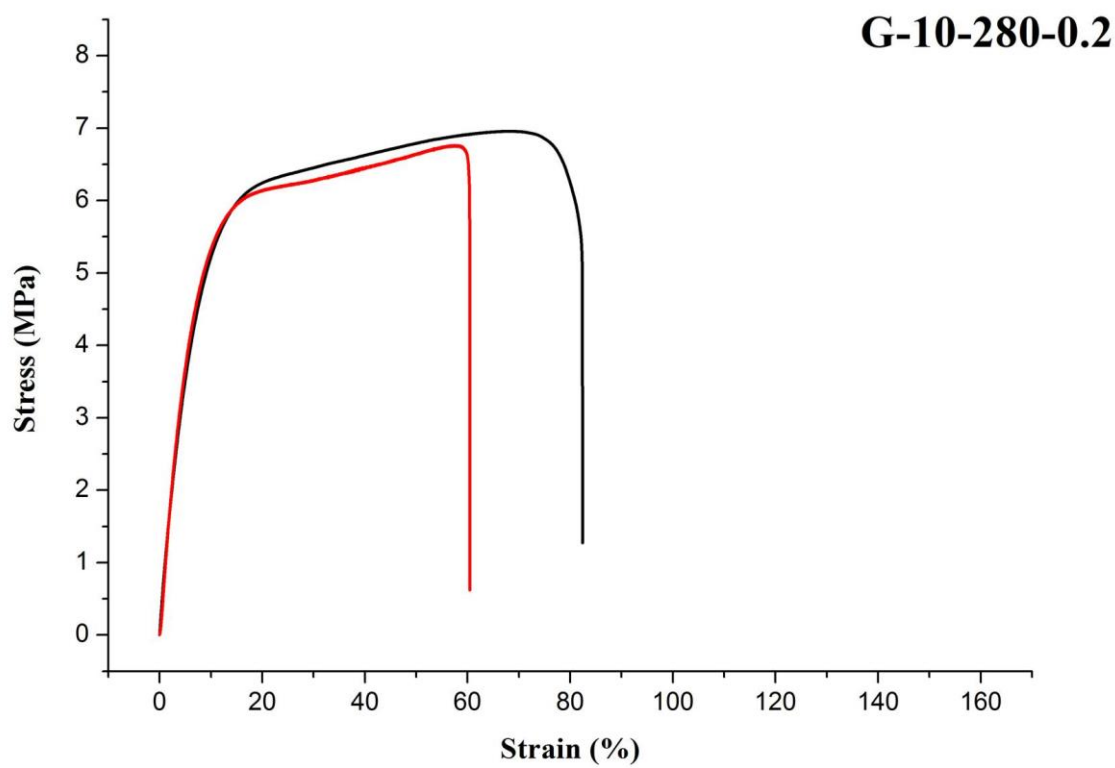
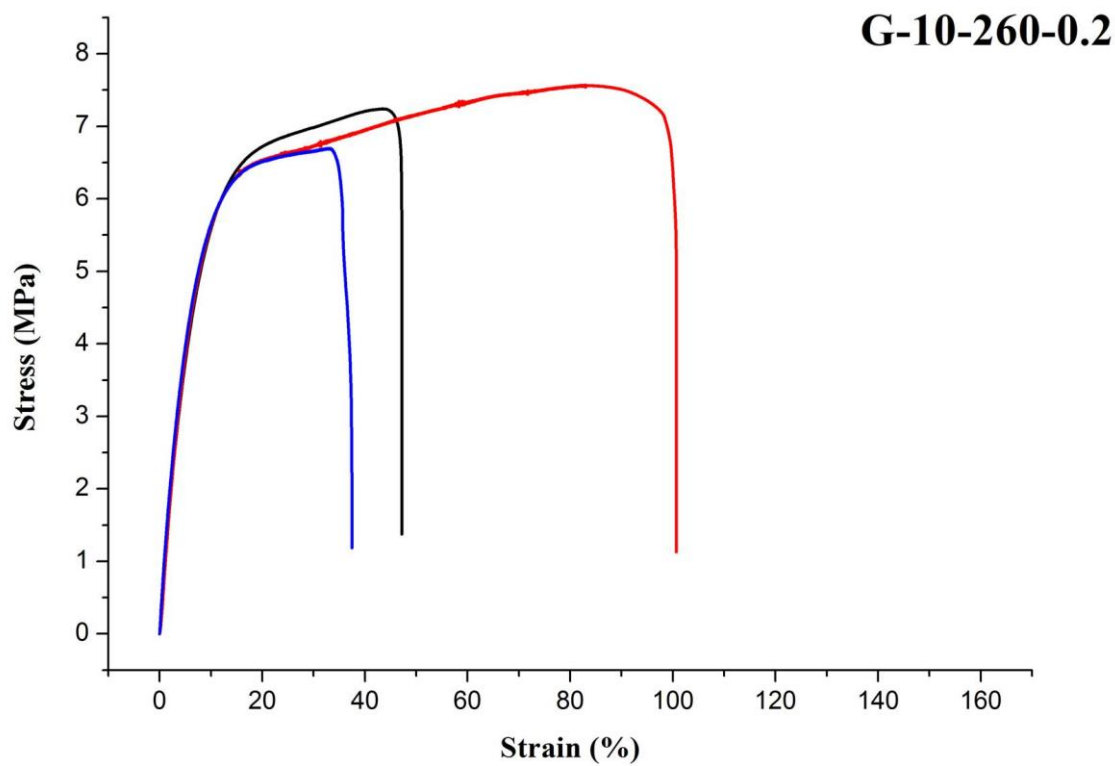












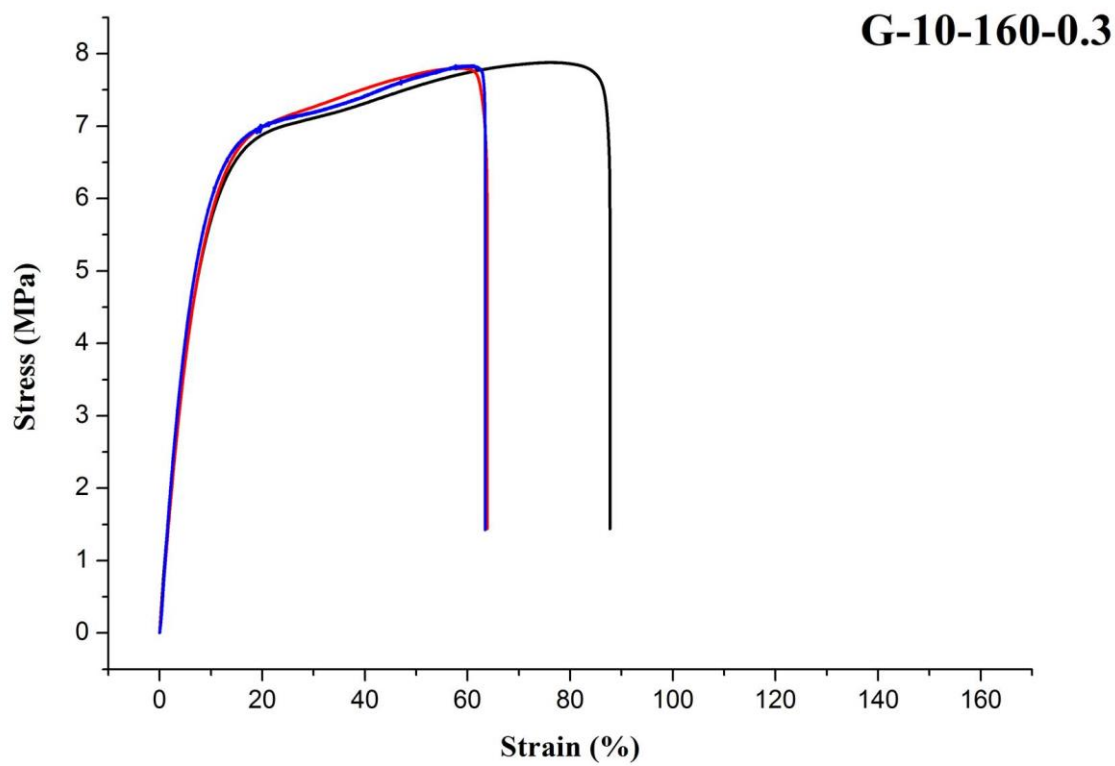
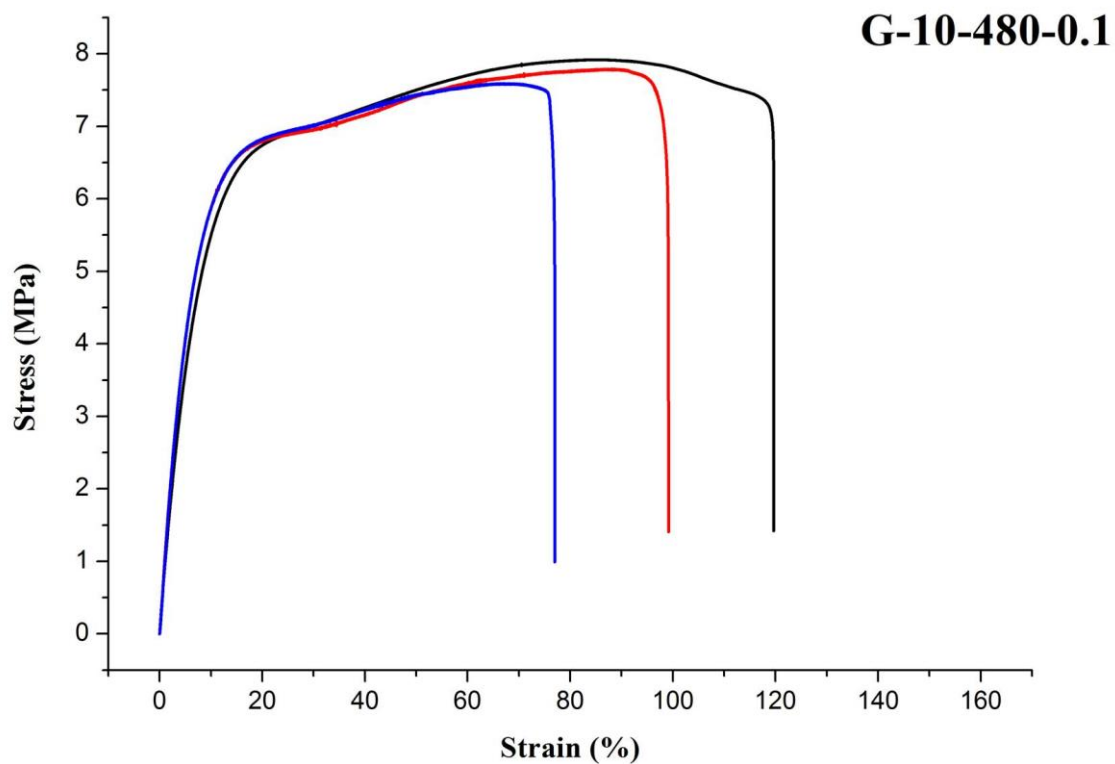


Figure B.1: Original stress-strain plots for HDPE tensile test ('G-X-X-X' represents 'Gaussian beam-power-scanning speed-scan spacing')

Appendix C: Resistivity claculation for silver paste tracks

Table C.1: The resistivity comparisons of silver paste tracks cured at different conditions

A. laser cured sample

| Power (W) | Scanning speed (mm/s) | Resistivity (*10 ⁻⁴ Ωcm) | | | Mean Resistivity (*10 ⁻⁴ Ωcm) | Standard Deviation |
|---------------|--------------------------|--|------|------|---|-----------------------|
| Gaussian beam | | | | | | |
| 1.5 | 1 | 2.61 | 2.65 | 2.76 | 2.67 | 0.08 |
| 1.9 | 1 | 2.24 | 2.34 | 2.58 | 2.39 | 0.17 |
| 2.3 | 0.1 | 0.96 | 0.96 | 1.02 | 0.98 | 0.03 |
| 2.3 | 0.3 | 0.74 | 0.79 | 0.82 | 0.78 | 0.04 |
| 2.3 | 0.6 | 1.17 | 1.16 | 1.24 | 1.19 | 0.04 |
| 2.3 | 1 | 1.33 | 1.38 | 1.42 | 1.38 | 0.05 |
| 2.3 | 2 | 1.5 | 1.51 | 1.56 | 1.52 | 0.03 |
| 2.3 | 3 | 2.25 | 2.34 | 2.38 | 2.32 | 0.07 |
| 2.7 | 1 | 1.42 | 1.43 | 1.54 | 1.46 | 0.07 |
| 3.1 | 1 | 2.33 | 2.5 | 2.56 | 2.46 | 0.12 |
| Pedestal beam | | | | | | |
| 1.5 | 1 | 2.79 | 2.86 | 2.91 | 2.85 | 0.06 |
| 1.9 | 1 | 1.7 | 1.71 | 1.84 | 1.75 | 0.08 |
| 2.3 | 0.1 | 0.64 | 0.68 | 0.73 | 0.68 | 0.05 |
| 2.3 | 0.3 | 0.61 | 0.66 | 0.67 | 0.65 | 0.03 |
| 2.3 | 0.6 | 1.04 | 1.14 | 1.17 | 1.12 | 0.07 |
| 2.3 | 1 | 1.58 | 1.66 | 1.66 | 1.63 | 0.05 |
| 2.3 | 2 | 1.69 | 1.8 | 1.84 | 1.78 | 0.08 |
| 2.3 | 3 | 1.85 | 1.95 | 2.04 | 1.95 | 0.10 |
| 2.7 | 1 | 1.28 | 1.31 | 1.35 | 1.31 | 0.04 |
| 3.1 | 1 | 1.31 | 1.31 | 1.37 | 1.33 | 0.03 |

B. oven cured sample

| Temperature (°C) | Time (h) | Resistivity (*10 ⁻⁴ Ωcm) | | | Mean Resistivity (*10 ⁻⁴ Ωcm) | Standard Deviation |
|---------------------|----------|--|------|------|---|-----------------------|
| 150 | 0.5 | 1.28 | 1.34 | 1.35 | 1.32 | 0.04 |

Note: the cross-section area for all samples are used as 0.0875mm²

Appendix D: Resistivity calculation for copper/HDPE tracks

Table D.1: The resistivity comparisons of sintered copper/HDPE mixture at different conditions (the measured length is fixed as 1cm)

| Copper content | Beam shape | Power (W) | Scanning speed (mm/s) | Resistance value (Ω/cm) | | | Cross-section area ($\ast 10^{-4}\text{cm}^2$) | Mean Resistivity ($\ast 10^{-4}\Omega\text{cm}$) | Standard Deviation |
|-------------------|------------|-----------|-----------------------|---|-------|-------|--|--|--------------------|
| Single track scan | | | | | | | | | |
| 30% | G | 10 | 120 | N/A | N/A | N/A | 2.79 | N/A | N/A |
| 30% | G | 10 | 100 | N/A | N/A | N/A | 4.02 | N/A | N/A |
| 30% | G | 10 | 80 | 15.28 | 15.73 | 18.32 | 5.85 | 96.19 | 9.59 |
| 30% | G | 15 | 120 | 12.22 | 14.13 | 19.52 | 6.04 | 92.35 | 22.86 |
| 30% | G | 15 | 100 | 5.73 | 6.71 | 6.72 | 6.28 | 40.11 | 3.57 |
| 30% | G | 15 | 80 | 6.11 | 6.18 | 6.64 | 7.42 | 46.82 | 2.13 |
| 30% | G | 20 | 120 | 4.97 | 5.52 | 5.54 | 6.1 | 32.59 | 1.97 |
| 30% | G | 20 | 100 | 3.14 | 3.92 | 4.08 | 7.51 | 27.89 | 3.77 |
| 30% | G | 20 | 80 | 3.32 | 3.37 | 3.48 | 7.85 | 26.61 | 0.64 |
| 40% | G | 20 | 120 | 4.03 | 4.2 | 4.86 | 3.61 | 15.75 | 1.58 |
| 50% | G | 20 | 120 | 3.07 | 3.51 | 3.51 | 2.2 | 7.34 | 0.55 |
| 60% | G | 10 | 120 | N/A | N/A | N/A | 5.26 | N/A | N/A |
| 60% | G | 10 | 100 | 5.29 | 5.41 | 5.45 | 5.88 | 31.65 | 0.48 |
| 60% | G | 10 | 80 | 1.72 | 1.89 | 2.01 | 6.41 | 12.01 | 0.93 |
| 60% | G | 15 | 120 | 3.43 | 3.44 | 3.58 | 5.44 | 18.95 | 0.45 |
| 60% | G | 15 | 100 | 1.58 | 1.77 | 1.79 | 5.68 | 9.73 | 0.65 |
| 60% | G | 15 | 80 | 1.23 | 1.41 | 1.72 | 6.51 | 9.46 | 1.61 |
| 60% | G | 20 | 140 | 2.44 | 2.82 | 3.16 | 3.23 | 9.07 | 1.16 |
| 60% | G | 20 | 120 | 0.94 | 1.21 | 1.33 | 3.11 | 3.61 | 0.62 |
| 60% | G | 20 | 100 | 0.62 | 0.62 | 0.65 | 3.36 | 2.12 | 0.05 |
| 60% | G | 20 | 80 | 0.41 | 0.42 | 0.44 | 4.59 | 1.94 | 0.07 |

| | | | | | | | | | |
|--------------------|---|----|-----|-------|-------|-------|------|--------|-------|
| 60% | G | 20 | 60 | 0.8 | 0.85 | 0.85 | 6.32 | 5.27 | 0.18 |
| 60% | G | 20 | 40 | 16.33 | 16.82 | 19.05 | 6.97 | 121.28 | 10.10 |
| 60% | G | 25 | 120 | 1.38 | 1.51 | 1.55 | 3.35 | 4.96 | 0.29 |
| 60% | G | 30 | 120 | 3.68 | 4.42 | 4.73 | 4.96 | 21.21 | 2.67 |
| 60% | G | 35 | 120 | 33.19 | 35.31 | 45.34 | 5.23 | 198.46 | 33.94 |
| 60% | G | 40 | 120 | N/A | N/A | N/A | 5.92 | N/A | N/A |
| 60% | G | 8 | 60 | 1.33 | 1.35 | 1.49 | 2.46 | 3.42 | 0.21 |
| 60% | P | 8 | 60 | 1.13 | 1.24 | 1.25 | 2.51 | 3.03 | 0.17 |
| 60% | G | 8 | 40 | 0.73 | 0.85 | 1.02 | 3.47 | 3.01 | 0.51 |
| 60% | P | 8 | 40 | 0.89 | 0.94 | 1.02 | 3.02 | 2.87 | 0.20 |
| 60% | G | 8 | 20 | 0.37 | 0.39 | 0.39 | 5.79 | 2.22 | 0.07 |
| 60% | P | 8 | 20 | 0.42 | 0.43 | 0.49 | 5.68 | 2.54 | 0.22 |
| 70% | G | 20 | 120 | 1.17 | 1.52 | 1.58 | 3.3 | 4.68 | 0.73 |
| 100% | G | 20 | 120 | N/A | N/A | N/A | 1.86 | N/A | N/A |
| | | | | | | | | | |
| Raster scan | | | | | | | | | |
| 60% | G | 10 | 120 | 0.7 | 0.71 | 0.82 | 4.82 | 3.58 | 0.32 |
| 60% | G | 10 | 100 | 0.37 | 0.48 | 0.52 | 5.71 | 2.61 | 0.44 |
| 60% | G | 10 | 80 | 0.42 | 0.42 | 0.47 | 6.83 | 2.98 | 0.19 |
| 60% | G | 15 | 120 | 0.14 | 0.15 | 0.17 | 6.08 | 0.93 | 0.09 |
| 60% | G | 15 | 100 | 0.12 | 0.16 | 0.18 | 6.74 | 1.03 | 0.20 |
| 60% | G | 15 | 80 | 0.09 | 0.09 | 0.11 | 7.51 | 0.73 | 0.08 |
| 60% | G | 20 | 120 | 0.12 | 0.12 | 0.13 | 6.41 | 0.79 | 0.03 |
| 60% | G | 20 | 100 | 0.06 | 0.06 | 0.06 | 7.12 | 0.43 | 0 |
| 60% | G | 20 | 80 | 0.04 | 0.04 | 0.05 | 8.06 | 0.35 | 0.04 |
| | | | | | | | | | |